PRECISION ENGINEERING CENTER

2000 ANNUAL REPORT
VOLUME XVIII
January 2001

Sponsors:

3M Corporation
Burleigh Instruments
Eastman Kodak Company
International Business Machines Corporation
Los Alamos National Laboratory
National Science Foundation
Oak Ridge National Laboratory
Vistakon, Johnson & Johnson Vision Products

Faculty:

Thomas Dow, Editor
Greg Buckner
Jeffrey Eischen
Karl Falter
Dieter Griffis
Hans Hallen
Andrey Kuznetsov
Paul Ro
Phil Russell
Ronald Scattergood
Albert Shih
David Youden

Graduate Students:

Brad Austin
Markus Bauer
Matthew Cerniway
David Gill
Matias Heinrich
David Kametz
Byoung Loh
Michael Long
Bryan Love
Edward Miller
Gang Mou
Winton Panusittikorn
Jun Qu
Brian Rhoney
Qun Wan
Tao Wu

Undergraduate Students:

Jason Stevens

Staff:

Kenneth Garrard
Ena Meng
Alexander Sohn

TABLE OF CONTENTS

METROLOGY

ACTUATION

CONTROL

FABRICATION

SUMMARY

The goals of the Precision Engineering Center are: 1) to improve the understanding and capability of precision metrology, actuation, manufacturing and assembly processes; and 2) to train a new generation of engineers and scientists with the background and experience to transfer this new knowledge to industry. Because the problems related to precision engineering originate from a variety of sources, significant progress can only be achieved by applying a multidisciplinary approach; one in which the faculty, students, staff and sponsors work together to identify important research issues and find the optimum solutions. Such an environment has been created and nurtured at the PEC over the past 18 years and the new technology developed as well as the 70 graduates attest to the quality of the results.

The 2000 Annual Report summarizes the progress over the past year by the faculty, students and staff in the Precision Engineering Center. During the past year, this group included 6 faculty, 12 graduate students, 1 undergraduate student, 2 full-time technical staff members and 1 administrative staff member. Representing two different Departments from the College of Engineering, this diverse group of scientists and engineers provides a wealth of experience to address precision engineering problems. The format of this Annual Report separates the research effort into individual projects, however, this should not hide the significant interaction that occurs between among the faculty, staff and students. Weekly seminars by the students and faculty provide information and feedback as well as practice in presentation technique. Teamwork and group interactions are a hallmark of research at the PEC and this contributes to both the quality of the research as well as the training of the graduates.

The summaries of individual projects that follow are arranged in the same order as the body of the report, that is the four broad categories of 1) metrology, 2) actuation, 3) control and 4) fabrication.

1) METROLOGY

The emphasis of the metrology projects has been to develop new techniques that can be used to characterize surface structure and shape as well as measure important parameters such as tool force.

Lapping Plate Charging Lapping the air bearing surface of a hard disk head is one of the last steps in the production process. This surface is about 1 mm square and must have a surface finish less than 1 nm and be flat to the order of 10 nm. The goal of this research is to optimize the preparation of the lap plate used to produce this surface. The current technique involves creating randomly overlapping circular scratches and then charging the peaks of this surface with sub-micrometer diamonds. The randomness of this texturing process is a suspect in the lack of repeatability in the head lapping results. As a result, new plate preparation processes are being evaluated as well as techniques to measure the effectiveness of the charging process.

Bend Effect Due to Mechanical Scribing Putting a scratch across the surface of a thin plate can change the shape of that plate. This process has been used to make subtle corrections to the figure error of hard disk heads. The goal of this project is to study the role of load, scribe geometry, speed and number of scribes on the resulting shape of a hard disk head. A test system consisting of a microhardness tester with a motorized stage was used to produce controlled diamond scribes on ceramic samples. The bending distortion is a result of the residual stresses generated by the scribing operation and data from the measurements were analyzed using computer software to extract the net bending effect. An analytical model for the bend effect based on the residual stresses due to line-force dipoles was developed.

Laser Scribing For Precision Shape Modification Another method of modifying the shape of hard disk heads involves laser rather than mechanical scribing. Like the mechanical scribing, a laser scribing system produces curvature by inducing residual stress into the slider. Predicting the curvature created by a pattern of scribes is important to control the final shape of the sliding surface. Using finite element analysis, a force system that produces stresses similar to the laser scribing has been identified. A library of scribing results have been built using this model that allow, through superposition, the shape of complicated scribing patterns to be predicted. Ultimately, the inverse problem will be solved, that is finding a scribing pattern to generate a desired change in shape.

Measuring Hydrated Optical Surfaces Measuring the surface characteristics of compliant optical materials filled with fluid presents some unique challenges: 1) few, if any, instruments are capable of performing measurements in a fluid, 2) the material has a low modulus and any contact load deflects the surface and influences the results, and 3) the refractive index change at the surface of the material is very small because it is submerged in fluid. Given these challenges, the best method for measuring surface finish of these materials is by scanning probe microscopy in a fluid cell. A technique for making such measurements is presented and the results of surface finish measurements are described.

Design Of The Polar Profilometer *Polaris* Profilometers for measuring form and roughness have traditionally been based on rectangular coordinates, but such designs have limitations when measuring certain geometries, for example, high aspect-ratio optics whose shape is more polar than rectangular in nature. To meet this need, a polar profilometer has been designed and is being built at the PEC. This device will measure both concave and convex parts ranging from hemispheres to aspheres within a circular measurement field 50 mm in diameter. The target resolution is no less than 100 nm with an overall accuracy of at least 500 nm.

Control and Data Acquisition Systems for *Polaris* The machine controls and data acquisition components for the polar profilometer have been selected and the user interface software design is nearing completion. Operating procedures have been established for part setup, alignment, reference path specification and measurement. The hardware platform is a Delta Tau UMAC controller coupled to an IBM PC via USB. This choice offers significant advantages for system integration and represents the future direction of flexible machine controls. The user interface software is designed to run on any PC and as a result can evolve independent of the real-time control software and hardware.

2) ACTUATION

Real-time control is a necessary technique to improve the precision — accuracy and repeatability — of a fabrication or measurement process. The metrology activities discussed above are intended to develop tools or devices to measure shape, force or properties. Equally important are improved actuators with the ability to create the motion necessary to correct the error.

Design of a Ultrasonic Piezoelectric Motor A new design for an ultrasonic motor is being developed that uses independent, orthogonal, ultrasonic motions of the tip of a piezoelectric actuator to move a slideway. Several designs have been built involving independently driven piezoelectric elements, one generating the normal load at the interface and the second generating the tangential driving force. The challenge in developing this motor are 1) the actuator needs to have two different mode shapes at nearly the same frequency and 2) each mode shape must be exclusively excited by one actuator and not by the other. Finite element analysis (FEA) has been used to include all significant features such as the anisotropy of the piezoelectric material, the exact properties and dimensions of the actuators (including any glue joints) when developing each design. The mode shapes and natural frequencies for each prototype have been measured, compared with the computer models and an optimized design has evolved.

Development of a Piezo Actuator for Cryogenic Environments The Next Generation Space Telescope has a large mirror that must collapse to fit in the cargo bay of the Shuttle Orbiter. Once transported to the cryogenic environment of space (20 to 60 Kelvin), the mirror must be unfolded and the focal point adjusted using many small actuators. These actuators need a stroke of 10 mm, resolution on the order of 10 nm, a design life of 10,000 to 100,000 cycles and must be able to hold their position in a power-off mode. The PEC is developing actuator designs for this application that are built around an 80-pitch screw actuated by piezoelectric motors. The concept involves a fixed nut to support the screw and a driven nut to rotate it. A brake is used to hold the screw when the driven nut is retracted at the end of each actuation cycle.

Design of Ultrasonic Flexural Wave Resonator Structures A miniature cooling system for microelectronics has been conceived that uses a vibrating piezoelectric beam to increase convective heat transfer. One of the key issues is the optimal design of the resonator structures. Natural frequencies and amplitudes of vibration predicted by a finite element analysis are used as the criteria to determine the appropriate dimensions of the resonator systems. Currently, length and width combinations of 2mm by 1mm and 4mm by 2mm are being investigated with different boundary conditions. The goal is to find an acceptable thickness range that will result in the first-mode resonance being in the ultrasonic range, that is, greater than 30 kHz. The effect of a constant rate voltage field is also discussed.

Ultrasonic Acoustic Streaming as a Cooling Mechanism The cooling effect of ultrasonic acoustic streaming of the air between two plates is being modeled. One plate is the fixed heat source from a chip on IC board, for example, and the other is a vibrating PZT plate with a frequency in the ultrasonic range. The fluid flow and energy equations are written in terms of perturbations on top of the harmonic solution. The first order (linear function of the perturbation term) equations have been solved and the results are shown. This solution will be used as a driving force term in the solution of the higher order equations. The cooling effect associated with steady acoustic streaming regime, the emphasis of this project, appears in the second order terms.

3) CONTROL

Precision control problems involve both the characterization of the electromechanical system and the selection of hardware and software to implement the control algorithm. As a consequence, study of each of these aspects are important research topics for the PEC.

Enhanced Convective Heat Transfer using Acoustic Streaming The heat transfer associated with acoustic streaming induced by ultrasonic flexural vibrations is being investigated. Two distinctive acoustic streaming patterns of the flexural vibrations are observed. However, acoustic streaming velocity from computational fluid dynamics (CFD) simulation exceeds the theoretically estimated velocity by a factor ranging from 10 to 100. Both CFD simulation and analytical analysis reveal that the acoustic streaming velocity is proportional to the square of the vibration amplitude and the wavelength of the vibrating beam that decreases with the excitation frequency. It is observed that the streaming velocity increases significantly if an open ended channel is used and decreases with the excitation frequency.

Control of Friction-Based Object Transport Using Two-Mode Ultrasonic Excitation Control of a transport system that employs friction force to drive an object on an ultrasonic flexural vibrating beam is described. The mechanism of a friction drive is analyzed and the potential to automate the object transport prototype is described. Hertzian contact theory, a modified spring model and Coulomb friction were used to model the normal force and driving friction. Simulation results of the estimated slider displacement verify the accuracy of the friction model. A sliding mode controller is designed for the object transport prototype and the results of this control scheme operating at a low sampling frequency of 10 Hz are compared with the result of PID control. It is shown that the trajectory performance of the sliding mode control is superior to that of PID control.

4) FABRICATION

High-speed milling, plastic replication and a new technique for diamond turning have been the focus of the fabrication process research over the past year.

Tool Deflection Compensation A technique to compensate for deflection of small milling tools (diameter < 1 mm) has been demonstrated. This open loop technique involves: 1) predicting the cutting and thrust forces, 2) applying these forces to the tool, 3) calculating the tool deflection, 4) finding the magnitude of the error and finally 5) creating a new tool path to eliminate this error. Two experiments were used to demonstrate the effectiveness of this compensation technique; a slot and a large circular groove. Each experiment reduced the error due to tool deflection by an order of magnitude from 20-50 μm to 2-5 μm.

Precision Replication of Optics The fields of optical communication, photonics, and display technologies require the development of high-volume yet high-precision production methods. Molded polymer optics fulfill many of the requirements for these parts, but still present challenges. The objective of this research is to investigate the replication of features in precision optics and the co-molding of these optical surfaces onto thermally stable substrates. Results have shown that nanometer size features can be successfully replicated in polymer optics by UV cure and injection molding. An injection molding machine has been delivered and injection molding process variables have been studied to reduce the form error of replicated optics. Modifications to this machine have also begun to co-mold thin polymer optics onto glass substrates.

Vibration Assisted Machining (VAM): the *UltraMill* Turning has been the precision manufacturing method of choice over milling due to the combination of relatively short machining time and high-quality surface finish from the single crystal diamond tools. However, a major advantage of milling is the ability to uncouple the cutting speed from the material feed rate. A hybrid system is being developed that combines the advantage of milling and turning by driving the tool in a high-speed, small-displacement elliptical cutting motion. Falling under the classification of Vibration Assisted Machining (VAM), the UltraMill (UM) research is also exploring the details of the tool-chip interaction during each cutting cycle. Cutting force reduction is a key advantage of this process and forces were reduced by as much as 50% verses standard cutting without any increase in surface roughness. Under development is a higher speed version of the UM, ~8 kHz or 480,000 rpm equivalent. The effects of tool wear in elliptical milling and the potential of diamond milling of non-typical materials, i.e. steel and ceramics, will be investigated.

1 LAPPING PLATE CHARGING

David A. Kametz
Graduate Student
Jason M. Stevens
Undergraduate Student
Thomas A. Dow
Professor
Mechanical and Aerospace Engineering

Lapping the air bearing surface is one of the last steps in the production of hard disk heads. This surface is about 1 mm square and must have a surface finish less than 1 nm and be flat to the order of 10 nm. This challenging task must be accomplished while at the same time placing the read head at a fixed height above the flying surface. The head material is a tough ceramic (AlTiC) and the lapping is accomplished with diamonds impregnated into a tin lap surface. The goal of this research is to optimize the preparation of the lap surface to best accomplish the task of lapping the head. The current technique involves creating overlapping circular scratches on the lap surface with a diamond coated texturing ring, and then charging the surface with sub-micrometer diamonds. This charging process is accomplished by lapping the tin plate with a flat alumina ring flooded with a slurry containing the diamond particles. This process produces a random series of scratches, the details of which are described in this report including the magnitude and variation of the surface roughness, skewness, kurtosis, bearing ratio and peak spacing. The randomness of this texturing process is a suspect in the lack of repeatability in the head lapping results. As a result, a new plate preparation process is being evaluated. This process involves grooving the plate with a diamond tool followed by charging with the alumina ring. The parameters in this process (groove pitch, depth and land ratio) are being evaluated to find the best values for generating a deterministic lapping process.

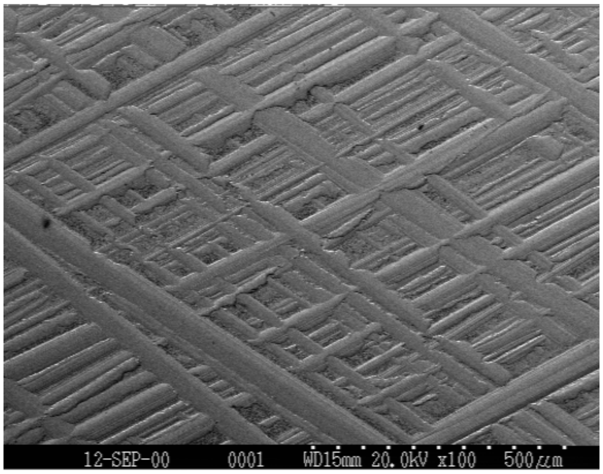

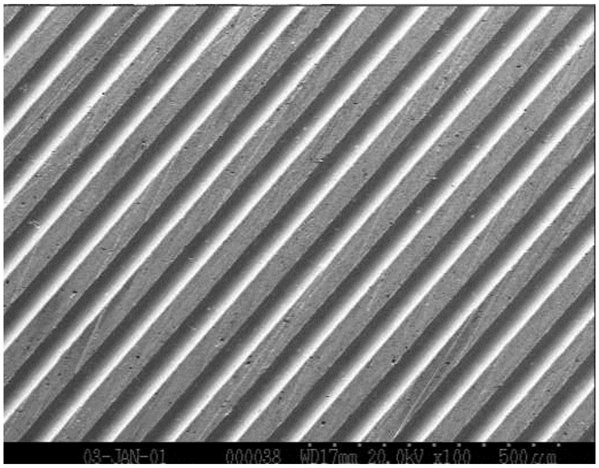

1.1 INTRODUCTION

As the final step in the creation of a hard disk head, the flying surfaces are lapped on a diamond-charged tin lap surface. This process gives the head the required geometry and also produces the desired surface finish. The current process begins with a newly machined tin lap plate. This plate is placed in a lapping machine and a steel ring with coarse plated abrasive is loaded against it. The tin and the texturing ring are brought into contact to create a series of overlapping circular scratches on the plate surface. The texturing ring is then replaced with a smooth alumina ring and the process is repeated except that a fine diamond slurry is spread on the plate surface. The interaction of the alumina surface and the tin plate creates flat plateaus at the intersections of the grooves and pushes diamond into these areas. The result is a flat tin surface with a number of randomly spaced flat regions charged with fine diamond abrasive (size $< 0.5\ \mu$m). This tin lap is used to create the flying surface and is reused after a specific number of heads are polished. One of the drawbacks of the current process is that the texturing/charging process is not too repeatable and different lapping rates are observed for different lapping plates.

The goals of this effort are to correlate the charging of the lapping plates to the lapping process and to develop techniques to measure the quality of the charging process before lapping. IBM has donated an Engis lapping machine for use in this project. This machine is being used to study the charging process to find a more repeatable technique than the current texturing ring method. Once a charging technique is developed, the charged laps will be used at IBM to produce test heads. The quality of these heads will be evaluated both at IBM and the PEC with respect to the material removal rate, surface finish and form error.

1.2 PLATE PREPARATION

The plates used to lap the hard disk heads are tin alloy charged with diamond particles. The plates are first roughened to produce grooves and lands for the polishing process. The diamonds are embedded into the plateaus on the top of the lands and the grooves act as reservoirs to remove the lapping debris from the tin/head interface. The features produced by this roughening process are thought to play an important role in the quality of the heads and this process is being investigated. Two approaches are being studied, texturing and grooving.

1.2.1 TEXTURED LAP PLATE

The texturing process involves rotating a diamond coated “texturing” ring over the surface of the machined tin lap plate. The steel texturing ring has diamond particles on the order of 100 μm in diameter plated in a nickel layer onto the surface. This ring is worn against a steel or cast iron plate to flatten the diamonds until the surface finish of the textured tin plate is 0.64 ± 0.08 μm.

The geometry of the texturing process is shown in Figure 1. The 350 mm diameter tin plate has an aluminum base with a bonded layer of tin alloy on the surface approximately 10 mm thick. The texturing ring has a diameter equal to the radius of the lapping plate. The ring is loaded against the plate and held in position with two supports, but is not driven by the motor. The motion of the lap plate drives the ring at a rotational speed nearly equal to the lap speed in the direction shown.

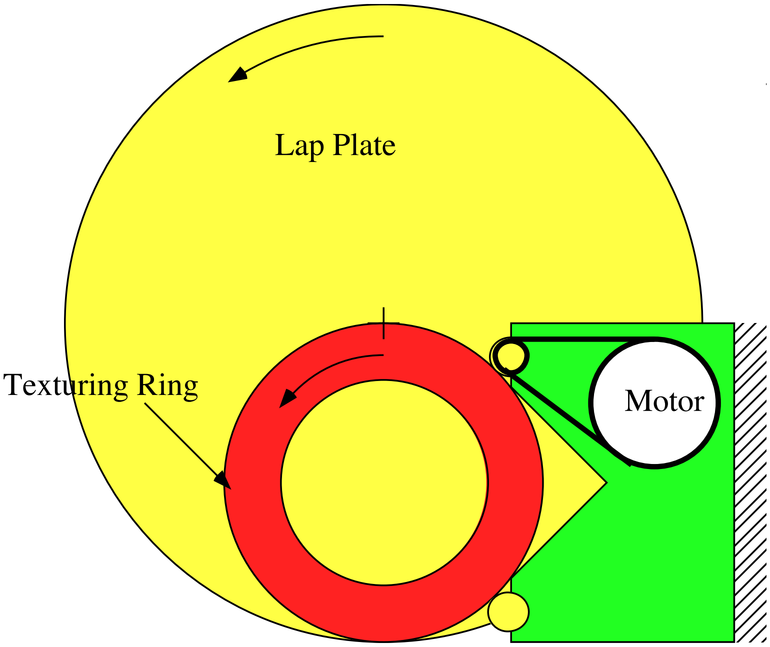

Figure 1. Texturing ring on the lap plate

A plugged lap plate was used for the measurements shown in this report because it makes possible the measurement of the sections in a SEM. In this plate, circular holes (25 mm diameter) are cut in the tin surface and plugs are held in these holes with small, fine pitch screws. One problem with this technique is the softness of the tin plugs and damage to the threads of these plugs when they are installed into the aluminum base. Future plugged plates should be made with removable aluminum sections with tin bonded to them. A sketch of the plate with the location of the plugs is shown in Figure 2.

Each of the plugs was measured to determine the repeatability of the texturing process throughout the area of the plate. Relationships between radial distance from the center of the lapping plate and roughness of the section were studied. The parts were examined visually with a Zeiss microscope, scanned with a Talysurf profilometer and evaluated at high resolution with a scanning electron microscope.

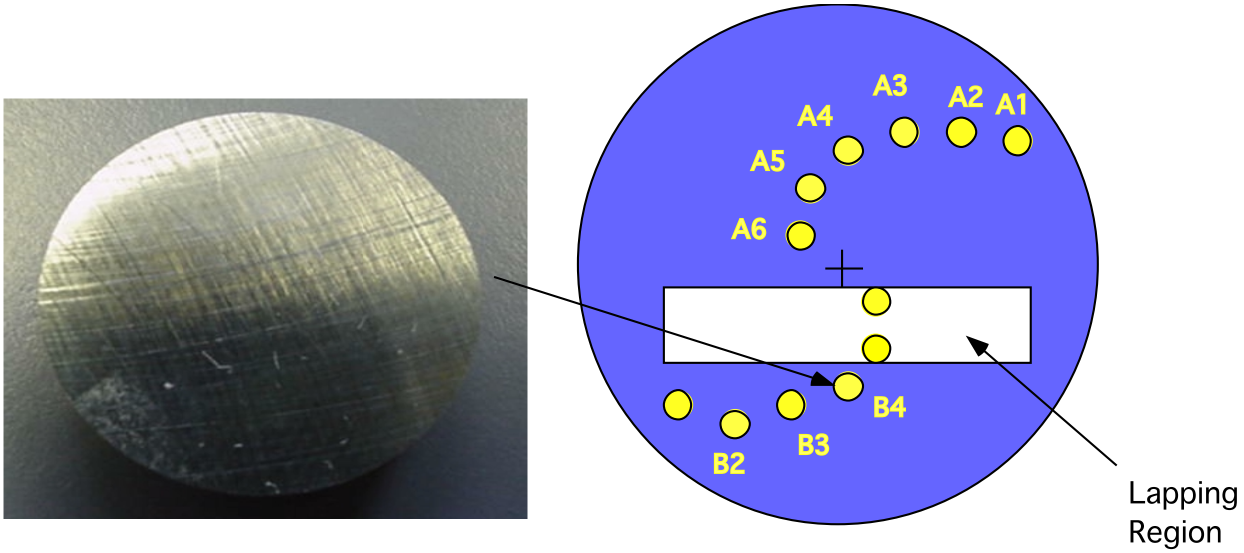

Figure 2. Plugged lapping plate showing the location of the plugs (A1-A6 and B1-B6) and a sample of the textured surface of the 25 mm diameter plugs

Light Microscope All of the tin samples were viewed under a microscope to locate any noticeable differences in the surfaces. They were viewed starting with a 50X magnification then stepped through 100X, 200X, and 500X. Photographs were made at 50X and 500X for each of the samples. The 50X and 500X magnification images were studied and compared, but no major differences could be found to relate position and roughness. Figure 3 shows 50X and 500X photographs of specimen A3. Figure 4 is 50X and 500X images of specimen B3. These are representative of all of the textured surfaces. They show a series of nearly orthogonal grooves from 5 to 45 micrometers wide with a spacing of 2 to 70 micrometers.

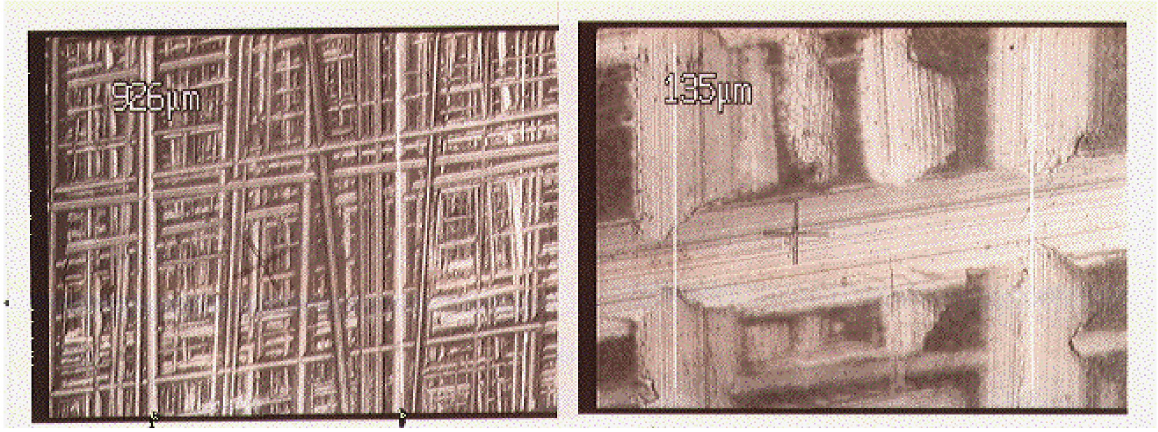

Figure 3. Light microscope image of textured specimen (A3) at 50X (left) and 500X (right)

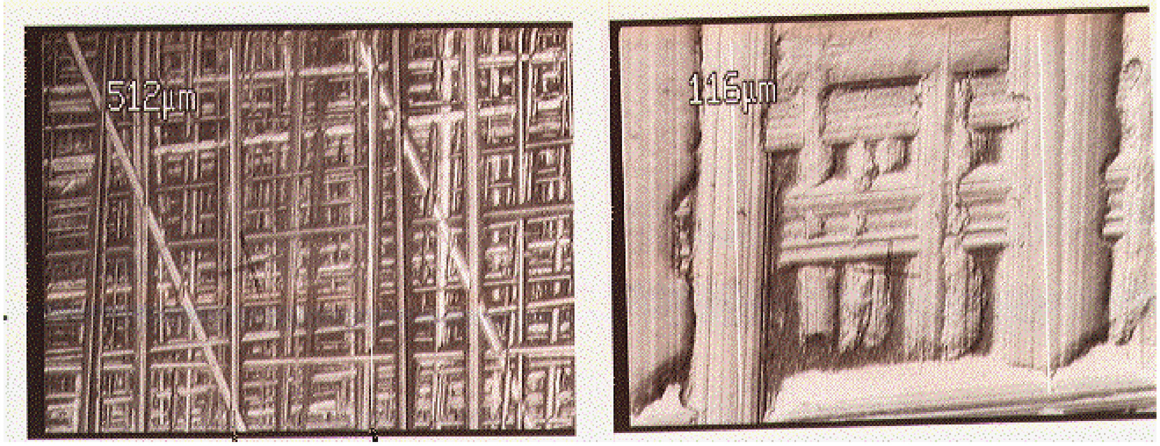

Figure 4. Light microscope image of textured specimen (B3) at 50X (left) and 500X (right)

The surfaces often showed random grooves such as the two diagonal scratches observed in Figure 4. These patterns are a result of the random motion of the texturing ring and the lack of a positive drive system that would produce a fixed relationship between the rotation of the ring and the plate.

Talysurf To provide a quantitative measure of the surface roughness, each surface was scanned in two orthogonal directions using the Talysurf profilometer. The two scans were 20 mm in length and made at 90° angles to each other to see the effect of orientation. Each plug was labeled with X and Y reference directions to define the angle for each scan. Seven of the twelve parts were found to have a raised section in the center caused by the attachment screws deforming the soft tin surface. For these parts, three printouts were made. For each of the affected parts, a single scan of the full surface in the X direction was made. Two other scans were evaluated over part of the surface. These scans started at the surface edge and continued to just before the raised surface. Scans were first analyzed over the entire 20 mm length. Additional scans were analyzed over a 150 μm length to compare with the high-magnification, light microscope pictures.

The top image in Figure 5 shows the full width of specimen A3 illustrating the raised section in the center of the tin plug. This raised region is probably due to distortion of the soft tin from the screw holding it to the aluminum substructure. The lower trace shows the first 7 mm of the surface and clearly illustrates the flat tops on the surface created by the charging process. The profile of the top is very flat compared to the variation in the depth of the grooves. This difference will be evident as other methods of evaluating the surface are discussed.

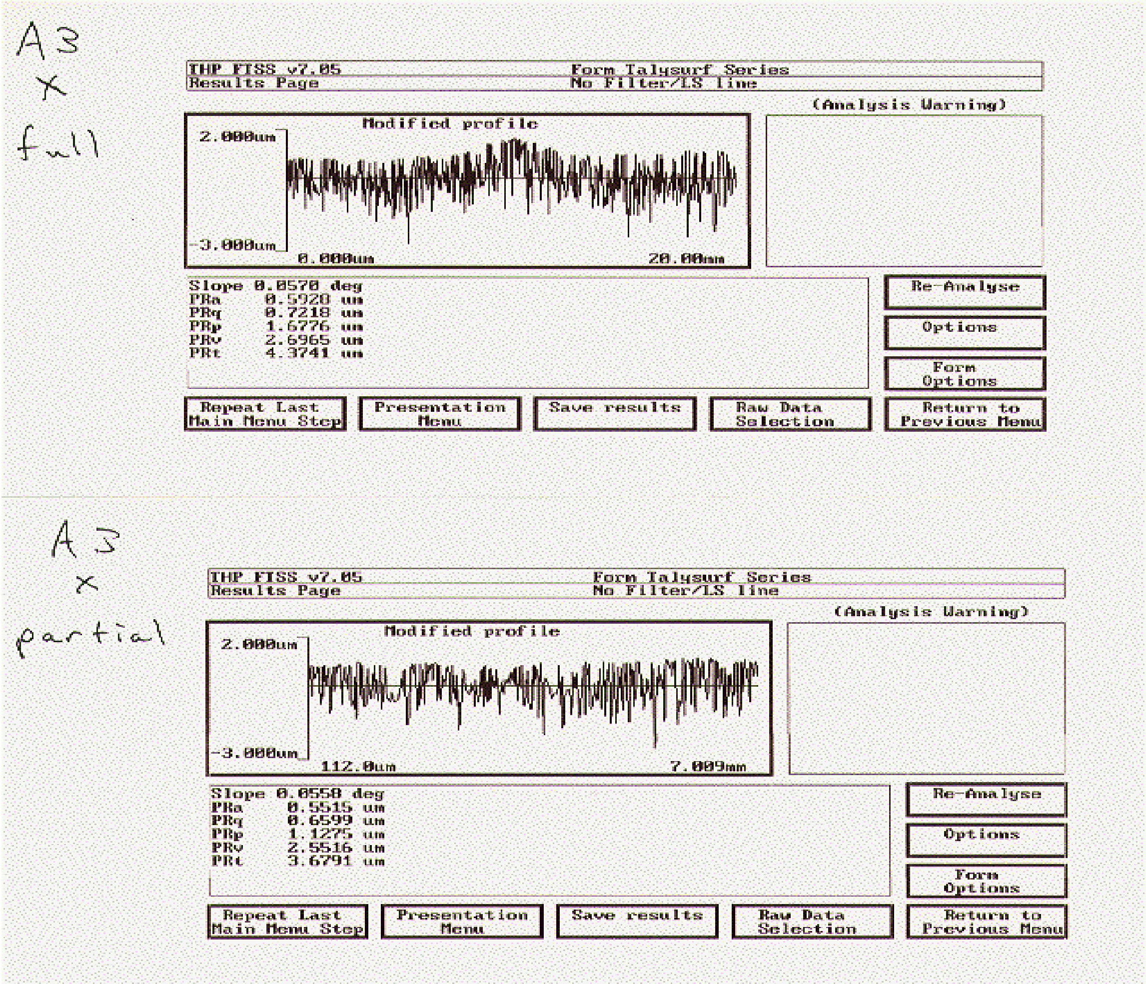

A3
x
full

```
THP FTSS v7.05                    Form Talysurf Series
Results Page                      No Filter/LS line
                                            (Analysis Warning)
              Modified profile
 2.000um
-3.000um
           0.000um                     20.00mm
Slope 0.0570 deg
PRa      0.5920 um
PRq      0.7218 um
PRp      1.6776 um
PRv      2.6965 um
PRt      4.3741 um
```

A3
x
partial

```
THP FTSS v7.05                    Form Talysurf Series
Results Page                      No Filter/LS line
                                            (Analysis Warning)
              Modified profile
 2.000um
-3.000um
           112.0um                     7.009mm
Slope 0.0558 deg
PRa      0.5515 um
PRq      0.6599 um
PRp      1.1275 um
PRv      2.5516 um
PRt      3.6791 um
```

Figure 5. Talysurf image of the surface of the textured tin plate. The top surface shows the raised section in the center of the plug and the lower trace is for the first third of the upper trace.

The magnitude of the surface roughness is an important parameter in evaluating the effectiveness of the texturing process. The Talysurf profiles above indicate the parameters available including average roughness, RMS roughness, height of maximum peak, depth of minimum valley and peak to valley value. The traces above have RMS roughness values between 0.66 and 0.72 μm. Values of these parameters were measured in two orthogonal directions (labeled X and Y) and values for the plugs on the A side were averaged and plotted against radius. The same was done for the plugs on the B side. The results are discussed later in this report.

Figure 6 shows a magnified region of the specimen A3 in both the X and Y directions. The width of these traces is on the order of the 500X micrographs in Figures 3 and 4. In each case there are flat plateaus on the order of 20-30 μm wide and grooves on the order of 60-70 μm wide. However, the plateaus and the grooves are not uniform but reflect the random location of the grooves as the texturing ring rotates hundreds of times over the lap plate.

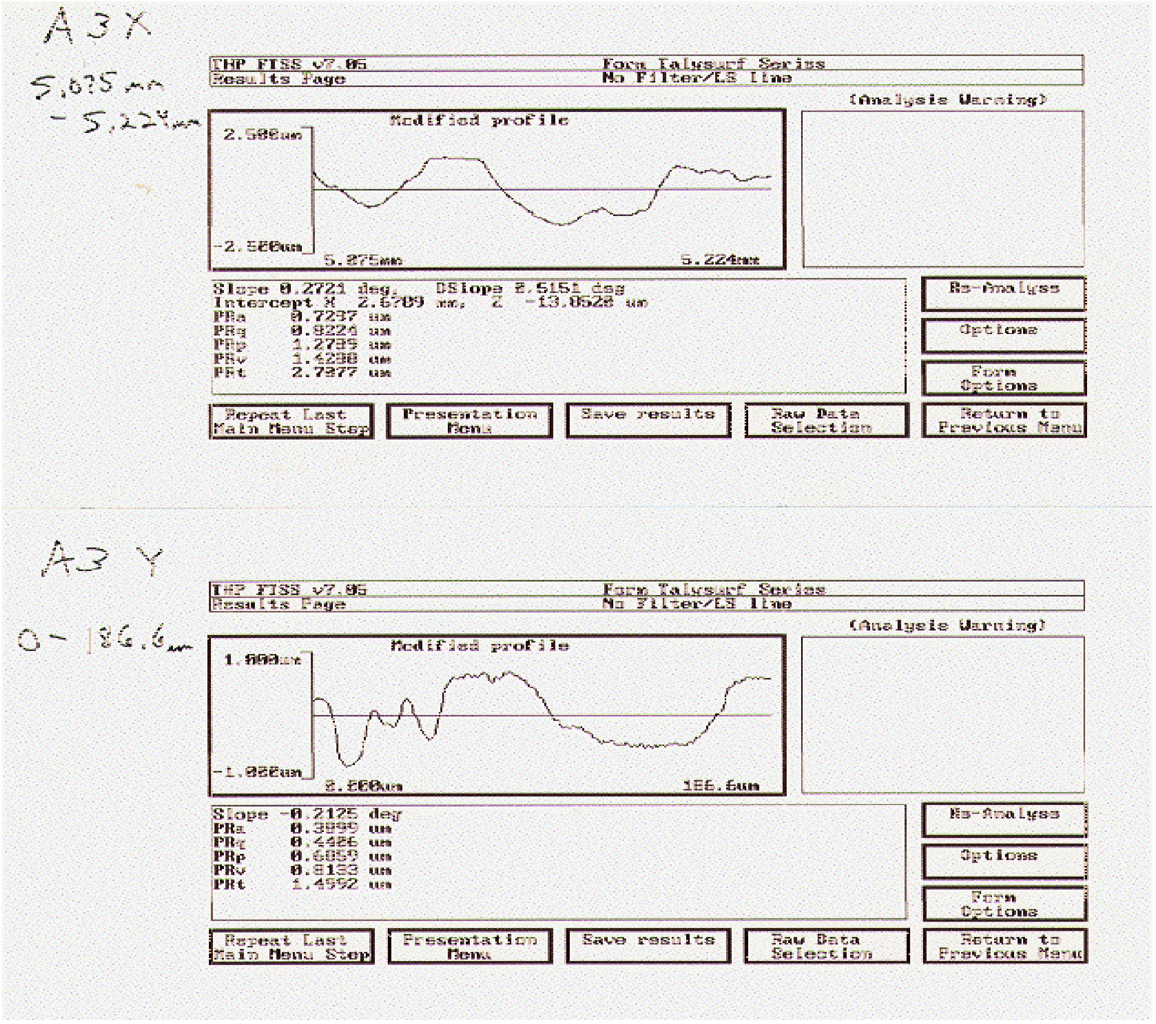

```
Slope 0.2721 deg.   DSlope 2.5151 deg
Intercept X  2.6709 mm,  Z  -13.0528 um
PRa     0.7237 um
PRq     0.8224 um
PRp     1.2739 um
PRv     1.4238 um
PRt     2.7277 um
```

```
Slope -0.2125 deg
PRa     0.3899 um
PRq     0.4486 um
PRp     0.6859 um
PRv     0.8133 um
PRt     1.4992 um
```

Figure 6. Talysurf traces of specimen A3 in the X and Y directions over a similar length to that depicted in the 500X micrographs (X trace width = 150 μm, Y trace = 186 μm)

Analysis of Talysurf Traces One goal of these measurements was to evaluate the repeatability of the textured surface parameters over the surface of the lap plate. Of interest are the following parameters:

1) Peak to peak (peak to valley) roughness – Difference between highest peak and lowest valley.
2) RMS average roughness – Distance from the mean line of the data to the average peak (or valley). This value is related to the square of the difference between individual points and the mean.
3) Skewness - Skewness is a statistical measure of the distribution of peaks and valleys that is proportional to the cube of the distance between individual points and the mean. If the skewness is zero, the peaks and valleys are uniformly distributed about the mean as a random (or normal) distribution would be. A positive skew indicates that there are more and/or

larger peaks than valleys on the surface. A negative skew would indicate more grooves or valleys in the surface.

4) Kurtosis - Kurtosis is proportional to the fourth power of the distance from point to mean and is a way of comparing the grooves and bumps on a surface to a normal distribution. A normal distribution has a kurtosis value of three. A surface with a higher number of extreme points in the peaks or valleys than a normal distribution would have a kurtosis greater than 3. Fewer extreme points away from the mean would yield a kurtosis less than 3.
5) Bearing Ratio - Bearing ratio is a measure of the amount of material available to support a load at some horizontal section of the trace. It takes into account the horizontal spacing of the peaks and valleys rather than just the magnitude as do the measurements described above. Bearing ratios can be specified at any height relative to the mean line. Since the height of the contact is not known, the bearing ratio was calculated at one standard deviation (equal to the RMS average of all the data or 0.622 μm) above the mean; in other words, the contact percentage at the average peak height.
6) Peak Spacing – Another measure of the horizontal distribution of the surface features is the average spacing of the features. Two spacing measurements were taken: the first is the mean spacing between all adjacent peaks, and the second the mean spacing between adjacent peaks that crossed through the mean line. In this case, little peaks on the top of the big peaks would not be counted.

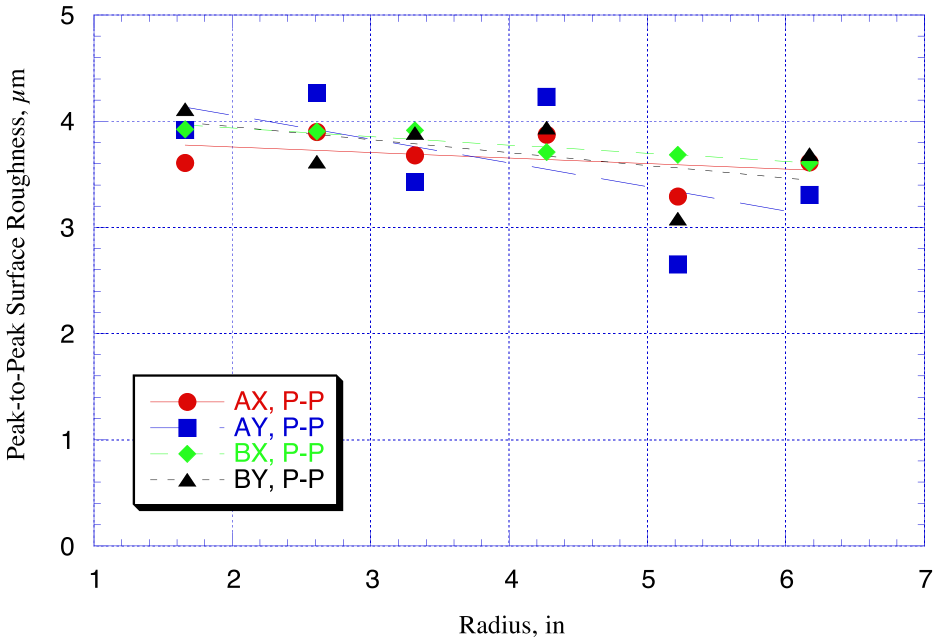

Figure 7. Peak-to-Peak surface roughness for all of the plate plug specimens vs. radius

The graphs in Figures 7 and 8 summarize the peak to peak and the RMS roughness measurments along two orthogonal directions on each specimen. The specimen number placement can be seen in Figure 2. The specimen numbers and radial locations are inversely related; for example the location of B6 is about 1 in. from the center of the plate and B1 is located at 6 in. The peak to peak and RMS values in each direction on each specimen tended to vary randomly, but the values decrease slightly as the radius increases. This trend is shown by the lines in each plot which are the best fit linear line for each group of specimens (A or B) in each direction (X or Y).

This particular lap plate had been used for lapping and the region of contact is illustrated in Figure 2. The lapping region covered the first two B specimens with the smallest radius. It was interesting to note that the center B specimens were rougher than the center A specimens, even though the B specimens had been lapped. These characteristics probably come from the lap plate preparation. The use of the plate for lapping appears to have no effect on peak to peak or RMS roughness.

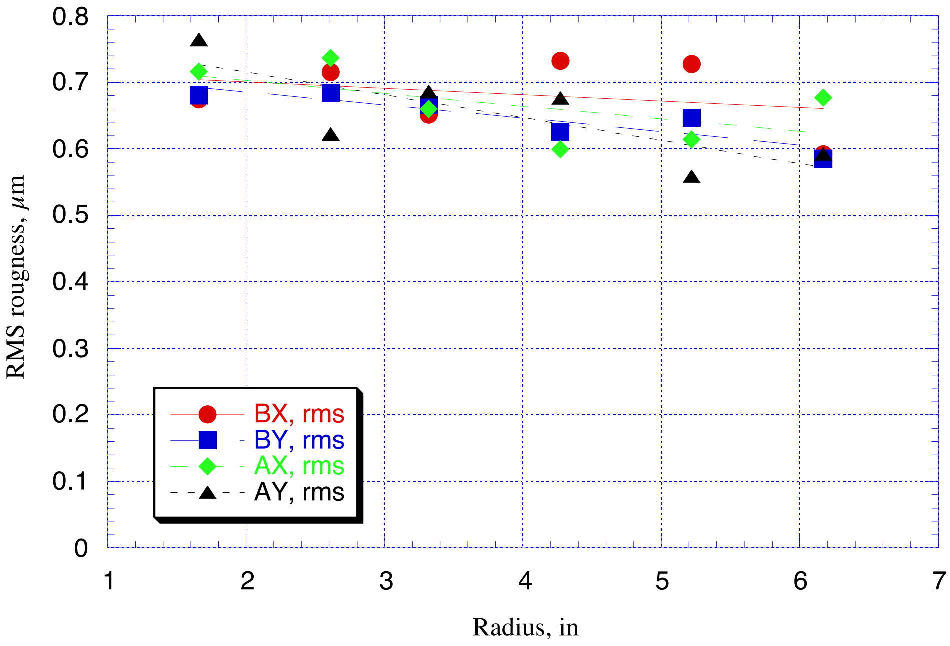

Figure 8. RMS average roughness of the plate plugs as a function of radius

The skewness of the peaks and valleys are plotted as a function of specimen and radius in Figure 9. The skewness of the surface features were all found to be negative indicating more valleys than peaks. This is a reasonable result since the charging process will wear down the peaks but has no effect on the valleys. The figure shows that there is a clear relationship between skewness and radius with the value growing in the negative direction with increasing radius. There is no clear explanation why such a trend might occur.

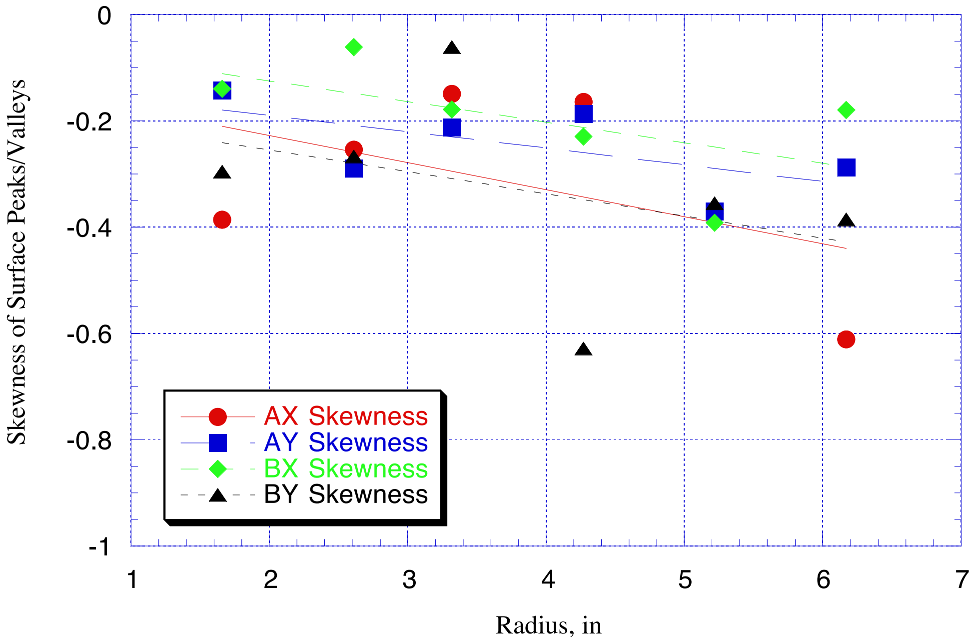

Figure 9. Skewness of the peaks and valley as a function of the plate radius

Figure 10 is a graph of kurtosis values for the different specimens in the different directions. The kurtosis values were all around 2.5 indicating fewer extreme points away from the mean than would occur if the features were truly random. These values remained nearly constant with radius. Thus the plate preparation would seem to give a similar distribution over the whole plate. The data does not indicate a difference between lapped and unlapped areas.

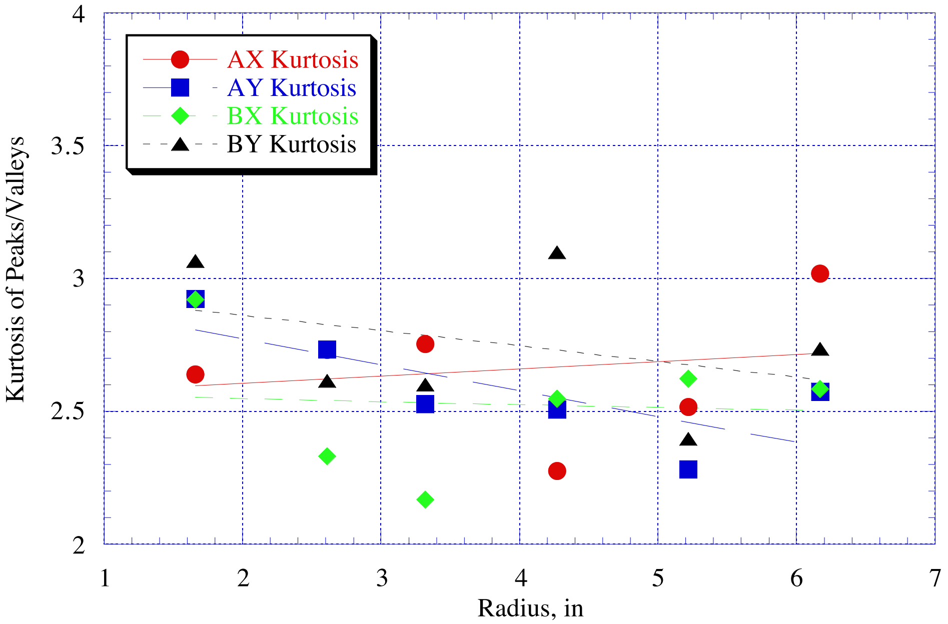

Figure 10. Kurtosis of the peaks and valleys as a function of plate radius

The bearing ratios measured at a distance of one RMS above the mean line ranged between 16% and 24%. Figure 11 is a plot of bearing ratio taken for each specimen in each direction at a height of 0.622 micrometers above the mean line. These values tend to remain fairly constant with radius.

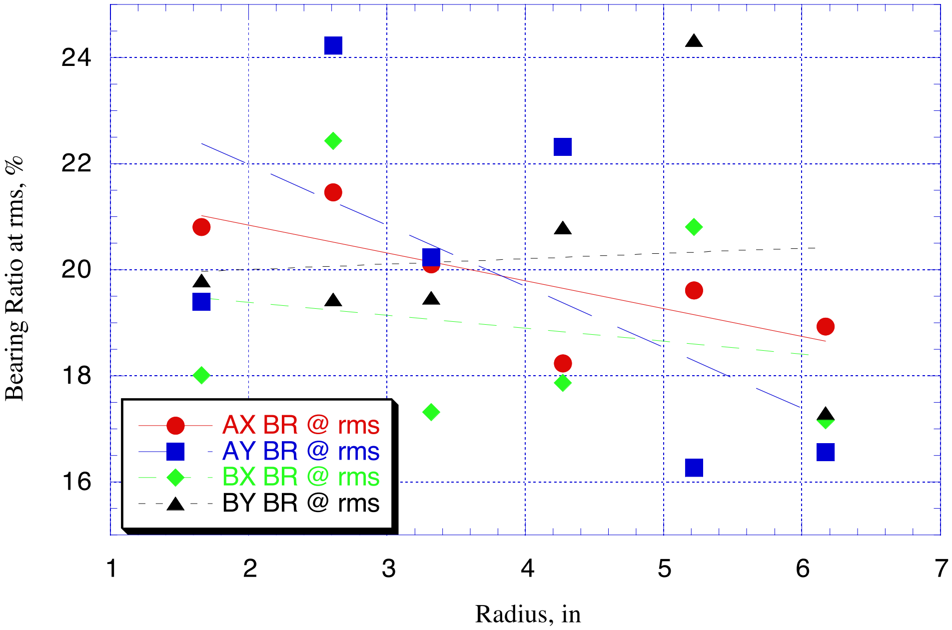

Figure 11. Bearing Ratio at one RMS from the mean surface

This measurement illustrates an interesting result: if the average contact length over the X and Y directions is 20%, the average areal contact is only 4%. This value will have an impact on the average lapping pressure as well as the wear of this plate during lapping against the hard AlTiC surface.

The final measurement of the distribution of peaks and valleys for the textured surface is the spacing of the peaks. This illustrates the horizontal separation of the peaks rather than their heights. Figure 12 shows the spacing of the adjacent peaks independent of their size. So a series of peaks on one of the larger plateaus would be measured. Figure 13 shows the average spacing of the major peaks; that is, those peaks that pass through the mean line. The mean spacing between peaks that crossed the mean was relatively constant with radius with an average of about 75 μm. The mean spacing between adjacent local peaks was much smaller and tended to decrease with radius. Figure 12 shows that values began around 20 μm and decreased to around 12 μm. These measurements are smaller than the data in Figure 13 because it is a measure of all the adjacent peaks. Figure 13 shows only the adjacent peaks where the valley between peaks is low enough to pass through the mean line.

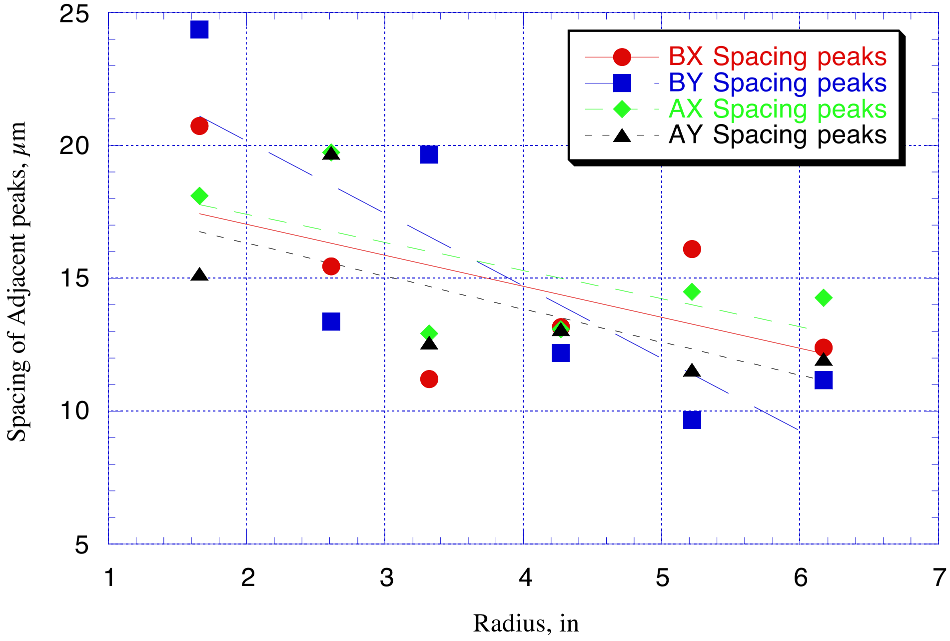

Figure 12. Average spacing of adjacent peaks on the specimen surfaces

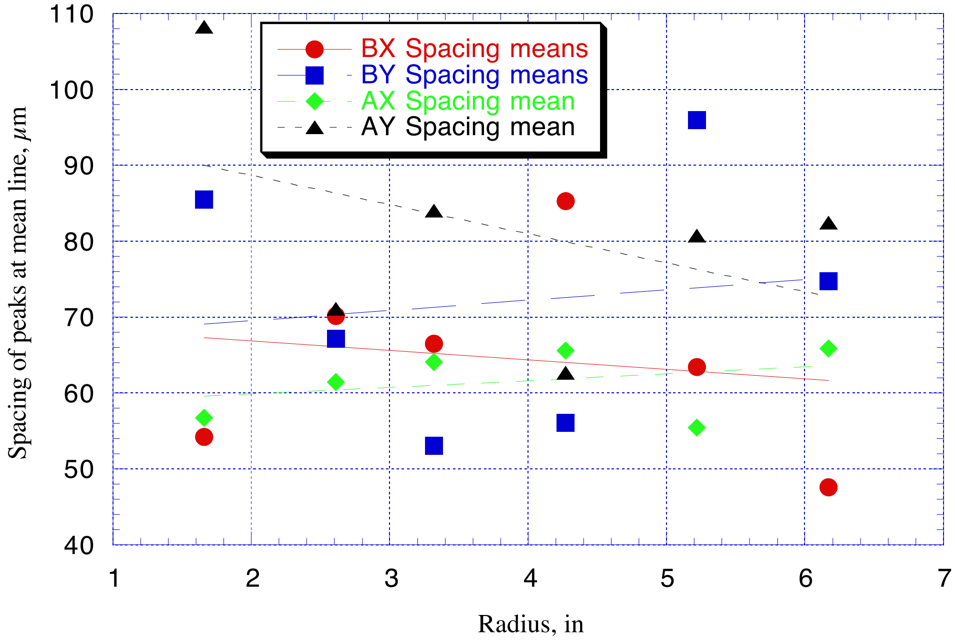

Figure 13. Average spacing of the more significant peaks that pass through the mean line

SEM Images Micrographs of the textured surfaces were made using a scanning electron microscope in the backscatter mode. This mode provides more contrast for the atomic mass of the chemical species in the field of view because the efficiency of the back scattered electron emission is dependent on atomic mass. The diamond grains (carbon) are more easily distinguished from the background (tin) surface. This enhanced contrast is also known as compositional or z-contrast.

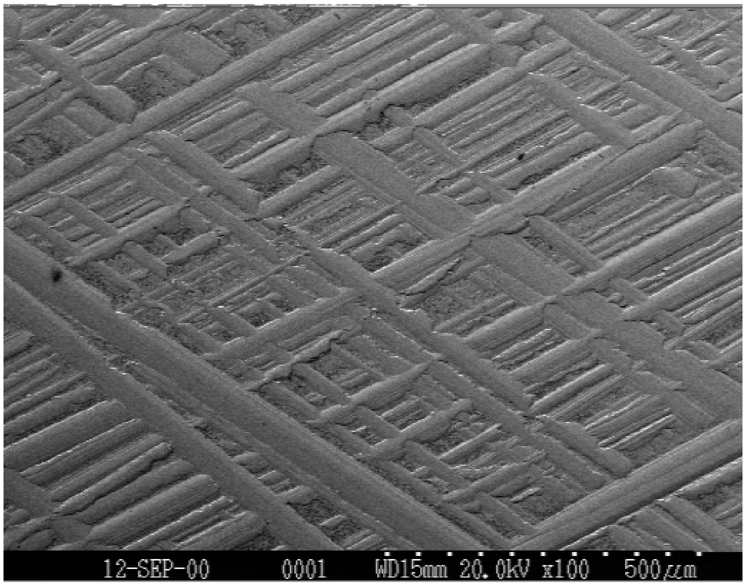

Figure 14. 100X image of the textured surface showing the overall features

Figure 14 shows the overall features of the textured surface at 100X, that is, a field of view of approximately 1 mm. The grooves are random in depth, width and location and are nominally orthogonal. The darker areas at the intersection of the grooves are the plateau areas charged with diamonds. Figure 15 is a 10x magnification of the center of Figure 14 showing several plateaus.

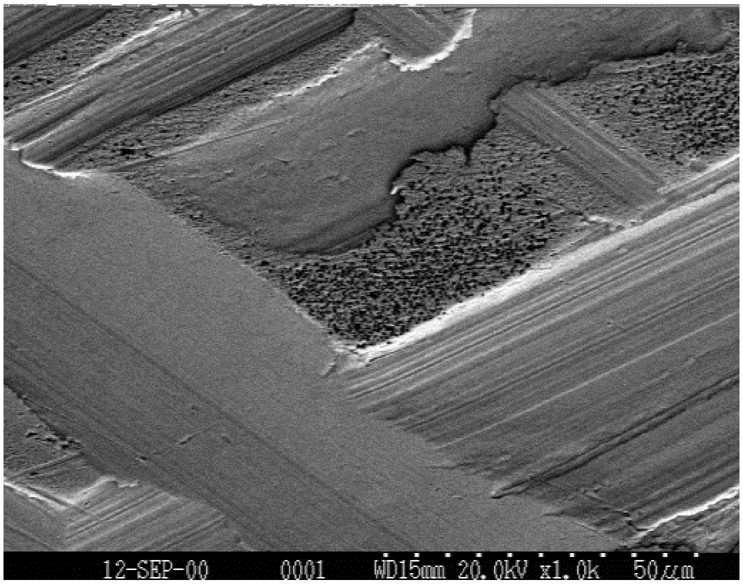

Figure 15. 1000X image of the surface showing plateau between grooves

Figure 15 shows a field of view of approximately 100 μm. In this figure, the size and distribution of the diamond charged plateaus are evident. Further magnification of the surface is shown at 3000X in Figure 16. This figure indicates the size of this plateau is 30 x 50 μm or an area of 1.5×10^{-9} m^2. If this area is used as an estimate of the average plateau, there would be about 500 contact spots in Figure 14 or about 0.2% contact. The estimate of 4% from the bearing ratio measurements is probably a better estimate because it is based on a much larger area.

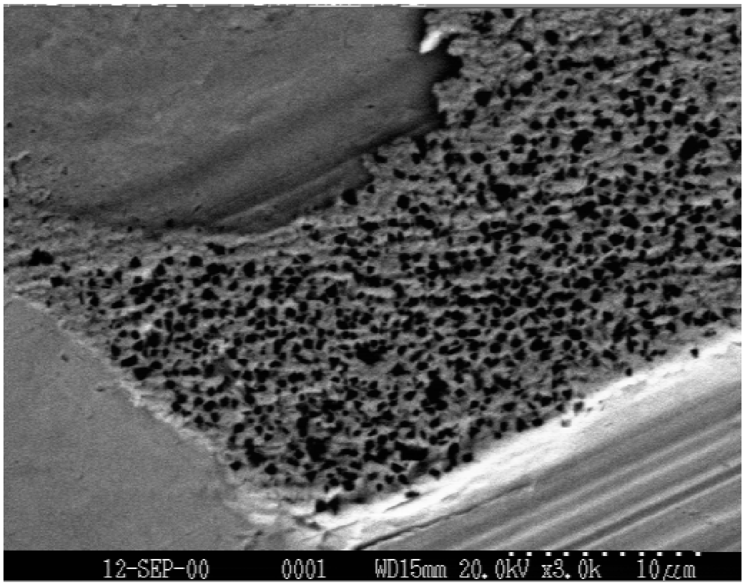

Figure 16. 3000X image of the plateau showing individual diamond grains (size 0.3-0.5 μm)

Conclusions The data generated showed that both the peak to peak and RMS roughness vary randomly, but decrease with radius. No perceivable differences were found between the sections of the plate that had been used to lap the heads and the other sections. The experiments also showed that the specimens near the center had less negative skewness than the outer regions. The skew values ranged between –0.12 and –0.45. The kurtosis values for the specimens were found to be between 2.35 and 3.00 with no particular pattern. The bearing ratio taken at the average RMS value was around 20% for all the parts and did not appear to be affected by location. Mean spacing between adjacent peaks of grooves that crossed the mean line was in the range of 60 to 80 micrometers, but remained fairly constant with radius. The mean spacing between all adjacent peaks was between 11 and 23 micrometers. These values decreased with radius showing a more random pattern as the radius increased. Based on the measurements, the texturing produces nearly random grooves on the surfaces with a mean contact area of 4%.

1.2.2 GROOVED PLATE

A more deterministic pattern of peaks and valleys was studied in the form of a spiral groove on the lap plate surface. This pattern can be produced rapidly using a lathe and the spacing and depth of the grooves can be changed easily. The geometry of the groove and the plateau geometry can be changed by using different quality tools such as single crystal or polycrystalline diamond tools. The parameters in the groove geometry are relatively straightforward: the pitch of the grooves, the width of the land, the depth of the groove and the shape of the groove are the only variables. A fluid flow model that will calculate the hydrodynamic fluid pressure as a result of the motion of the heads over this (or other) lapping surface is being developed and is discussed in a following section.

One sample plate was fabricated using the spiral groove geometry and specimens from that plate were measured in much the same way as the textured surface discussed in the first part of this report. The plate was mounted on the Nanoform 600 Diamond Turning Machine (DTM) and 100 μm was removed to clean up the face with a polycrystalline tool. Then the tin was finished with a 3 mm nose radius single crystal tool to a depth of 5 μm followed by a second pass at 1 μm. A spiral groove was then cut into the surface to a depth of 10 μm using a 40 μm radius single crystal tool. The pitch of the grooves is 90 μm and the ratio of land to groove is 47% (42μm land and 48 μm groove). A Talysurf trace of the groove before the plate was charged with diamond is shown in Figure 17.

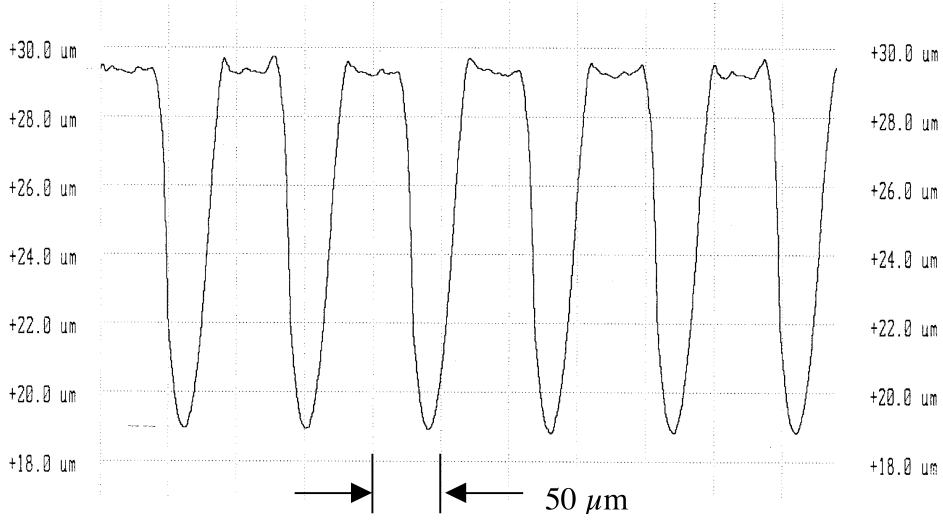

Figure 17. Talysurf image of machined lap plate

The depth of the grooves is approximately 10 μm but the top land surface is distorted as a result of making the grooves in this soft tin material. This effect is quite small in this case (< 0.5 μm) using a single crystal diamond, but could be much larger if a polycrystalline tool is used. The reason is that the single crystal tool has a much sharper edge leading to lower tool forces and less plowing than the polycrystalline tool.

Figure 18 shows the surface after the standard charging process has been completed. In this case the distorted lands have been flattened to less than 100 nm. A trace of the top of one of the lands showed a RMS roughness of 22 nm and a P-P value of 80 nm. One of the lands appears to have a relatively deep scratch. The SEM pictures described next show this same phenomenon.

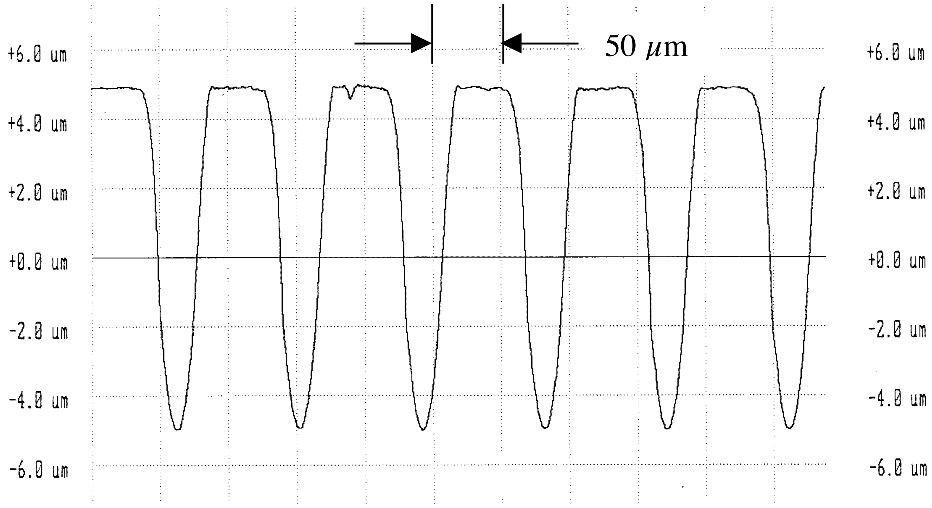

Figure 18. Talysurf of grooved plate after charging

SEM Micrographs The surfaces of the grooved plate were evaluated in the SEM to see if the charging process produced a diamond pattern similar to the textured plate. The backscatter mode was again used to enhance the contrast between the diamond particles and the tin substrate.

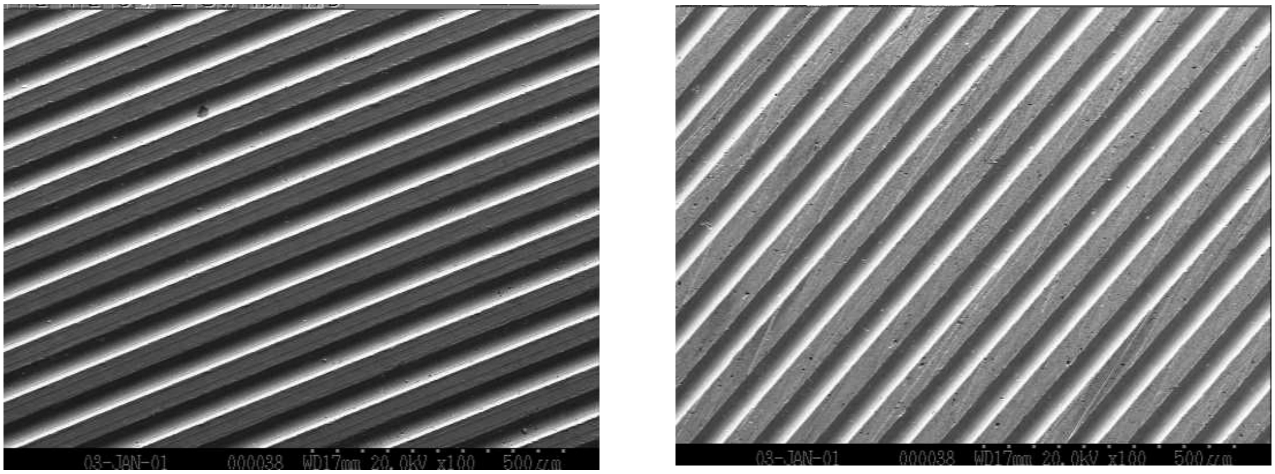

Figure 19. 100X SEM images of Grooved tin lap plate
Left: before charging Right: after charging

Figure 19 shows the surfaces at 100X with the machine surface at the left and the charged surface at the right. Compare this figure to Figure 14 to provide a striking contrast between a deterministic and a random texturing process. But this comparison also shows much larger area of contact for the particular groove-land geometry selected for this first test. The area of contact is on the order of 50% in Figure 19 compared to a tenth of this value for the textured surface shown in Figure 14. More effort is needed to study the effect of the land area on the lapping process.

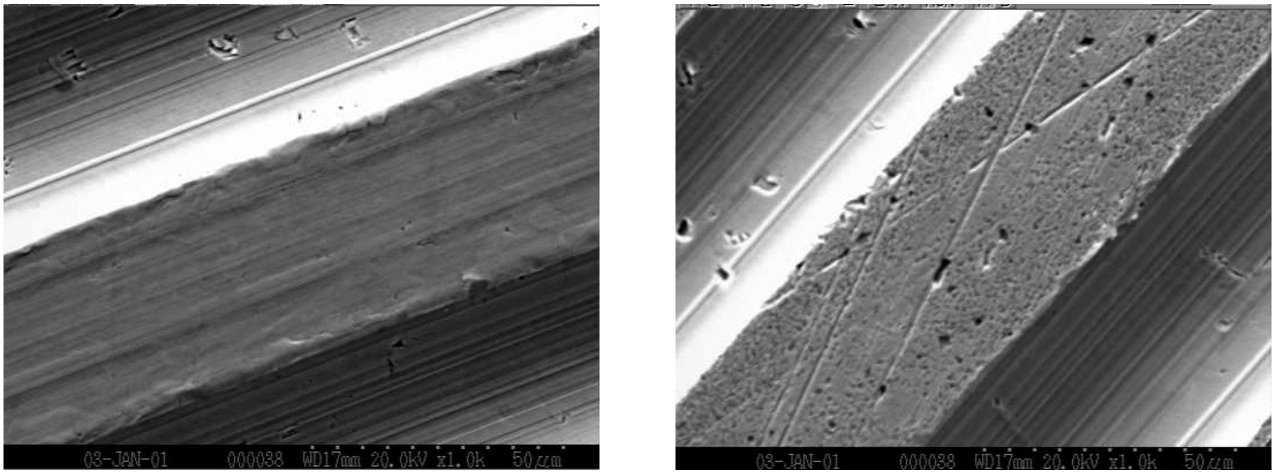

Figure 20. 1000X SEM images of grooved plate
Left: before charging Right: after charging

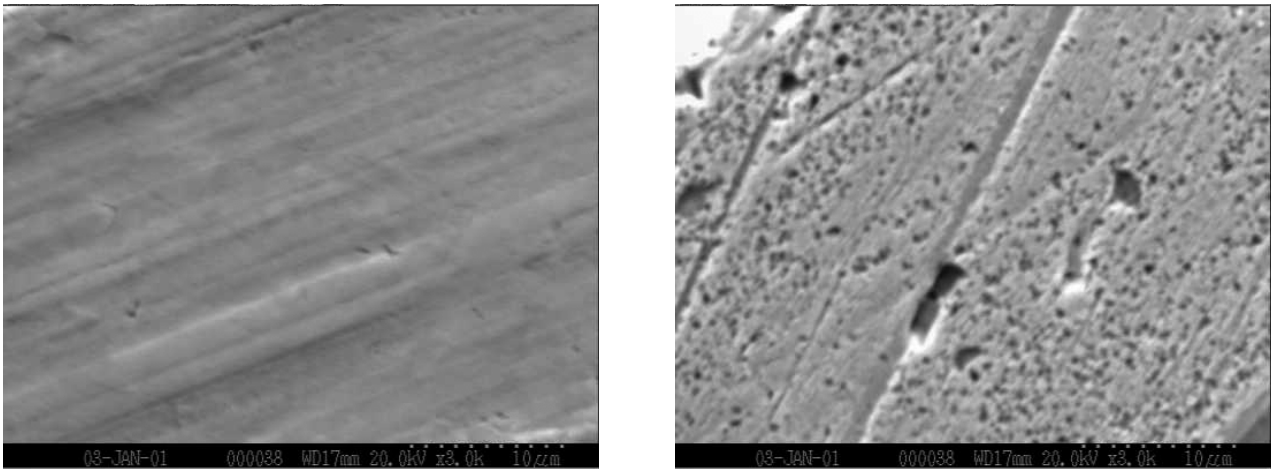

Figure 21. 3000X SEM images of grooved plate
Left: before charging Right: after charging

The higher magnification images in Figure 20 illustrate the change in the flatness of the land as a result of the charging process. Note that on the uncharged land at the left, features of the machining process are visible as are the raised edges from cutting the groove. The charged land on the right shows a much flatter surface and a series of scratches from the charging process. Also note in this picture what appears to be a series of defects or inclusions that may be pulling out of the surface and causing the visible scratches. Different tin lap materials are being evaluated and will be studied to see if the material plays a role in the lapping process.

The highest magnification pictures in Figure 21 show an uncharged surface on the left characterized by features in the machining direction and a charged surface at right characterized by a uniform array of diamonds embedded in the tin surface. The small dots on the lower right are spaced at 1 μm and this scale corroborates the 0.3-0.5 μm size of the diamonds. The quantity of the charged diamonds in this region looks less dense than the textured surface in Figure 16. However, this may be due to the quality of this SEM as it seems to have more contrast and better focus than Figure 21.

1.2.3 FILM THICKNESS MODEL

The motion of the rows of hard disks over the surface of the lapping plate will cause the water/glycol lubricant to be pulled along with them. As this fluid encounters the features on the lap surface it can generate a hydrodynamic film that tends to separate the heads from the lap surface. If this hydrodynamic force exceeds the static loading, contact between the heads and the lap surface will be reduced and the lapping process will stop.

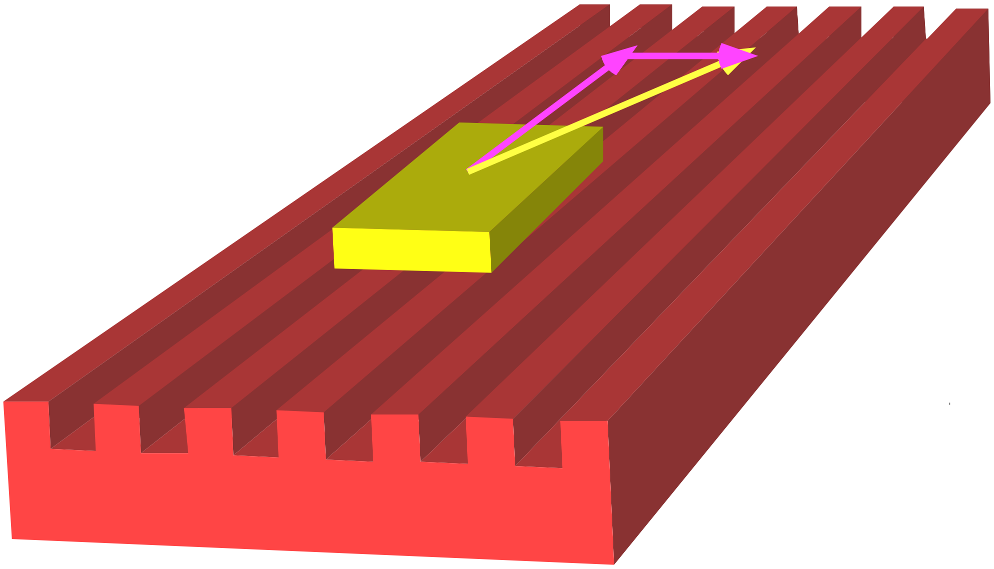

Figure 22. Sketch of the head moving over the lap surface showing the velocity components

The spiral groove lap surface can be characterized by a series of grooves and lands, with different spacing and directions depending on the fabrication technique. In general then, the surface can be characterized in Figure 22. The direction of the motion of the head (or rows of heads) can be divided into that perpendicular to the grooves and those along the groove direction. For the case of the textured plate, there will be intersecting grooves.

The model for a step bearing can be constructed by taking the component of the velocity that is normal to the grooves and calculating the hydrodynamic forces that are developed. The parameters of interest are defined in Figure 23.

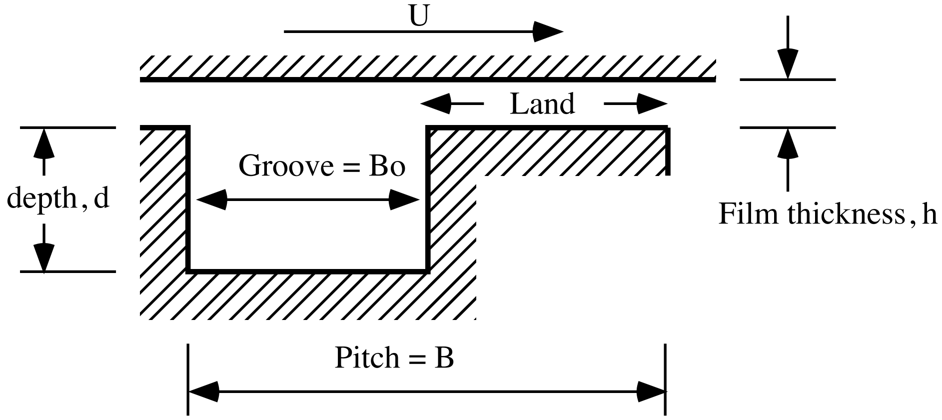

Figure 23. Definition of the parameters important to the hydrodynamic film generation

The peak pressure over this step bearing per unit length, *L*, (into the page) occurs at the edge of the land and can be written as

$$P_p = \frac{6\mu U d}{\dfrac{(h+d)^3}{B_0} + \dfrac{h^3}{B - B_0}} \tag{1}$$

where

μ = viscosity of the lubricant, Pa sec

U = velocity component perpendicular to the steps, m/s

h = film thickness, m

d = depth of grooves, m

B = pitch of the steps, m

B_0 = width of the groove, m

The vertical force, F_v, generated as the head sweeps across one step can be written as:

$$F_v = \frac{P_p}{2} BL \tag{2}$$

One of the parameters of interest is the proportion of the pitch allocated to groove and to land. Define Land Ratio, *LR*, as the ratio of land to pitch and the vertical force can be written as:

$$F_v = \mu UWLB\left[\frac{3d}{\frac{(d+h)^3}{1-LR}+\frac{h^3}{LR}}\right] \tag{3}$$

where W is the width of the slider (in the direction of the grooves) and L is the length perpendicular to the grooves.

The following is an example of the use of these equations to find the force generated on an area equivalent to 24 rows of heads moving perpendicular to the grooves. The baseline material properties and geometry of the bearing are as follows:

$\mu = 0.021$ Pa sec (ethylene glycol at room temperature)
$U = 0.111$ m/s (maximum speed of current kiss lapping)
h = 0.5 μm (film thickness equivalent to max diamond size)
d = 10 μm or variable (depth of groove)
B = 100 μm or variable(pitch of grooves)
B_0 = 50 μm or variable (Land Ratio = 0.5)
L = 12 rows long = 14.4 mm
W = 2 rows wide = 94 mm

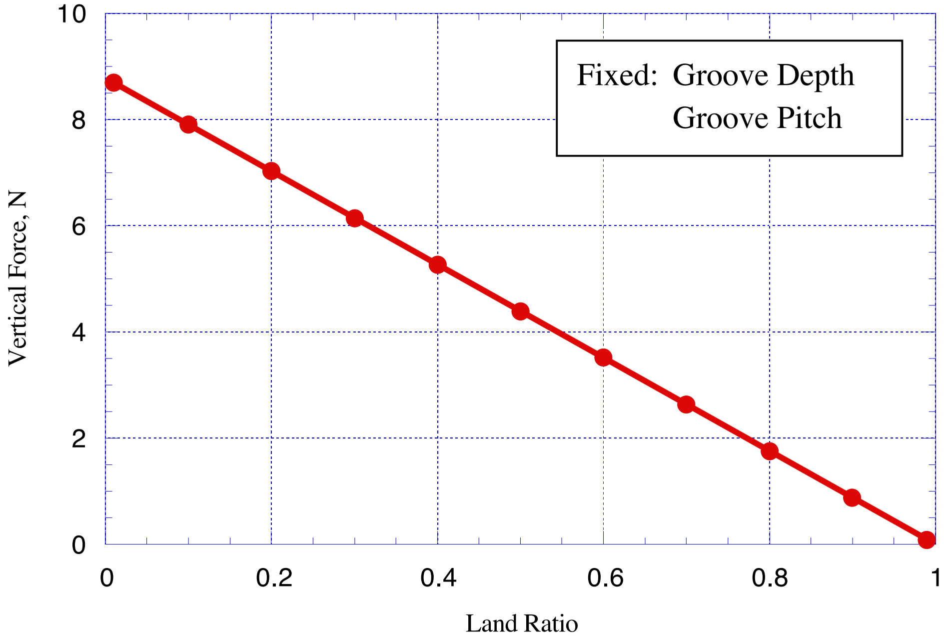

Figure 24. Relationship between hydrodynamic film force and Land Ratio

Land Ratio Reducing the relative area of the land will increase the hydrodynamic film pressure and the lift during lapping. Figure 24 shows the effect of changing the Land Ratio in Equation (3) from 0 (all groove) to 1 (all land). If the loading on the heads is larger than 4 N at a LR = 0.5, the hydrodynamic forces will be offset by the preload (~70 N) and contact will occur.

Groove Depth Setting the Land Ratio equal to 0.5, the groove depth can be varied to see the effect of depth over a reasonable range. As the groove depth goes below 6 μm, the forces become significant and can overcome the preload reducing the contact between lap and heads.

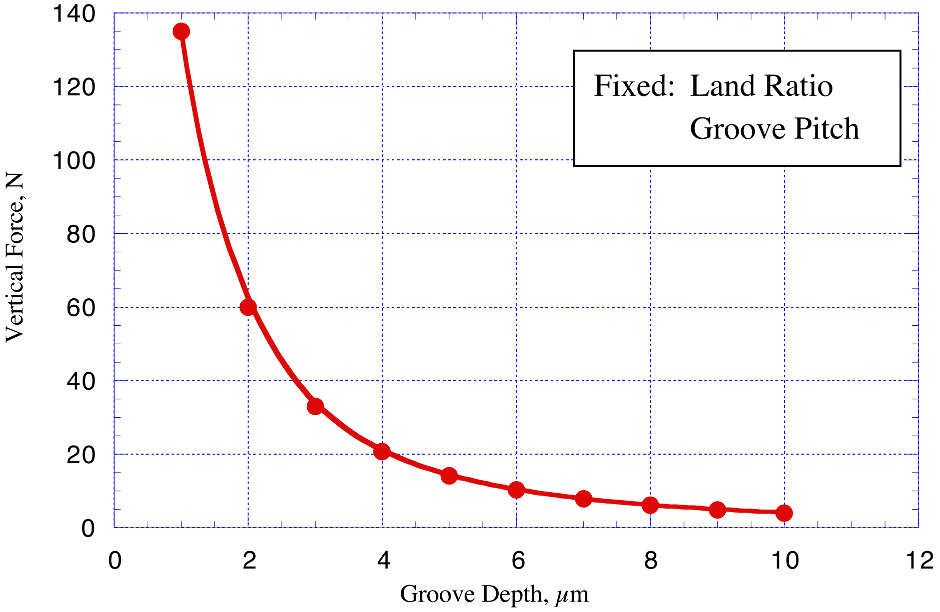

Figure 25. Influence of Groove Depth on the hydrodynamic forces generated

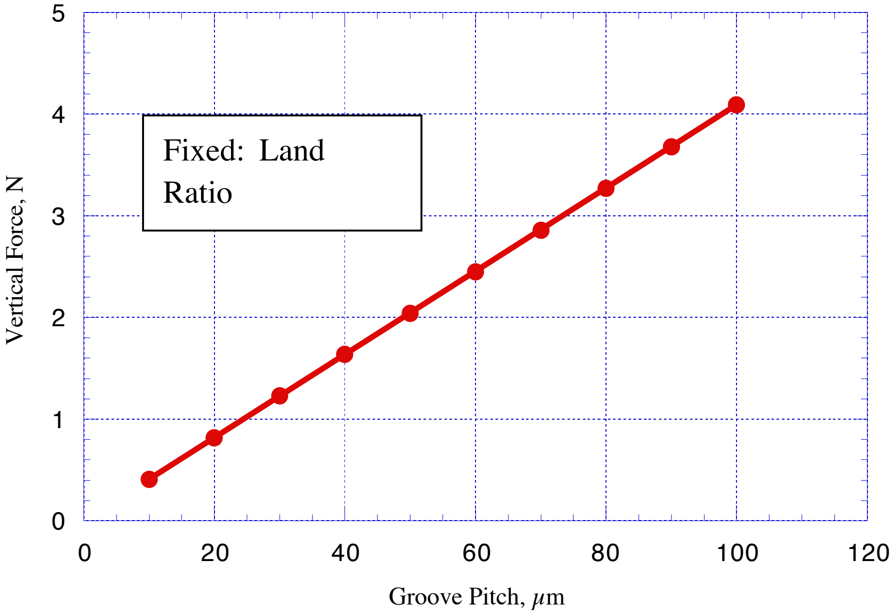

Figure 26. Influence of the Groove Pitch on the hydrodynamic forces.

Groove Spacing If the groove spacing (or pitch) is reduced (holding everything else constant), the vertical force will be reduced as shown in Figure 26. The reason for this effect is that if the length of the bearing is subdivided into short step bearings, each will generate a smaller peak pressure and if added together will generate less lift than if the whole length is a single bearing.

Frictional Forces The force on the rows of heads from the shear of the lubricant film can be estimated in much the same way as for the vertical force. An expression using the same parameters from Equations 1-3 is:

$$F_f = \mu UWL\left[\frac{3d^2}{\frac{(d+h)^3}{(1-LR)}+\frac{h^3}{LR}}+\frac{(1-LR)}{(d+h)}+\frac{LR}{h}\right] \tag{4}$$

The same evaluation of the parameters of interest can be performed as in the previous vertical force using the same fixed and variable parameters.

Land Ratio Figure 27 show the influence of land ratio on the friction force. The friction force is linearly proportional to the land ratio with the smallest value when the land is small compared to the groove width or Land Ratio << 1. As the land grows, so does the friction but the value is very small, less than 1 N.

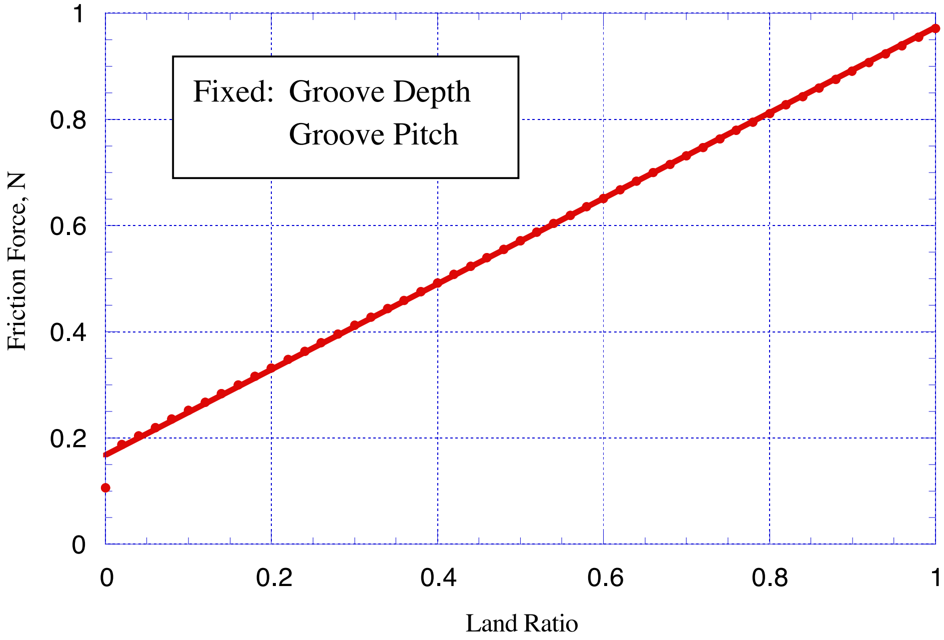

Figure 27. Effect of land ratio on the friction force

Groove Depth The effect of changing the depth of the groove on the friction force is shown in Figure 28. In this case the friction force grows as the depth of the groove is reduced, much like the lift shown in Figure 25. If the groove depth is kept larger than 10 μm, the friction force will be small.

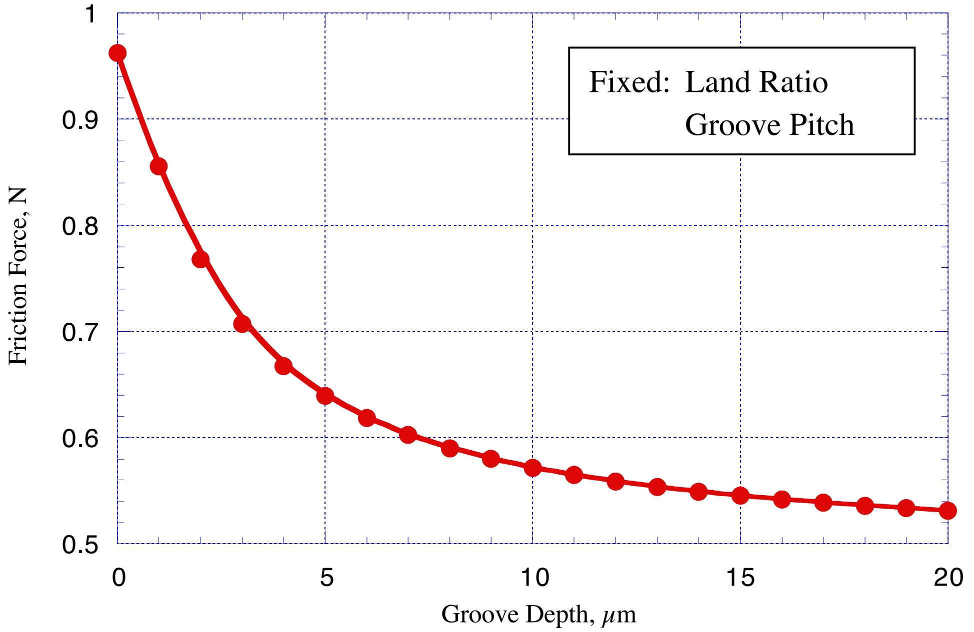

Figure 28. Effect of groove depth on the friction force

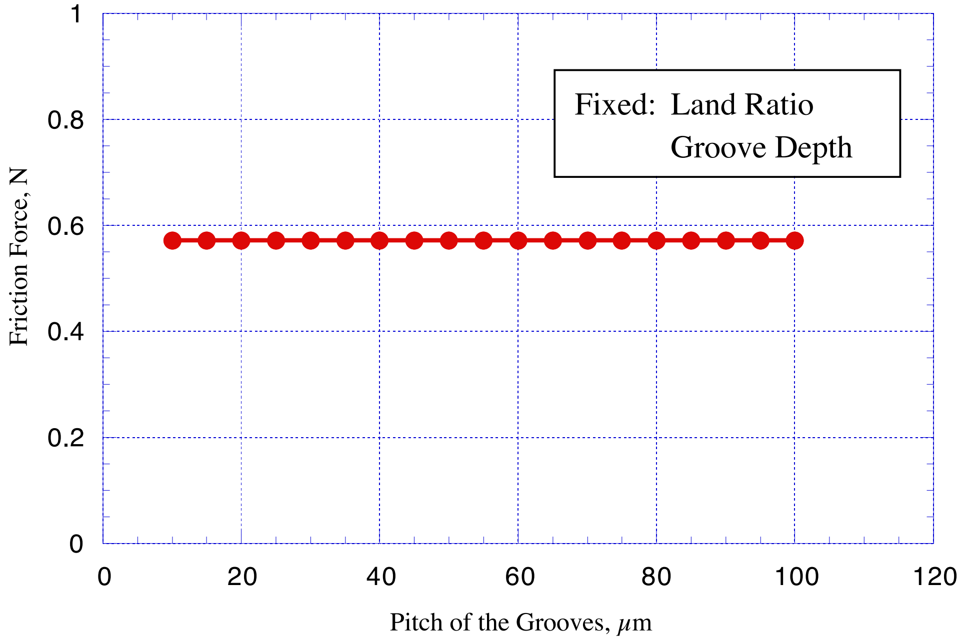

Figure 29. Effect of groove pitch on the friction force

Groove Spacing The last parameter to be discussed is the spacing, or pitch, of the grooves shown in Figure 29. For the lift in Figure 26, the effect of reducing the pitch was to reduce the vertical force generated in the bearing. However, changing the pitch has no effect on the friction force. The result is the same if a single step is used or if the length is subdivided into a number of shorter step bearings. The reason is that in both of these cases, half of the bearing is a land and half is a groove and it is the area of each that determines the friction.

1.3 FUNCTIONAL SPECIFICATION OF LAP PLATE

To provide a means to improve the repeatability of the lapping process, a check on the quality of the lapping plate is needed. One way to do this would be to measure the friction required to slide a head (or row of heads) over the lap surface. Another technique would be to oscillate the lap plate on 3 AlTiC pads and see the amplitude of vibration that lead to break-away. This is another way to find the friction at the interface. As the lap plate preparation process matures at the PEC, techniques for assessing the quality will be studied.

1.4 CONCLUSIONS AND FUTURE WORK

The emphasis from the effort this year has been to evaluate the current lap plate preparation process and measure the surface features produced. This effort began with an evaluation of the current texturing process and measurement of the magnitude and variability of the features produced. One of the conclusions was a realization of the randomness of the scratches and plateaus created and the need for a more repeatable technique.

One possibility is a spiral groove. This pattern can be produced rapidly on a lathe and the repeatability is excellent. One of the goals of the future work is to develop the details of the optimum geometry.

Finding a way to qualify the performance of the lap plates is another future goal. Measuring the friction at the interface would seem to be a logical technique but developing a quick and easy method will be the challenge.

2 BEND EFFECT DUE TO MECHANICAL SCRIBING

Brad W. Austin
Graduate Student (MS thesis completed July 2000)
Ronald O. Scattergood
Professor
Department of Materials Science and Engineering

A test system consisting of a microhardness tester and a motorized stage was used to produce controlled diamond scribes on ceramic samples. A bending distortion is produced as a result of the residual stresses generated by the scribing operation. The change in sample shape was measured using an optical profilometer. Data from the measurement tool were analyzed using computer software to extract the net bending effect. An analytical model for the bend effect based on the residual stresses due to line-force dipoles was developed. The adjustable parameter in the model was calibrated using bend angle measurements and the model was verified by comparing predicted displacement profiles with measured profiles. The line-force dipole model gave a very good representation of the bend effect. The results of this investigation have application for curvature adjustment techniques used for hard disk read-write heads.

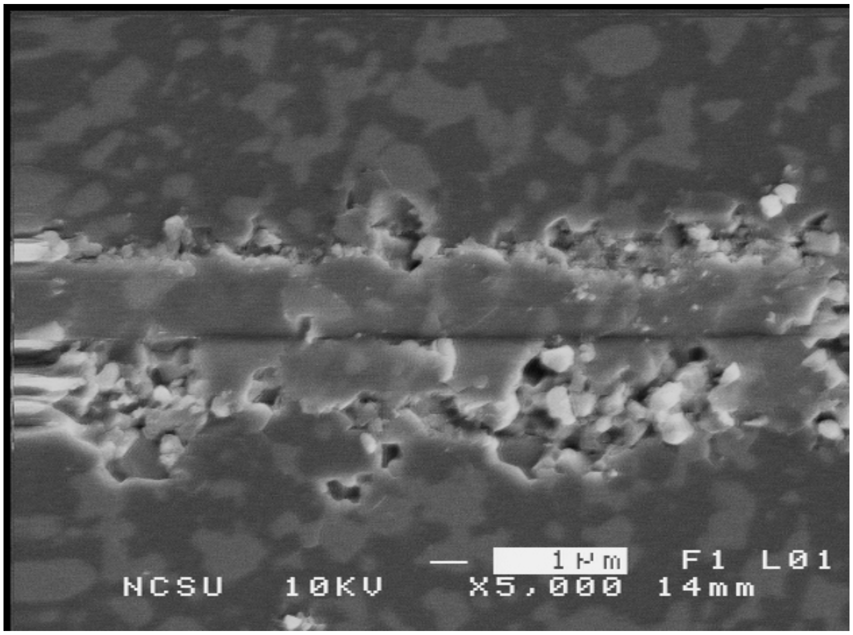

2.1 INTRODUCTION

The read write elements used in modern hard disk drives are attached to small pieces of ceramic called sliders (disk read-write heads). When the disk spins, it creates a very small layer of moving air just above the surface that causes the slider to fly very close to the magnetic surface. This flying is controlled through the air bearing surface (ABS) of the slider. The shape of the slider is critical for determining the fly height, and the fly height is proportional to the limit of the media bit density of the system. As fly height is reduced, bit density can be increased. In modern hard drive systems, fly height is less than 25 nm [1]. To fix the fly height, specific curvatures must be given to the slider. The curvature height of the slider is typically the order of just a few nanometers across a 1 mm^2 face. These minute curvatures are produced using curvature adjustment techniques (CATs). One such CAT is diamond scribing of the ABS side of the slider. When a sharp diamond point is translated across the surface of a ceramic sample, a scribe trace is generated. This is a source of residual stress. The stress is due to the elastic-plastic constraint associated with the deformed material that is displaced from the trace. When a scribe is made across a sample in the form of a thin plate, for example a slider, the residual stresses will cause bending distortions orthogonal to the scribe direction (the bend effect). When properly controlled, these distortions can be used to adjust the curvature. This has been done empirically for applications. The objective of this study was to develop an analytical model to describe the bend effect due to diamond scribing and to verify this model with suitable experiments. The scribing experiments were done using AlTiC, a sintered ceramic composite consisting of TiC particles in an Al_2O_3 matrix. This material is used by the data storage industry for the manufacture of disk read-write heads. The development of a model for the bend effect will facilitate better control of the manufacturing process.

2.2 DETAILS OF THE PROJECT

2.2.1 EXPERIMENTS

A Zwik microhardness tester shown in Figure 1a was used as the platform for the scribing tests. To produce a scribe at a constant speed, a motorized translation stage was fixed to the base of the hardness tester. This allowed the stage to be moved at a constant speed. The stage was mounted such that the direction of motorized movement could be aligned with the scribe direction for a Dynatex V4-64 diamond scribing tool shown in Figure 1b. This is a standard, three-faced diamond tool used in the semiconductor industry. For the tests done here, the Dynatex tool shank was mounted at an angle of 58^0

from the surface of the sample to be scribed. At this position the angle between the cutting edge in Figure 1b and the sample surface was 3^0. The normal force on the scribing tip was controlled by placing weights on the loading pan of the microhardness tester. For the tests reported here, the normal force ranged from 0.3 to 1.8 N. Higher loads caused excessive wear and chipping damage on the scribing tip. SEM observations of the tip edge were made during the tests and the tip was replaced whenever damage was observed.

The AlTiC ceramic used for the tests contained 65 vol% Al_2O_3 and 35 vol% TiC. The microstructure consists of polycrystalline Al_2O_3 with a grain size of about 1 μm and TiC particles about 1 μm in diameter. The samples used for the scribing tests were polished AlTiC rectangles measuring approximately 1.0 mm x 1.0 mm x 0.3 mm. These are the same size as the ceramic sliders used in current generation disk storage systems. For most tests, 3 equally spaced scribes were made across the width of a sample with the middle scribe centered on the sample span.

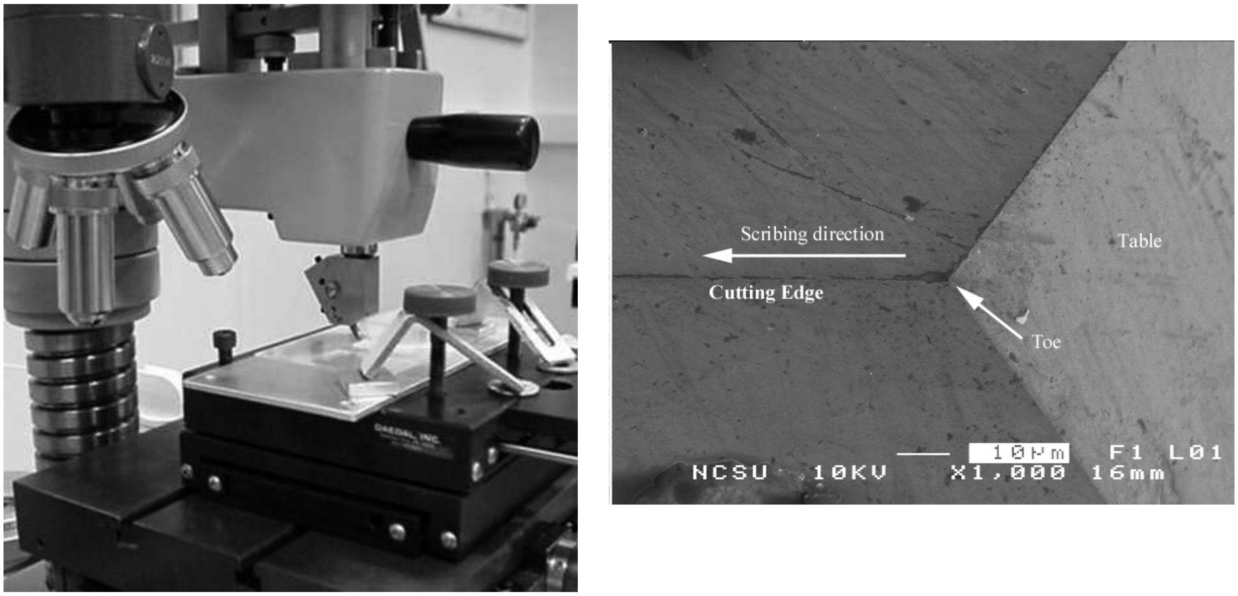

(a) Test system for scribing (b) SEM of the Dynatex scribe tip

Figure 1. Testing system and scribing tip.

A New View optical profilometer was used to measure the 2D surface height profiles of the test samples. Measurements were taken before and after scribing. To analyze data from the profilometer, the initial measurement had to be subtracted, point by point, from the measurement taken after scribing. This was accomplished by importing both sets of data into a file and aligning fiducial marks. The edges of the samples proved to be very good fuducials. The initial data was then subtracted from the final data point by point.

The resulting data set was the net effect of the scribe without any effects from the original shape of the sample. Finally, a straight line with appropriate slope was subtracted from this net effect data to offset the influence of sample tilt during measurement. Figure 2a shows a typical example of the 2D surface profiles obtained using three scribes per sample. The scribe traces were made on the top surface of the samples and the bending occurs downward. Linear profiles were extracted from the 2D surface profile data to obtain the average bend-displacement profiles orthogonal to the scribe direction. Figure 2b shows a typical bend-displacement profile. The sharp peaks present in the profile occur at the three scribe positions. The peaks are due to drop-out of the profilometer data at the high slope regions adjacent to scribe traces. Displacement profiles of the kind shown in Figure 2b are the experimental data that were used for calibration and verification of the bend-effect model described in the next section.

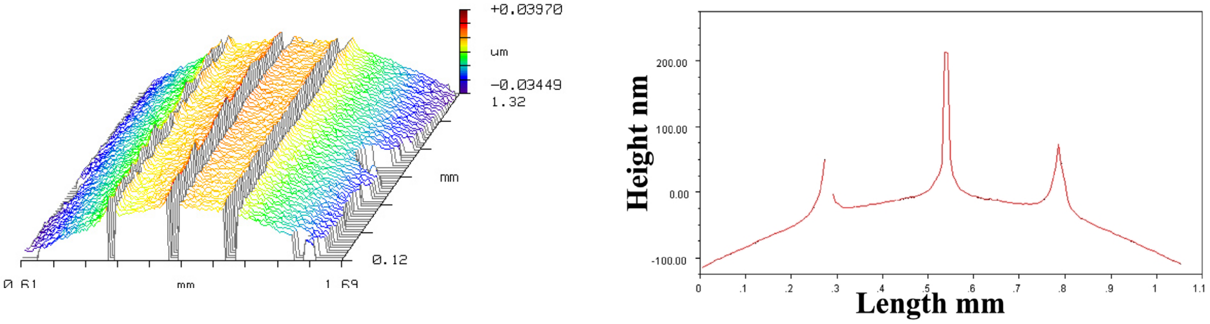

(a) Surface profile data for scribing

(b) Linear profile data for scibing

Figure 2. Optical profilometer data for scribing tests.

2.2.2 DEVELOPMENT OF THE MODEL

The elastic-plastic deformation zone along a diamond-scribe scribe trace will be modeled as the line force dipole shown in Figure 3. The dipole forces act outward from the scribe trace because the elastic unloading of the plastically deformed and displaced material must produce outward forces on the surrounding elastic material. A force-dipole model consisting of orthogonal dipole forces acting on the surface of an elastic half space, termed the "blister" field, was introduced by Yoffe [2] as a model for the residual stresses due to indentations. The scribe can be viewed as the superposition of dipole blister fields [3]. Superposition of the blister fields for scribing (continuous indentation) produces the line-force dipole representation shown in Figure 3. The line-force dipole stresses for an isotropic elastic half space can obtained from standard elasticity solutions [4] by adding the stresses due to two oppositely directed line forces where F is the force per unit length and a is the inter-line spacing. The limiting case of infinitesimal line-force dipole stresses will be used for the model calculations. These follow by taking the limit a -> 0 and F ->

∞ such that B = Fa remains finite. B is defined as the dipole strength (N). B is the adjustable parameter in the model. Using the coordinates shown in Figure 3, the infinitesimal line-force dipole stresses, σ^{D}_{yy} and σ^{D}_{xy}, for an elastic half space are given in Equatioon [1].

$$\sigma^{D}_{yy} = \frac{2B}{\pi}\frac{y^{2}\left(-3x^{2}+y^{2}\right)}{\left(x^{2}+y^{2}\right)^{3}} \tag{1}$$
$$\sigma^{D}_{xy} = \frac{4B}{\pi}\frac{xy\left(y^{2}-x^{2}\right)}{\left(x^{2}+y^{2}\right)^{3}}$$

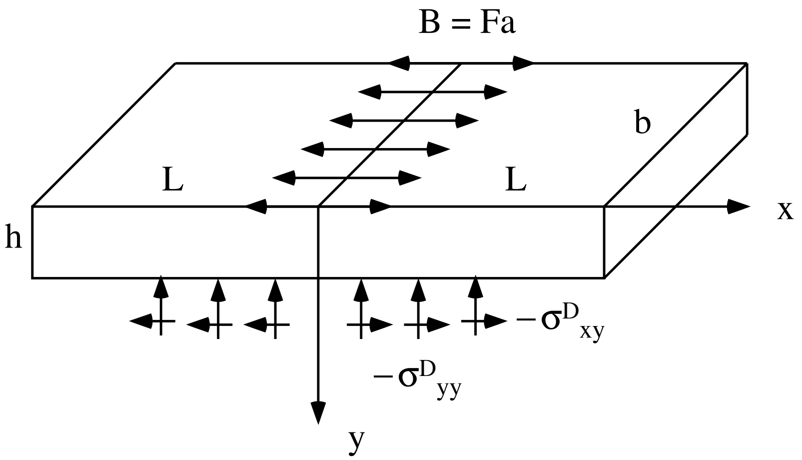

Figure 3. Geometry for the line force-dipole model.

For the analysis of the bend effect in finite-size plates, consider the 2L x h x b thin plate with a scribe along its centerline shown in Figure 3. The finite-body stress solution requires that the stress field tractions due to the line-force dipole vanish on the plate surfaces. If the plate thickness h is small compared to its length 2L and width b, the magnitude of the half-space stresses, σ^{D}_{yy} and σ^{D}_{xy}, acting on the plate edges is negligible and their effects can be ignored. However, the stresses acting on the bottom surface of the plate cannot be ignored. Since there is no resultant force due to the line-force dipole, the equilibrium configuration can be approximated by applying the reversed stresses, $-\sigma^{D}_{yy}$ and $-\sigma^{D}_{xy}$, to the bottom of the plate and solving a 2D beam-bending (plane strain) problem using these stresses as loading functions. This procedure will insure equilibrium of forces and moments acting on any cross section of the rectangular plate. When solving the beam-bending problem, it is important to include both the normal and the shear stresses in the beam loading function. FEM calculations show that the bend effect calculated using this procedure is within a few percent of the numerical solution [5]. The analytical beam-bending solutions for a single scribe centered on the plate span in Figure

3 are given in Equation [2].. Since the problem is 2D, the results are independent of the beam width b. X = x/h is the normalized distance along the plate.

$$
\begin{aligned}
\phi(X) &= -\frac{6B}{\pi E h^2}\left[\tan^{-1}(X)+\frac{X}{1+X^2}\right] = \frac{6B}{\pi E h^2} f(X) \\
\delta(X) &= -\frac{6B}{\pi E h}\left[X\tan^{-1}(X)\right] = \frac{6B}{\pi E h} g(X)
\end{aligned}
\tag{2}
$$

The beam bend-angle, *ϕ(X)*, and displacement, *δ(X)*, are defined as shown in Figure 4a. The functions *f(X)* and *g(X)* for a single central scribe are shown in Figure 4b and these are symmetric with respect to the center at *X* = 0. The bend-angle function *f(X)* approaches the value *-π/2* when *X* = *x/h* is greater than about 3. The deflection function *g(X)* becomes linear as *f(X)* approaches *-π/2*. This means that the bending effect appears as a localized "hinge" which spans a distance the order of *3h* outward from each side of the scribe trace at *X* = *0.*

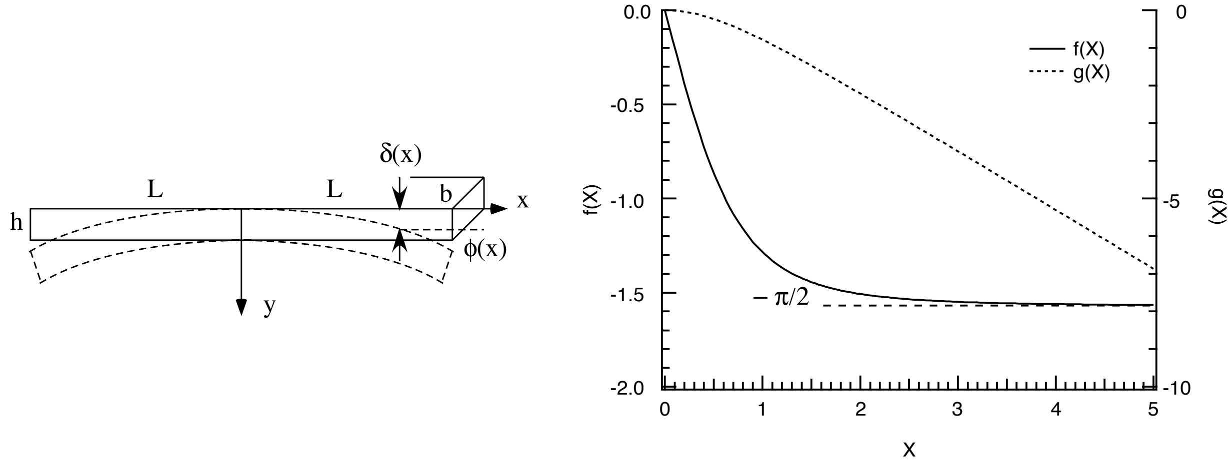

(a) Bend angle ϕ and displacement δ

(b) f(X) and g(X) functions – single scribe

Figure 4. Parameters and functions required for the bend-effect model.

The bend-effect for multiple scribes across the width of a plate sample can be obtained from the superposition of the single-scribe functions in Equation (2), suitably offset in the X coordinate to account for the change of scribe position. Superposition is required in order to compare the model predictions with data from samples containing multiple scribes. Multiple scribes increase the overall deflections due to the bend effect and thereby reduce the scatter in the measured profilometer data. Most of the testing on the

AlTiC samples was done using three scribes, however, some testing was done using a larger number of scribes.

A primary objective of this study was to develop and verify a model which predicts the plate displacement profile, $\delta(x)$, for given scribing conditions. The important parameters for scribing using a specified material are the scribe-tip geometry and the normal load applied during scribing. Scribing speed and other parameters were found to be second order over the operating ranges of interest. For a given scribe-tip geometry and material, the approach taken [5] was to make measurements of the average bend angle (total angle divided by the number of scribes), ϕ_{meas}, as a function of the normal load, W, applied during scribing. Values for the bend angle were determined from the measured displacement profile data in the region where the angle becomes constant (Figure 4b). The evaluation of the adjustable parameter B in the model was made by comparing experimental data for ϕ_{meas} with the model predictions. The dipole strength B can then be plotted as a function of scribe load W to obtain a "calibration curve". A new calibration will be needed if the material or scribe-tip geometry are changed. The model is verified by comparing the form of the measured beam displacement profiles with the model predictions for the profiles.

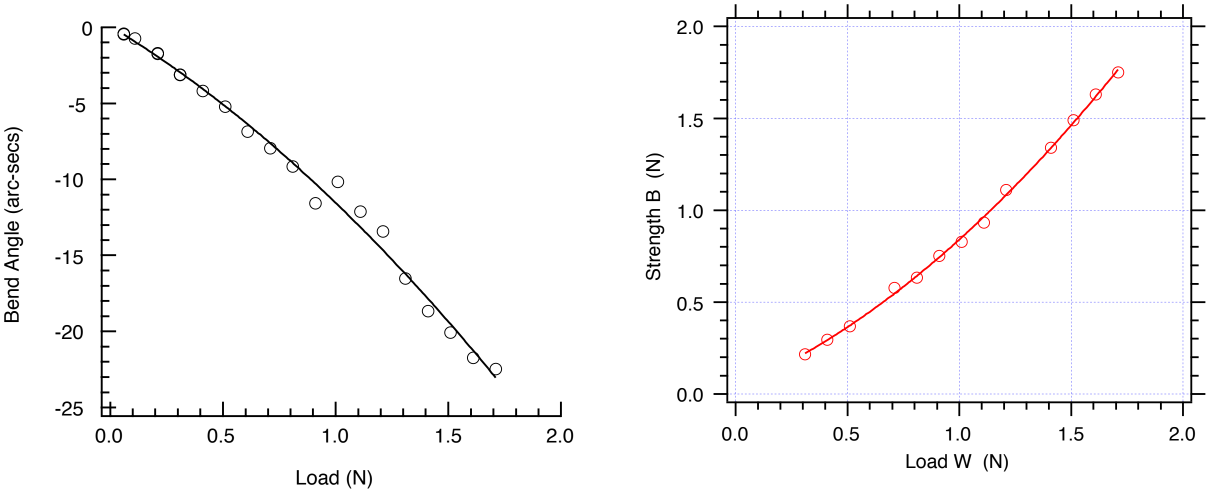

(a) (b)

Figure 5. (a) Measured bend angle (arc seconds) per scribe vs the normal load (N) applied during scribing. (b) The dipole strength (N) vs the normal load (N) applied during scribing.

Figure 5a shows the measured data, ϕ_{meas} vs W, for scribes made on the AlTiC samples using the Dynatex scribe tip and three scibes per sample. All test data in Figure 5a were obtained with undamaged scribe tips. It was found that chipping along the cutting edge of the tip often occurred at the higher loads and this changed the results. It was difficult to perform tests without chipping for $W > 1.8$ N and this set the upper limit for the load range. Using appropriate superposition of the single-scribe functions in Equation [2] to obtain the model prediction for the average bend-angle for three-scribes per sample tests, the data in Figure 5a were used evaluate the dipole strength *B* as a function of *W*. The results obtained are shown in Figure 5b. The *B* vs *W* relation is closely approximated by the second-order power law (solid curve in the figure)

$$B = 0.0332 + 0.516W + 0.291W^2 \tag{3}$$

Equation [3] is the required calibration curve for the AlTiC material scribed using Dynatex V4-64 diamond scribing tips with a 3° surface cutting angle.

2.2.3 VERIFICATION OF THE MODEL

Verification of the model was done by comparing the measured displacement profiles with the model profiles, $\delta(X)$, obtained using appropriate superpositions of Equation [2] for the test conditions. The required values of the dipole strength *B* were obtained from Equation [3]. Figures 7 and 8 show typical examples of the comparisons for a range of scribing loads, *W*, for the test conditions indicated. The spacing between scribes is d and 2L is the sample span. The agreement was very good over the range of loads used. The large spikes on the measured profiles (solid) correspond to the scribe trace positions.

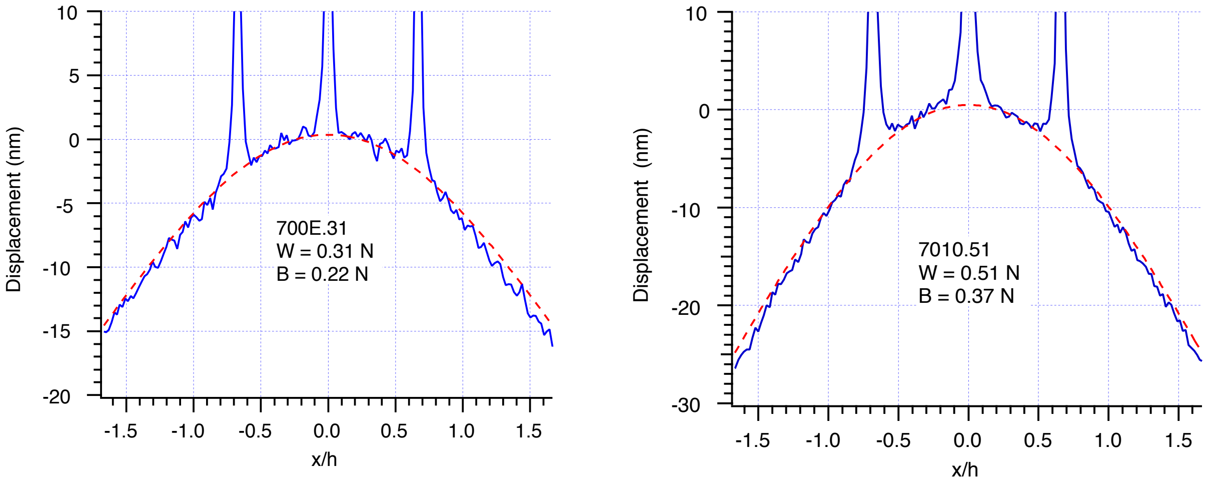

(a) W = 0.31N, d = 0.2 mm, 2L = 1.1 mm (b) W = 0.51N, d = 0.2 mm, 2L = 1.2 mm

Figure 6. Measured (solid) and model (dashed) profiles for the test conditions indicated.

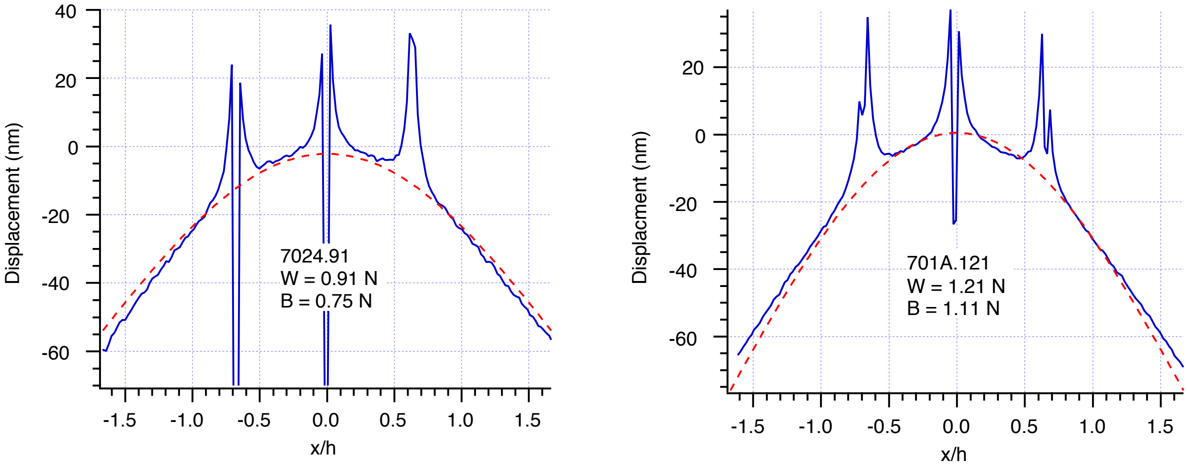

(a) W = 0.91N, d = 0.2 mm, 2L = 1.1 mm

(b) W = 1.21N, d = 0.2 mm, 2L = 1.0 mm

Figure 7. Measured (solid) and model (dashed) profiles for the test conditions indicated.

Figures 6 and 7 show comparisons for test samples that were used to obtain the calibration curve in Figure 5a. This should be a “universal” calibration in that it should be applicable to any test conditions for the given AlTiC material, not just those test conditions used for the calibration curve. To demonstate that this is the case, Figure 8 shows comparisons for samples that were not tested under conditions used for Figures 6 and 7. In particular, the number of scibes was increased and the scribing load decreased (Figure 8a), or the number of scribes was increased, the scribing load decreased and the sample span increased (Figure 8b). The agreement with the model is again very good.

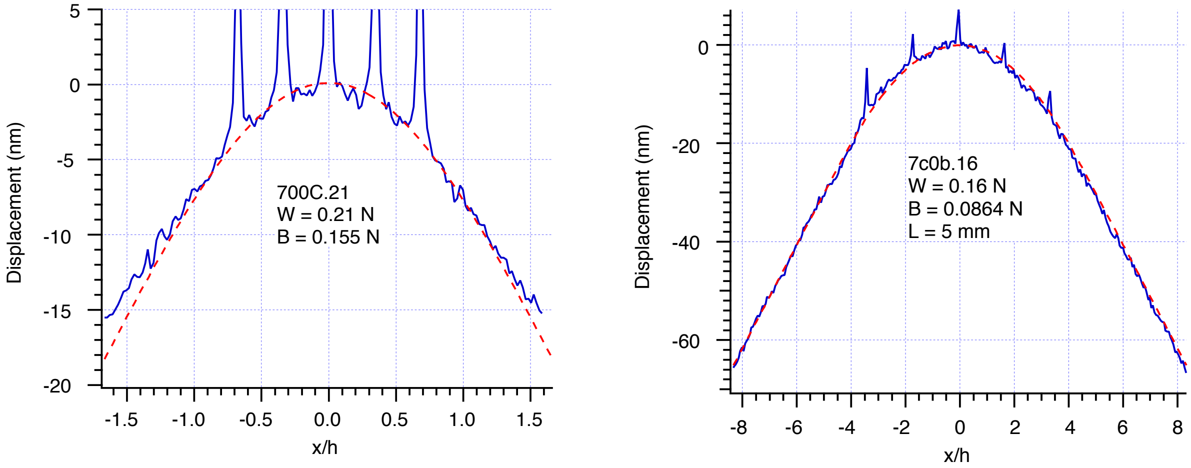

(a) W = 0.21 N, d = 0.1 mm, 2L = 1.0 mm
with 5 scribes per test sample

(b) W = 0.16 N, d = 0.5 mm, 2L = 5.2 mm
with 5 scribes per test sample

Figure 8. Measured (solid) and model (dashed) profiles for the test conditions indicated.

2.3 CONCLUSIONS

This study has shown that a beam-bending model based on a line-force dipole model for the residual stresses generated during diamond scribing gives a very good representation of the bend effect in sintered AlTiC ceramic material. Results not shown here were also obtained for glass and for other types of scribing tips [5]. The agreement with the model predictions was also very good in those cases. The significance of the results goes beyond the details of the analytical model developed here. One can anticipate that line-force dipole representations combined with plate theory or FEM analysis can be used to model the bend effect for more complex cases such as multiple, asymmetric partial scribes made on plate samples. In these cases, the resulting curvatures will be much more complex than simple 2D beam bending. Furthermore, other scribing methods that introduce residual stress, for example laser scribing, should also be amenable to suitably modified line force dipole models. Other material classes such as metals or polymers could also be treated. In that context, extensions of the studies reported here are currently being pursued [6].

REFERENCES

1. Tam, A. C., C. C. Poon, L. Crawforth, and P. M. Lundquist, “Stress On The Dotted Line”, Data Storage No. 6, 29, 1999.

2. Yoffe, E. H., “Elastic Stress Fields Caused by Indenting Brittle Materials”, Phil Mag.A,
vol. 46, no. 4, 617, 1982.

3. Ahn, Y., T. N. Farris and S. Chandraskar, “Elastic Stress Fields Caused by Sliding Microindentation of Brittle Materials”, Proc. of the Int. Conf. On Machining of Advanced Materials, S. Jahanimir, ed., NIST Spec. Publ. 847, 71, 1993.

4. Johnson, K. L., “Contact Mechanics”, Cambridge Univ. Press, p.17, 1985.

5. Austin, B. W., MS Thesis, North Carolina State University, 2000.

6. Love, B. M., MS Thesis, North Carolina State University, in progress 2001.

3 MODELING LASER SCRIBING FOR USE AS A PRECISION SHAPING TECHNIQUE

Bryan M. Love
Graduate Student
Jeffrey W. Eischen
Associate Professor
Department of Mechanical and Aerospace Engineering

Accurately controlling the shape of the read/write head structures is critical in the performance of a modern hard disk drive. The sliders investigated are composed of alumina and titanium carbide (AlTiC) and act as an air bearing when passing over the disks. Controlling the curvature of the slider is of primary importance. A laser scribing system that produces curvature by inducing residual stress into the slider can be utilized. Predicting the curvature created by a pattern of scribes is of great importance to increase the control over the sliders' shape. Using finite element analysis a force system that produces stresses similar to the laser scribing is applied. The curvatures created by the force system are calibrated to experimental measurements. The model was then further verified by predicting the shape of several other experimental scribing geometries with high accuracy. Further tests of the model will be conducted on other scribing geometries. When the accuracy of this model is assured, a library of scribing results can be built which will allow, through superposition, to predict the shape of complicated scribing patterns. Ultimately, with this library of scribe results, a scribing pattern could be generated to give a desired shape—extending the ability to control the shape of sliders, and allowing progress to the next level of hard drive speed and reliability.

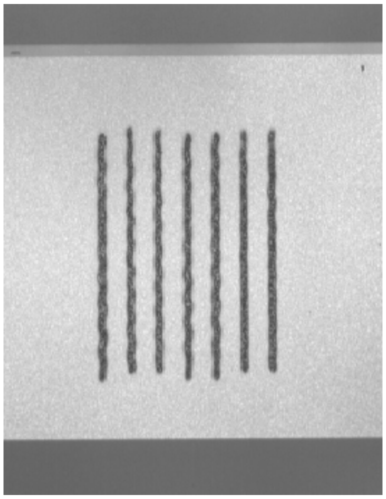

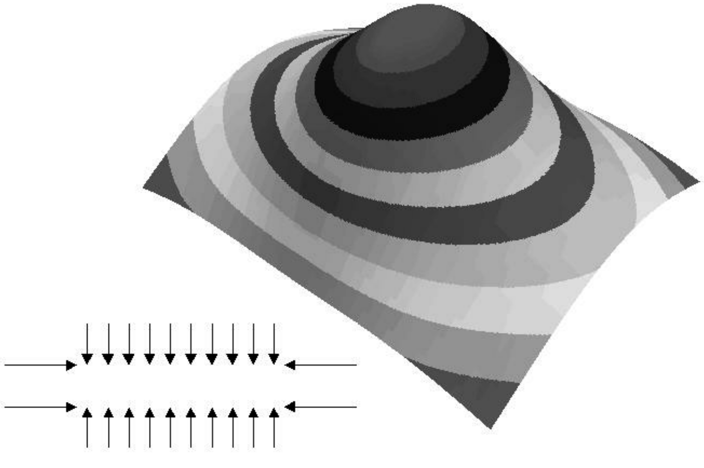

3.1 INTRODUCTION

In a modern hard disk drive, the flying height of the read/write head is one of the primary influences on data storage density and hard drive speed. The read/write head is contained within a slider that acts as an air bearing—therefore the shape of the slider directly determines the flying height of the read/write head. The flying height in modern hard drives has dropped below 25 nanometers; thus accurate control of the slider's shape is necessary to increase performance [1]. Controlling this shape is very demanding—the peak-to-valley deflections of the slider are on the order of nanometers (while the slider itself is approximately 1.2 mm by 1 mm).

There exists a technique using laser scribing that allows controlled adjustment of the curvature of the slider. The system relies on a pulsed laser to create localized residual stress, which results in very small deflections of the slider. The system, while operational and experimentally tested, uses a closed-loop measurement and scribing system (along with experimental history) to determine where scribes are placed [1]. In an effort to speed production, as well as control the curvatures of the slider more accurately, a model is sought which would allow theoretical determination of the curvatures produced by a scribe or a set of scribes. Such a model would allow theoretical determination of a scribing pattern that would produce a desired shape, without resulting to tedious experiments to determine the effects of various scribe geometries. Also, with a well-developed model, the system could be used to "flatten" sliders that already contained too much deflection or to remove asymmetries in the shape of the slider while producing the final shape desired by the designers.

3.2 LASER SCRIBING

3.2.1 BACKGROUND AND NOMENCLATURE

The sliders under investigation are fabricated from an alumina-titanium carbide (AlTiC) wafer, and when finished, measure 1.2 mm by 1.0 mm by 0.3 mm. The two large surfaces of the slider are known as the ABS (air bearing surface) and the flex side (shown in Figure 1). The curvature that is critical to operation is the curvature of the ABS side. Laser scribes deflect the slider towards the scribe, so all scribing is performed on the flex side (Figure 1 shows a slider with the desirable curvature).

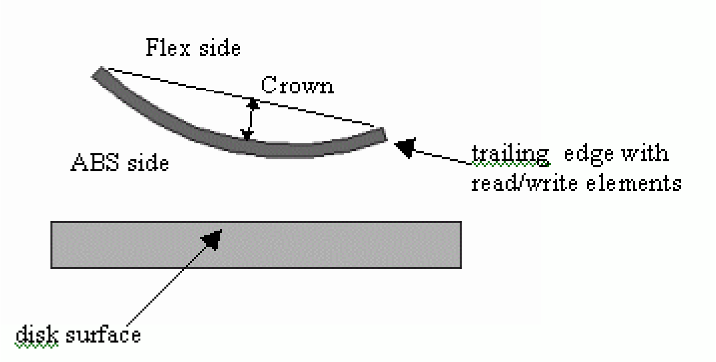

Figure 1. Slider Geometry

To parameterize the shape of the slider (both before and after scribing), a biquadratic curve fit is utilized, giving three critical curvature parameters that indicate the shape of the ABS side. These three curvatures, known as crown, camber and twist, are defined as follows:

$$
\begin{gathered}
z = C_0 + C_1x + C_2y + C_3x^2 + C_4y^2 + C_5xy \\
Crown = -C_3L^2/4 \\
Camber = -C_4L^2/4 \\
Twist = -C_5L^2
\end{gathered}
\tag{1}
$$

where $L = 1$ mm, and x, y, and z are defined in Figure 2 below. Note that crown is the curvature in the flying direction (see Figure 1), camber is perpendicular to crown, and twist is an asymmetry in the curvature.

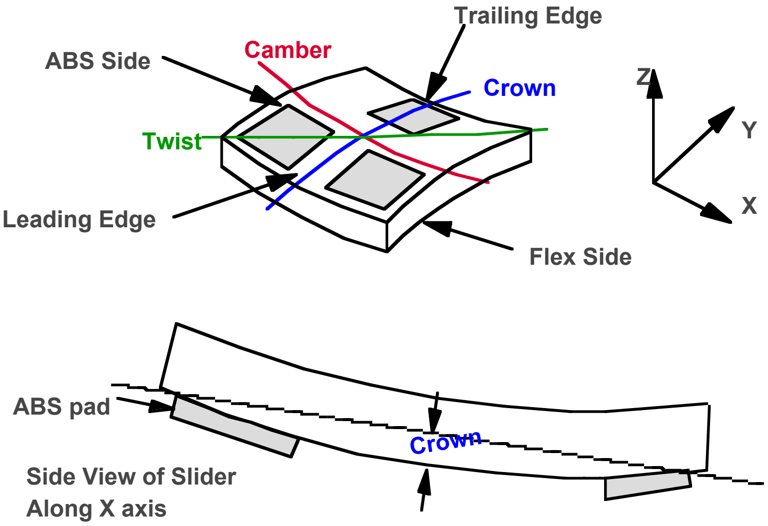

Figure 2. IBM Curvature Notation

The biquadratic curve fit assumes a constant curvature in the x and y directions, and while this is not strictly true, it addresses some of the metrology issues. The alumina and titanium carbide grains have different optical properties; therefore, the surface roughness of the sliders when measured with an optical instrument is very high compared to the deflections created by scribes. The constant curvature assumption allows nanometer level curvatures to be detected when the surface roughness is on the order of 100 nm.

The laser scribes are formed with a pulsed laser focused on the surface of the slider—the laser melts a small amount of material that, after solidification, forms a localized stress field, resulting in deformation of the slider. When the "dots" created by the laser pulses reach a critical spacing, the amount of deflection created "saturates", and the dots appear as a continuous line approximately 40 µm wide. The amount of deflection generated depends on the dot spacing, the laser power, and the geometry of the scribe.

Currently, sliders are scribed with nearly full-length scribes in the x and y directions, without scribes crossing (most sliders have scribes in a single direction). This scribing pattern allows for precise control over either crown or camber, but given that scribes produce a nearly constant crown/camber ratio, the other is fixed. Also, twist (which represents a major problem) cannot be created (nor compensated for) by symmetrical scribing patterns.

3.2.2 THEORETICAL MODELING

To model the deflections created by laser scribing, an adaptation of the line-dipole force model used by Austin and Scattergood was implemented [2]. The line dipole solution modeled a *mechanical* scribe as two sets of line forces separated by a small distance. However, for the mechanical scribing case, the scribe produced curvature perpendicular to the scribe, but not parallel curvature. So, to produce this parallel curvature as seen in the laser scribe, a set of forces parallel to the scribe were added. Two different force models were developed for the laser scribe, one with a distributed parallel force (Figure 3a, line forces $\underline{F}_m$) and another with concentrated forces at the end of the scribe (Figure 3b, forces F_m). Since each of these force models has loads in both *x* and *y* directions and the loads have endpoints, the theoretical beam theory solution (as performed by Scattergood and Austin) is not a practical way to solve this problem. However, numerical methods

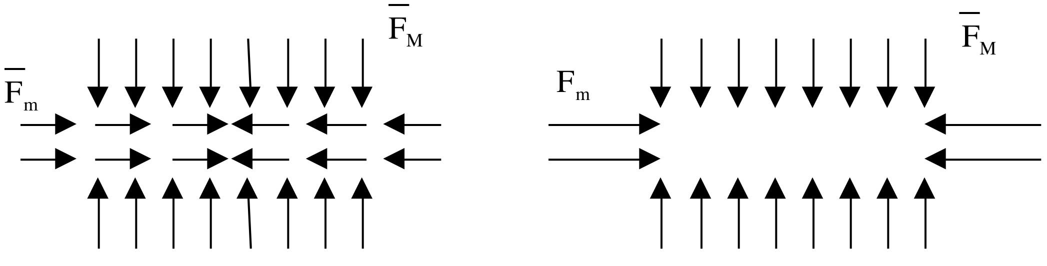

(a) (b)

Figure 3. Laser Scribing Force

such as finite element analysis can be used to solve a problem of this geometry effectively—thus allowing a solution to the force model based on solid mechanics.

As with the mechanical scribing model, this model requires calibration with a “control group” of laser scribes. For a symmetrical scribing pattern, there are two desired quantities (camber and crown) and two variables in the finite element analysis (the ratio F_m/F_M and a linear scaling factor). So, given the curvatures from one laser scribe pattern, the model can be calibrated and then used to predict other scribing patterns.

3.2.3 EXPERIMENTAL SOLUTIONS

In order to calibrate the model (and test the calibration), several different sets of measurements were made using the laser scribing system and interferometer. Several preliminary issues were addressed initially. The sliders are measured and scribed as a part of a “row” of 44 sliders connected along the side (in the *y* direction), as seen in Figure 4. The slider was measured before *and* after scribing (the row bar is *not* initially flat) on a Wyko interferometer and between measurements. Since the part is moved from the measurement device for scribing, repeatability is an issue. To test the measuring system, a row was measured on the Wyko, then moved to the scribing system, then moved back to the Wyko and measured again. The repeatability of the measurement is approximately 0.15 nm for both crown and camber.

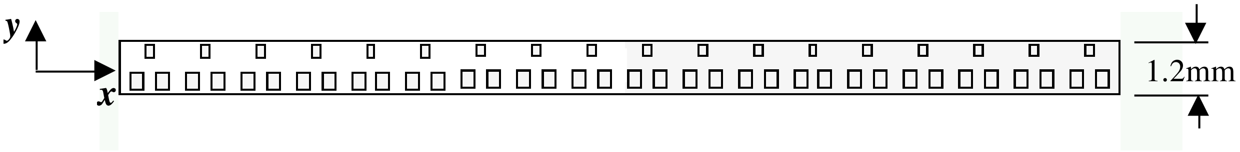

Figure 4. Portion of Row Bar

The repeatability of the curvature measurement had several important implications. First, it demands that every experimental scribing pattern be produced on multiple sliders. Averaging the curvatures given by each set helps eliminate any error caused by repeatability. Second, it dismissed using a single scribe for calibration purposes. Single scribes (whether in the *x* or *y* direction) create a maximum of 0.6 nm of curvature, and with a repeatability error of 0.15 nm (on both the before *and* after measurements), it would take a large set of sliders for the averaging to eliminate any measurement errors. Finally, the inability to use a single scribe calibration set raises the issue of superposition—namely if three scribes on a slider can be modeled as the sum of three single scribes. If superposition is obeyed, then modeling the scribes is relatively simple. However, if there is interaction between the scribes and superposition does not hold, the interaction effect must also be modeled for realistic results.

The question of superposition was the motivation behind initial experiments done because of its importance in the modeling. A simple experiment was designed to test superposition: seven scribes in the *y* direction, each with a length of 800 µm, were placed at evenly spaced intervals on the slider (at positions of 0.28, 0.36, 0.44, 0.52, 0.50, 0.68, and 0.76 mm along the *x* axis of the slider). Then two other sets of sliders were scribed with patterns that should (given that superposition is obeyed) sum to the original set: one set contained three scribes at 0.36, 0.52, and 0.68 mm and the other contained four scribes at the remaining four positions. Figure 5 below shows the three scribing arrangements and their average crown and camber (each result is the average of 11 sliders).

The superposition proved to be very accurate (an error of 2.5% or 0.12 nm—well within the repeatability error), even at the relatively close scribe spacing (80 µm). The low error seen in this experiment allows the scribes to be modeled individually and then summed to find the result for a multiple scribe pattern—a technique which allows a large number of patterns to be modeled from a relatively small number of results.

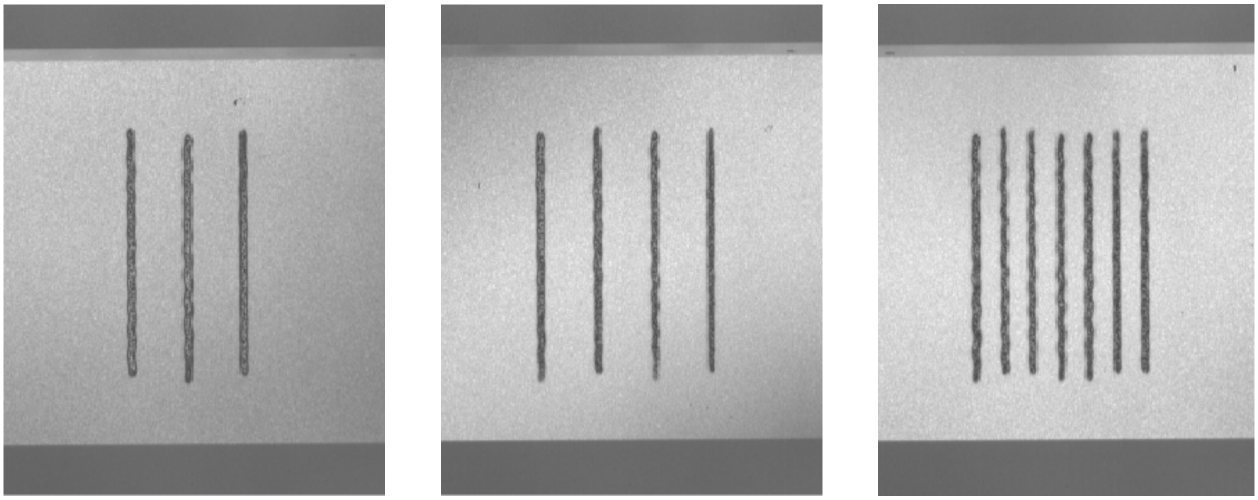

3 scribes (0.36, 0.52, 0.68)
Crown: 1.91 nm
Camber: 2.35 nm

4 scribes (0.28, 0.44, 0.60, 0.76) Crown: 2.84 nm
Camber: 2.94 nm

7 scribes (all of previous)
Crown: 4.64 nm
Camber: 5.37 nm

Figure 5. Superposition Experiment

The rest of the experiments were designed to give a representative sample of the types of scribing that could be in industrial practice. The scribes must be along the *x* or *y* axes, but they can have varying lengths and the spacing between scribes can vary as well. The first set of experiments was designed to test the effects of scribe length on the curvature of the slider. Using a single scribe direction (*y*) and spacing (80 µm), three scribes were placed on the slider, with the length of the scribes varying from 600 µm to 1000 µm (the maximum size allowed). Each scribing experiment was conducted on 11 sliders, and the results are shown in Figure 6.

Varying the scribe length yielded some interesting results—camber decreased as the scribes were shortened (as would be expected), however crown did not decrease. This result was unexpected, and poses a problem for modeling purposes. This result is discussed in detail in the *Calibration and Modeling* section. Also, note that twist is not reported for any of the above cases because, as expected, a symmetrical scribing pattern generates no appreciable twist (any twist shown during the experiments is well within the repeatability error of the measurement).

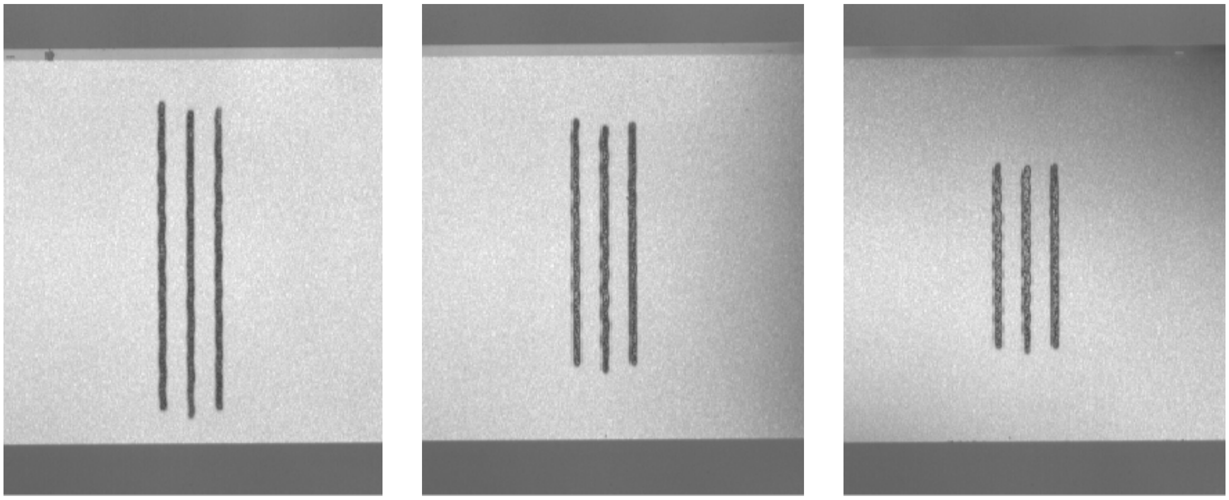

Length 1000 µm
Crown: 1.65 nm
Camber: 2.65 nm

Length 800 µm
Crown: 1.82 nm
Camber: 2.55 nm

Length 600 µm
Crown: 1.66 nm
Camber: 1.96 nm

Figure 6. Scribe Length Experiments

Scribe spacing was also varied in a similar fashion. Using a fixed length (1000 µm), three scribes were placed on sliders with three different spacings (40 µm, 80 µm, and 240 µm). The average of 11 sliders is shown in Figure 7. Also, the data for the superposition and length trials can be used to give another example of scribe spacing with 800 µm-long scribes with spacings of 80 µm and 160 µm.

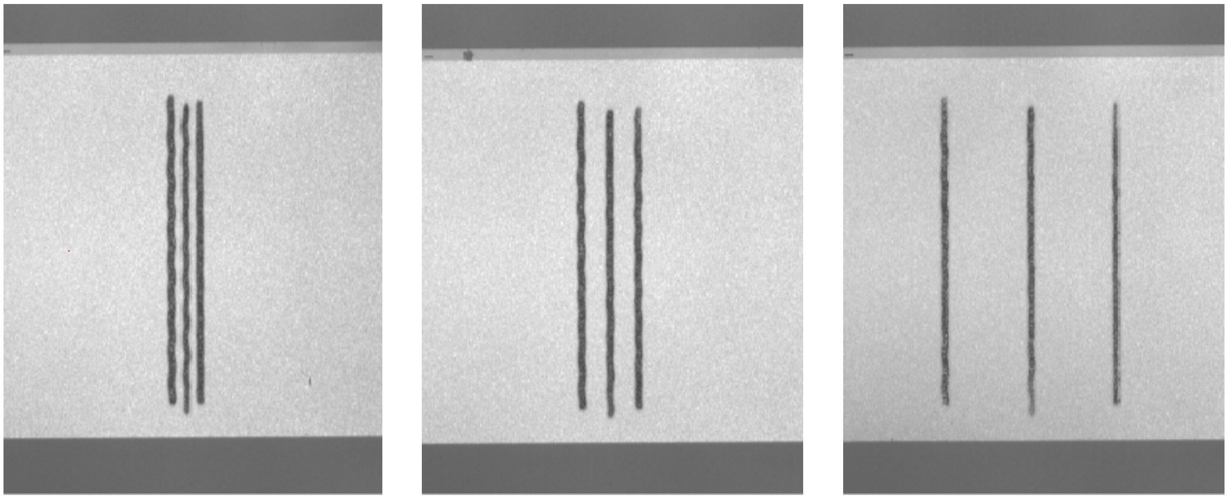

Spacing 40 µm
Crown: 1.58 nm
Camber: 2.54 nm

Spacing 80 µm
Crown: 1.65 nm
Camber: 2.65 nm

Spacing 240 µm
Crown: 1.56 nm
Camber: 1.83 nm

Figure 7. Scribe Spacing Experiments

The results listed previously account for the two major variables for scribes in the *y* direction (spacing and length). A similar complement of experiments for scribes in the *x* direction (lengths of 1030, 747, 556, and 365µm and spacings of 40, 80, and 200µm) helps explore directional dependence (if any). Using these results, the model for the scribing can be calibrated from one of the experiments, and the remainder of the experiments can be used to verify the model. The range of experiments encompasses the range of parameters that can be varied—therefore, if a model can predict the curvatures in all of the various experiments, then it can be used to *theoretically* predict the curvatures generated by any scribing pattern.

3.2.4 CALIBRATION AND MODELING

Modeling the scribed sliders consists of applying a force system to a linear elastic finite element mesh, as discussed in *Theoretical Modeling*. The linear elastic finite element model allows linear scaling—the deflections are directly proportional to load and inversely proportional to material properties. This property allows scaling for calibration purposes—the actual material properties and stresses created by the scribing can be compensated for by a constant factor during calibration. The linear elastic analyses also inherently obey superposition.

The finite element model utilizes a fine mesh near the scribe line (to capture the localized stresses caused by the scribing), but a coarse mesh away from the affected area (in order to reduce solution time). Either of the force systems (shown in Figure 3) can be applied to the mesh at any location on the slider to model the scribe. To best simulate the scribe geometry, the separation of the line dipoles was set at 40 μm (approximately the same as the scribe widths seen in the experiments) and the length is set depending on the scribing geometry.

As previously mentioned, this modeling technique requires calibration with an experimental result that shows the curvature for a given scribing geometry. Using superposition, the scribing pattern of one of the experimental data sets is modeled, and the deflections from the finite element analysis are fitted with the same biquadratic as the experimental data. The crown, camber, and twist numbers from the model are compared with the experimental data. If the numbers do not coincide, there are two things that can be adjusted in the model: the ratio of the forces F_m/F_M (which determines the "shape" of the deflection), and the linear scaling factor (which determines the actual magnitude of deflection). Once the model is calibrated to one of the experimental results, different scribing geometries can be created and compared with their experimental analogues and the model can be verified.

The experiment that was initially taken for calibration was three y-direction scribes with 80 μm spacing (Figure 7, middle picture). Using the distributed force model (Figure 3a) with parameters $\underline{F}_M$ = 33 unit force/unit length and $\underline{F}_m$ = 2.4 unit force/unit length, the finite element analysis yielded a crown of 136.01 and a camber of 220.92. Recall that the finite element results can be scaled by a constant to the correct magnitude, so the ratio of crown to camber is of importance. The ratio of crown to camber for the experimental case was 0.623, while the finite element analysis yielded a crown to camber ratio of 0.616 (error of 1.12%). This calibration yielded the results in Table 1 for seven other cases (all *y* direction scribes):

Table 1. Calibration with Distributed Force Scribing Model

No. of scribes	*Scribe length*	*Scribe spacing*	*Crown/camber experimental*	*Crown/camber predicted*	*% error*
3	1000 μm	240 μm	0.852	0.835	2.04%
3	1000 μm	40 μm	0.622	0.600	3.61%
3	800 μm	160 μm	0.813	0.541	33.48%
3	800 μm	80 μm	0.714	0.487	31.72%
4	800 μm	160 μm	0.966	0.613	36.57%
7	800 μm	80 μm	0.864	0.580	32.92%
3	600 μm	80 μm	0.847	0.367	56.62%

Obviously, the distributed force model yields poor results. Interestingly, the calibration holds well for scribes of the same length (but different spacings), but it fails when the scribe length is changed.

Calibrating the end-force scribing model (Figure 3b) on the same experimental case (3 *y* scribes, length 1000 µm, spacing 80 µm), yields F_M = 33 unit force/unit length and F_m = 0.82 unit force. The finite element analysis yields a crown of 130.96 and a camber of 213.03, which gives a crown to camber ratio of 0.615 (compared to an experimental value of 0.623, a 1.27% error). The seven other cases yielded the results shown in Table 2 with this calibration.

Table 2. Calibration with End Force Scribing Model

No. of scribes	*Scribe length*	*Scribe spacing*	*Crown/camber experimental*	*Crown/camber predicted*	*% error*
3	1000 µm	240 µm	0.852	0.833	2.24%
3	1000 µm	40 µm	0.622	0.599	3.75%
3	800 µm	160 µm	0.813	0.843	3.72%
3	800 µm	80 µm	0.714	0.756	5.92%
4	800 µm	160 µm	0.966	0.962	0.45%
7	800 µm	80 µm	0.864	0.907	4.96%
3	600 µm	80 µm	0.847	0.844	0.37%

The end force scribing model yielded much more accurate results—over the entire range of lengths and spacings, the maximum shape error was 6%.

One plausible mechanism that would validate the end force model involves the process by which the scribe is produced. As mentioned previously, the scribe is actually a collection of “dots” created by the pulsed laser placed close together. If the residual stress induced by the scribe is created by the resolidification of the melted material, each dot’s stress in the scribe direction would be cancelled by the dots on either side. Except for the dots on the end, which would create tensile stresses on the end (similar to the end force model).

The end force model predicts the shape of the scribe sliders quite well, as shown above. However, for a full calibration, a linear factor must be introduced to establish the actual magnitude of the curvatures. As mentioned previously, the magnitude of the curvatures does not necessarily obey intuition or solid mechanics (if the assumption of the same material is true). For example, in the scribe length study (see Figure 6), the longer scribes did not necessarily produce more deflection than the shorter ones (a result that intuition *and* finite elements produces). However, the finite element model does produce the correct shape (crown to camber ratio). The influences on this linear factor are the material properties and the strength of the scribe—both of which could be influenced by the change in material. Upon further examination, it was found that all of the sliders that did not match the full calibration within 5% error came from the *same row*—possible indication that material properties are causing the error. A possible remedy for this would be to calibrate each row on one slider with a test pattern. Further investigation will reveal if this is necessary. But overall, the end-force model does show a great deal of promise—it predicts the shape of the sliders with good accuracy and, barring a single row, produces excellent results for the overall magnitudes of the curvatures.

3.2.5 FUTURE MODELING

Several further steps must be taken in order to have a complete model capable of modeling a scribe of any length or direction. These include:

- extending the scribing geometry to include scribes in the *x* direction
- exploring sources of error (model geometry, load application, etc)
- modeling new scribe geometries and verifying their curvatures experimentally
- develop models that generate twist
- construct a library of solutions

Extending the model to include *x*-direction scribes is relatively simple: a new mesh must be developed, scribing geometries tested with the calibration found above, and results verified with the experiments conducted.

The model is currently fairly accurate, thus pinpointing further sources of error is difficult. One possible source of error involves the model geometry—experimentally, the sliders are scribed and measured as part of a row (which is 44 sliders attached together), while the model's geometry just includes a single slider. While modeling an entire row is impractical, there are symmetry conditions and other finite element techniques to help approximate this extended geometry

Once the model is verified and its accuracy assured, the remainder of the modeling is designed to develop a library of solutions. Since superposition is obeyed, a collection of single scribe results can be summed to give complicated scribe geometries. Of primary interest are scribing arrangements that generate twist—twist is one of the primary problems in slider processing. A final verification of the model could be conducted by theoretically modeling a scribe pattern that generates twist, and then performing the experiment and comparing results.

3.3 CONCLUSION

Through experimentation and finite element modeling, it was shown that the curvature produced by laser scribing can be predicted theoretically. A finite element mesh with an appropriate force system (in this case, a line dipole with parallel end forces) can be calibrated using experimental results, and then used to predict other scribe geometries. Since superposition is obeyed, single scribe results can be modeled theoretically and then added to construct more complicated geometries.

The preliminary investigation into calibrating the model has shown very good results. Further investigation with varying scribe geometries will be explored over the next few months. With a fully calibrated model, a library of single scribe solutions can be created. This library could be used to construct a scribing pattern based on a desired shape—allowing more sophisticated control over the scribing system and ultimately, better shape control of the sliders.

REFERENCES

1. Tam, A.C., et. al., Manufacturing: Stress on the Dotted Line, IBM Corp., Almaden Research Center, December 1999.

2. Austin, B.W. and R.O. Scattergood, Precision Engineering Center, 2000 Annual Report.

4 SURFACE METROLOGY OF COMPLIANT MATERIALS IN FLUID

Alex Sohn
PEC Staff Member

Measuring the surface characteristics of compliant optical materials in fluid presents some unique challenges. First, not many instruments are capable of performing measurements in fluid. Second, if the material has a low modulus, any contact deflects the surface and therefore influences the measurement. Finally, the refractive index change at the surface of the material is very small because it is it is submerged in fluid. This all but excludes optical profilometry for measuring these surfaces. Given these limitations, the best method for measuring surface characteristics of these materials is by scanning probe microscopy. The ability to acquire measurements in a fluid and small probing forces make SPM the ideal vehicle for characterizing compliant optical materials in fluid.

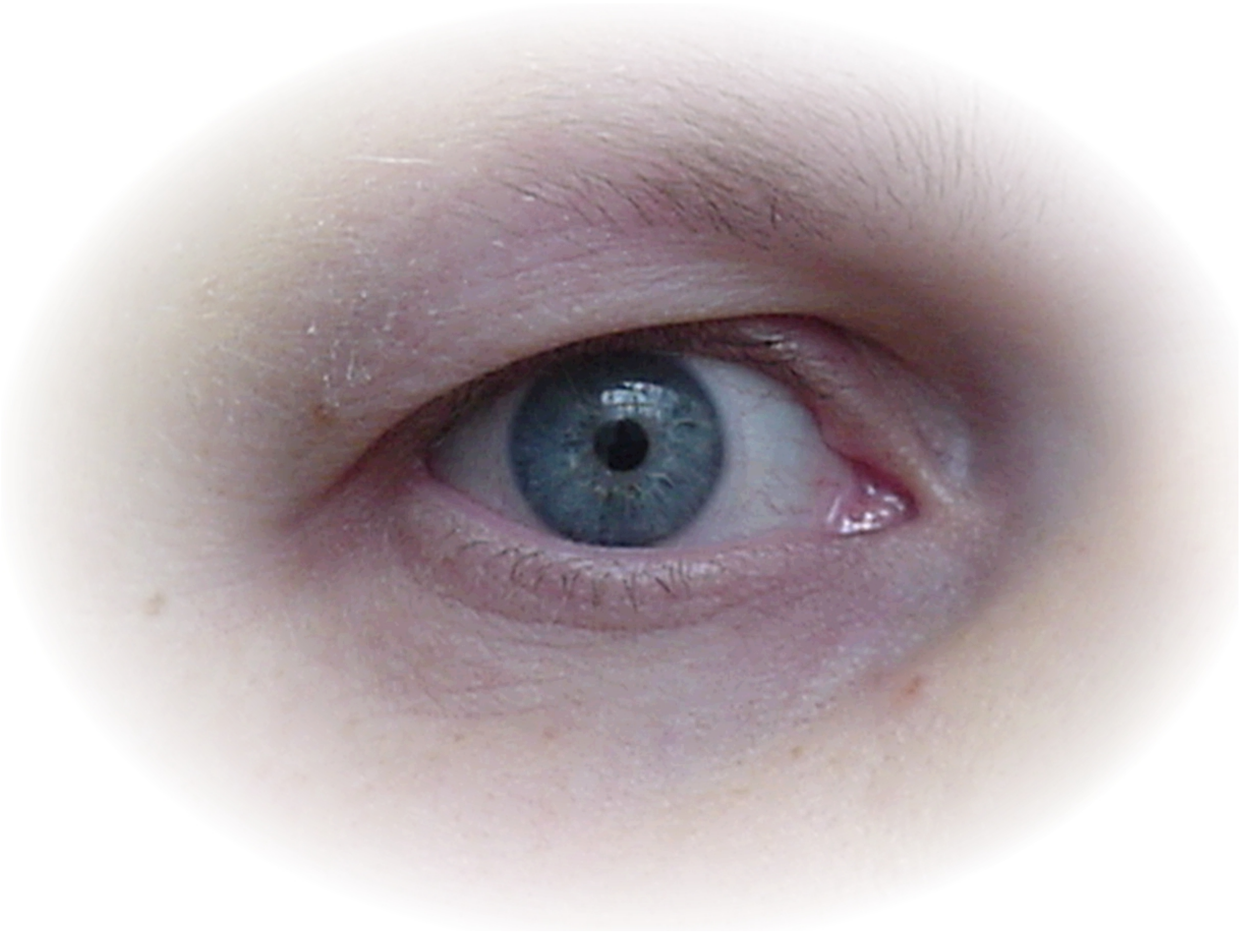

4.1 INTRODUCTION

An important aspect of improving the manufacturing processes for compliant optical devices is the metrology used to gauge the results of these processes. Dimensional metrology focuses on two distinct areas: overall shape and surface characteristics. Shape measurements entail probing the power and large-scale distortions of a lens for example. Such measurements are exceedingly difficult to perform on soft materials, especially in fluid. Surface characteristics are mainly concerned with roughness and play an important role in the efficiency and imaging capability of optical devices.

Surface metrology of compliant optical materials in fluid faces three distinct obstacles associated with the unique physical characteristics of such materials. First, many of these materials are composed mainly of water and must therefore remain hydrated for meaningful measurements. Many instruments normally used for surface metrology would not tolerate the presence of water during measurement. Electron microscopes require the sample to be in an evacuated environment – a condition incompatible with the presence of water. Second, for materials that are very compliant, even the smallest of contact forces will impact the measurement. Therefore,

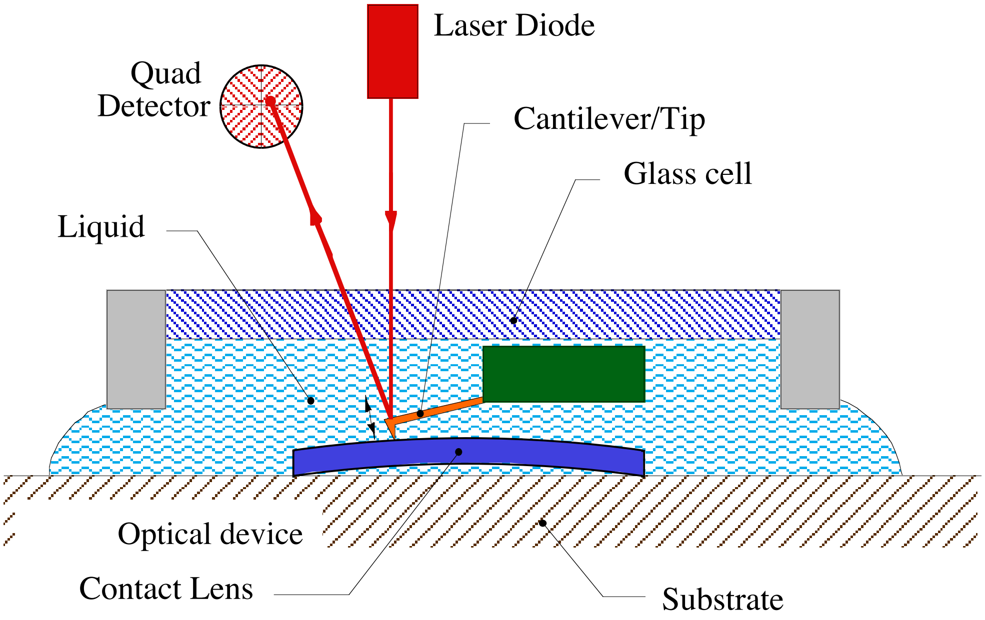

Figure 1. Fluid cell Scanning Probe Microscopy uses a standard atomic force microscope with the cantilever/tip in a fluid cell. The tip and the fluid are separated from the rest of the SPM by a glass plate that allows the cantilever to be probed by a laser beam from a laser diode. Deflections of the beam can then be detected on a position sensitive detector.

a profilometer such as a Talysurf or Dektak could not be used. Finally, when a device is submerged in fluid, it becomes nearly invisible in the fluid due to the minute difference in refractive index between the optical sample and water. This excludes the possibility of using an optical profilometer for measuring the such a device.

Currently, the only reliable means for measuring the surfaces of compliant optical materials in fluid is with a fluid-cell SPM shown in Figure 1. The fluid-cell SPM is essentially an Atomic Force Microscope with the probe tip placed in a fluid. To defeat the effects of surface tension, the cell is capped with a glass slide over the probe cantilever. The glass slide also provides a flat interface from fluid to air so that the laser beam used to probe the deflection of the cantilever can pass between the materials unimpeded. As the probe tip is scanned across the surface of the device, the deflections of the cantilever are sensed by an optical detector and recorded. Deflections as small as 1 Å can be detected, though depending on the machine used, noise may limit resolution to about 1 nm. The size of the area measured is usually limited in a SPM by the stroke of the piezo actuators that position the probe tip. This stroke is generally around 40 μm, making the maximum measurement patch 40 μm by 40 μm.

The instrument, shown in Figure 2, was used for the measurements described here. It is a Digital Instruments/Veeco Dimension 3000 AFM available at the N.C. State Analytical Instrumentation Facility (AIF). The large sample capacity, motorized positioner, and ability to use a fluid cell make this the instrument of choice for the study of compliant optical materials in fluid.

Figure 2. The Dimension 3000 AFM is capable of accommodating large samples and a fluid cell.

4.2 SAMPLE PREPARATION

The most complex step in the procedure for measuring the surfaces of compliant optics is sample preparation. Fixturing wet materials to a substrate is fraught with complications. The optical devices tested here were thin, nearly hemispherical membranes. First, the samples were too fragile to support themselves when placed on a surface. Second, the fluid acts as a film bearing, allowing the sample to slide on the substrate with very little friction. Third, the samples tear easily, so any mechanical clamp that applies a significant amount of force locally can damage the sample. Finally, the fluid on and in the samples prevents the use of surface adhesives such as double-stick tape.

The usual method used for fixturing these devices for SPM measurement, illustrated in Figure 3, makes use of the inherent geometry of the device. A circular section of about 8 mm diameter is first cut or trepanned from the center of the dome-shaped device. This section is then allowed to dehydrate somewhat around the perimeter until it develops a small amount of surface tack. At this point, the sample is pressed flat against the substrate (usually silicon or glass) convex side up. The sample thus acts like a suction cup, holding itself to the substrate. The substrate and sample is then transferred to the SPM for measurement.

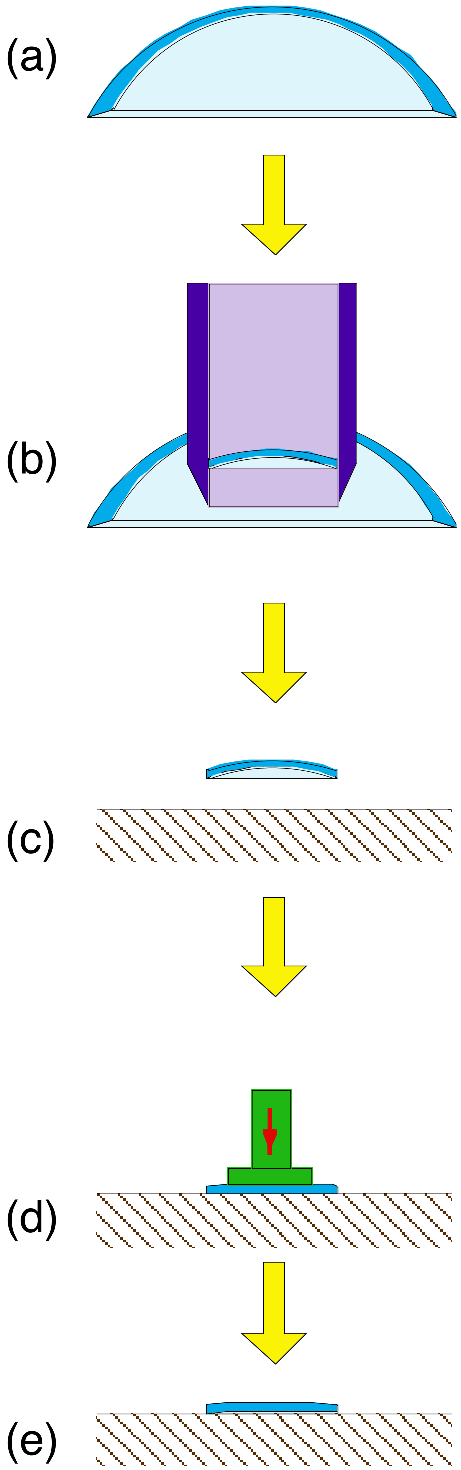

Figure 3. Schematic of standard sample preparation. The device (a) has a circular section removed from its center (b) is placed on a substrate (c) and then flattened (d) to hold itself to the surface via its own suction (e).

This method does, however, have several drawbacks. Only the convex side of the sample can be measured. If turned over to measure the concave side, it would try to lift its edges and become detached as soon as it was hydrated. Also, the sample can only be taken from the central region of the device, thus preventing areas near the perimeter from being measured. Damaged or incomplete samples cannot be measured either. Additionally, as the sample rehydrates, it does not remain attached to the surface. This allows only a short amount of time (about 15-20 minutes) to place the sample on the SPM, find the target area, engage the tip and measure. An experienced operator will not have a problem performing the measurements, but the aforementioned restrictions on the types of measurements and samples that can be measured require an alternative technique to augment the standard one.

The main impetus for developing an alternative mounting technique was the need to measure the surface finish of the concave or inside surface of a sample. As previously mentioned, this is difficult to do with the standard sample preparation scheme. Several attempts were made to apply this method to concave side measurements with little success. As long as the samples remained partially dehydrated, they remained fixed to the surface. About three to five minutes after they were placed in the fluid cell for measurement, however, they became detached from the substrate. As shown in Figure 4, the result of the sample becoming detached during a measurement is a worthless data set.

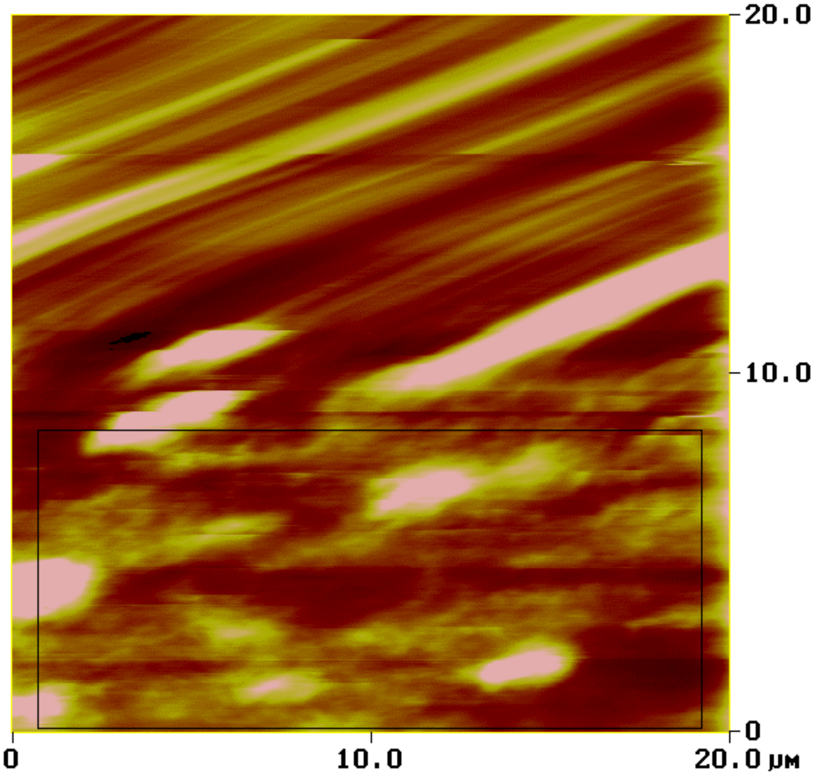

Figure 4. Poor results occur when the sample becomes detached during a measurement. In the picture, the probe was scanning from bottom to top. About halfway through the scan, the sample lost contact with the substrate.

Attempts were made to retain the sample by mechanical means, but these attempts met with little success. Clamping over a large area usually causes the material to squeeze out from under the clamp. Clamping at a small point causes tears that then make the clamp ineffective. Another disadvantage of mechanical clamping is one that was observed with the standard sample preparation procedure; that is, the sample is only retained around the perimeter, its center can be displaced horizontally due to the compliance of the material. This compliance gives non-repeatable results and prevents accurate surface analysis. An ideal way to retain the sample, therefore, would be to attach the entire back surface to the substrate.

4.3 ADHESIVE SAMPLE MOUNTING

A common way used to affix AFM samples to a substrate is to apply a double-stick tape to the interface. This secures the entire back surface of the sample, preventing lateral distortions during measurement. The method is also a simple way to rapidly prepare a large number of samples without expensive fixturing devices. The unfortunate disadvantage of this method is that it does not work in fluid.

There is, however, an adhesive that will bond in the presence of fluids. Cyanoacrylate, commonly known as Super Glue, will cure rapidly in the presence of water and can therefore be used to effectively bond wet objects. It has been used effectively for years as a medical adhesive for bonding open wounds that are seeping fluid.

To bond compliant samples to a substrate, two different application methods were explored. Initially, the sample was placed on a glass slide and surrounded with a thin bead of cyanoacrylate. The sample was effectively bonded to the surface and several measurements were attempted. As previously mentioned, however, having the sample attached only at the perimeter allows lateral displacement of the material as the stylus is dragged across the surface. Measurements using this fixturing method were therefore not reliable.

The second technique for applying the adhesive yielded much better results. As shown in Figure 5, a section of the device was removed and set aside. Next, a small amount of cyanoacrylate adhesive was applied to a dry glass slide. This globule of adhesive was then spread thin using a razor blade. The hydrated sample section was immediately pressed onto the adhesive for a few seconds. An opaque white film formed at the perimeter of the sample indicating that the adhesive had cured. With the sample firmly bonded across its entire surface, it was placed on the SPM stage. Initial views of the sample through the video microscope of the SPM revealed a crystalline or labyrinth-like structure.

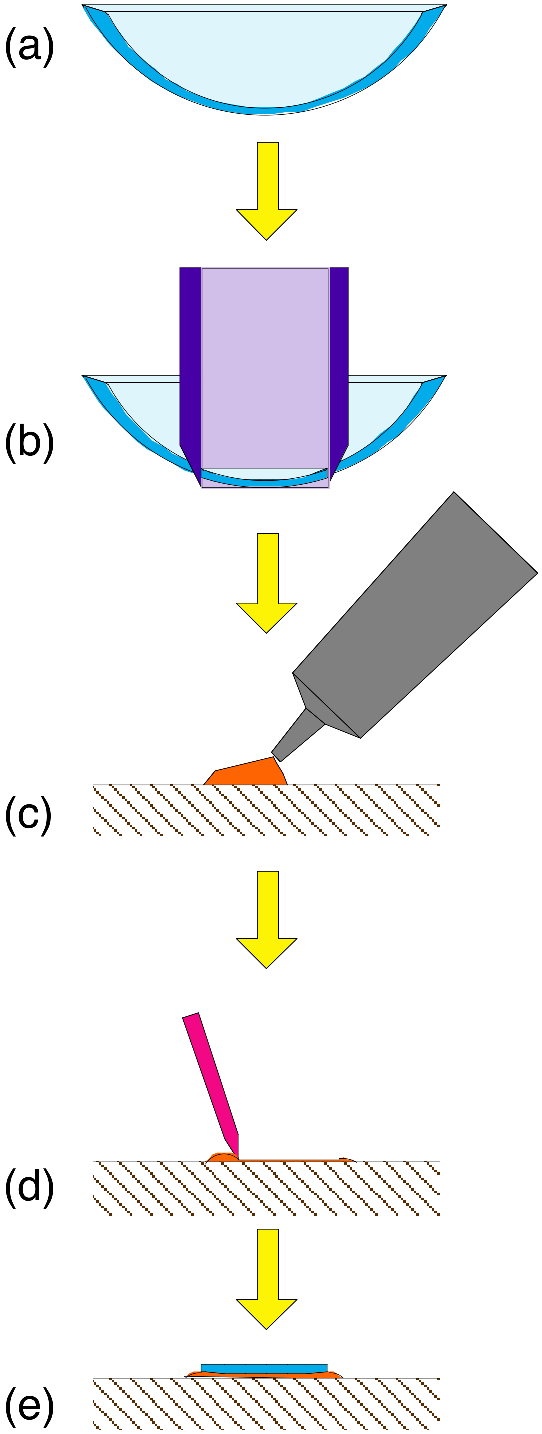

Figure 5. Adhesive Sample Bonding used for effective fixturing of semi-hemispherical samples. The sample (a) has a section removed (b), after which cyanoacrylate is applied to the substrate (c) and spread into a thin film (d), allowing the sample to be affixed to the surface (e).

This appears to have been a result of the adhesive interacting with the saline solution during polymerization. The structure was between the sample and the substrate and did not appear to have an impact on surface measurements.

Scans were made of several areas on the sample. Sample scans shown in Figures 6 and 7 show measurements to be both repeatable and able to resolve small features. Multiple scans across the same area revealed the same features in the same location on the scan – a previously unattainable result. Additionally, scans of different regions of the sample produced similar roughness values.

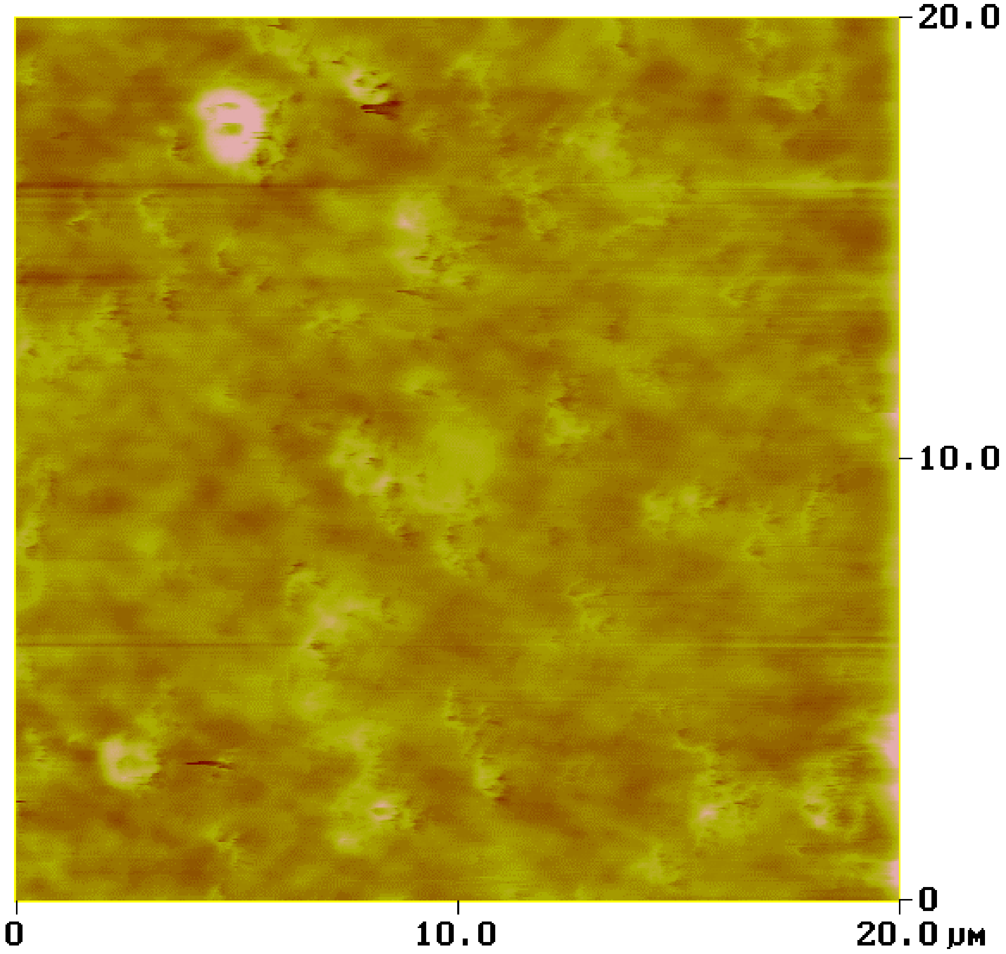

Figure 6. Successful Measurement using adhesive sample mounting technique. Results were repeatable between successive measurements as well as for different measurement areas. A roughness analysis is shown in Figure 7.

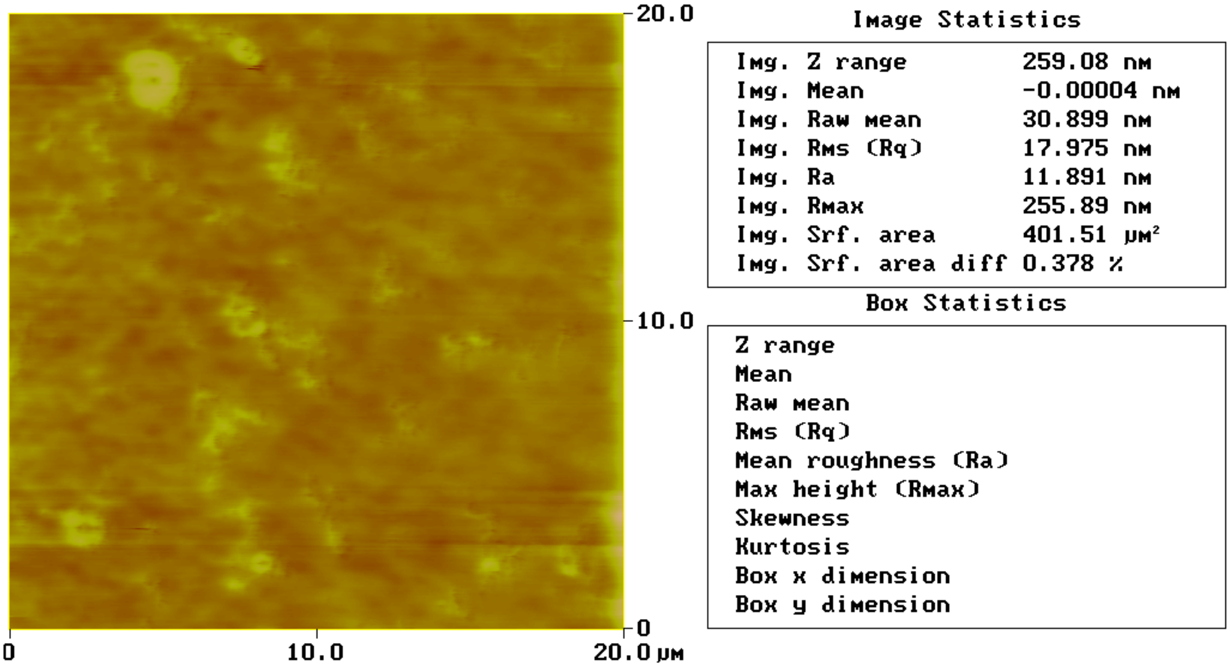

```
                 Image Statistics
Img. Z range          259.08 nm
Img. Mean             -0.00004 nm
Img. Raw mean         30.899 nm
Img. Rms (Rq)         17.975 nm
Img. Ra               11.891 nm
Img. Rmax             255.89 nm
Img. Srf. area        401.51 µm²
Img. Srf. area diff   0.378 %
                 Box Statistics
Z range
Mean
Raw mean
Rms (Rq)
Mean roughness (Ra)
Max height (Rmax)
Skewness
Kurtosis
Box x dimension
Box y dimension
```

Figure 7. Roughness Analysis of sample shown in Figure 6. Roughness values are of a magnitude (~20 nm Rms) that is consistent with those expected for an optical surface.

These results indicate that gluing the samples to a substrate is an excellent, if not superior way to stabilize hydrated contact lenses for SPM measurement. Several advantages of this method aside from repeatability exist. First, samples of any size and either surface can be fixtured. Second, the samples remain affixed to the surface for an indefinite amount of time, allowing multiple, repeatable measurements. Finally, the method is simple to execute and does not require the SPM operator to work in a hurried manner.

4.4 FUTURE WORK

With respect to the overall problem of measuring the surface properties of compliant optical materials in fluid in particular and low-modulus materials in general, there are still many uncertainties. Of primary concern is the influence of the SPM tip on the sample. There is always some deformation of the surface of the lens and there are tip/sample interactions that influence measurement results based on surface and fluid chemistry. Currently, surface measurement results are not independently verifiable with other instruments. Finding other methods to verify these results is as important as predicting potential measurement errors. There have also been improvements in SPM technology which could make measurements more accurate and reliable. The newest generation of scanning microscopes from DI/Veeco has the ability to perform tapping mode measurements in fluid. In this process, the cantilever tip is vibrated during measurement to eliminate lateral forces on the sample. This could have a substantial impact on measurements, especially on low modulus materials such as contact lenses. This instruments expected to be available in the AIF some time in 2001.

4.5 CONCLUSION

While measurements of surface roughness can be made on compliant optical materials in fluid using Scanning Probe Microscopy in a fluid cell, sample mounting techniques are essential to obtaining good measurement data. While established sample preparation techniques are adequate for measurements of convex surfaces, measurements of edge regions and concave surfaces require improvements. A new method involving fixing the samples to a glass substrate using cyanoacrylate adhesive is proposed. Multiple measurements have shown this mounting technique to be a stable, repeatable and simple to apply fixturing technique.

5 DESIGN OF THE POLAR PROFILOMETER *POLARIS*

Alex Sohn
Ken P. Garrard
PEC Staff Members

Profilometers have traditionally been based on cartesian geometries for performing form and roughness measurements. These designs, however, have limitations. Certain industries, those making high aspect-ratio optics in particular, require the measurement of geometries more polar than cartesian in nature. A polar profilometer has therefore been designed at the PEC. The device will measure parts from hemispheres to aspheres both concave and convex inside a circular measurement field 50 mm in diameter. This design can be used to measure surfaces with a resolution of no less than 100 nm and an overall accuracy of at least 500 nm.

As of February 2001, the design of Polaris is complete and construction has begun. As components are delivered, subassemblies are being tested. Completion of the project is scheduled for May 2001.

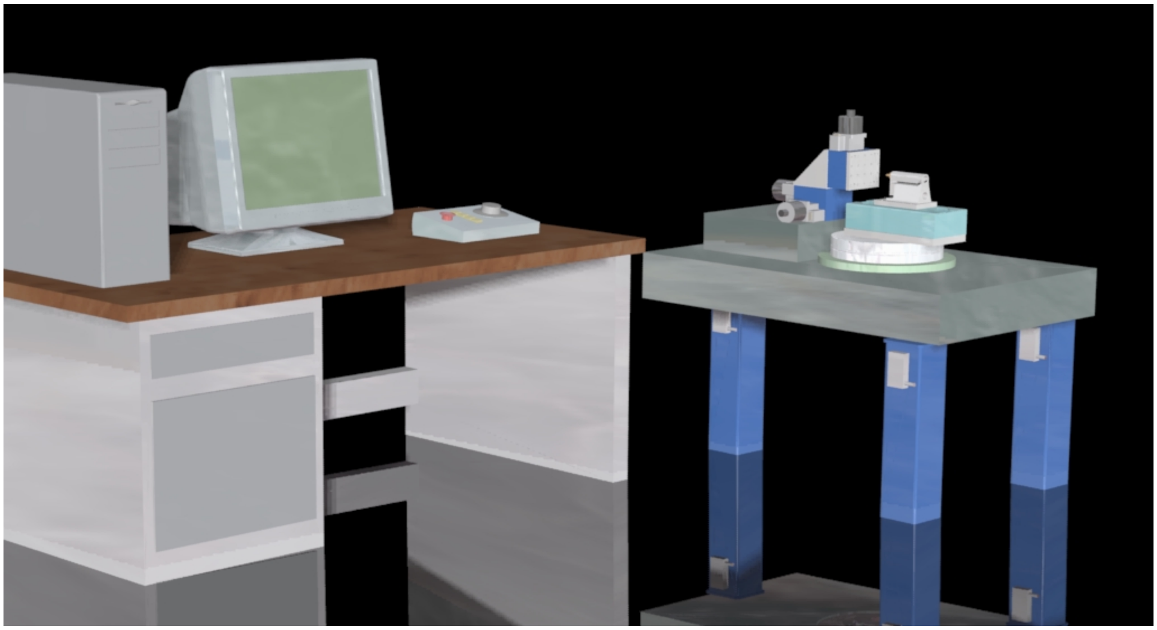

5.1 INTRODUCTION

Measuring parts with large slopes and aspect ratios presents a significant challenge for commercially available measurement systems. Optical profilometers are slope limited to a few degrees by the ratio of fringe spacing to camera resolution. Mechanical profilometers, on the other hand, are usually limited by the clearance angle of the tip and the non-perpendicular loading direction of the probe, both of which often limit the measurable slopes to less than 45° as shown in Figure 1(a). If, however, there were a way to keep the probe tip nominally perpendicular to the sample surface as shown in Figure 1 (b), the slope limitation of mechanical profilometers could be overcome.

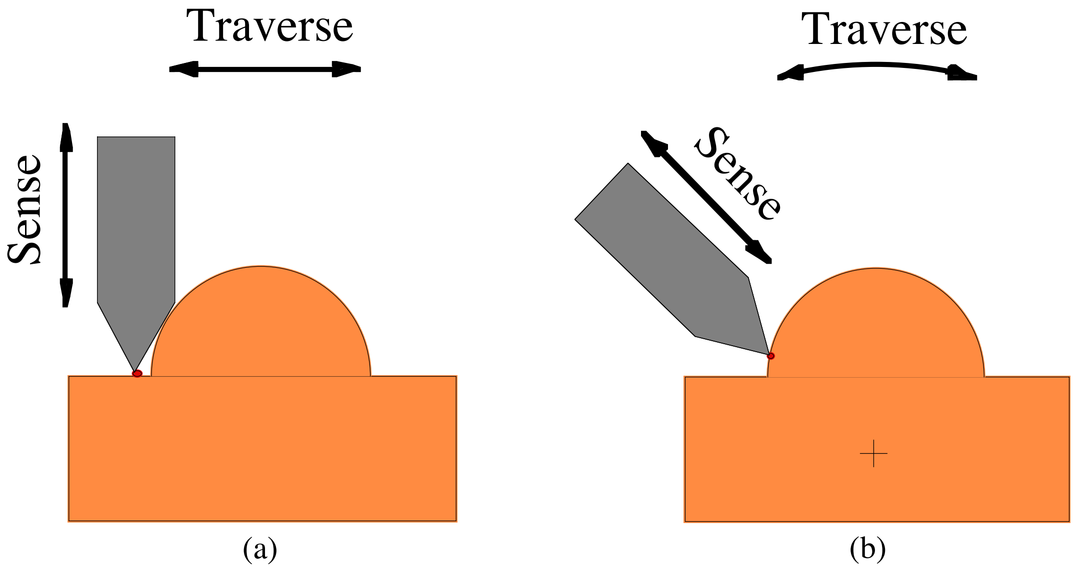

Figure 1. Traditional profilometers cannot adequately measure slopes greater than the clearance angle on their probes (a). Measurements will be incorrect when the clearance face of the probe, rather than the tip, contacts the part. If the probe can be rotated, however, measurements of surfaces with large slopes can be measured.

For many optical components, high aspect ratio aspheres for example, the geometry in section is much closer to having a polar rather than rectilinear symmetry. To measure such a component, it would be prudent to use a machine based on a polar coordinate system. The instrument being designed, called *Polaris*, is just such a machine.

Shown schematically in Figure 2, *Polaris* uses a horizontal air-bearing LVDT as the primary sensor. The LVDT is mounted on a linear bearing which, in turn, is mounted on a rotary bearing. The horizontal orientation minimizes the effect of gravity loading and allows the probe tip radius

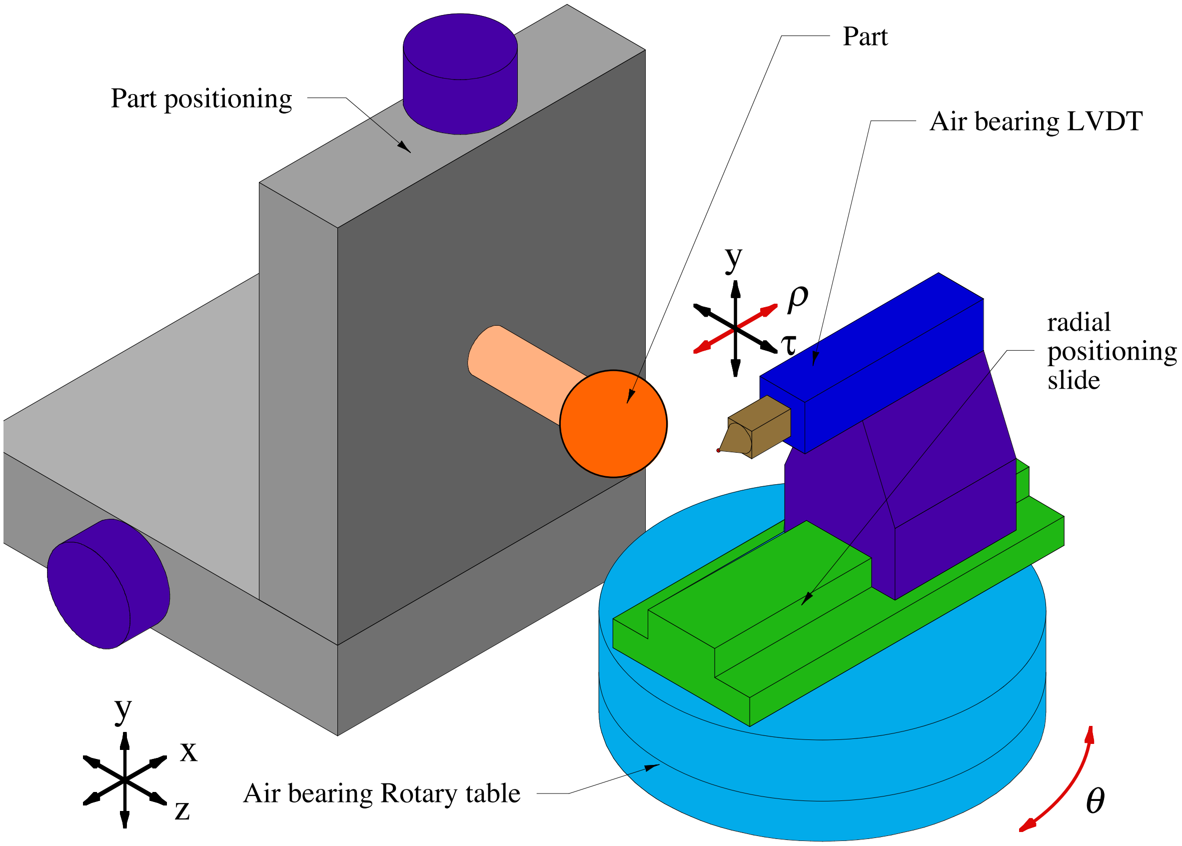

Figure 2. Schematic of *Polaris* rotary measurement machine. The orthogonal axes ρ, τ, and y are defined from the LVDT's reference frame

to be as small as 1 μm. The part to be measured is located on an independent XYZ stage for initial positioning. A rotary (θ) stage and the linear (R) stage are air bearings driven by direct-drive brushless motors to eliminate leadscrew errors with encoder feedback. To measure a part, the rotary axis and linear stage follow the nominal part profile while the air-bearing LVDT acts as a null probe, recording any deviations as a function of position. The data collected is then transformed into a measured part profile and displayed as a two-dimensional error plot.

The polar measuring machine will have the capability of gauging a nominally hemispherical object with submicrometer accuracy. The range of the device is ±25 mm in the radial direction and ±90° in angular direction. It can be used for nominally spherical object (convex or concave) in this size range but the size and shape of the tip can limit the measurement of certain features (e.g., a high aspect ratio concave groove).

5.2 DESIGN PROCESS

The design process for *Polaris* has gone from concept to selection of components, an error budget and review, to finalizing the design. One of the goals of this design was to make as much use of existing technology and off-the shelf components as possible – especially where high precision was required. Components were selected on the basis of specifications, capabilities and past experience with manufacturers. An error budget accounting for all significant geometric errors has been developed using the selected components to determine the viability of the design. Satisfactory conclusion of the error budget resulted in finalizing the design with a solid model of the mechanical system in Pro/Engineer and a preliminary user interface model.

5.2.1 COMPONENT SELECTION

Most of the components of the measuring machine are "off the shelf". The air-bearing LVDT is an AB-01 from Lion Precision with a linear range of 1 mm and a resolution of up to 1.2 nm. The LVDT is also capable of measuring with loads as small as 0.1 grams. The linear (R) air-bearing slide is a Dover ES-500 with integrated brushless linear motor and Heidenhain encoder with 10 nm position resolution. The rotary table (θ) is a 270 mm diameter air-bearing from Precitech Precision driven by an Aerotech brushless direct drive motor and a high-resolution (1.8 μrad) Heidenhain optical encoder. Vibration isolation is via a Fabreeka Precision-Aire self-leveling table supporting an epoxy slab. The three-axis positioner consists of a NEAT ball-bearing slide with microstepping stepper motor drives for part location to less than 1 μm in the X, Y, and Z directions. Finally, a Delta-Tau UMAC will control the motion of all the axes and collect data from the LVDT.

5.2.2 ERROR BUDGET

Constructing an error budget involves adding the individual errors of the components in an appropriate manner to create the error for the entire system. Roll, pitch, yaw, straightness, and displacement errors in the linear air bearing slide were added to radial, axial, and tilt errors in the rotary air bearing to obtain geometric errors. Thermal errors have also been evaluated by defining a thermal circuit. The following strategy was followed: based on the specifications of maximum errors of each component, a typical geometric error form was obtained. The shapes of the errors are somewhat subjective, but the maximum amplitudes are those given by the specifications. These geometric errors are combined in three dimensions for the entire range of motion of the machine to give an estimate of the maximum obtainable errors and their directions.

Figures 3 through5 show the total error in the ρ, or radial, direction (Figure 3), the τ or tangential direction (Figure 4) and the y or vertical direction (Figure 5). Each graph shows the total error (sum of the errors from all of the sources that influence the position in that direction) as a

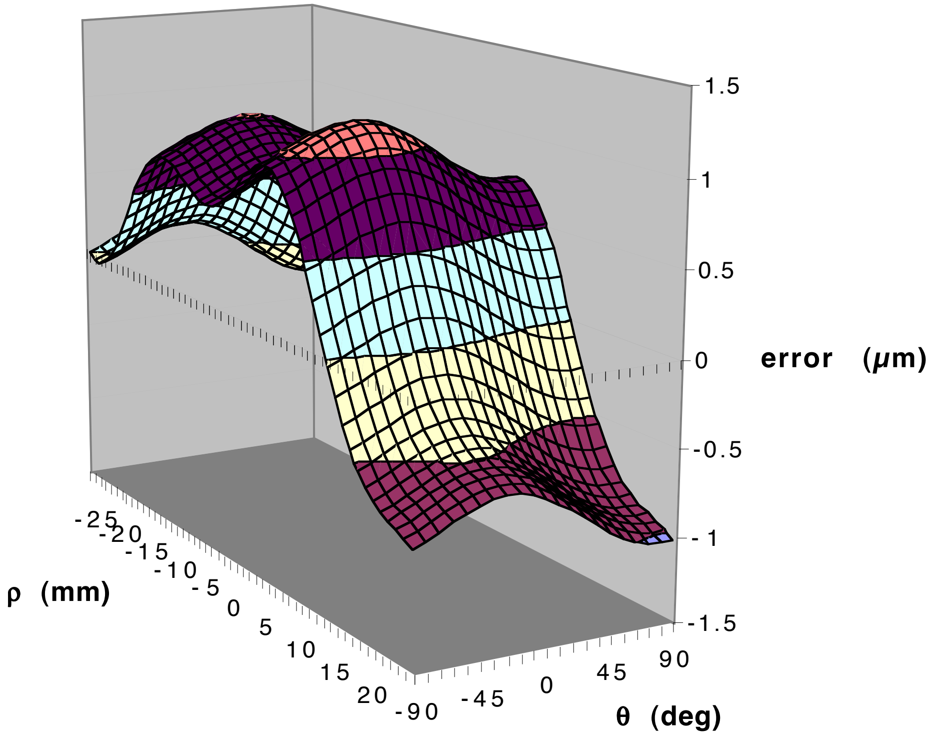

Figure 3. Total Radial Error. This error represents the error in the ρ-direction and is dominated by errors in the linear slide pitch.

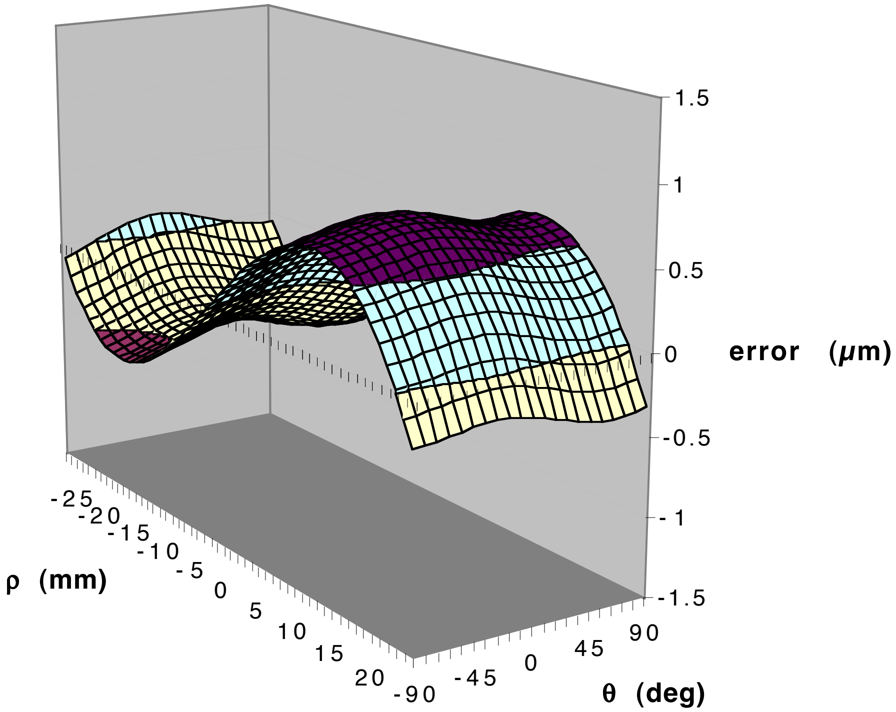

Figure 4. Total Tangential Error. The magnitude and influence of this error in the τ-direction are lower than for the radial errors due to smaller offsets and cosine error contributions, respectively.

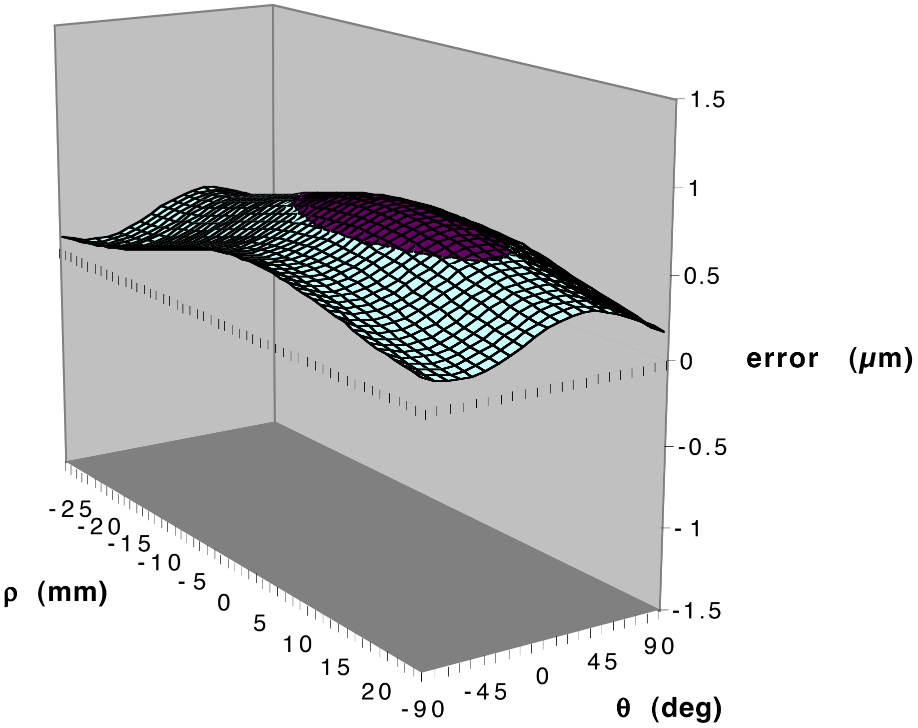

Figure 5. Total Vertical Error. This error is in the *y*-direction and the magnitude is less than the tangential error while its influence on measurements is smaller than the other directions.

function of the rotary axis from position – 90° to + 90° and the linear axis position from – 25 mm to + 25 mm. The P-P magnitude in the radial direction is the largest error at 2 μm, the tangential direction is about 1 μm and the vertical error is the smallest at 0.5 μm.

From the geometric error evaluation, it is clear that the errors in the radial direction are excessive. This is, however, less of a problem than it seems since this is a direction of motion and the *R*-axis can be moved to compensate for these errors. All that is required is an error map in the control system that will issue a correction value according to the *R* and *θ* positions. The error map will be constructed from experimental data since the errors presented here are not the same as those that will appear on the delivered components.

5.2.3 MECHANICAL DESIGN

A solid model of the machine was generated in Pro/Engineer. From this solid model, complete drawings as well as a three-dimensional analysis of the relative placement of components were obtained. The solid model aids in finding possible interference points and other problems early in process.

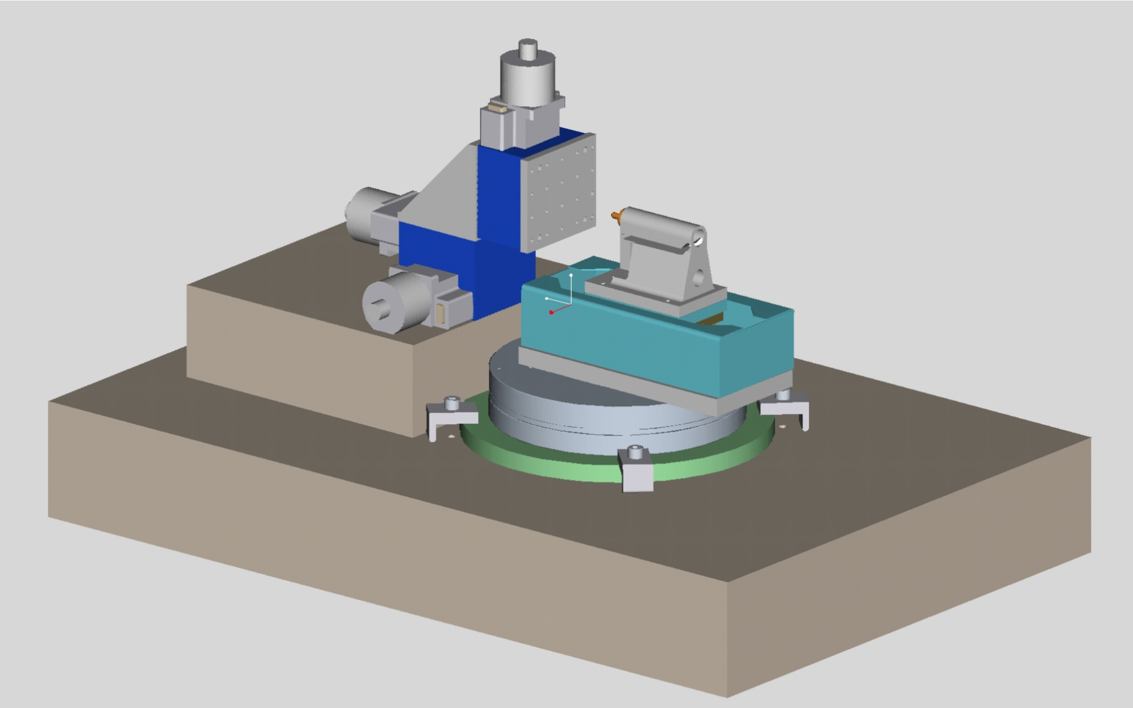

Figure 6. A solid model of the mechanical components of *Polaris*.

The critical components in the mechanical assembly shown in Figure 6 are the rotary table, the linear slide and the LVDT. These are the moving components in the system and it is therefore essential that they be mounted in a fashion that does not allow significant deflection due to the forces of motion or gravity. While the measurement forces are small, shifting loads and accelerations can cause deflections in a poor design. Also to be considered are Abbe offsets, since they can rarely be eliminated, only minimized. This manifests itself in how to prevent the stack of rotary axis, motor, encoder, linear slide, and LVDT from becoming to tall and generating large offsets in the vertical direction. By placing the motor drive, encoder and half of the air bearing of the rotary axis below the slab's surface, the

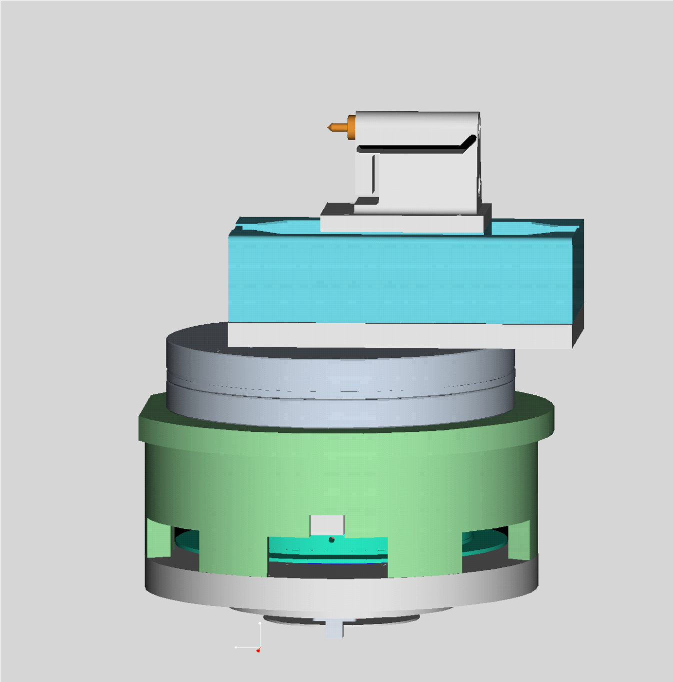

Figure 7. The rotary axis/linear axis/LVDT assembly can be removed and operated independently for testing.

entire assembly becomes much more stable due to the minimized offsets. An added benefit of this design is that thermal growth due to motor heating all takes place below the air bearing. While improving some design aspects, the rotary table arrangement does, however, have drawbacks that require their own solution. Since the motor and encoder reside within the table, access to them is limited. While frequent access is not required, adjustments to the working unit must be possible. The whole rotary axis/linear axis/LVDT assembly can therefore be removed from the machine as shown in Figure 7 and operated independently.

The three-axis positioner is intended solely for positioning parts prior to assembly. The axes will not be moved during measurement and can therefore be of a more economical ball way type.

Finally, the LVDT must be leveled to minimize gravitational effects on probing force and can also be used to determine probing force. Since the moving mass in the probe is 5.4 grams, a deflection of only 1° will change the probing force by as much as 0.1 grams. To permit adjustments to the leveling angle of the LVDT, the mounting post includes a system of flexures and a micrometer to allow adjustment of the tilt angle as shown in Figure 8. The tilt adjustment can also be used to dial in a specific probing force. To achieve this, the probe is first leveled then tilted to a specific angle ϕ and the force adjustment on the LVDT is turned to suspend the probe at its zero position. When the LVDT is the tilted back to its level position, the probing force F will be given by

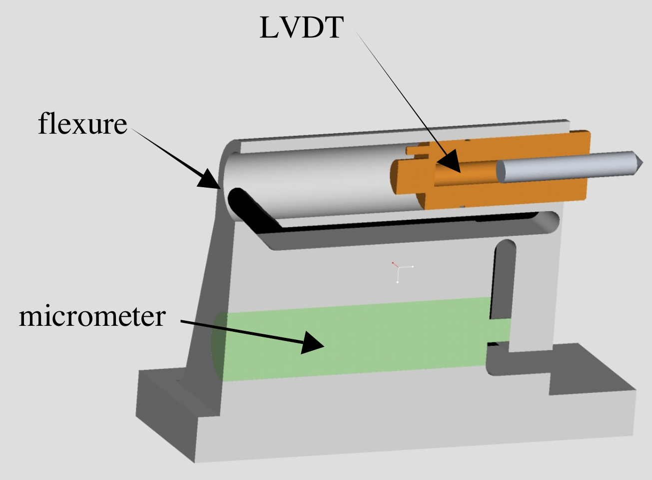

Figure 8. The LVDT resides in a fixture composed of a series of flexures and a motorized

$$F = mg\sin\phi, \tag{1}$$

where m is the moving mass of the probe and g is the gravitational acceleration.

5.2.4 Controller Design

Controller hardware such as the UMAC with peripherals, amplifiers, interlocks and power supplies reside inside a controller cabinet/desk along with the interface PC. Wiring diagrams, flow charts and state diagrams illustrate controller functions and layout (see Section 6: <u>Polaris Control and Data Acquisition</u>). Alternatives for the representation of this novel axis geometry with the UMAC coordinate system definition statements have been explored. Additionally, a scheme for the real-time correction of any significant rotation and translation errors identified by the error budget has been devised.

5.3 PROBE TESTING

5.3.1 MACHINE ORIGIN ALIGNMENT

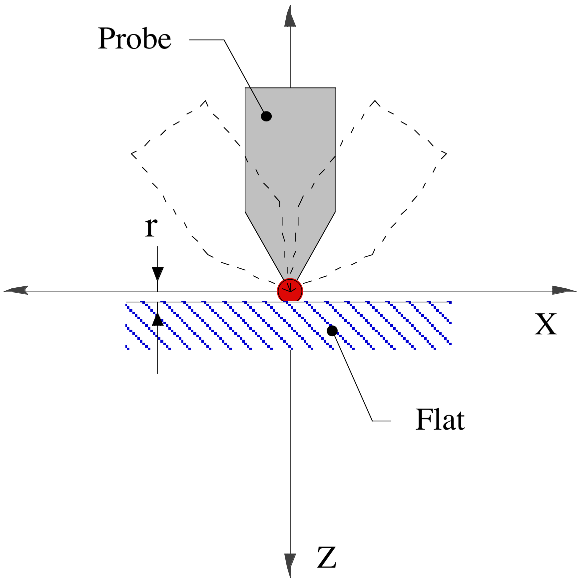

Figure 9. When the probe tip's center is aligned with the machine origin, rotation of the θ-axis will produce no appreciable deflection of the probe.

Before any measurements are made, the origin of the machine's measurement axes (R and θ) must be aligned with the LVDT. The primary criterion for this alignment is that the LVDT output be zero at $\rho = 0$ for all positions of θ. This means that for a probe tip with a radius of r, the LVDT should have a constant output of –r for all positions of θ if the center of the tip is positioned with its center at $\rho = 0$. One means of achieving this is by placing a flat plate at –r as shown in Figure 9. If the probe is truly centered, the LVDT output will not change as the rotary axis is traversed from –45° to 45°. If, however, there is an offset in either the ρ or τ directions, the probe output will change in a characteristic way for each direction.

For an offset of ρ_0 in the ρ-direction, the output of the LVDT will change as a function of the rotary axis position θ as shown in Figure 10 and by Equation (2):

$$\rho = \rho_0\left(\frac{1}{\cos\theta} - 1\right). \tag{2}$$

When an origin measurement is made and the ρ-offset is measured, the R-axis zero can be reset to eliminate the offset. In addition to ρ-offsets, there can be an offset in the τ-direction. This offset produces a different response when measured using the flat method. As shown in Figure 11, the response of the LVDT as a function of θ that can be written:

$$\rho = \tau_0(\tan\theta). \tag{3}$$

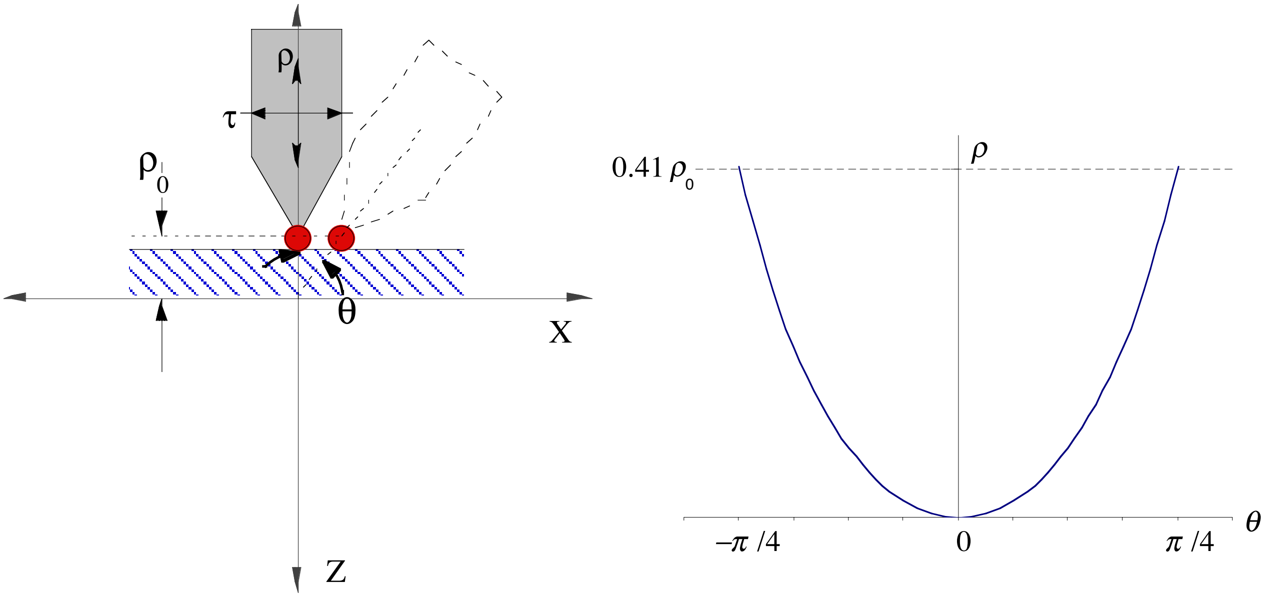

Figure 10. Schematic and plot of LVDT deflection with an offset of ρ_0 in the ρ-direction. The response as a function of θ can be used to determine the offset and adjust the machine.

Once again, this characteristic output can be used to detect and correct the offset – this time in the τ-direction. Since there are no axes of motion in this direction, the linear (*R*) slide will have to be moved slightly to eliminate the offset.

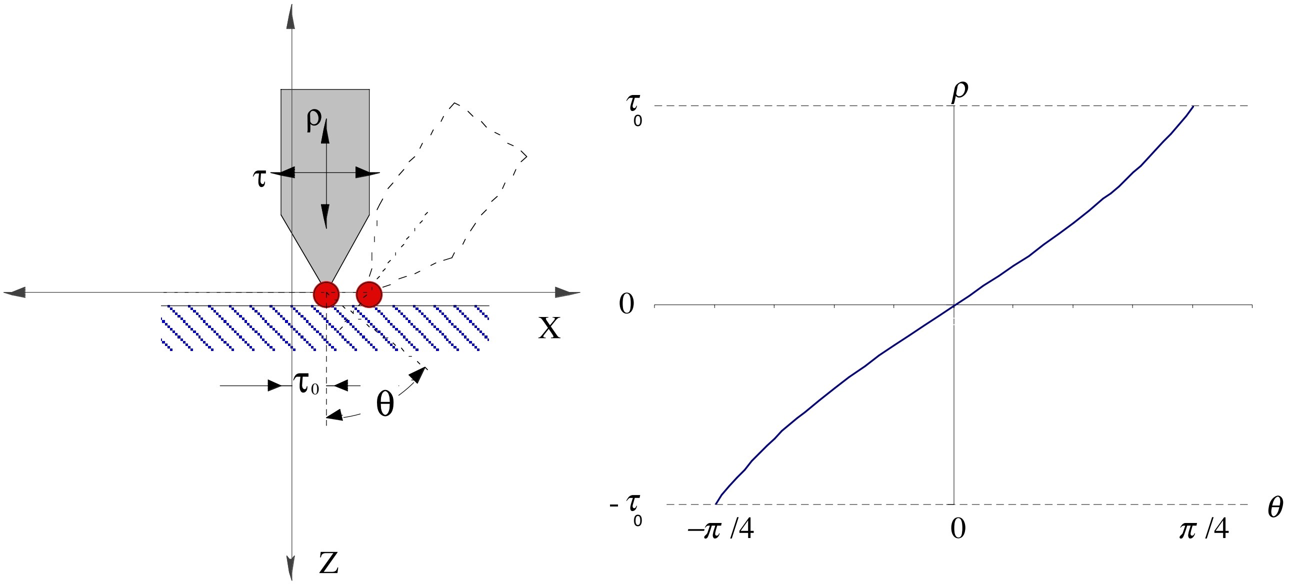

Figure 11. Schematic and plot of LVDT deflection with an offset of τ_0 in the τ-direction.

In the actual alignment procedure, the situation will be slightly more complex. A combination of offsets will produce an output of the LVDT according to the sum of Equations (1) and (2)

$$\rho = \rho_0\left(\frac{1}{\cos\theta} - 1\right) + \tau_0(\tan\theta). \tag{4}$$

Due to the potential range and complexity of the outputs as a function of θ, the data will either have to undergo a curve fit calculation in a plotting package or a set of several measurement iterations will have to be used to minimize the overall error. While the latter technique of measuring, adjusting, then measuring again to see if the error became smaller may not be as elegant as a computerized curve fit, similar operations such as tool centering in single point diamond turning have shown themselves to be more than adequate.

5.4 CONCLUSION

The design of the polar measurement machine *Polaris* is complete after numerous considerations and criteria have been satisfied. The error budget has verified the feasibility of the design and shown that the specified measurement accuracies can be obtained. Careful selection of commercially available components has resulted in a machine that can be constructed at a reasonable cost and in a timely fashion. Finally, a procedure for the critical alignment of the machine's measurement coordinate system has been devised that will make reliable, accurate measurements possible.

With careful consideration of precision engineering principles and good design, *Polaris* will be a capable machine with the ability to deliver measurements with a resolution of 100 nm and an overall accuracy of at least 500 nm. Completion of the machine is expected in late spring of 2001.

6 *POLARIS* CONTROL AND DATA ACQUISITION

Ken P. Garrard
Alex Sohn
PEC Staff Members

Polaris is a polar profilometer for measuring high-aspect optical surfaces. The machine controls and data acquisition components have been selected and the user interface software design is nearing completion. Operating procedures have been established for part setup, alignment, reference path specification and measurement. The hardware platform is a Delta Tau UMAC controller coupled to an IBM PC via USB. This choice offers significant advantages for system integration and represents the future direction of flexible machine controls. The user interface software is designed to run on any PC. As such it can evolve independent of the real-time control software and hardware.

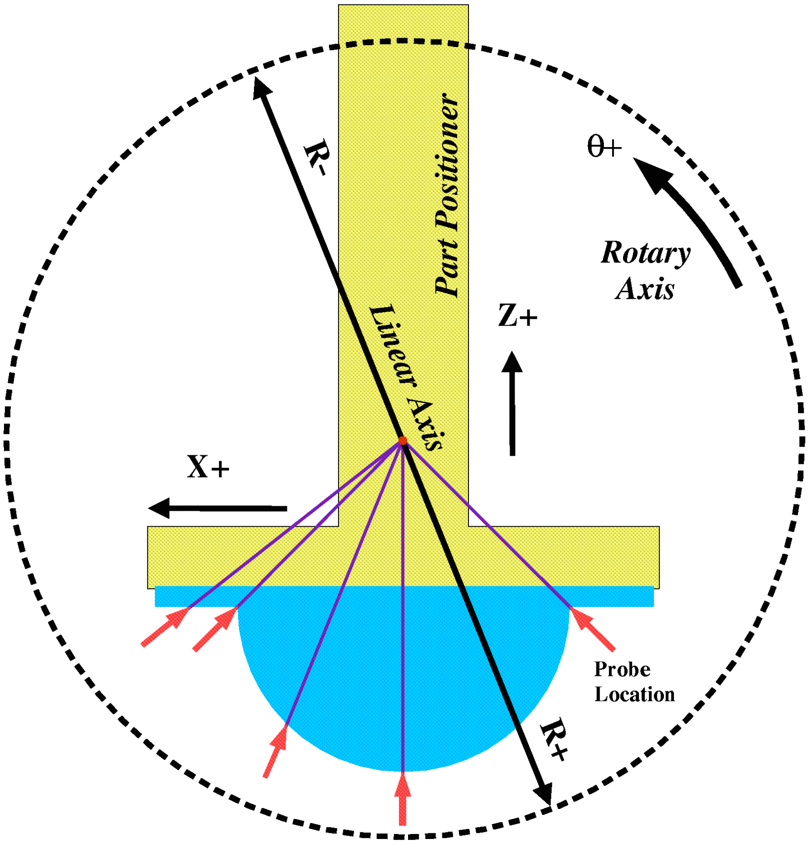

6.1 INTRODUCTION

The *Polaris* measuring machine is, in principle, a rotary TalySurf. The objective of the control system design is to give the operator an instrument interface that is similar in simplicity. However, *Polaris* motion will be more complex than the 1-dimensional TalySurf. The measurement of aspheric parts over large angular extent requires coordinated motion of the rotary stage and the stacked linear axis to maintain contact of the LVDT probe tip with the surface. The relatively short measurement range (100 μm), low bandwidth (100 Hz) and low probing force of the LVDT, coupled with the possibility of large slope changes on a sample, restrict the surface velocity of the probe to less than 1 mm/sec in the region of a discontinuity. The controller must traverse an ideal part profile that is derived from a user supplied description (e.g., zones and radii, point-to-point, etc) while collecting data from the LVDT (ρ), the rotary axis (θ) and the linear axis (R). The acquired data will be corrected for probe and machine characteristics (e.g., tip radius, axis straightness) and then compared to the reference part profile to generate error plots and standard form and finish parameters.

The Delta Tau UMAC (Universal Motion and Automation Controller) product line has been selected for *Polaris*. UMAC is simply PMAC (Programmable Multi-Axis Controller) packaged in UBUS form factor boards. UMAC provides a unique combination of functionality and flexibility for the construction of a fully integrated control and data acquisition system. Although widely used for machine control applications, UMAC is relatively rare as a data acquisition platform. It is appropriate for *Polaris* because the axis control and data acquisition functions are tightly linked. The LVDT signal (ρ) is both the primary measurement source and a secondary feedback for the R axis. The real-time positions of the R and θ axes, as well as their commanded reference positions, are required to construct an accurate surface profile and error map. UMAC supports several host system interfaces. The addition of an option card allows communication to the UMAC controller via USB or 10-Base-T Ethernet. Separation of the host PC from the controller provides numerous advantages for software development, hardware maintenance and reliable operation. The USB communication option was chosen for *Polaris* at the recommendation of Delta Tau.

The following sections provide details of the hardware component selection, software libraries and the software development tools selected for *Polaris*. The design of the control software for the UMAC and the user interface software for the host PC are also discussed along with the part description formats that will be available to the operator. Finally, operational details for the measurement of a typical part and the analysis options available to the operator are outlined.

6.2 COMPONENT SELECTION

The UMAC product line from Delta Tau Data Systems was selected as the controller for the *Polaris* machine. Delta Tau is the industry leader in high-precision machine control systems and provides the system integrator with the a wide range of options. The new UMAC system houses the control CPU (a Turbo PMAC2) and option cards in a 3U backplane. The host PC (if needed) can be a 3U PC/104 computer or a separate system. Communication with the UMAC is possible via RS-232/422 serial port, ethernet, USB, fieldbus, MACRO or firewire. Instead of embedding a PMAC processor card in a PC, the PC can now be embedded in the UMAC backplane or attached via a standard communication interface. This allows for a much more complex control system with more option cards (with no ISA bus slot, port address space or device driver limitations) and a more easily maintained and upgraded host computer. As an added benefit, the UMAC system is less expensive than a comparable PMAC system. A high-level system layout is shown in Figure 1. Connections among the software, UMAC and the machine components are shown.

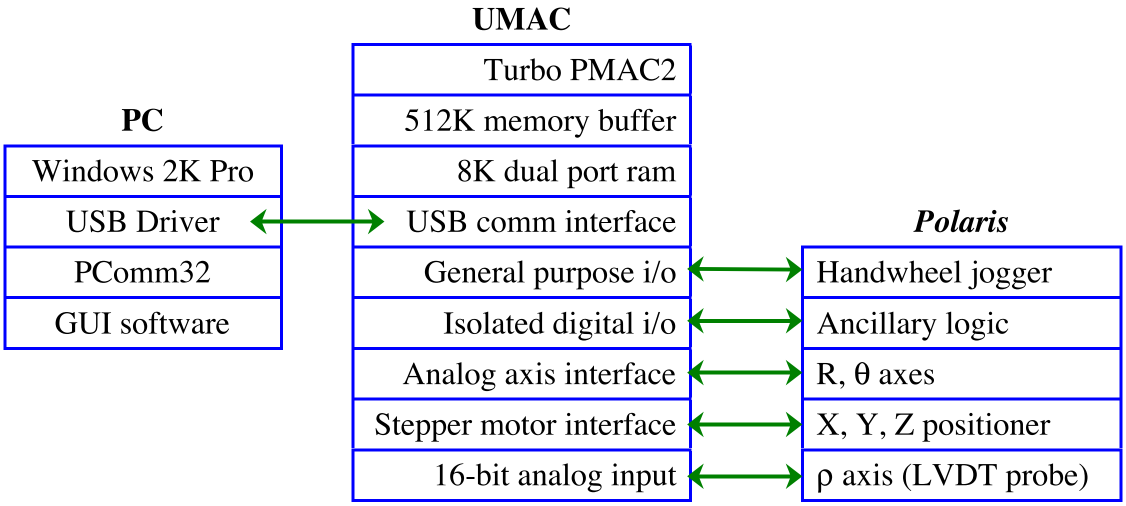

Figure 1. *Polaris* control system configuration.

6.2.1 DELTA TAU UMAC

The Delta Tau UMAC consists of a 3U backplane, an 80 MHz Motorola 56303 DSP card and option cards for a wide variety of I/O interfaces. A single processor system is capable of controlling up to 32 axes with the appropriate option cards. The configuration chosen for *Polaris* includes the Turbo PMAC2-3U CPU card with an additional 512K x 24 data memory buffer. Option cards support up to 4 commutated analog servo axes and 4 pulse-direction stepper motor axes. Home, overtravel, enable and error outputs for all axes are included as well as a handwheel jogger interface. Additional opto-isolated digital I/O (24 bits in, 24 bits out) is available for ancillary logic interfacing (e.g., the emergency stop circuit). A 4 channel 16-bit analog-to-digital converter card was purchased for data acquisition. The LVDT signal will be interfaced to one channel and the others will be used for machine calibration and geometric error analysis. Communication to the host PC is via a USB communications adapter card. The optional data memory buffer is large enough to contain an entire surface measurement. The standard 128K program memory buffer is also large enough for any anticipated reference surface specification. This greatly simplifies the programming task by eliminating the need for real-time communication between the host PC and the UMAC while a measurement run is active. Periodic update of the axes positions will be made via the USB connection; however the response of the host PC is not critical to the successful completion of a measurement. Acquired data will be transferred from the UMAC data buffer to the host only after the measurement motion program has finished.

6.2.2 HOST PC

The host PC is an IBM NetVista (866 MHz PIII) with 128MB RAM, a 20 GB hard drive, a 250 MB ZIP drive and a 19" Triniton monitor. It has no special requirements for interface to the UMAC other than an OHCI compliant USB port and the Windows 2000 Professional operating system. The OHCI (Open Host Controller Interface) is supported by all USB control chipsets except those manufactured by Intel and VIA. Windows 2000 is needed for compatibility of the USB device drivers with the Delta Tau PComm32 software library.

6.3 SOFTWARE DEVELOPMENT

The *Polaris* hardware platform contains two processors: the UMAC DSP for control and data acquisition functions and the host PC for the user control interface and data analysis. Software development tools from Delta Tau and Borland will be used. The UMAC, like all PMAC family control products, is more than a hardware platform. It contains firmware and custom ASICs that provide substantial functionality for the system integrator. Borland is the industry leader in PC-based software development tools. Their Visual Component Libraries (VCL) for C, C++, Java and Delphi provide a rich selection of reusable software tools for building application interfaces.

6.3.1 DELTA TAU

The Turbo PMAC2-3U motion control system includes firmware that performs six basic tasks in real-time: 1) servo loop update for up to 32 axes in 16 coordinate systems; 2) execution of up to 256 simultaneous motion programs; 3) sinusoidal or table-driven multi-phase motor commutation; 4) execution of up to 64 PLC programs; 5) housekeeping functions such as overtravel limit checks and watchdog timer reset; and 6) host communications, including command interpretation and execution. The basic servo feedback loop is normally executed at 2.4 kHz and includes standard PID feedback, both acceleration and velocity feed forward and a notch filter. In addition, the UMAC trajectory generation algorithms include acceleration and velocity profiles for each motor (with a variable length lookahead buffer), blended linear, circular, B-spline, H-spline and NURB interpolation and 2D planar geometric error compensation. A significant feature for the *Polaris* machine is built-in forward and inverse kinematic functions for rectangular to polar coordinate system transformation. Forward and inverse kinematic program buffers can be defined for each coordinate system which specify a non-linear mapping between axes (logical) and motors (physical). This mapping may involve any number of motors and axes including virtual axes and may contain conditional and iterative solutions (i.e., each buffer is a program). For *Polaris*, the forward buffer defines X and Z in terms of R and θ and the inverse buffer defines R and θ in terms of X and Z. This allows the controller to execute motion programs and jog commands that are specified in cartesian coordinates even though the machine axes are in a polar orientation.

PEWIN32 The Delta Tau executive program for Windows, PEWIN32, provides configuration, testing and programming support for the UMAC controller. From initial card setup to downloading and executing motion programs and PLCs, PEWIN32 is an indispensable tool for the system integrator. In addition to a simple terminal interface for communicating with UMAC, it includes a program editor, motor jog controls and access to the low-level I/O functions of any option card.

The most important feature of PEWIN32 is the motor and system tuning utility. The *AutoTune* procedure excites the system with a variety of signals, measures the response and based upon the input of desired system characteristics from the user (e.g., bandwidth and damping) suggests a new set of values for the proportional, integral, derivative, velocity feed forward and acceleration feed forward gains. The user may also select the magnitude and type of excitation signals used for tuning. A notch filter is available for damping an unwanted resonant mode in a motor's dynamics. The notch filter parameters may also be configured to act as a 1st or 2nd order low-pass filter or a velocity loop integrator. The filter is implemented as part of the trajectory generation algorithm to avoid impacting the stability and responsiveness of the feedback loop.

PComm32 Pcomm32 is the 32-bit Windows device driver package for developing custom software that communicates with a PMAC or UMAC control system. It is compatible with both Borland and Microsoft development products, including C/C++ and Delphi. PComm32 consists of three components: the PMAC.DLL library, a corresponding function header file and the driver PMAC.SYS. The programmer communicates with UMAC by calling routines from the library which send messages to the driver. The driver communicates with the UMAC card directly. The library consists of over 130 functions grouped into seven categories.

1) Initialization and Configuration
2) ASCII Communication
3) Program Download
4) Dual Ported Ram (DPR)
5) Host Interrupt
6) Variable Read/Write
7) Utility

Two features of the library are particularly noteworthy. First, any command that can be entered into a PEWIN32 terminal window can be sent via the ASCII communication functions. Second, a UMAC card will automatically update reserved regions of its DPR with real-time motor and coordinate system information (e.g., axis positions and motor velocities). There is also reserved DPR for automatic update of user specified UMAC variables and a DPR area that emulates the UMAC hardware control panel connector. These later functions include motor home, motor jog, program run, program stop, feed hold and feedrate override.

USB The universal serial bus connection is enabled as a UMAC communication mechanism with the ACC-54E option card in the UBUS backplane and the installation of two device driver files on the host PC and a plug-and-play information file. Communication between PComm32 and the UMAC uses the same mechanism (and configuration parameters) as if the UMAC were located on the host PC system bus. In fact, its data transfer rate is similar to that of the ISA bus version of PMAC. There is no performance penalty for locating the UMAC in a backplane separate from the host PC.

6.3.2 BORLAND SOFTWARE TOOLS

Borland software development tools have been selected for programming the user control interface and data acquisition software. The VCLs (Visual Component Library) supplied with JBuilder (Java), C++Builder (C/C++) and Delphi (Object Pascal) contain substantial libraries of reusable code for constructing standard interface features such as menus, frames (i.e., windows), buttons, toolbars, data paths, scroll bars, etc. Java is the language of choice for object oriented software development and JBuilder is the premier Java environment. Based on information from Delta Tau, Java has not yet been used to develop a UMAC controller interface; however, any language that can invoke a routine in a Windows DLL (e.g., PComm32) can be used to code a UI for UMAC. On the other hand, Delphi is listed by Delta Tau as a supported development platform. It is anticipated that the host PC software will be programmed using JBuilder. It is possible and entirely reasonable to use both JBuilder and Delphi in the same application. It is also desirable to separate the control interface and data analysis tasks into two separate applications as the later is more likely to grow and change as further analysis capabilities are needed. For example, the control system interface routines can be written in Object Pascal with

Delphi and the data display, analysis and plotting routines can be written in Java. A large number of component libraries for both software systems are available from vendors other than Borland.

6.4 UMAC CONTROLS

Three categories of UMAC software must be supplied by the system integrator (i.e., the PEC): the control system setup (motor gains, velocity limits, etc), motion programs that move the axes through a desired trajectory and PLCs that monitor critical non-servo loop machine functions.

6.4.1 CONTROL PARAMETERS

Two categories of static information will be maintained within the UMAC controller. First, a large amount of configuration data is generated during the motor setup, tuning and coordinate system definition procedures. This data will be stored in nonvolatile memory on the UMAC CPU card and in a backup file on the host PC. Second, to meet the target accuracy specifications for *Polaris*, a geometric error compensation table must be generated for the R axis. This error is due to a pitching motion as the linear stage is extended and can be corrected by the controller with a simple 1-dimensional table lookup. It is not anticipated that a more complex compensation geometry will be needed; however the UMAC does support two dimensional planar compensation. That is a measurement error, $\Delta\rho$, can be defined in terms of R and θ. As an alternative for a metrology instrument, errors that do not result in large unwanted axis motions can be dealt with during the analysis of acquired data.

6.4.2 MOTION PROGRAMS

The UMAC will not execute predefined motion programs as in a machine tool G-code interpreter. Each input part specification will be translated into a motion program that is downloaded to the UMAC for a measurement. For spherical and flat profiles, this translation is a straightforward syntactic mapping from the user's input file into the PMAC motion programming language. For other conic and aspheric surfaces, a series of closely spaced way-points will be generated from the user input and the UMAC will be commanded to perform spline interpolation between the points.

6.4.3 PLCS

Software PLCs are background tasks continuously interleaved with servo loops, commutation updates and motion programs. For *Polaris,* PLCs will be used to perform error checking, service inputs from the handwheel jogger, monitor data collection and synchronize post-measurement data buffer transfer. A hardware emergency stop circuit based on relays will be utilized to halt motion in the event of either E-Stop actuation, axis runaway or axis overtravel. A startup PLC will be used to initialize UMAC, PC communications and command the motors to hold position until a motion program or jog command is received from the host.

6.5 OPERATOR INTERFACE

The user interface software will be graphically oriented utilizing the customary metaphors for user control: floating windows, mouse, buttons, both pull-down and pop-up menus, scroll bars, etc. Although data analysis is not the focus of this project, a 2D plot of both the raw measurement data and a surface error plot over a user determined range with a variable zoom factor will be provided. Measurement data files will be stored in a simple, tabular text format for easy import into other software packages for further analysis. By separating the machine control interface and the data analysis applications, enhancements of one can be performed with minimal impact on the other.

6.5.1 PART SPECIFICATION

Two general formats for a reference surface have been identified for components to be measured by *Polaris*. The simplest is a list of (x,z) data points interpolated by a linear function. The other format is based upon the general equation of an optical surface of revolution as given by Equation (1).

$$z = \frac{cx^2}{1+\sqrt{1-(K+1)x^2c^2}} + a_1x^4 + a_2x^6 + a_3x^8 \cdots \qquad (1)$$

where,

z = sag of the surface parallel to the z axis,
x = radial distance from axis of revolution,
c = surface curvature = $1/R$,
a_1, a_2, a_3 … are aspheric deformation constants,
and K is the conic constant.

Table 1. Conic surfaces as defined by *K* in equation (1).

$K \leq -1$	Hyperboloid
$K = -1$	Paraboloid
$-1 < K < 0$	Prolate Ellipsoid (rotation about the major axis)
$K > 0$	Oblate Ellipsoid (rotation about the minor axis)
K = 0	Sphere

Table 1 shows the relationship between the value of *K* and the four conic surfaces. If nonzero aspheric polynomial coefficients are needed to describe a surface, then an (x,z) point-to-point data file must be generated with appropriate spacing.

Input data files are constructed by specifying a surface curvature in concentric zones beginning at the presumed rotational center of the part. Each curve zone also specifies boundary point coordinates to limit the extent of the segment. Curvature is explicitly stated with R and K values or implied by closely spaced (x,z) data points. A missing (or zero) value for R or K indicates flat and spherical surfaces respectively.

The coordinates of the center of curvature must also be given to resolve an ambiguity inherent in interpolating quadratic motion. That is, for any finite radius there are four possible paths between two points. Knowing the center point eliminates two of the possibilities and the usual convention is to select the shorter of the two remaining arcs as shown in Figure 2. In the special case of subtending an arc of exactly 180° the number of possible paths is reduced to two and the center point location is the midpoint of the line segment connecting the start and end points. More information is needed to select between the two arcs; however this rare case is easily handled by simply splitting the curve specification into multiple sub-180° sections. In theory, *Polaris* can measure a part through more than 180° of θ axis rotation; the input specification requires that such a surface be defined by at least two arc segments.

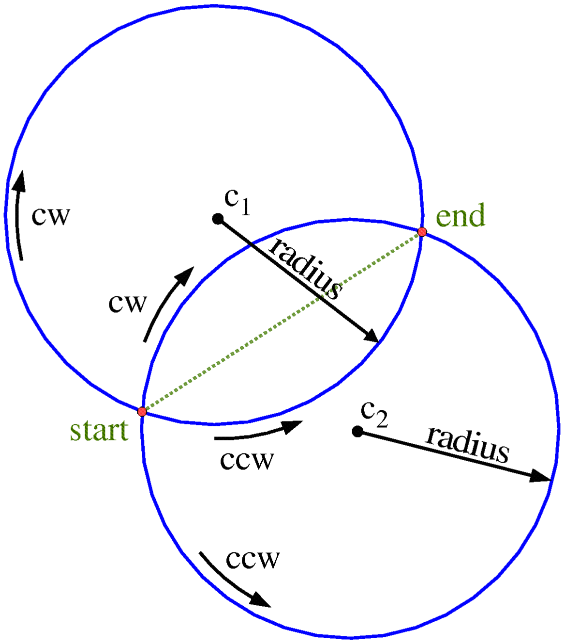

Figure 2. Arc selection for circular interpolation.

Another technique that is commonly used for machine tool programming is to specify the direction of motion between the start and end points; either clockwise or counter-clockwise. In this case, the two possible center locations can be found by solving a quadratic equation and then selecting the center that yields the correct direction of motion between the start and end points over the shortest arc length. The special case of 180° segments is also resolved by this method.

Four forms of part shape commands are accepted by *Polaris*. These are enumerated in Table 2. Each form specifies the surface curvature over a numbered zone (starting with 1). The zone numbers have no significance other than as an identifying tag for a region of a part. The conic constant, K, is optional in Form A and its absence implies spherical curvature. A simple flat segment is easily defined by Form B. An arbitrary surface may be defined by a list of points as in

Forms C or D. The **beginlist** and **endlist** keywords are used to delimit the list of points within the file. Form D is provided as an editing convenience for large or computer generated data sets.

Table 2. *Polaris* input command file formats.

	Parameters						
Form A	zone #	Radius	X_{center}	Z_{center}	$X_{boundary}$	$Z_{boundary}$	[K]
Form B	zone #	$X_{boundary}$	$Z_{boundary}$				
Form C	zone #	**beginlist**					
		x_0	z_0				
		x_1	z_1				
		…	…				
		x_n	z_n				
		endlist					
Form D	zone #	**import**	*filename*				

Two other issues must be considered in the part specification process. First, it is common to specify only half of the surface of a rotationally symmetric part. The *Polaris* input file dialog will have an option that generates the symmetric reflection of a part about the line X=0. The reflected zones will be denoted by negative zone # values. This is done so that the user can measure both halves of a surface or restrict the range of a measurement to any number of adjacent zones without editing an existing part file.

The other issue concerns the measurement of a surface that is described in a cartesian coordinate system that is not the same as that defined by *Polaris*. The *Polaris* axis naming and direction conventions are show in Figure 3. Note that *Polaris* defines right-handed cartesian measurement axes with the positive Z direction being away from the center of the rotary axis (i.e., into the three axis positioner) and positive X to the left as viewed from above. For each input file, the interface software will give the user the opportunity to negate all incoming X and/or Z coordinates so that an existing surface description file can be reflected to match the directions of the *Polaris* axes.

It is the responsibility of the operator to ensure that the programmed measurement path for a mounted surface conforms to the *Polaris* coordinate conventions before initiating axis motion. The coordinate system of a measurement is that of the 3 axis part positioner in the plane of the probe (i.e., cartesian XZ). As an example consider a simple convex spherical surface. As the probe is moved from the center of the part to the outside, the probe tip must move in the positive *Polaris* Z direction to maintain contact with the surface. So the radius center coordinates must be in the positive Z direction, that is in the same direction as the relative motion of the probe. For a concave spherical surface, the probe tip moves in the negative *Polaris* Z direction as a scan progresses from the part center to the outside edge.

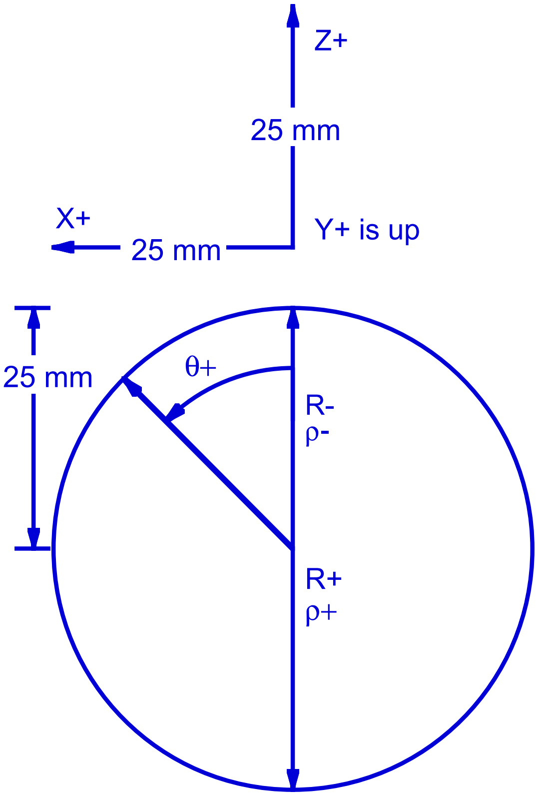

XYZ Part Positioner

- Cartesian Coordinates
- Right Handed
- ± 25 mm range for each axis

Measurement Stage

- Polar Coordinates
- ± 25 mm R range
- ± 500 μm ρ range
- ± 90° θ range

Convex Measurement ⇒ R+
Concave Measurement ⇒ R-

Figure 3. *Polaris* axis and coordinate system conventions.

6.6 MACHINE OPERATION

Polaris operating procedures are being developed for calibration, part setup, measurement and data analysis. The remainder of this section discusses setup, measurement and data analysis. Calibration is reviewed in Section 5, Design of the Polar Profilometer *Polaris*.

6.6.1 ALIGNMENT AND PART SETUP

Before initiating measurement motion, it is essential that a part be properly mounted on the XYZ positioner and aligned parallel with the Z axis to a few degrees. Machine calibration will orient the R, ρ, and Z axes parallel with one another and in the same plane at a known X location. For a part that was produced by machining, alignment may be very straightforward as the back surface of the part usually provides a reference flat. For parts with curvature on both sides an appropriate fixture will be needed. Alignment ensures that the part locating procedure (i.e., "crowning") will successfully find the center of the part and that the probe will traverse the part through the same plane in which it is defined. Tilt in the XZ plane and rotation in the XY plane will not affect the determination of a part radius or an error map and can be easily removed from measured data. However part alignment errors may result in unplanned excursions of the R axis as the controller attempts to keep the LVDT probe within range. These motions should be minimized by proper alignment.

Tilt in the YZ plane does affect a radius determination by making the part appear smaller to the probe. But this error is small provided that the probe tip intersects the axis of part symmetry (e.g., the optical axis or the X=0 line) during measurement. Even if the part is tilted this point will be found by a vertical (Y direction) "crowning" procedure similar to that used on a TalySurf. For example, a hemispherical convex part of 25 mm radius that is tilted one-half of a degree in the YZ plane would result in a measurement sag error of about 1 μm. The cosine relationship between YZ tilt angle (σ) and the Z direction sag of a measurement that determines the magnitude of the this error is given by Equation (2). Clearly for measurements over a large Z range, minimizing tilt is critical if sub-micrometer accuracy is desired.

$$Z_{error} = Z_{actual}(1 - \cos\alpha) \tag{2}$$

After supplying a part surface specification file to the control software, the user must determine the location of the part in the coordinate system of the measuring instrument. This is done by finding a reference point on the surface with the probe. Both the machine coordinates and the part program coordinates of this point must be identified to the control software. The problem is the same as that of defining work offsets prior to a machining process and is solved in a similar manner. This common reference point could be anywhere on the surface, but the most convenient point whose location can be easily determined by trial and error is the apex of curvature (or "crown") along the centerline of the part. A flat region of a part could be easily used to offset the Z axis, but is of little value for determining an X offset. By manually adjusting the XYZ positioner stage while maintaining probe contact with the surface and observing the LVDT output, the operator can find the high spot in the X and Y directions independently. Adjustments of the Z axis may require jogging the R axis to keep the LVDT in range. This procedure is essentially the same as that used by the TalySurf except that Z direction motions are made by two opposing axes (the Z stepper motor and the R axis). The alignment procedure is manual and the only requirement of the user is that *Polaris* be informed of the measuring offsets (in X and Z) before initiating a measurement. The software will allow the user to either select the current machine position or enter coordinates or offsets to define the reference point.

6.6.2 MEASUREMENT

After a part is mounted and aligned, the part specification file can be converted directly into X and Z motion commands for the UMAC controller. Forward and inverse kinematic routines in the UMAC will be used to translate these cartesian surface motions into polar motions of the R and θ axes. The measurement process is reduced to simply following a prescribed motion path and recording axis positions and LVDT probe deflections. However, the successful completion of a measurement depends on two additional factors: the LVDT range selected and the shape and size of the probe. If the part specification and the properly aligned surface are identical, then the LVDT will not deflect at all during a measurement. However, any misalignment or surface error will cause the probe to deflect, and this deflection must be accounted for by the R axis trajectory calculations internal to the UMAC to continue the measurement. A simple example of a convex hemisphere as show in Figure 4 illustrates several key points. First, note that a very small error can cause a very large deflection when approaching features such as inside corners or outside edges. The axes must be moving slow enough in these regions to react before the LVDT range is exceeded. The LVDT has a selectable measurement range of 1000, 100, 10 and 1 μm at a resolution of 150, 20, 3 and 2.5 nm respectively.

Second, a surface can be measured at many Z axis positions by simply moving R and Z in tandem during setup. For the case of a single zone of curvature, the ideal location of the part is to have the radial center at the center of rotation of the θ axis. In this case, the R axis would not move during a measurement except in response to a large probe deflection. Multiple zones with varying centers of curvature and flat regions require a more thoughtful setup process that includes knowledge of the included angle of the probe tip. For the surface of Figure 4, both the spherical and the flat regions are to be measured. In this case, rotating the probe about the radial center of the convex curved surface would place the probe parallel to the part when it approaches the flat regions on either side of the sphere. The R and Z axes must both be moved in the positive Z direction so that the probe contacts the surface within its measurement window. The optimal solution is shown in Figure 4 as the intersection of the part centerline with the bisector of the two part tangent lines that have a maximal slope difference. For this example the hemisphere and the flat intersection is 90°. Note that the probe is normal to the surface at three positions, the apex of the hemisphere and the two exact corners. Moving the R and Z axes so that the θ axis rotates about this optimal point is the responsibility of the operator; however it need not be determined exactly unless

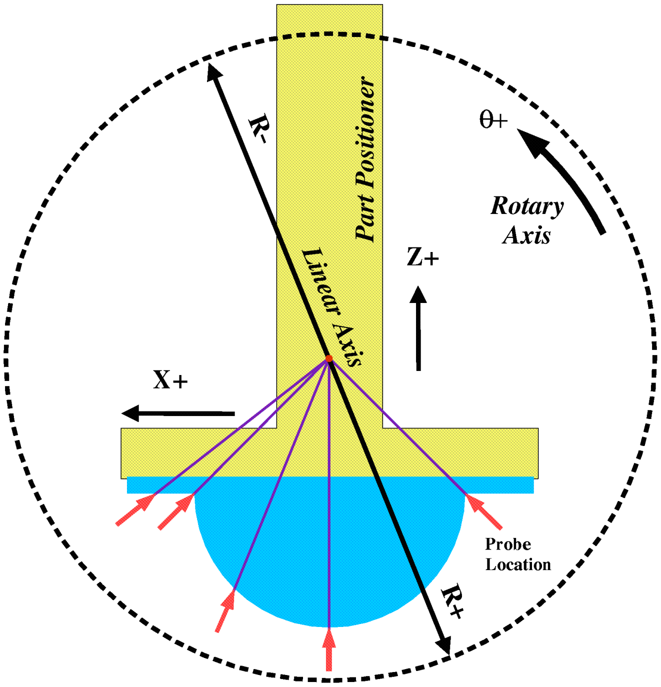

Figure 4. Measurement of a convex hemisphere.

the full angular range of the probe tip is needed for a measurement. Software analysis of a part specification file will calculate tangent lines for the curved regions and suggest a rotational center location relative to the part geometry for the operator.

6.6.3 DATA DISPLAY AND ANALYSIS

During a measurement the computer display will contain both text and graphical indicators of the positions of all three live axes (R, θ and ρ) as well as the probe location in cartesian (X and Z) coordinates. A real-time error calculation will also be displayed. But this raw data has little meaning until the measurement is completed and the XY tilt is removed. Strip chart graphic displays of the real-time LVDT deflection and XZ probe position will also be developed.

After completion of a measurement, the acquired data set will be transferred from the UMAC data memory buffer to the host PC. A variety of plots of both the current and previously acquired data sets can then be produced offline. The plots produced by *Polaris* will be relatively simple as it is not the goal of this project to replicate the extensive range of scientific graphical analysis packages available. Emphasis is placed on the ability to 1) determine immediately if the measurement was successful in acquiring gap free data over the intended surface range, 2) produce an error plot, 3) identify specific feature locations and distances graphically with the mouse and/or cursors and 4) save the data in a tabular text format. The *Polaris* plotting functions will operate on either the current data set, a previously saved data set or a reference path. The ability to plot two data sets in the same window is an important capability that will be included. The two data sets may have the same or independent axis scaling and ranges. In the former case, region selection, zooming, axis pan, cursor lines and markers may be applied to compare one measurement with another (e.g., the front and back of the same part). Since two measurements are unlikely to be based on an identical axis setup and may not represent surfaces defined with the same coordinate origin, tools for rotation and translation of one data set relative to the other will be included.

6.7 CONCLUSION

Polaris control hardware components have been selected, purchased and received. Software tools have been identified and evaluated. A high-level design of the fundamental operator interface has been developed in conjunction with operating procedures for the part description, setup, alignment and measurement activities. The separation of the data acquisition and analysis activities from the control activities, both in the UMAC and on the host, is a key to the successful implementation of the software components and their integration with the controller and machine hardware.

7 DESIGN OF A LINEAR HIGH PRECISION ULTRASONIC PIEZOELECTRIC MOTOR

Markus G. Bauer
Graduate Student
Thomas A. Dow
Professor
Department of Mechanical and Aerospace Engineering

To understand the operating principles of linear ultrasonic piezoelectric motors, a motor made by Nanomotion Ltd. was examined and a model of the driving process was developed. A new motor is now being designed that uses the same driving process but improves resolution, speed, efficiency and especially controllability by allowing the independent excitation of the vibrations that generate the alternating normal force and the sliding motion of the tip. All designs involve at least two independently driven piezoelectric elements, one generating the normal load at the interface and the second generating the tangential driving force. The greatest challenges in developing this motor are 1) the actuator needs to have two different mode shapes at nearly the same frequency and 2) each mode shape must be exclusively excited by one actuator and not by the other. Simple mass-spring models and analytical solutions based on vibrations of simple beams are suitable methods to approximate a possible design, but proved to be ineffective models to generate designs with two resonances within the required 500 Hz error margin. To successfully model the actuator and predict the dynamic properties of a future prototype, finite element analysis (FEA) has been most successful. The model includes all significant features that have to be considered such as the anisotropy of the piezoelectric material and the exact properties and dimensions of the actuators (including the glue joints). Several prototypes have been built, and the resulting mode shapes and natural frequencies have been measured and compared to the computer models. The design concepts as well as the modeling techniques have been iteratively improved.

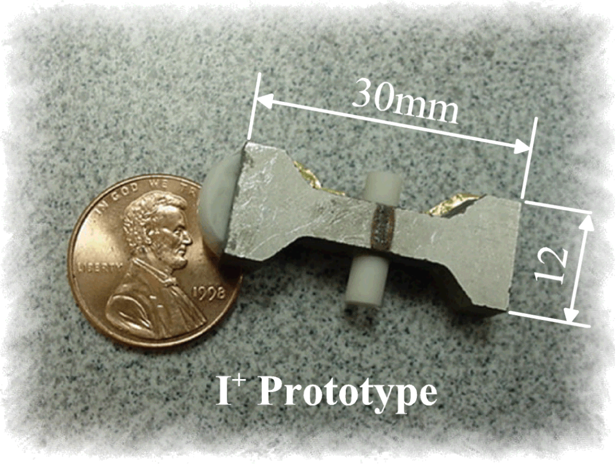

7.1 INTRODUCTION

Ultrasonic piezoelectric motors can be designed to use either traveling waves or standing waves to generate motion. Piezoelectric standing wave motors, the emphasis of this project, use a combination of flexural, torsional or longitudinal vibrations of a piezoelectric actuator. One vibration produces a normal force, while the other vibration generates motion that is perpendicular to the normal force. This combination creates a friction based driving force between one stationary component, the motor, and the object to be moved.

A standing-wave motor produced by Nanomotion Ltd [1] as illustrated in Figure 1, was used to study the driving process. This motor uses the first longitudinal resonance of the piezoelectric material to generate a sinusoidal normal force and the third bending resonance to generate a force in the direction of motion. It is made from a single block of piezoelectric material divided into 4 sections.

Generally speaking, any structure that can be made to vibrate in orthogonal directions with sufficient magnitude can be used as a motor. However, the direction of slideway motion can only be reversed if the phase between the vibration normal to the motor-slideway interface and the vibration in the direction of the slideway motion can be changed. The Nanomotion motor reverses the direction of slideway motion by exciting different regions of the actuator. Measurements showed that the phase could be either +20° or –20°, based on which electrodes are activated (1 and 4 or 2 and 3). The velocity can be controlled by the amplitude of the excitation.

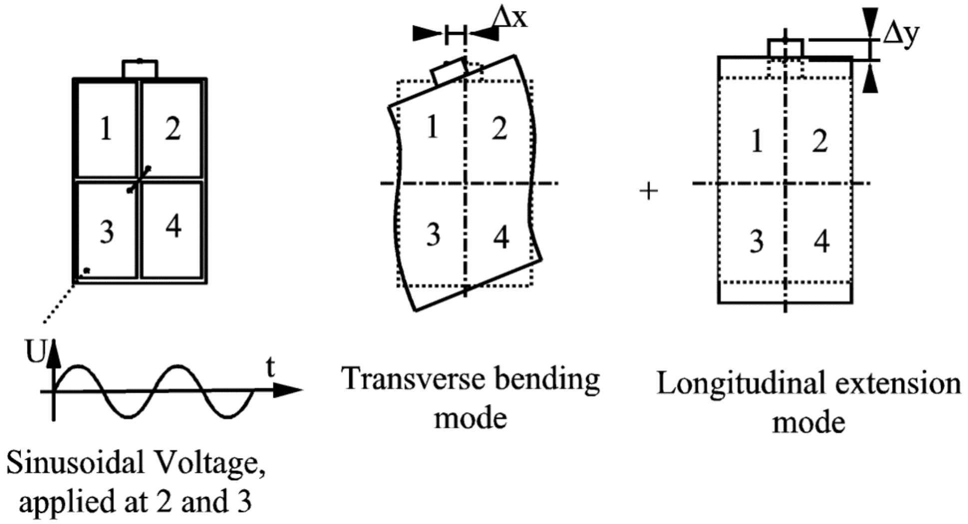

Figure 1. Nanomotion Motor, Mode Shapes

In the case of the Nanomotion motor, the slideway velocity is not proportional to the excitation of the actuator. Since the motor is preloaded against the slideway, the thrust force at the tip must overcome the static friction between tip and slideway, which results in a non-linear behavior as sketched in Figure 2. Inverting the driving voltage can also reverse the direction of motion, but this was not implemented in the Nanomotion Motor. The slideway does not move until the excitation voltage reaches about half its maximum value. In addition, the transition from standstill to sliding changes with the frictional properties along the sliding surface. This requires a very large controller gain for slow slideway motion, which is likely to cause instability in the control algorithm.

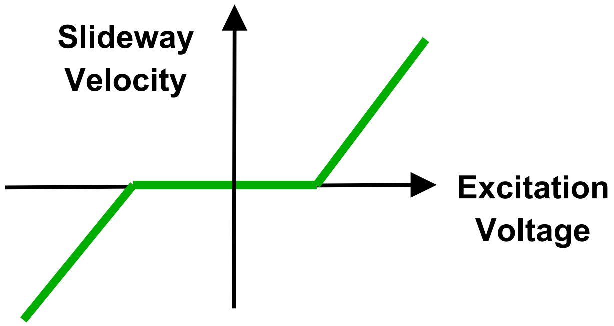

Figure 2. Slideway Velocity vs. excitation Voltage (Nanomotion motor)

The analysis of the driving process of the Nanomotion motor as an example for all piezoelectric standing wave motors, showed that the amplitudes of the vibrations and the phase between them are the most important parameters that influence the performance of the motor.

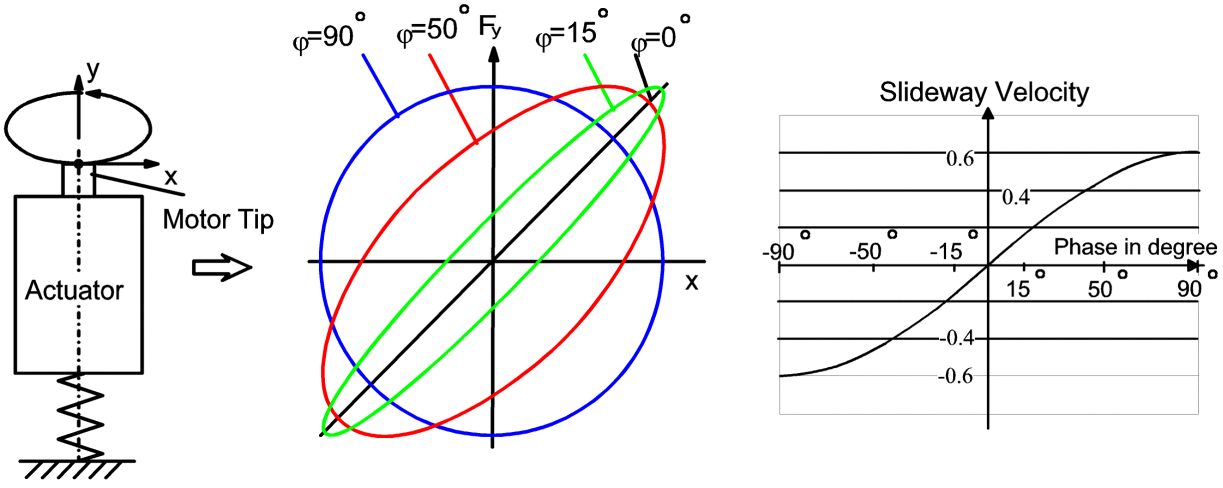

Motion of the Motor Tip

Figure 3. Influence of the phase between normal force and motion (in m/s)

Figure 3 shows the motion of the motor tip translates into actuator motion. The geometry of the actuator it not of interest. For the analysis of the driving process, it is assumed that the actuator is capable of generating a vibration at the tip in the sliding direction (x-direction as in Figure 3 and a dynamic normal force (y-direction as in Figure 3). These vibrations are excited at the same frequency, so there is a constant phase relationship between them and the force-motion ellipse (Figure 3, middle) is constant in time.

The model that was used to calculate the slideway velocity as a function of phase in Figure 3 (right) assumes that there are no slip-stick effects. If the vibration normal to the sliding surface can be set such that only a very small thrust force is needed to overcome static friction, slip stick effects can be avoided and, the phase would be the best parameter to control the slideway motion. A phase of 0° between force and motion will not generate slideway motion, 90° results in maximum slideway velocity in one direction and -90° (or 270°) changes the direction of slideway motion. The relationship between phase and slideway velocity is not quite proportional, but it is continuous and thus does not tend towards instability.

7.2 PROTOTYPES

The main objective of this project, as far as the mechanical design in concerned, is to design a prototype that allows the independent excitation of dynamic normal force and sliding motion (the sliding motion is proportional to the friction based thrust force). Then all parameters that determine the shape of the "sliding motion – normal force" ellipse, shown in Figure 3, can be changed to control the slideway motion.

The major requirements for the dynamic behavior of the actuator are:

1) The two resonances of interest must be within 500 Hz, so that one excitation frequency excites both resonances.
2) Both resonances must (virtually) not be coupled: the excitation of one vibration mode does not excite the other and vice versa.
3) The prototype must be able to generate a dynamic normal force in the order of ± 20 N.
4) The resonances must not change significantly over time.
5) Special attention must be brought to the "boundary conditions" of the actuator, for design as well as for the modeling of the prototypes:
    a) How and where is the motor supported,
    b) What influences do preload spring and the tip have on both resonant frequency and the corresponding mode shapes.

7.2.1 L-SHAPED PROTOTYPE

The design principle for the first prototype of the standing wave motor was to use two orthogonal piezoelectric actuators glued at right angles to a metal block to which the tip was attached and to excite each at a longitudinal resonance. This design is shown to the left in Figure 4. The two masses at the ends were added to adjust the position of the vibration nodes or points of zero amplitude. The location of these nodes is an important aspect of the design because this is where the motor is attached to the frame to support the drive loads.

Actuator 1 provides excitation in the direction of slideway motion, and Actuator 2 changes the normal load at the contact point between the ceramic tip on the motor and the slideway drive surface. The springs are used to preload the two actuators to keep them compressed and avoid damage to the brittle ceramic.

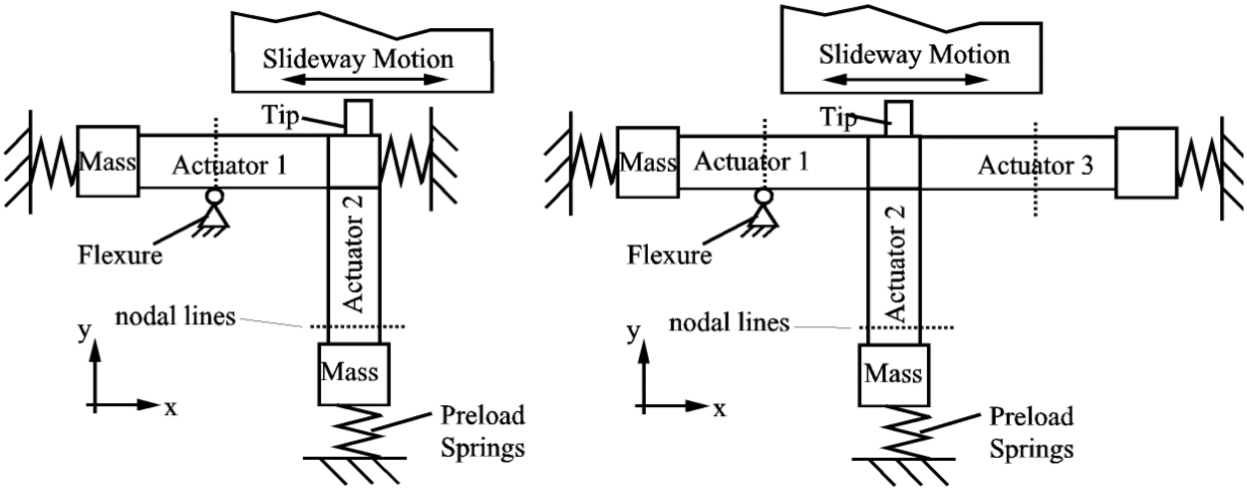

Figure 4. L-shaped Prototype (left) and T-shaped Prototype (right).

Experiments showed that, when Actuator 2 was excited with ± 100V at 44.8 kHz, the motor produced considerable slideway motion (in only one direction) and a pushing force of approximately 5 N. The excitation of actuator 1 does not influence the motor's performance significantly. A change in phase between both excitations changes the magnitude of the pushing force and slideway velocity to some extent, but does not allow a reversal of the direction of motion. The excitation of actuator 2 causes the tip to vibrate in the y-direction which excites a bending vibration in actuator 1, which then makes actuator 2 bend as well. The tip motion caused by the bending motion of actuator 1 is in larger than the tip motion caused by the longitudinal vibration when actuator 1 is excited. Consequently the excitation of actuator 2 alone generates a "force-motion ellipse" at the tip, which is sufficient to move the slideway.

7.2.2 T-SHAPED PROTOTYPE

The T-shaped geometry in Prototype 2 was introduced to add symmetry to the L-shaped design with respect to the bending motion of Actuator 1 when Actuator 2 is excited. In this design, the tip does not bend and no sliding motion is caused by excitation of Actuator 2. It is not possible to improve the behavior of the other actuator in the same way, because the tip has to be pressed against the slideway. When Actuators 1 and 3 are excited to generate sliding motion, bending motion occurs in Actuator 2. The dimensions of the motor can be chosen such that rotation of the tip is small, but it cannot be eliminated entirely by symmetry (as for the other direction). Consequently, longitudinal excitation of Actuators 1 and 3 results in bending motion of Actuator 2, which in turn leads to bending in Actuators 1 and 3. Since bending of these is part of the mode that generates the normal force at the tip, the longitudinal excitation of Actuators 1 and 3 also results in a dynamic normal force at the tip. Thus both modes are still coupled, although the advantage of this prototype is that the effect of one mode on the other is much smaller than in the L-shaped prototype.

Experimental Results Experiments showed that a dynamic normal force of +/- 30N can be generated with a voltage of ±100 V applied to Actuator 2. Unlike Prototype 1, the excitation of Actuator 2 in Prototype 2 predominantly generates a dynamic normal force at the tip (while the thrust force is very small). A maximum slideway velocity was measured at about 0.5 m/s, when both actuators were simultaneously excited**.**

One disadvantage of this motor is that the natural frequency of the mode that generates the thrust force is about 1.5kHz above the resonance that generates the normal force. This difference has to be reduced to 500 Hz for the motor to function. No matter how well the analysis is done to develop the motor it is virtually impossible to build it such that both resonances are at exactly the same frequency. Therefore it must be possible to modify the length or width of one actuator or the attached mass to fine-tune the motor. This is not possible, because all alterations of the L-shaped and T-shapes prototypes influenced both mode shapes and resonant frequencies to about the same extent. If, for example, the length of one actuator is reduced, each individual resonance increases, but the difference between both resonances does not change significantly.

Thermal effects Measurements of the frequency spectrum of the actuator were very repeatable and showed that the resonances were about 1.5 kHz apart. However, when the motor was driving the slideway, after about 5 minutes of operation the motor performance decreased. Repeated measurements of the frequency spectrum showed that the resonance had changed. Eventually the prototype came apart at the glue joints.

Whereas measurements of the frequency spectrum usually take a few seconds, constant excitation at resonance caused the actuator to get very hot. Temperature measurements on the steel mass at the bottom of actuator 2 and at the connection between the actuators (aluminum) showed that the temperature increased well above 70° C. The steel mass was replaced with a ceramic mass to see if the magnetic permeability or the electrical conductivity of the material was a problem. This seemed to solve the problem at first, but further experiments showed that using the steel mass, heat that is generated in the actuator is quickly conducted through the steel and can be measured at the surface. A ceramic mass does not conduct heat, so even if heat is generated in the middle of the actuator, it cannot be detected at the surface.

The generation of heat in the prototype can be linked to the strain energy in the vibrating system that is dissipated by damping. A simulation of the prototype was developed by assuming that the amplitude of the vibration is 10 μm and that all components have the (low) damping loss of the piezo-ceramic material. Under these conditions, the temperature within the actuator reached asteady state temperature of about 60° C, which would barely be acceptable for stable operation of the motor. Since the epoxy-glue has a considerably higher damping loss and experiences higher strain than the rest of the actuator, it can be assumed that most of the heat is generated within the glue joints. The poor heat conductivity of the piezoelectric material makes it even more difficult to measure but it also keeps the heat where it causes most harm. When the glue reaches its temperature limit, the polymers within the glue disintegrate and the actuator falls apart.

To lower the amount of kinetic energy that is transformed into heat, the same actuator could be made from a single piece of piezoelectric material and thus eliminate the glue joints between the actuators). Because this change requires an almost entirely new analysis, a new actuator design should be used to better solve the problem of coupling between both modes and to improve the way the prototype can be tuned after it has been built and tested.

7.2.3 I-SHAPED PROTOTYPE

The motivation for the development of the I-shaped prototype, as illustrated in Figure 5, is to eliminate the glue joints found in the first two prototypes as well as the problem of the coupling between different mode shapes. The basic idea is to use a longitudinal and a bending resonance in a beam shaped actuator. Both resonances will be geometrically independent (uncoupled) and the bending resonance will not excite the longitudinal resonance as long as the design is symmetric in all directions.

This design does not have highly stressed glue joints. The main glue joint is loaded in shear and not in tension and compression as was the case in the previous designs. Because these resonances are determined by fewer factors than those of the T-shaped prototype, the dynamic

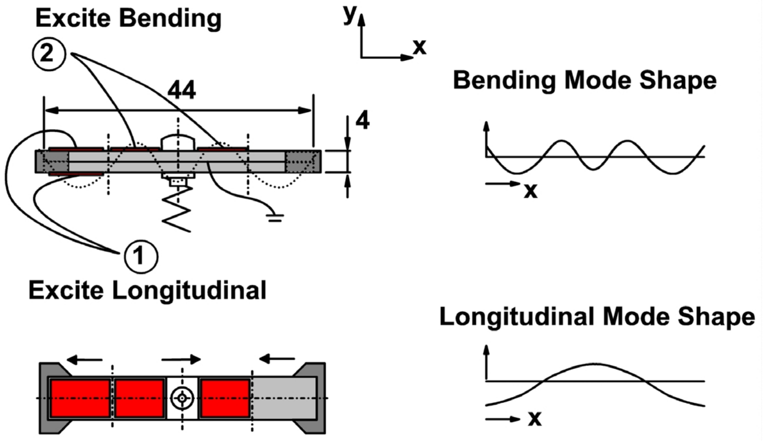

Figure 5. I-shaped Prototype

analysis of the I-shape is relatively straightforward. Analytical solutions for simple beam vibrations can be used to approximate the desired dynamic behavior followed by FEA models to obtain more precise results.

The I-shaped prototype uses the fifth bending mode to generate a dynamic normal force and the second longitudinal mode to generate sliding motion in a very similar manner to the T-shaped prototype 2. Picking the second longitudinal mode means that the motor can be supported at the two nodes of the second longitudinal mode shape. This also means that the motor needs to have a bending mode that has nodes at these two locations. To use the first bending mode would be most desirable, but its resonance is much too low. The third bending mode (as well as all modes with even numbers) could not be used because the node locations could not be made to match the nodes of the longitudinal mode. However, using the fifth bending mode, dimensions could be found such that both resonant frequencies and node locations match. The best tip location is in the middle of the actuator (as shown in Figure 5), because that is the location on an anti-node of both mode shapes and the bending mode does not have a component in the longitudinal direction of the actuator. Thus the bending vibration will only generate a dynamic normal force and no sliding motion or thrust force.

The electric field is applied between one of the electrodes on the outer surface (1) or (2) and the brass electrode in the center. Applying a sinusoidal voltage at the outer electrodes (1) extends and contracts the upper half of the actuator and thus excites the bending mode. An electric field that extends across the actuator will excite the longitudinal mode of vibration. This is done by applying voltage to the inner electrodes (2). Because these two modes are orthogonal, it is virtually impossible to have any interaction between them.

Performance Initial measurements of the frequency spectrum for the forces at the tip indicated that the resonances for the normal force and for the thrust force differed by about 2 kHz. This difference was carefully reduced by adjusting the mass at the ends of the motor.

This prototype was not capable of generating slideway motion. Even after both resonances had been adjusted to be close to the driving frequency of 63.1 kHz, the dynamic normal force of ± 4 N was too small to overcome the static frictional forces induced by the static preload. Although the I-shaped Prototype has not been tested with the highest possible electrical field (± 800V at the electrodes), extrapolation of measurements at lower excitation voltages suggests that the required dynamic normal force of ± 20 N cannot be achieved.

A new prototype had to be developed that is more efficient in generating a dynamic normal force, but still exhibits the major advantages of the I-shaped prototype: 1) a straightforward design process, 2) a mechanism to fine-tune the resonances and 3) heat generation within an acceptable limit.

7.2.4 I$^+$ PROTOTYPE

The basic ideas of the design concept of the I$^+$ prototype are 1) to use the modes of the lowest possible order and 2) to use a longitudinal mode to generate the dynamic normal force. In general, the lower the order of a vibration, the larger the amplitude for the same kinetic energy. Apart from other problems, the L- and T-shaped prototypes easily generated the required dynamic normal force using the first longitudinal resonance of Actuator 2, whereas the fifth bending mode was not nearly as efficient in the I-shaped prototype. Thus, the new design should use the first longitudinal resonance to generate the dynamic normal force in combination with the advantages of the I-shaped design.

Because the only feasible location for the motor support is at the common nodes of both resonances, using the first longitudinal resonance of a beam-shaped actuator means that the motor can only be supported at one node (which is in the middle of the actuator). Consequently, the bending mode that generates the thrust force at the tip must have a node in the center of the actuator as well.

Geometry A sketch of the I$^+$ design is shown in Figure 6. Both pieces of piezoelectric material have the opposite polarization direction, so that the excitation of electrodes 1 and 2 with inverse voltages will cause the upper section of the actuator to expand while the lower section contracts which excites predominantly the second bending mode. This concept is very similar to the I-shaped design. Applying the same voltage to electrodes 3 and 4 (see Figure 6) makes both sections between the electrodes expand and contract at the same time and thus excites the first longitudinal mode. Note that when both vibrations are excited, the entire volume of the actuator is being used.

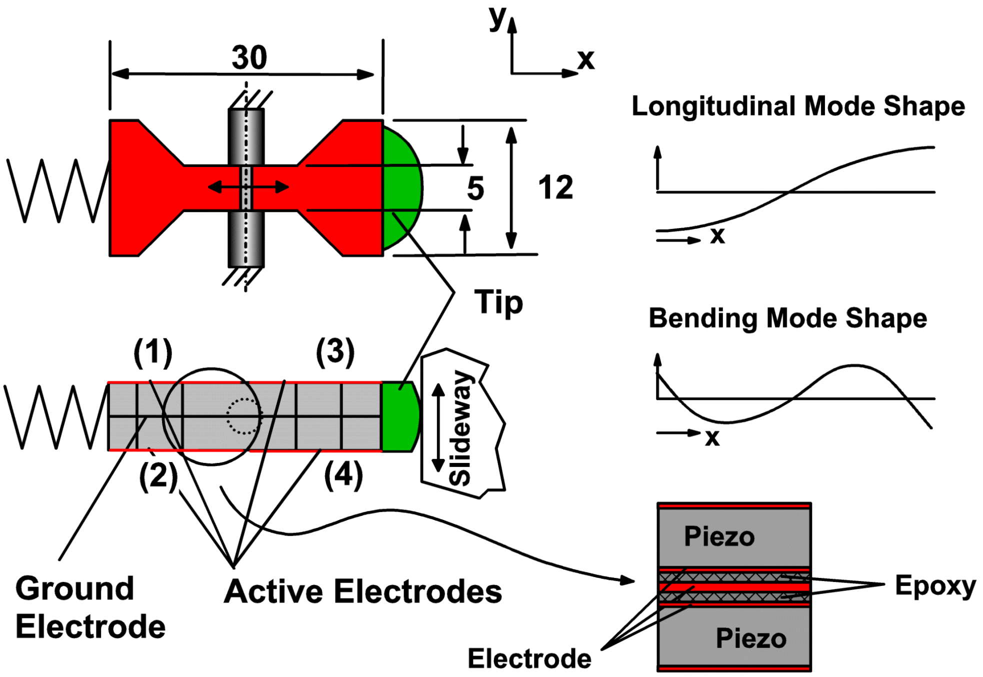

Figure 6. I^+ Prototype

This prototype is dimensioned such that the first longitudinal and the second bending resonance (s-shape) can be excited at 47.1 kHz. If the design is symmetrical with respect to its center, both mode shapes have a common node at the center. This simplifies the design process, because only the resonant frequencies have to be considered during the design process.

Actuator Construction An improvement over the previous prototype lies in the composition of the actuator. With the I-shaped prototype the electrodes on the sides of the piezoelectric plate that are close to the center electrode were removed when the thickness of the piezos was reduced from 3 to 2 mm.

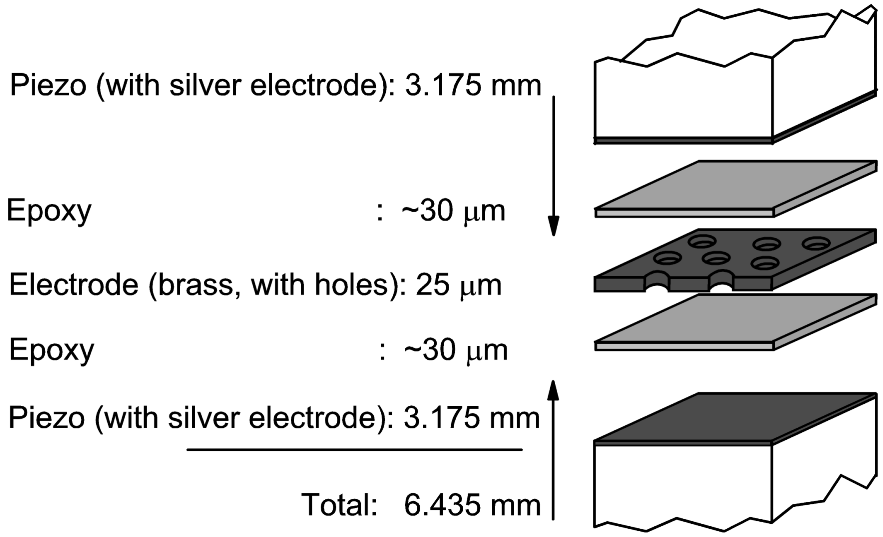

Figure 7. Composition of the actuator (I^+)

The electric field has to go from the outer electrode through the piezo, then through the epoxy layer to the center electrode (which is the electrical ground for all signals). For the I^+ design, the silver electrodes were left on both surfaces of the piezo when they were glued to the center electrode. The idea is that the glue acts from the silver electrode on the surface of the piezo through the holes of the center electrode to the surface of the other piezo. The surface roughness of the center electrode, especially around the holes, in combination with a very thin epoxy layer will allow the center electrode and the silver electrode on the surface of the piezo to contact. Then, the electric field does not diminish over the width of the epoxy layer. A stronger field is left to excite the piezo.

Experiments showed that the first version of the I^+ Prototype was capable of generating the required dynamic normal force of ± 20 N and the longitudinal resonance was within 200 Hz of the predicted frequency. However, the bending resonance was about 4 kHz higher than expected. After the original FEA model had been checked for errors and the dimensions of the prototype were compared to the model no errors could be found. To solely investigate the dynamics of the actuator without any influences from the preload and the tip-slideway contact, experiments were performed where the actuator was not preloaded and thus not in contact with the slideway. The model was altered accordingly. The measured resonant frequencies, mode shapes and amplitudes were in agreement with all predictions. Thus, the problem that the bending resonance is 4 kHz higher than predicted, has to be due to incorrect modeling of the boundary conditions.

Boundary Conditions When a FEA model of the motor is made, boundary conditions at 3 locations have to be considered: (1) the support (in the middle of the actuator), (2) the preload spring and (3) the point contact between the tip and the slideway.

1) The dynamic model is designed without the support. It is later added at the node location and neither resonant frequency nor node locations change.
2) The preload spring is too soft to make a difference if not modeled correctly. Its mass and especially rotational inertia do make a difference. The preload spring mass is modeled as a 0.5 mm plate at the end of the actuator, but the overall effect is too small to explain a 4 kHz deviation even in the worst case.
3) The tip-slideway contact has been modeled (since the first prototype) using the equations for Hertzian deflection. This stiffness would be decreasing for increasing preloads (as the area of contact increases). For all dynamic motor models, linear springs were used with a stiffness equal to the stiffness of the Hertzian contact at the static preload. As the longitudinal resonances for the T-shaped and the I^+ prototypes were exactly as predicted, this linearization seems to works very well.

All models so far had been designed under the assumption that the tip does not lose contact with the slideway, and that it slides on a surface in the direction of the slideway motion. Since the frictional forces under sliding conditions must be much smaller than the stiffness and inertia of the actuator, no boundary conditions were used at the tip in the sliding direction. Under the conditions that only the resonance in the sliding direction is excited, the tip would not lose contact with the slideway. Thus the motion of the tip would be restricted, which would increase the resonance. Whether or not the tip slides along the slideway surface consequently has a significant influence on the boundary conditions needed to design an appropriate model. To determine these conditions, spring elements were added to the FEA model of the I^+ prototype and their stiffness was adjusted to match the measurements.

Experimental Results Figure 8 shows how the bending resonance changes with increasing excitation. Up to an excitation of about 150 V a clear peak can be identified at about 42.0 kHz. This is still about 900 Hz above the predicted value, down from 4 kHz without the additional stiffness. For excitations of 200 V and higher, the peak frequency does not change but the top of the peak looks like it has been cut off. For the conditions of this experiment, the tip starts sliding at an excitation between 150 and 200 V. This voltage will decrease when an additional vibration normal to the sliding surface is present. The importance of this discovery is that the resonant frequency depends on the stiffness of the static tip-slideway contact, even when the tip is sliding along the slideway surface.

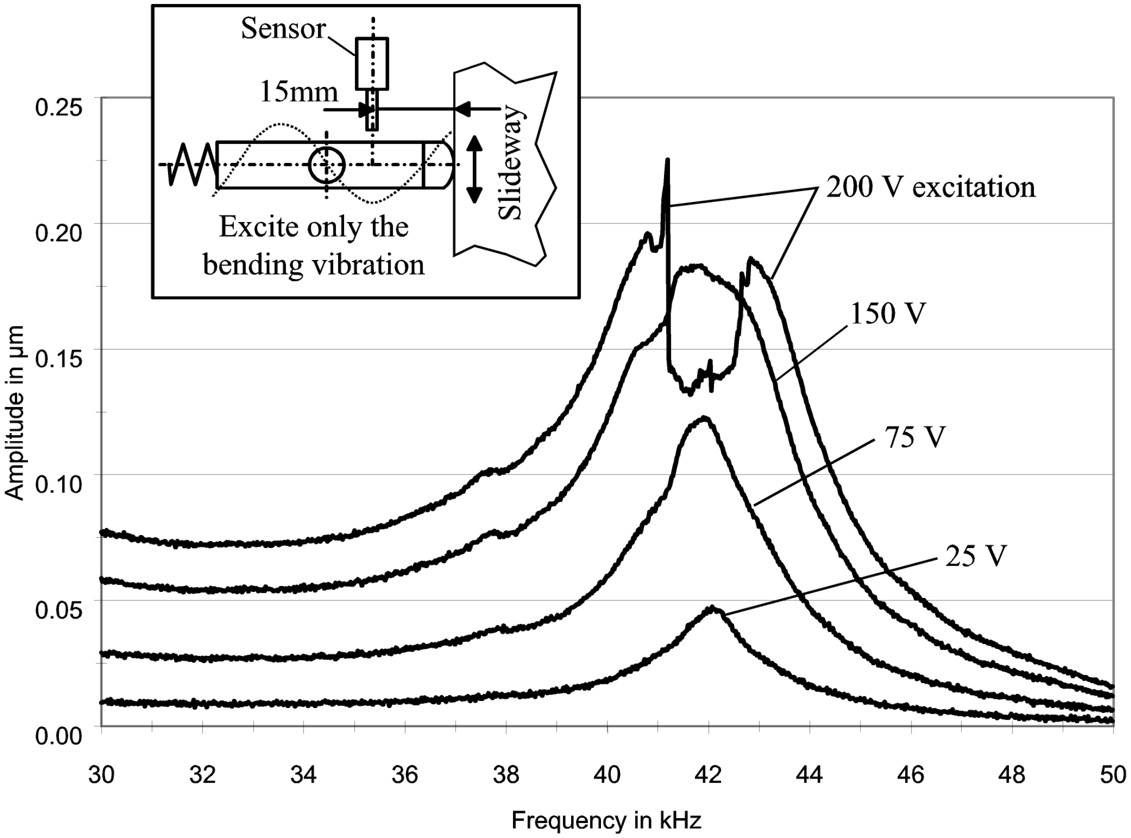

Figure 8. Measurement of the bending vibration

The longitudinal resonance of the I^+ prototype was measured at 41.1 kHz (predicted: 41.275), and this prototype is capable of driving the slideway in both directions as a function of the phase between the excitation of longitudinal and bending vibration.

Future Work Before the final evaluation of the performance of this prototype can be completed, the motor support must be improved and both resonances must be moved closer together. A soft support consisting of two rubber cylinders was used in the current prototype because the softer it is the less potential it has to affect the dynamic properties of the motor. However, soft support does not only reduce the bandwidth of the motor-slideway system as already mentioned, but it may allow the driving forces to rotate the motor. If the motor is not perfectly aligned with the slideway, a certain component of the longitudinal vibration that is supposed to generate only a dynamic normal force also acts in the sliding direction. In terms of controlling the slideway position this means that the phase between both vibrations, at which the slideway does not move, shifts with the alignment of the motor. The motor support needs to be redesigned to better constrain the rotation of the motor. The motor must retain the ability to move normal to the slideway surface so that the preload does not significantly change on an uneven slideway surface and that the motor does not get damaged when the preload is suddenly removed.

7.3 CONCLUSION

The L-shaped prototype was capable of moving a slideway. The design goals were not fulfilled, because the direction of motion could not be controlled. Improvements led to the T-shaped design, which produced a working prototype, but it had serious limitations. The amplitudes of the resonances are the largest of all prototypes built so far and both of the resonant frequencies of interest are only 1.5 kHz apart. This design also allows the motor to be supported at the two common nodes of the corresponding mode shapes. This stiff support increases the bandwidth of the motor-slideway system and prevents the motor from changing its alignment during operation. However problems with this design include the fact that the resonances are still coupled to a small extent, due to the complex geometry of the actuator. Heat generation within the glue joints caused by damping loss in combination with poor heat conductivity of the surrounding piezoelectric material makes the glue joints fail after a few minutes of continuous operation. A T-shaped prototype made from one piece of piezoelectric material (with only one glue joint) is theoretically possible, but very unlikely without compromising its stability.

A different motor concept in combination with improved dynamic models led to the design of the I^+ Prototype, the most promising motor so far. The resonances of interest are virtually not coupled and their frequencies can easily be adjusted. Initial experiments show that the phase angle alone can be used to control the motion of a slideway or rotor. A temperature increase of the actuator during operation has not been detected but the exact properties or limits of this design remain to be determined.

The actuator concept used in the I and I^+ prototypes demonstrated that the combination of bending and longitudinal vibrations of the same simple actuator provides minimal coupling between the two resonances. The longitudinal resonance, however, can much more efficiently generate the dynamic normal force than a bending resonance. In general, the amplitude of a vibration decreases with the order of the resonance (for the same excitation energy). For this reason, the I^+ prototype uses resonances of the lowest possible order (first longitudinal and second bending), but this limits the number of support locations. The soft motor support as shown on the current prototype is a problem, because misalignment changes the effective phase angle for zero slideway velocity and also decreases the bandwidth of the motor-slideway system. Final modification of this design will include optimizing the motor support.

REFERENCES

1. US Patent #5616980, April 1, 1997.

8 DEVELOPMENT OF A PIEZO ACTUATOR FOR CRYOGENIC ENVIRONMENTS

Matias D. Heinrich
Graduate Student
Dr. Thomas Dow
Professor
Department of Mechanical and Aerospace Engineering

The Next Generation Space Telescope is designed to utilize a large optical mirror that must collapse to fit in the cargo bay of the Shuttle Orbiter. Once transported to the cryogenic environment of space (20 to 60 Kelvin), the mirror must be unfolded and the focal point adjusted using many small actuators. These actuators need a stroke of 10 mm, resolution on the order of 10 nm and a design life of 10,000 to 100,000 cycles. Also, these actuators must be able to hold their position in a power-off mode. The exact quantity of actuators is undecided but is expected to be in the range of 100 to 2,500. Conventional low voltage piezoelectric materials offer a low cost and low power consumption solution but extremely reduced strokes in cryogenic temperatures. Current prototypes are designed utilizing this conventional material but new single crystal piezoelectric materials are being developed at TRS Ceramics. These new ceramics are capable of producing strains in cryogenic environments similar to those of conventional piezoelectrics at room temperature but have a greater compliance. The current prototypes are built around precision 80 pitch screws that have inherent power-off holding for axial loads. Active clamping on the latest design is achieved by jamming the screw between two nuts thus minimizing unwanted radial motion of the screw. Rotation of the screw is accomplished by a third rotational nut that has an interference fit with the screw. The difference between static and dynamic friction is sufficient at the interface to turn the screw and yet slip to allow the rotational nut to be repositioned.

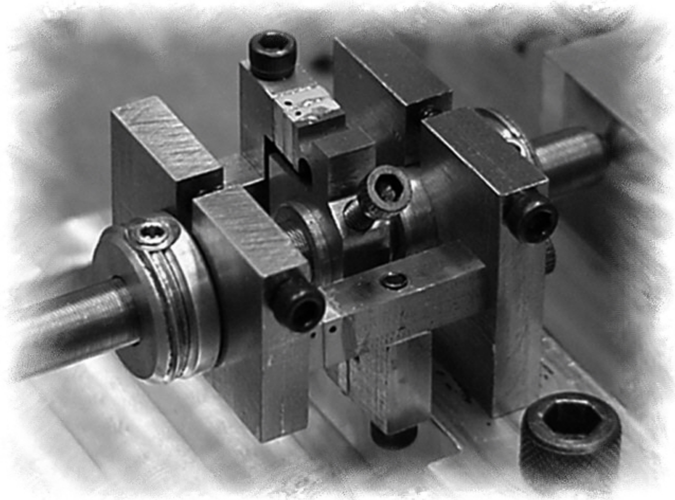

8.1 INTRODUCTION

The Next Generation Space Telescope (NGST) planned to launch in 2008 will utilize a large mirror with a diameter of approximately eight meters. While the Hubble Space Telescope (HST) will be taken out of commission in 2010, the NGST will be a replacement that will also look at the infrared spectrum of light [1]. As the universe is expanding and stars move away from our galaxy at some fraction of the speed of light, the perceived wavelength emitted from these stars increases to the infrared spectrum. This range of wavelengths relates to a visible spectrum using a relativistic version of the Doppler shift equation. This change in perceived wavelength is called a redshift because the visible emitted light is now in the infrared spectrum.

The transportation vehicle (Space Shuttle Orbiter) has a capacity for an object only 4.57 m in width. Therefore the new mirror must be able to fold for transportation. When the mirror is unfolded, the focal point must be adjusted by an array of actuators pushing along the non-reflective side of the mirror. These actuators must have both high-resolution static positioning capability to focus the optical surface and power off set-and-hold capability to conserve the onboard power supply. Some of the requirements are listed below in Table 1.

Table 1. Primary Requirements for the NGST Actuator

Property	Requirement	Goal
Resolution (nm)	<20	<10
Lifecycles	>10,000	>100,000
Stroke (mm)	>6	>10
Operating temperature range (K)	20-60	20-300
Calibration Mode Heat Dissipation (mW)	<5	<0.5
Operation Mode Heat Dissipation (mW)	<0.05	<0.005
Mass (g)	<40	<20
Outside Diamter (cm)	<5	<1
Creep, Operating Mode (nm/day)	<0.1	<0.01
Thermal Stability, Operating Mode (nm/K)	<50	<20
Axial Force, Set & Hold, Operating Mode (N)	>0.5	>1
Axial Stiffness (N/um)	>1	>1
Power Consumption, Calibration Mode (W)	<1	<0.1

Linear motors utilizing piezoelectric crystals seem obvious solutions using products such as Burliegh's Inchworm® or the New Focus Picomotor®. However, piezo ceramics show extremely diminished strain in cryogenic temperatures (approximately one-sixth of that at room temperature). Recently, TRS Ceramics from State College, Pennsylvania, has developed a single crystal piezoelectric material. This material is capable of producing strains in cryogenic environments similar to those of conventional piezo ceramics at room temperature. Adding this new material to the Inchworm or Picomotor could make them potential candidates for this application. Other challenges still remain to be addressed including unwanted displacement (glitch), size, weight, power off set-and-hold and significantly higher compliance of the single crystal material.

8.2 MOTOR DESIGNS

Traditionally, there are two types of precision motors: The first is an Inertia Clamp design, such as the New Focus Picomotor® and the second is an Active Clamp design (Burleigh Inchworm®). The PEC has designed several Active Clamping motors around a modified #8-80 and 1/4”-80 fine pitch screws. These prototypes are known as Cryoworms

8.2.1 INERTIA CLAMP DESIGN

Conventional piezoelectric ceramics are often used for precision motion control such as in the New Focus Picomotor [3] seen in Figure 1. This device depends on the difference between the static and dynamic coefficient of friction at the screw/nut interface to convert the small displacement of the piezoelectric crystal to a useful rotation of the screw. The slightly elongated nut is distorted by the expansion a piezoelectric actuator (PZT). The rapid expansion coupled with the inertia of the screw will force the threads on each side of the nut to slide (low dynamic friction) in opposite directions. When the piezo is slowly retracted, the static friction on the threads provides the torque to turn the screw in the stationary nut and thus extend the end of the screw.

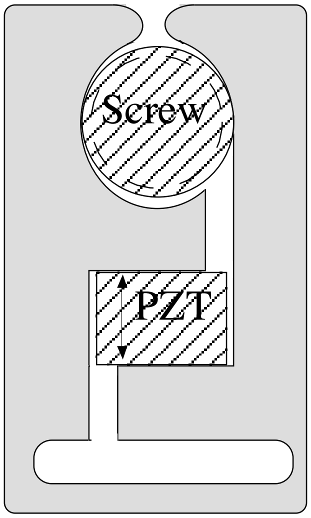

Figure 1: New Focus Picomotor

The Picomotor is a relatively inexpensive device (~$440 without an amplifier) but in its current state is not acceptable for the cryogenic environment. First, the difference between the static and dynamic friction coefficients needed for the operation of the Picomotor may not be the same in space as in room conditions. Second, the strain available from the standard polycrystalline material is severely reduced at low temperatures and thus reducing the stroke per cycle.

Another inertia clamping system is the University of Arizona, Steward Observatory design shown in Figure 2. This design also utilizes the fine pitch screw but instead of piezoelectric material, it uses electromagnetic actuators to produce an impulse force. A brief, high energy impact transfers motion from the electromagnetic actuator to the arm of the outside nut and

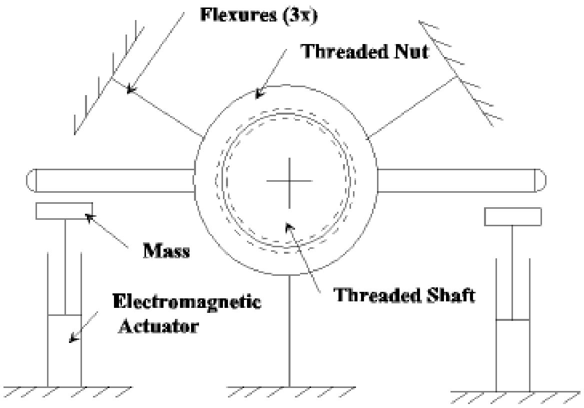

Figure 2. Steward Observatory Design

allows the nut to overcome static friction and begin to rotate on the screw as seen in Figure 3. As the nut is forced to slow down because of the flexures and the friction at the interface, the relative velocity between the screw and the nut approaches zero increasing the interface friction to the static value. The larger interface friction then pulls the screw along to the nominal position of the nut. The screw has now turned a small amount.

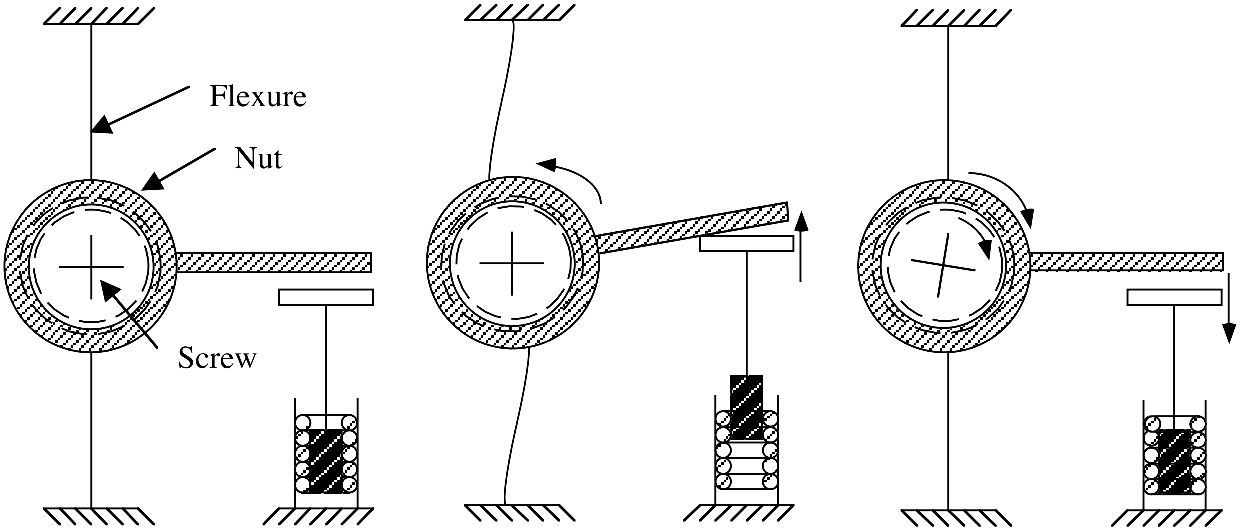

Figure 3. Motion of Simplified Steward Observatory Design

The flexures around the nut are 120° and would be easy to preload since tensioning one flexure carries the same tension to the other flexures. Preload is very important in this design to both maximize the effect of one stroke and minimize hysteresis when the actuator changes direction. This is due to the flexures not returning to their nominal position because the return force approaches zero as the deflected angle of the flexure approaches zero. This concept is shown in Figure 4.

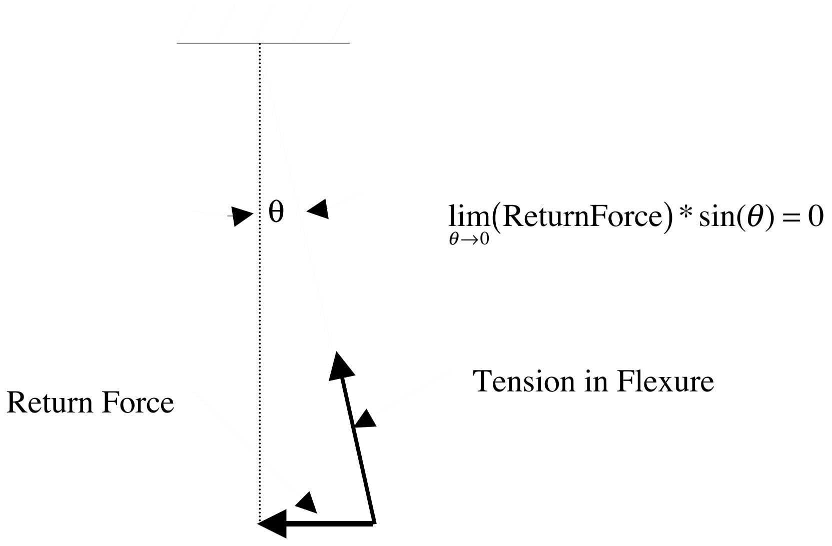

Figure 4. Diminishing Return Force of Flexures

To model the Steward Observatory Design and learn more about the dynamics, a simplified model was designed and is represented in Figure 3. The number of flexures was reduced to two and using a fixed-fixed beam equation, the resistance force of the flexures on the outside of the nut could be estimated. The increase in tension of the flexures as the nut rotates was considered, however the increase in length is a cosine error of the rotation and therefore has a small effect on the tension.

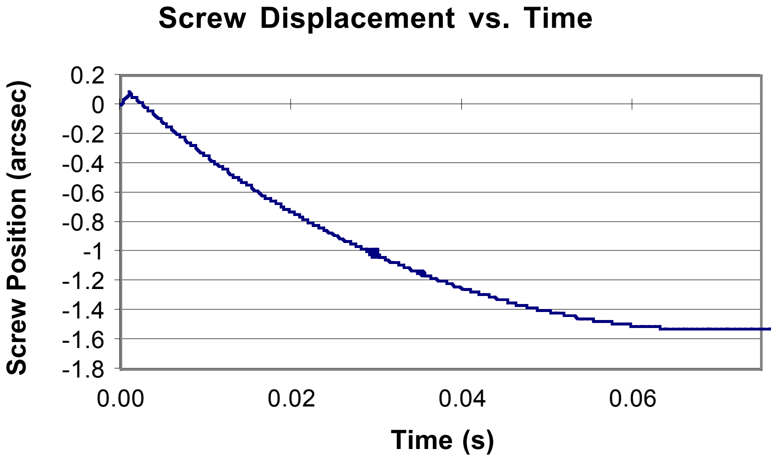

Figure 5. Screw Position vs. Time for One Cycle

To understand the kinematics of the system, a finite difference program was written to calculate the friction forces, position of the nut and screw, and flexure forces as a function of time. Figure 5 plots the screw position for one cycle. This shows an initial, small displacement in the positive direction but a much larger final displacement in the negative direction.

Variables such as the inertia of screw and nut, initial velocity, flexure geometry, etc. were varied to study the final displacement of the screw and learn how sensitive the system is to each components' dimensions. Figure 6 shows the final screw displacement (arcseconds) as a function of the preload (the axial force on the screw) per cycle. It is evident from this figure that the proper preload is an important variable to maximize the stroke of the system.

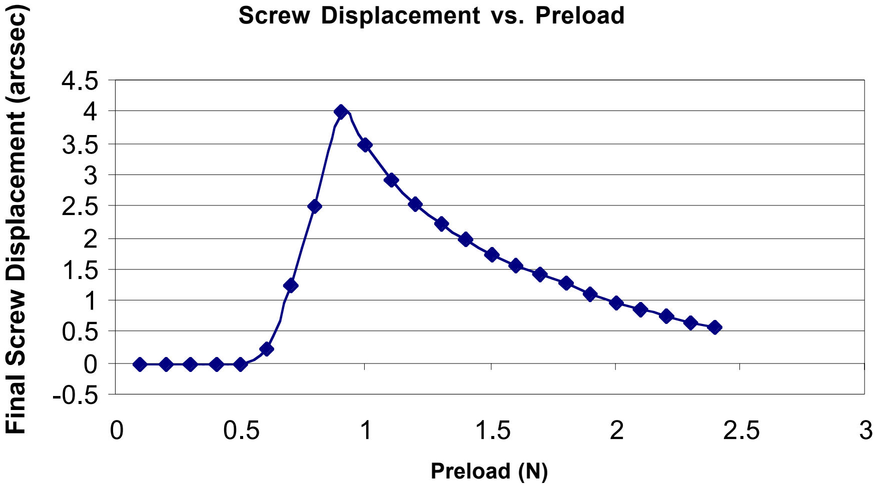

Figure 6. Effect of Preload on Screw Displacement per Cycle

One of the unexpected results from the model was that a single actuator could drive the screw both forward and backward. By significantly increasing the high energy impact of the actuator, the nut overcomes static friction during both the initial rotation and while returning to the nominal position. The reduced damping (friction) allows the nut to overshoot the nominal position before coming to a stop and reestablishing static friction. Finally, as the nut returns to the nominal position, static friction is maintained and the screw rotates with the nut. The displacement of the screw during this cycle can be seen in Figure 7.

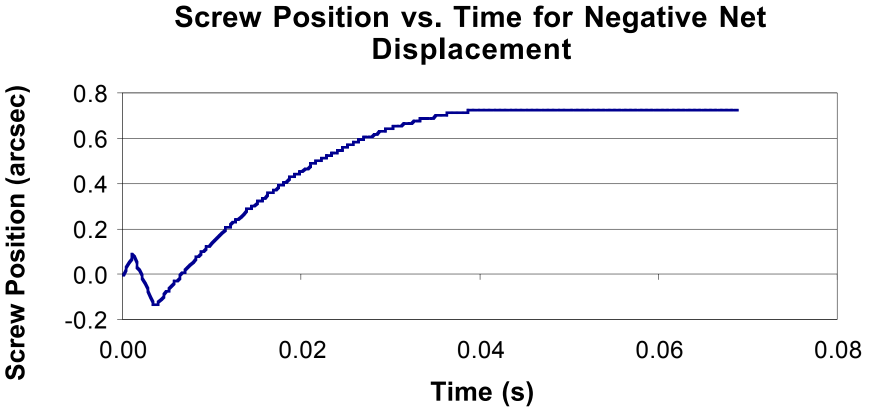

Figure 7. Screw Position vs. Time (Reverse Motion)

8.2.2 ACTIVE CLAMP DESIGNS

An active clamp design differs from an inertia clamp in that it uses physical clamping to provide motion. Burleigh's Inchworm® [2] is a commercial example of such a design. These types of actuators rely on a clamping-displacing-unclamping-retracting cycle on a slideway or bar. The PEC developed several designs based around a fine pitch screw using a cycle similar to that of the Inchworm®. The actuators designated as the "Cryoworm" use one piezoelectric actuator for clamping and a second piezoelectric actuator to cause rotation.

Mark 1 The first candidate design presented in Figure 8 served as a starting point. The rotational actuator turns the screw with respect to a stationary nut extending the end and applying a force to the mirror surface. The design is more complicated than the Picomotor because it requires two (instead of one) piezoelectric actuators to reduce the dependence on the static/dynamic friction difference. The clamping PZT at lower left in Figure 8 is used to increase the diameter of the actuator nut and thus unclamp the nut from the screw (or at least reduce the force). The rotation actuator rotates the actuator nut with respect to the stationary nut. The stationary nut supports the load. To operate the system, the clamping actuator contracts and clamps the actuator nut to the screw. The rotational actuator expands to rotate the screw and extend the end. The clamping PZT then expands and the rotational PZT contracts to reposition and repeat the cycle.

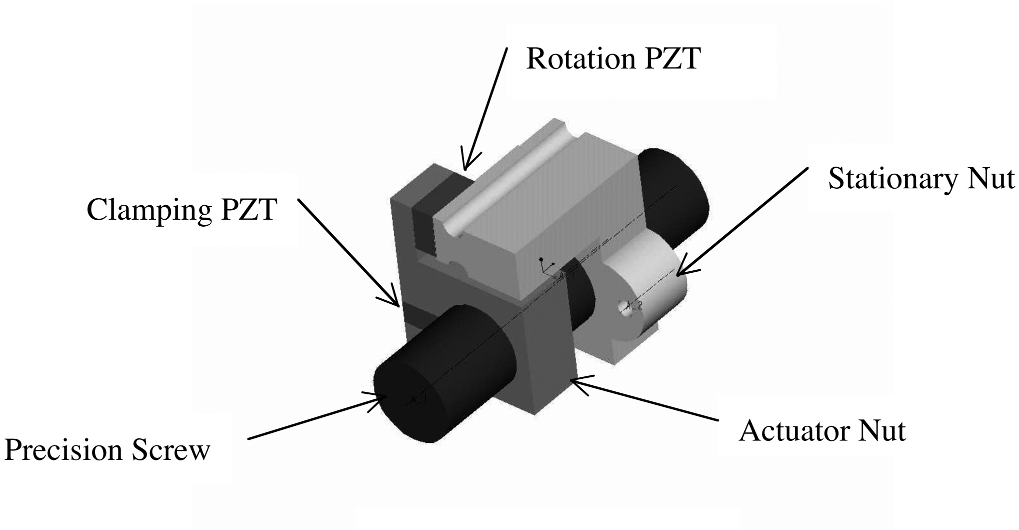

Figure 8. Mark 1

The geometry of the actuator nut plays a key role in the design because of the extremely small displacement of the piezoelectric actuators used. These low voltage actuators (60 V max) are 5 mm x 5mm x 2.1mm and have a stroke of 2.4 um at max voltage. The geometric tolerances for both the actuator nut and the precision screw have to be on the order of 1μm, especially the diameter variation. The clamping of the nut on the screw was studied to find the forces and point of contact between them. Also, the change in shape of the nut when the piezo is actuated was studied. FEM and analytical models were used to find the hoop, radial, and shear stress on the nut. The nut and screw can be approximated by a simple design shown in Figure 9. The screw in the deformable nut fits half way between the hinging (flexure) part of the nut and the actuator. The effective stroke at the point the nut and the screw (at Datum B) meet is about half the full stroke of the actuator (at Datum A).

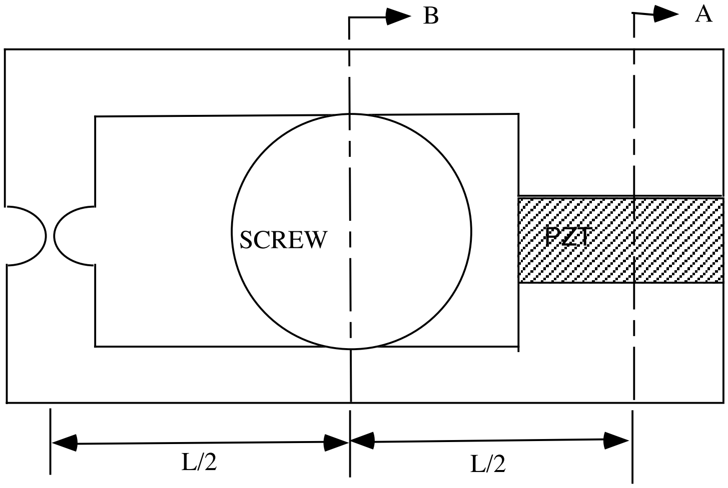

Figure 9. Simplified Model of Clamping Nut

The precision screws purchased from Newport Corporation where found to have a diameter variation of ±25 μm along the length of the screw or about 20 times the stroke of the clamping nut discussed above. So while this design could be made to work at some specific location along the screw, it could not function over the 10 mm stroke required of the device

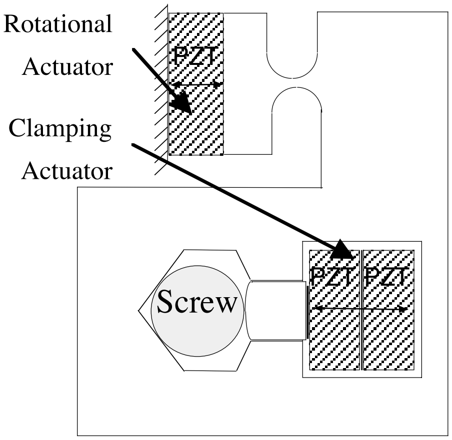

Figure 10. Clamping Nut of Cryoworm

Mark 2 To overcome the stroke/geometry limitations of this first design, a new geometry was introduced as shown in Figure 10. It was built around a modified #8-80 screw where the threads were machined off part of the length. This was done using a ball end mill on a high-speed spindle mounted on a diamond turning machine (DTM). The straightness of the axes on the DTM produced a cylinder with a diameter variation of less then a micrometer. This machined region allows the nut to clamp the screw on a smooth surface reducing unwanted motion and wear of the alumina tip and creates a more constant clamping force. As in the first design, a second threaded nut that is connected to ground converts the rotational motion into axial motion as illustrated in Figure 11.

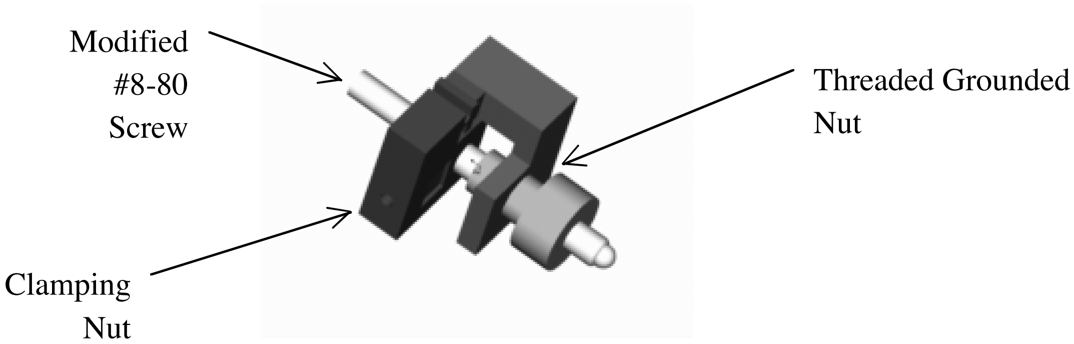

Figure 11. Solid Model of Mark 2 Prototyupe

Figure 12 shows 3 cycles of the clamp/rotation process. The process starts with the rotational actuator, which is energized at about 8 seconds in Figure 12. A large step in the displacement of the end of the screw accompanies this actuation step because the screw is pushed radially in the stationary nut and the screw tends to move axially due to the shape of the threads. The clamp actuator is then actuated (at 10 sec) to attach the screw to the clamping nut. This action also moves the screw in the nut and produces a step. The next step is to de-energize the rotational actuator (at 14 sec) which results in a drop in the displacement by removing the side load on the screw. Finally, the clamp force is removed from the screw at 16 sec and the new position of the end of the screw is reached. For the three cycles shown in Figure 12, the average motion for each step is 3.6 nm.

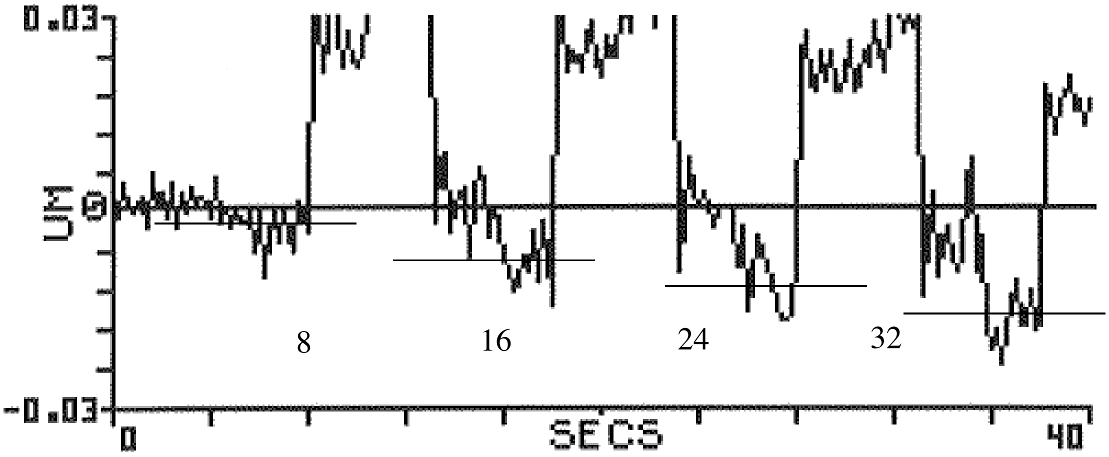

Figure 12. Capacitance Gage Measurement of Three Cycles

A large preload on the end of the screw will reduce the step deflection discussed above by keeping the screw centered in the nut. The stiffness of the flexure both axially and rotationally plays an important role on the operation of the motor. If it is too stiff in bending, it will induce a radial force on the screw but no rotation. If the axial stiffness is too low, it will waste the small stroke of the piezoelectric stack without causing rotation. This affect of a radial force on the screw can be seen in Figure 13.

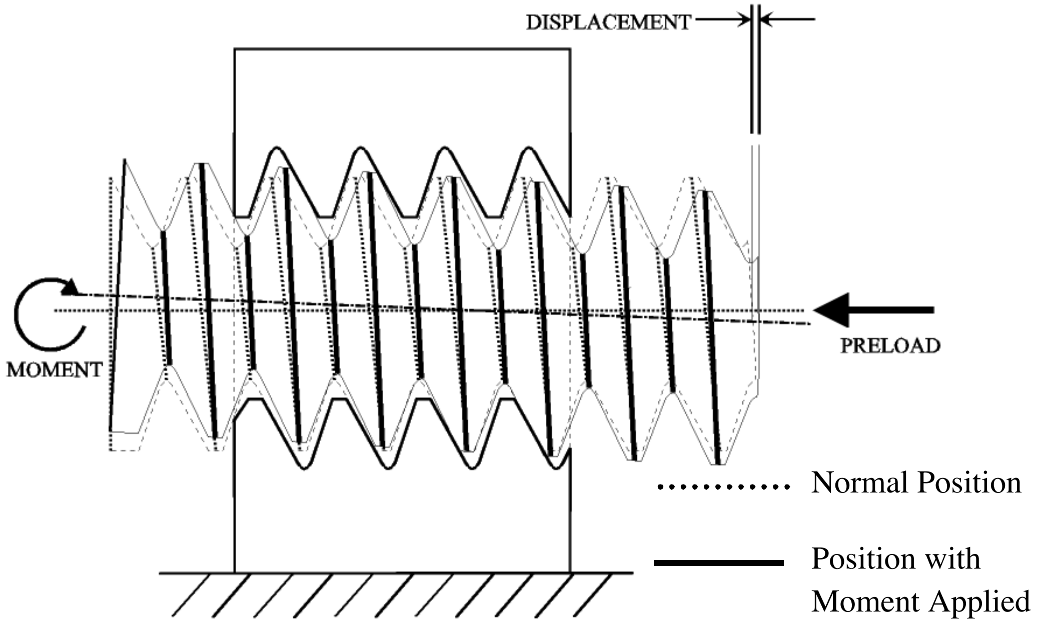

Figure 13. Axial Displacement of Screw due to Applied Moments

During the clamping portion of the cycle the magnitude of the unwanted motion was found to vary with angular rotation. Any eccentricity between the axis of the threaded portion and the axis of the machined portion of the screw can create a moment that rotates the screw slightly.

Mark 3 To improve on the design, the qualities to consider were: a) eliminate the need to modify an existing screw and b) modify the rotational nut to reduce the radial force applied to the screw when energizing the rotational actuators. A new design, Mark 3, was developed to overcome these flaws and is pictured in Figure 14. The solution to the clamping glitch was to use an actuator and push two threaded nuts apart. The jamming actuators push the end plates apart. The end plates transmit this force to the threaded brass nuts.

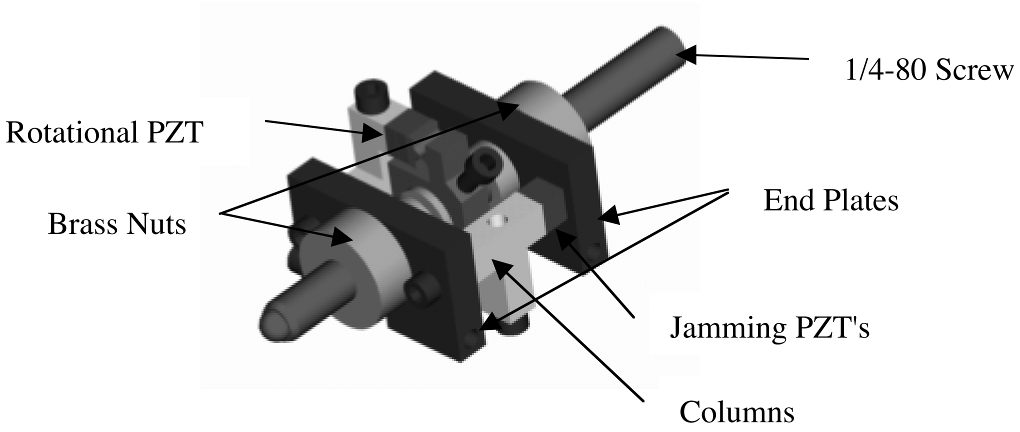

Figure 14: Solid Model of Mark 3 Prototype

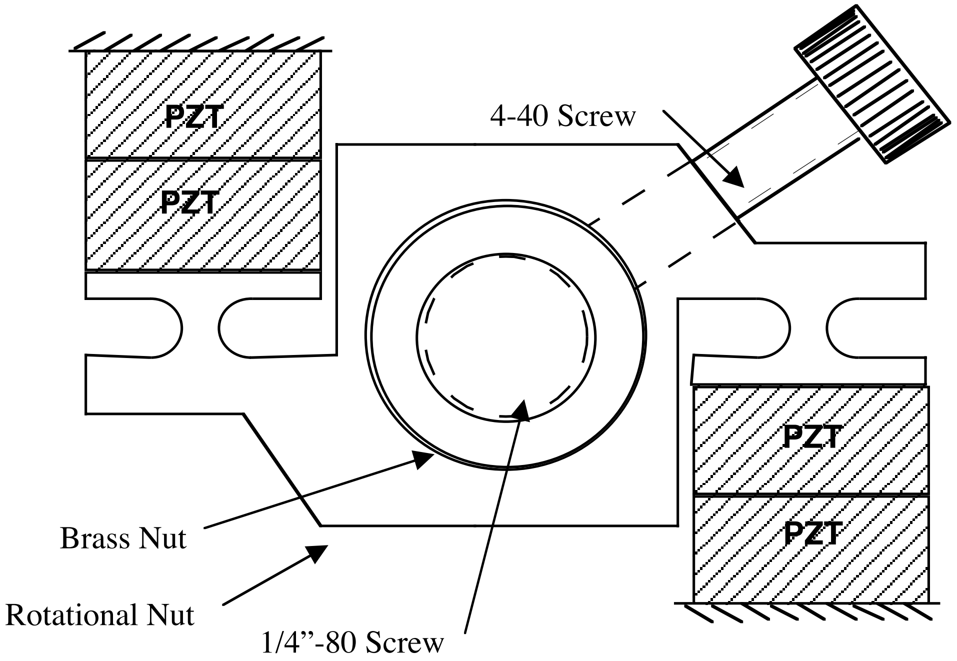

Figure 15. Rotational Flexure Nut with All Interfacing Components

The radial force created when expanding the rotational actuator was compensated by adding a second flexure and actuator stack. Opposing forces created when energizing the rotational actuators are canceled out. The cross section of the rotational flexure nut is shown in Figure 15. The rotational nut has a 4-40 screw that is used to preload (or conform) the brass nut. The interference fit between the brass nut and the precision screw allows a torque to be transmitted from the rotational flexure nut to the screw.

To operate this design, two square waves, 90° out of phase, are required. One square wave expands the end plates and locks the screw and the second square wave rotates the rotational nut. For one full cycle of the motor, the first step is to energize the rotational actuators, which creates a moment on the 1/4”-80 screw through the rotational nut. This screw moves with the rotational nut because of the preload. The next step is to energize the locking actuators, which locks the screw to ground. Then, the rotational actuators are denergized. The rotational nut returns to its nominal position because the torque caused by locking the screw is greater then the torque created by the preload between the screw and rotational nut. The final step is to denergize the locking actuators and the cycle starts again.

An elasticity model was created to calculate the expected resistance torque of the system when the locking actuators were turned on (see Figure 16). The resistance torque value is needed to set the preload between the rotational nut and the screw.

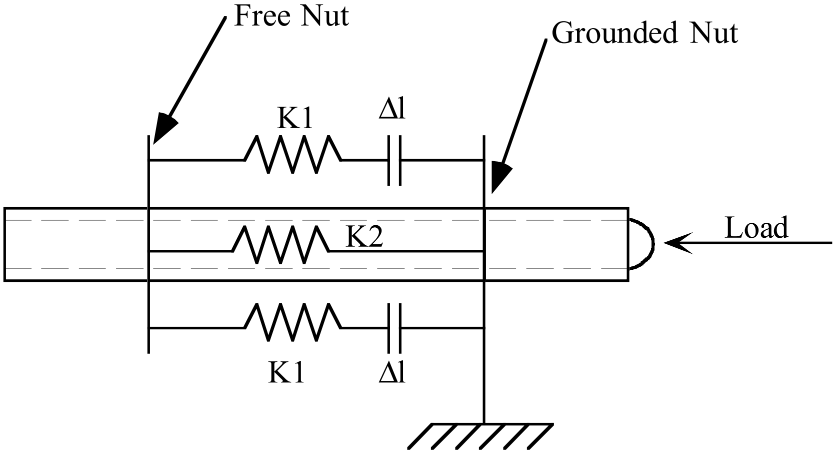

Figure 16: Basic Elasticity Model

8.3 CONCLUSION

Two different types of piezoelectric motors have been discussed; inertia and active clamping. The inertia clamps can be built with a wider variety of actuators and allow greater tolerance in dimensions for operation. A major concern is variation in friction at the cryogenic temperature range of space (20-60 Kelvin) and the effect of that variation on resolution and displacement. There will also be a hysteresis effect when these motors switch the direction of travel. This is due to the deforming nut (New Focus Picomotor®) and flexures (Steward Observatory) not returning to the nominal position after every cycle.

The Mark 2 design showed that active clamping and rotation on a threaded screw can produce displacement but several things had to be overcome including relatively large unwanted displacements during the cycle. The Mark 3 includes features that work around both the sources of unwanted motion. Future work on the Mark 3 design includes minimizing the remaining unwanted motion caused by locking the screw and finding the optimum torque for the rotational nut to turn the screw when the screw is unlocked yet allows slippage when the screw is locked.

8.3 APPENDIX A

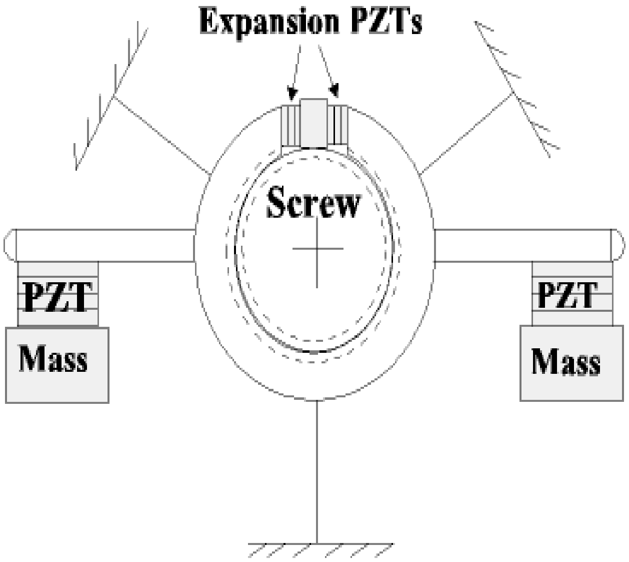

Figure 17: Alternative Active Clamping Design

The alternative active clamping design in Figure 17 utilizes three sets of PZT stacks. The expansion PZT stack is used to expand and contract the diameter of the nut. This nut acts as a type of clamping mechanism on the screw. The other two stacks extend from arms at either side of the nut. Masses are attached to the end of those stacks.

To create relative motion between the nut and screw, the expansion actuators are energized just before the mass actuator. This reduces the friction force that must be overcome to produce relative motion between the nut and screw. One of the two Mass PZT stacks is then energized which produces an equal and opposite force away from the mass. This force is converted to a torque on the nut that must be high enough to break static friction at the nut/screw interface. At the end of the Mass PZT stroke, the expansion PZTs are de-energized thereby clamping the nut onto the screw. The Mass PZT is then slowly de-energized. Meanwhile, the flexures return the nut to a close-to-nominal position. The screw has now turned a small amount.

REFERENCES

1. Brown, R.A. Hubble Space Telescope Web Site. "HST Second Decade," http://sso.stsci.edu/second_decade/.

2. Fasick, J.C., "Development of a Nanometer Resolution Constant Velocity Piezotranslator", MS These, N.C. State University, 1998.

9 DESIGN OF ULTRASONIC FLEXURAL WAVE RESONATOR STRUCTURES USING FINITE ELEMENT METHOD

Tao Wu
Graduate Student
Paul I. Ro
Associate Professor
Department of Mechanical and Aerospace Engineering

One of the key issues in developing a novel miniature cooling system for microelectronics is the optimal design of the resonator structures to generate the maximum cooling effect. Ultrasonic Flexural Wave based resonator structures are being designed by applying finite element method. Natural frequencies and amplitudes of vibration are used as the criteria to determine the appropriate dimensions of the resonator systems. Length and width combinations of 2mm by 1mm and 4mm by 2mm are being investigated under different boundary conditions for acceptable thickness ranges that result in the first-mode resonance at the ultrasonic frequency range. The effect of constant rate voltage field is also investigated.

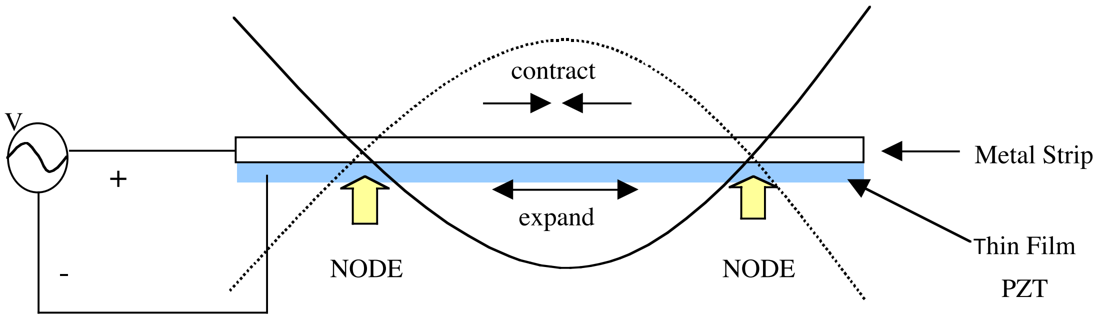

9.1 INTRODUCTION

In high-density electronics, the removal of generated heat has always been a major concern of designers, both electrical and thermal. Currently for computer processors, the best available technique for cooling is a combination of heat sink and fan. However, as the size of the electronic and mechanical components get smaller and performance requirement more stringent, cooling using the conventional fans may limit the miniaturization of these components without the comparable reduction in fan size. Moreover, as the complexity of microelectronic systems continues to increase, directing airflow to each component of the system becomes more constrained. This motivates the use of the Ultrasonic Flexural Wave (UFW) generated on the thin beam resonator as a miniature cooling system. The ultrasonic nature affords two essential features of the UFW based cooling system; 1) Effective cooling that derives from a high rate of acoustic streaming of air that causes convective heat transfer away from a heat source near the resonating structure, and 2) noise-free operation which is recognized as an important consumer benefit. Other benefits include the power efficiency, design simplicity, etc.

How to design the resonator such that the maximum heat can be taken away from the chip is one of the key issues in developing the miniature cooling system. Some experiments showed that the temperature drop generated by UFW is roughly linearly proportional to the vibration amplitude of wave. So this activity is aimed at finding the optimal dimensions for the chip-size resonator structure to obtain the desired wave amplitude using finite element method, thus providing design guidance for a prototype system.

9.2 BACKGROUND

Since the development of the first electronic digital computer, removal of heat has played a key role in insuring the reliable operation of each successive generation of computers while maintaining acceptable low circuit temperatures. Historical trends that have made this problem progressively more difficult involve the development of ever larger scales of circuit integration on a single chip and the arrangement of multiple chips in closer proximity on a module. The need to accommodate these trends while controlling chip junction temperatures provides a significant set of analytical and experimental challenges to thermal engineering [1, 2]. By using common circuit packaging techniques, Figure 1 was constructed based on operating limits and thermal performance experience [3]. This "thermal performance map" is valid for planar arrays of components. The two main parameters that drive the choice of base cooling technology are the maximum device power (or dissipation intensity) and the ensemble-average heat flux. High values of either of these two parameters result in a difficult cooling situation. Current trends are causing the operating points for computers to move upward and to the right on the performance map.

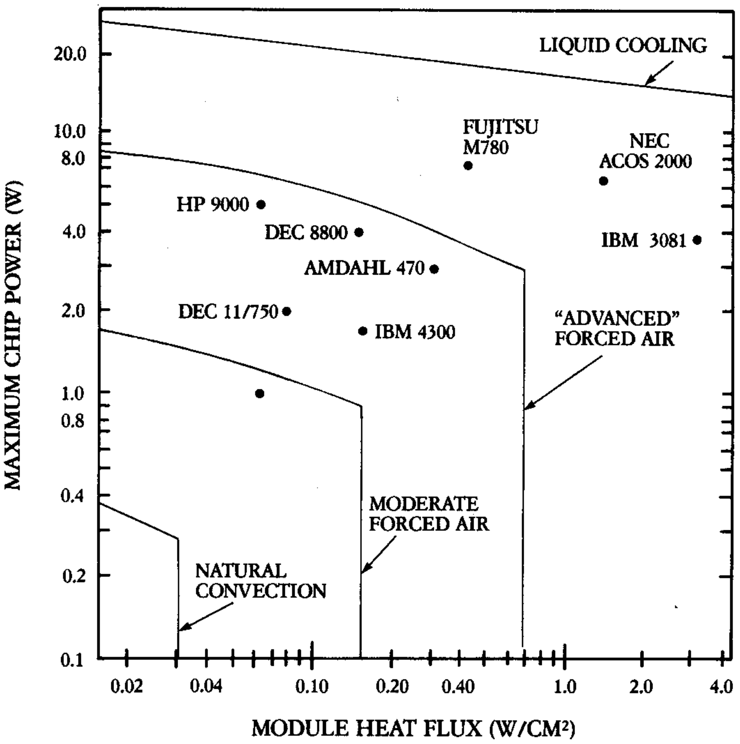

Figure 1. Module-level thermal performance map (from [3])

The main purpose of cooling chips is to keep the junction temperature at a level ensuring that the Mean Time Between Failure (MTBF) of the subsystem is acceptable [4]. Chips are supplied with a specified FIT (Failure In Time) rate. The FIT rate is directly linked with the junction temperature of the device [5], the dependence is exponential and follows the Arrhenius law. The junction temperature range is a tradeoff between reliability, electrical performance and cooling approach. However, an upper limit of 85°C for junction temperature is commonly used in computer industry. Generally speaking, there are two kinds of cooling techniques: air-cooling and liquid-cooling.

9.2.1 AIR COOLING SYSTEMS

For decades, air has been the preferred fluid for cooling electronic packages ranging from printed circuit boards to chips and multichip modules. Its desired attributes relate to simplicity, low cost, ease of maintenance, and high reliability. Accordingly, an extensive knowledge base has been developed to facilitate the design of related cooling systems. However, due to the poor thermal properties of air compared with water, it becomes necessary to use extended surfaces, commonly termed as heat sinks.

Heat Sink Flow through heat sinks refer to heat sinks wherein the flow enters the heat sink from one end and travels more or less in a straight line to exit at the other end. The linearly extruded aluminum heat sink is one of the simplest and most cost-effective heat sink designs [6]. Such heat sinks are commonly used for many applications, but are limited to relatively low-power dissipation due to the limitation of total surface area per volume. This difficulty can be somewhat overcome by using epoxy-bonded fin heat sinks. The epoxy interface does, however, add a thermal resistance to the system [7]. Pin-fin heat sinks are also commonly used and have the added advantage of not requiring specific positioning relative to flow direction. However, for parallel heat sinks it is important to design the heat sink accounting for all air flow paths, since the air can bypass the heat sink if other low-resistance paths exist [8].

Impingement Air Cooling Some of the difficulties arising in flow through heat sinks relate to the pressure field in the actual system and the air temperature rise due to upstream power dissipation. A heat sink designed for general use and tested for specific air flow rate and inlet air temperature may end up in a system where the air reaches the heat sink at a significantly higher temperature and may even bypass the heat sink if the least-resistance path lies around the heat sink instead of through it [9]. One method to overcome these difficulties is to use air impingement [9,10] where the air is ducted directly to the heat sink and forced through it. This approach is costly and requires some additional space in the direction perpendicular to the boards. Most of the impingement applications use pin-fins [11], while some utilize straight fins [12].

Hybrid Air-water Cooling With the dramatic increase in power density, use of serial air flow alone would result in a substantial temperature rise in the cooling air from inlet to outlet. So a means of controlling the temperature of the cooling air as it passed through a column of boards was required. The challenge was met through the development of a hybrid cooling scheme [13]. With this scheme, heat continues to be removed from the modules of cards by the flowing air. The hot air, however, passes through the air-liquid heat exchanger before arriving at the next board. Analysis of chip junction temperatures in an electronics frame demonstrated reductions in the maximum junction temperature, mean junction temperature, and the range of junction temperatures with the hybrid scheme [14].

9.2.2 LIQUID COOLING SYSTEM

Compared with gases, liquids have superior thermal properties. Their ability to transfer heat by convection, and thus, to provide smaller thermal resistance, substantially exceed that of gases. Liquid cooling can be categorized into two types: Indirect liquid cooling and direct liquid cooling.

Indirect Liquid Cooling Indirect liquid cooling refers to the cooling method for which the heat dissipating electronic components are physically separated from the liquid. As applied to multichip modules, indirect liquid cooling involves attachment of cold plate to the module. Heat removed from a chip or chip package is transferred through an intermediate structure before reaching the cold plate, through which the liquid coolant is pumped. A well-known example of indirect liquid cooling is the thermal conduction module (TCM) used on the IBM 3080X/3090 series of computers [15]. It should be noted that in TCM, to cool the chips on the module, it is conceptually desired to bring the water-cooled cold-plate surface as "thermally" close to the chips as possible. However, allowances should be made for variations in chip heights and locations resulting from the manufacturing and assembly processes, nonuniform thermal expansion or contraction across whatever thermal path is provided. These considerations led to the development of TCM utilizing a spring-loaded mechanical piston touching each chip. An increase in cooling capacity was achieved by refinement and optimization of the piston geometry, bringing the cooling water closer to the chips, reducing the module-to-chip plate thermal interface resistance, and improving heat transfer to water flowing through the cold plate.

Direct (immersion) Liquid Cooling Direct immersion liquid cooling has long been recognized as a potential method to satisfy integrated circuit chip cooling requirement [16]. Because this cooling method maintains physical contact between the coolant and the electronic components, the coolant must have a very large dielectric strength and good chemical compatibility with the components. Typically such coolants are characterized by low boiling points. Experimental cooling systems were built and used to investigate and demonstrate the feasibility of direct immersion liquid cooling with flow-boiling of fluorocarbon liquids [17]. However, because of some difficulties in implementation, until now there are no commercial computers using phase change with dielectric liquid. The only exception is Cray [18], but they use forced convection in dielectric liquid.

9.2.3 THERMAL MANAGEMENT IN NOTEBOOKS

Notebook is a special case of electronics. Because of the high performance processors and new features in notebooks, higher power dissipation is generated inside the notebooks. This creates a greater need for high performance thermal solutions without increasing size and weight. Four configurations tested in the notebook that meet the required thermal design target of 6.5W of CPU power with 4W of board power are summarized in [19].

Heat Sink and Aluminum Plate One L-shaped aluminum plate was attached to the tape carrier package (TCP) case using thermal grease. As mentioned before, to reduce the thermal resistance from the heat sink to the ambient air, a large surface area is needed for the heat sink. The actual size of the heat sink used in a notebook depends on the available space of the notebook and other complementary thermal enhancements.

Heat Pipe Connected to the Keyboard Since there is little space for a large heat sink in the notebook, the bottom of the keyboard provides a large surface area for heat dissipation. In this configuration, the keyboard is used as a heat sink.

Heat Pipe Connected to an Outside Aluminum Plate To reduce the heating of the components inside the notebook caused by the power dissipation of the CPU, the best passive solution is to conduct the heat out of the system and dissipate it to the outside ambient. Compared with the results of the previous two configurations, the component temperatures of the heat pipe connected to the outside aluminum plate setup are much lower.

Fan/Heat Sink In this configuration, a fan/heat sink was attached to the thermal plane of the board. Because of the forced convection, there are few hot spots in the system. However, there are two issues with active solutions using a fan; one is the power consumption, and the other is the noise and reliability of the fans. Currently the best available technique for cooling in computer processors is a combination of heat sink and fan. However, a need is great to replace this old technique by smaller and more efficient alternatives. Due to the significant features of ultrasonic waves, the UFW based miniature cooling system is proposed.

9.3 SIMULATION METHOD

9.3.1 RESONATOR STRUCTURE

The resonator structure consists of two parts; a piezoelectric layer and an aluminum beam which is on the top of the PZT, as shown in Figure 2. The voltage is applied on the PZT.

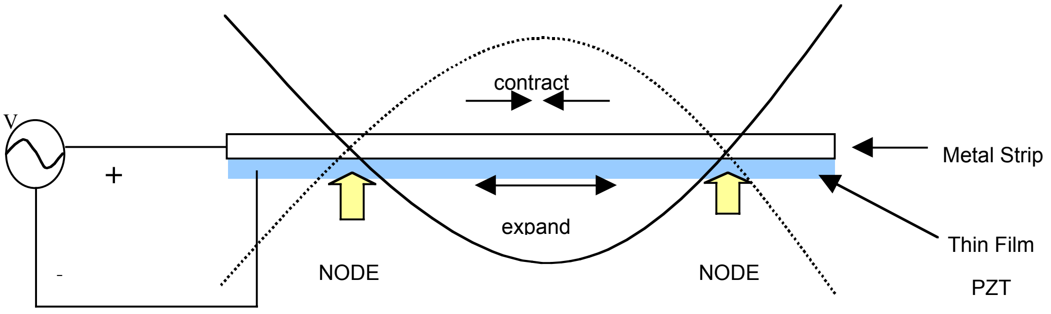

Figure 2. Resonator structure

To simplify the fabrication process, length, width and thickness of PZT layer are the same as those of aluminum strip, respectively. So the thickness of the resonator structure is twice the PZT thickness. The piezoelectric transducer is made of PZT4 material with its polarization direction aligned along the Z axis.

9.3.2 NATURAL FREQUENCIES AND MODE SHAPES

The natural frequencies and mode shapes are important parameters in the design of a structure under dynamic loading conditions. In this paper, a commercial finite element analysis software ANSYS5.6 was used to perform the modal and harmonic analyses. For ANSYS analyses, the resonator structure is constructed by bounding the PZT strip with the same size and thickness aluminum as in the unimorph. Grids consisting of 10(L)×5(W), 20×10, 40×20 cells were tested. Little variation in the parameters of interest, i.e., natural frequencies and displacements, was observed between the two highest grid density solutions. The final mesh size of the resonator structure used was 20×10.

9.4 RESULTS AND DISCUSSIONS

9.4.1 CONSTANT VOLTAGE FIELD

Constant voltage field of 5 volt is imposed on PZT resonator at this point. Two boundary conditions are considered:

- Both ends of the structure are fixed
- Only one end is fixed

9.4.2 BOTH-ENDS FIXED STRUCTURE

From experience, it is believed that the good choice of ratio between length and width is 2:1 for this cooling structure, the following two cases were investigated:

(1) Length of PZT is 2mm, width is 1mm
(2) Length of PZT is 4mm, width is 2mm

For the first case, that is, dimension is 2mm by 1mm, the PZT thickness is varied from 1 μm to 40 μm, which indicates that the thickness of the resonator structure is varied from 2μm to 80μm. From the ANSYS results, it is found that only when the thickness of the resonator is greater than 20μm (the thickness of PZT is greater than 10μm) will the first resonance frequency be in the ultrasonic range. Figure 3 is the modal and harmonic analysis results when the PZT thickness is 10μm. In the right panel, the two curves represent the displacement versus frequency at point P1(0.5mm,1mm) and P2(0.6mm,1mm). These two points are believed to have the maximum displacements when the structure resonates at the first natural frequency. Figures 4 and 5 show the fundamental resonance frequencies and its corresponding amplitudes versus the thickness of PZT (≥ 10μm). With an increase in PZT thickness (see Figures 4 and 5), the fundamental resonance frequency increases while the corresponding amplitude decreases. Because the cooling effect (temperature drop) is roughly as a linear function of the vibration amplitude, the PZT thickness range between 10μm and 13μm is acceptable for the 2mm by 1mm structure with both ends fixed.

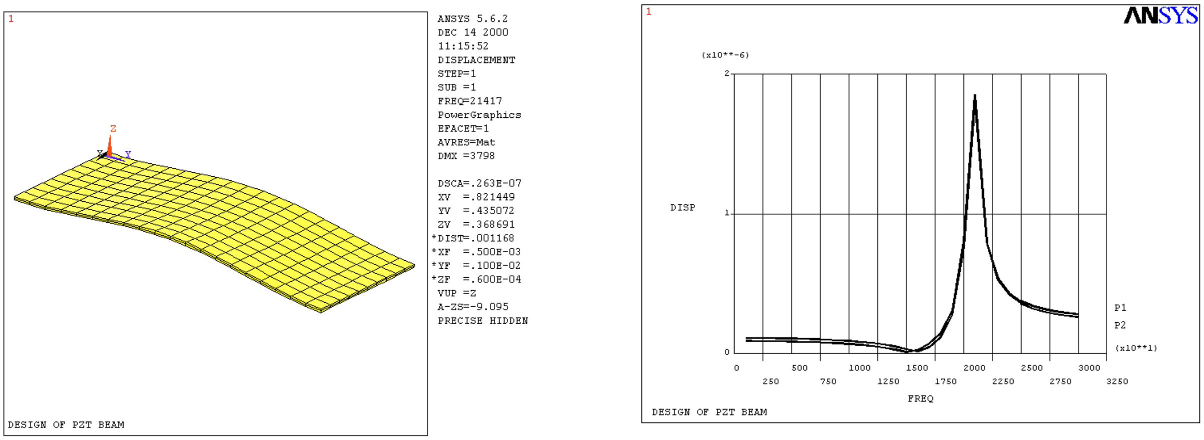

Figure 3. Modal and harmonic analysis results when thickness is 10μm (2mm×1mm, both ends fixed)

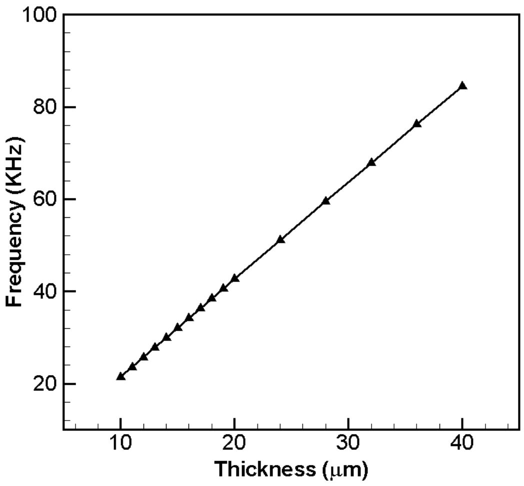

Figure 4. Variation of the first resonance frequency with PZT thickness (2mm×1mm, both ends fixed)

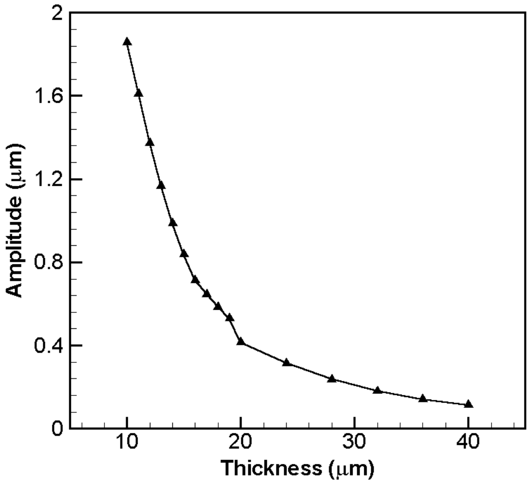

Figure 5. Variation of the amplitude with PZT thickness (2mm×1mm, both ends fixed)

The same procedure is performed for the second case, that is, 4mm by 2mm structure. In this case, the fundamental ultrasonic resonance frequency can be obtained only when the PZT thickness is greater than 40μm. Figure 6 depicts the modal and harmonic analysis results for the

PZT thickness of 40µm (for the point P1(1mm,2mm) and P2(1.2mm,2mm)). The fundamental resonance frequencies and their corresponding amplitudes versus the thickness of PZT (≥ 40µm) are plotted in Figures 7 and 8. As shown in the figures, the PZT thickness range between 42µm and 52µm is acceptable for the 4mm by 2mm structure with both ends fixed.

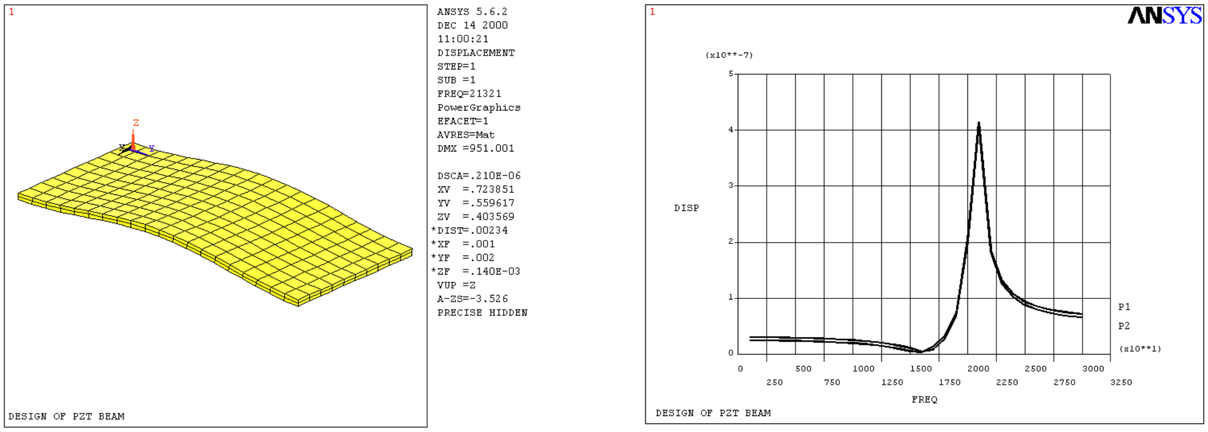

Figure 6. Modal and harmonic analysis result when thickness is 40µm (4mm×2mm, both ends fixed)

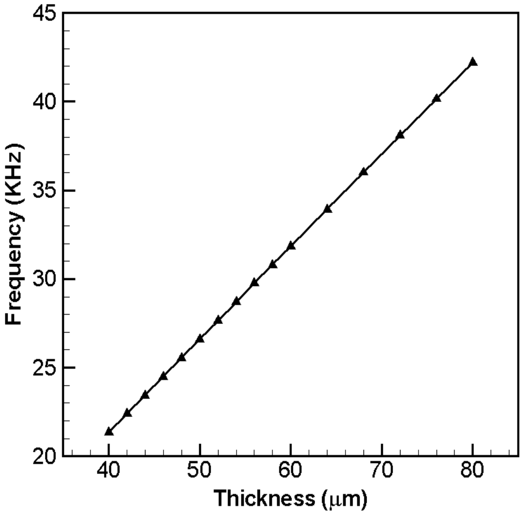

Figure 7. Variation of the first resonance frequency with PZT thickness (4mm× 2mm, both ends fixed)

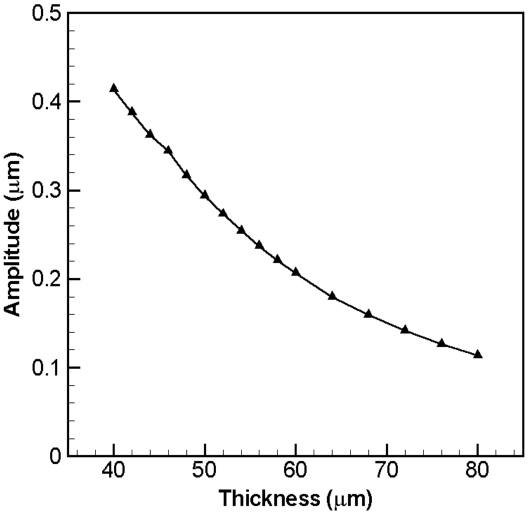

Figure 8. Variation of the amplitude with PZT thickness (4mm×2mm, both ends fixed)

9.4.3 ONE-END FIXED STRUCTURE

Considering the boundary condition with only one end fixed, the following two cases were simulated:

(1) Length of PZT is 2mm, width is 1mm
(2) Length of PZT is 4mm, width is 2mm

For the 2mm by 1mm structure, the fundamental ultrasonic resonance frequency can not be achieved until the PZT thickness reaches 62µm. Figure 9 is the modal and harmonic analysis results for the PZT thickness of 62µm. In the right panel, the two curves are the displacement versus frequency for the point P1(0, 2mm) and P2(1mm, 2mm). Figure 10 and 11 show the variation of the first resonance frequencies in the ultrasonic range (may be non-fundamental) and their corresponding amplitudes with respect to the PZT thickness. It is observed that when the PZT thickness reaches 62µm, the first resonance frequency in the ultrasonic range has a significant decrease, while the amplitude has a tendency to increase. In terms of power efficiency and amplitude, the acceptable PZT thickness range is from 62µm to 80µm for the 2mm by 1mm case with one end fixed.

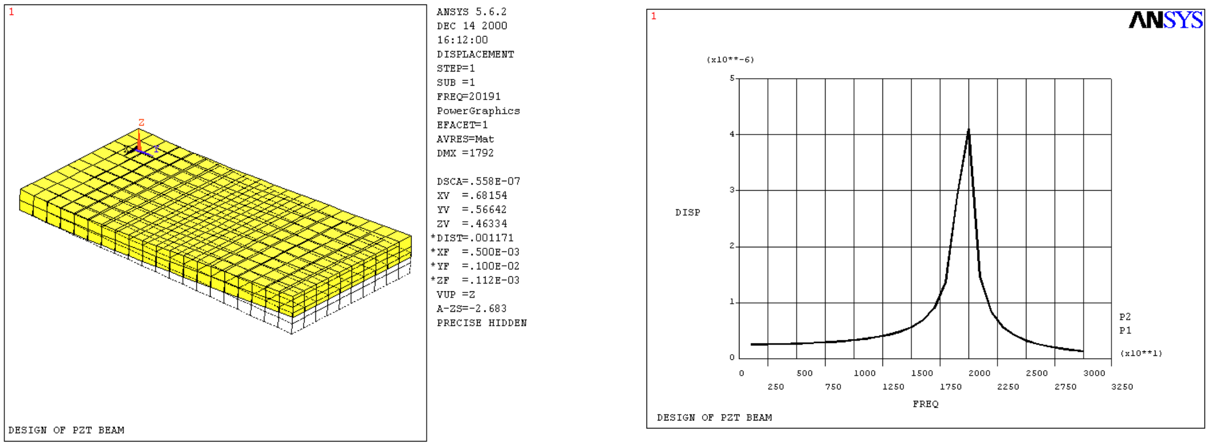

Figure 9. Modal and harmonic analysis results when thickness is 62µm (2mm×1mm, one end fixed)

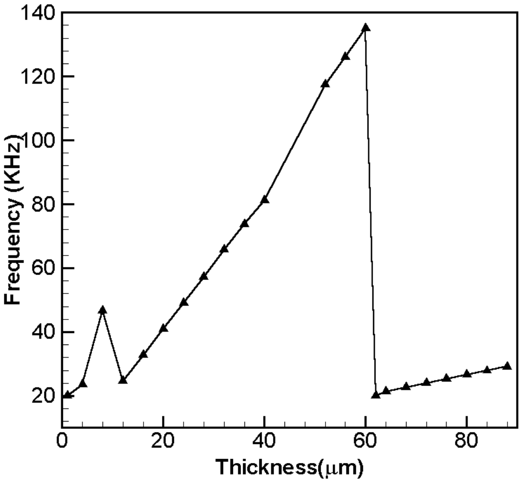

Figure 10. Variation of the first ultrasonic resonance frequency with PZT thickness (2mm× 1mm, one end fixed)

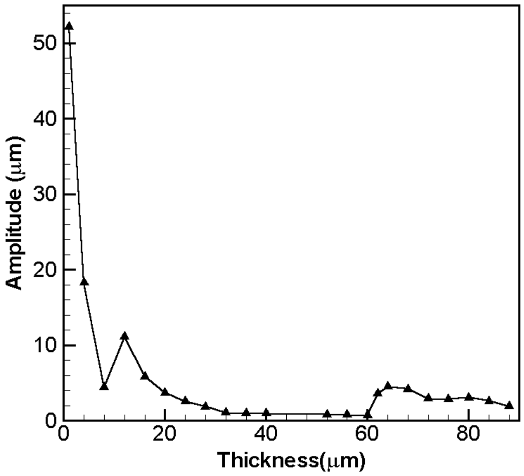

Figure 11 Variation of the amplitude with PZT thickness (2mm×1mm, one end fixed)

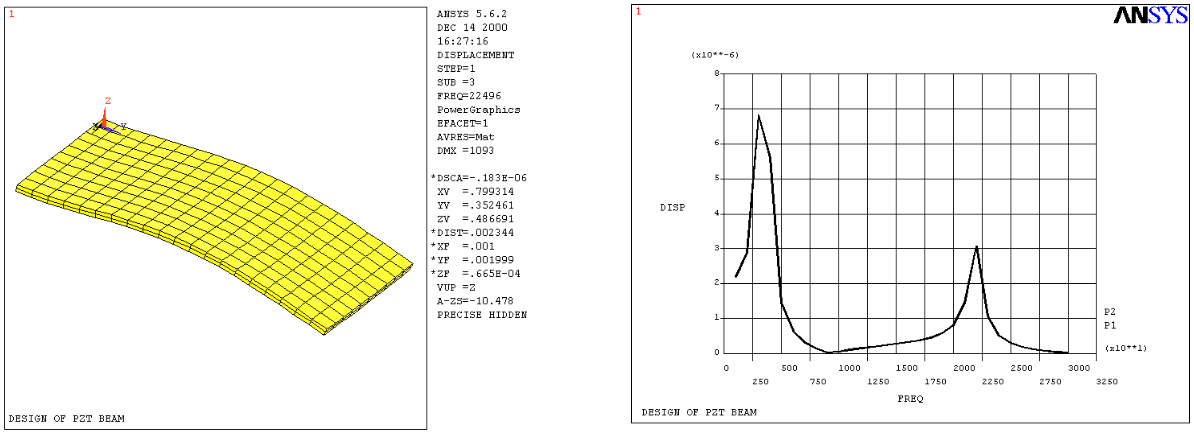

```
ANSYS 5.6.2
DEC 14 2000
16:27:16
DISPLACEMENT
STEP=1
SUB =3
FREQ=22496
PowerGraphics
EFACET=1
AVRES=Mat
DMX =1093

*DSCA=-.183E-06
 XV  =.799314
 YV  =.352461
 ZV  =.486691
*DIST=.002344
*XF  =.001
*YF  =.001999
*ZF  =.665E-04
 VUP =Z
 A-ZS=-10.478
 PRECISE HIDDEN
```

Figure 12 Modal and harmonic analysis result when thickness is 44μm (4mm×2mm, one end fixed)

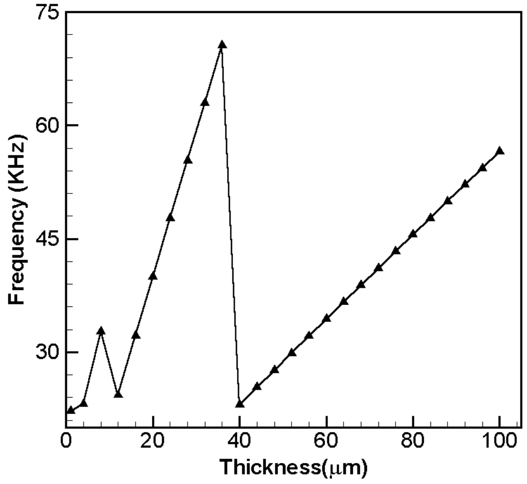

Figure 13. Variation of the first ultrasonic resonance frequency with PZT thickness (4mm× 2mm, one end fixed)

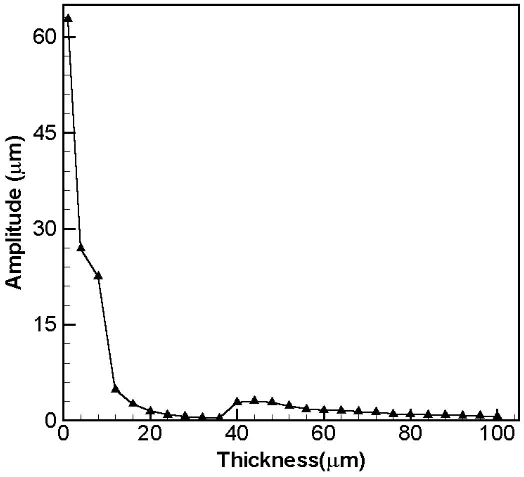

Figure 14. Variation of the amplitude with PZT thickness (4mm×2mm, one end fixed)

The same procedure is performed for the 4mm long, 2mm wide PZT. Varying the PZT thickness from 1μm to 100μm, the first resonance frequency is always in the sonic range. So a tradeoff has to be made between the power efficiency (number of mode shape) and amplitude. Figure 12 is the modal and harmonic analysis results in this case when the PZT thickness is 44μm (the first ultrasonic resonance frequency is the 3rd mode at this thickness). Figures 13 and 14 depict the variation of the first resonance frequencies in the ultrasonic range and its corresponding amplitudes with respect to the PZT thickness. It can be concluded that the acceptable PZT thickness range is from 40μm to 52μm for the 4mm by 2mm case with one end fixed.

9.4.4 CONSTANT RATE VOLTAGE FIELD

Figure 15 shows the amplitude versus applied voltage for the 4mm by 2mm by 88μm resonator structure at the third mode shape, i.e., the first ultrasonic natural frequency. Given the dimension of the structure, the amplitude is a linear function of the applied voltage. So larger voltage can be applied to obtain larger amplitudes.

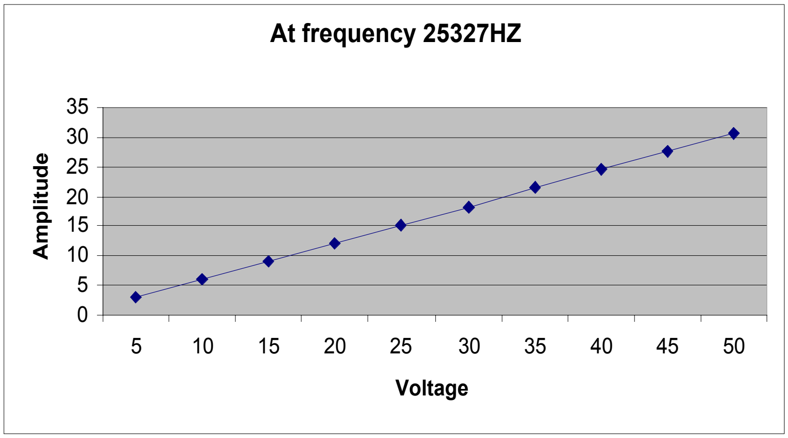

Figure 15. Variation of amplitude with applied voltage

9.5 CONCLUSIONS

To design the chip-size cooling system, simulation results and recommendations for the sizes of PZT are given. Four cases were investigated when constant voltage (5 volt) is applied on top of PZT:

- For 2mm by 1mm structure with both ends fixed, the PZT thickness range between 10µm and 13µm is acceptable.
- For 4mm by 2mm structure with both ends fixed, the PZT thickness range between 42µm and 52µm is acceptable.
- For 2mm by 1mm structure with only one end fixed, the acceptable PZT thickness range is from 62µm to 80µm.
- For 4mm by 2mm structure with only one end fixed, the acceptable PZT thickness range is from 40µm to 52µm.
- The effect of constant rate voltage field is also investigated.

REFERENCES

1. Bergles, A. E., “The evolution of cooling technology for electrical, electronic, and microelectronic equipment”, ASME HTD, Vol. 57, pp. 1-9, June, 1986.

2. Nakayama, W. and A. E. Bergles, “Cooling electronic equipment: past, present and future”, in Heat Transfer in electronic and Microelectronic Equipment, A.E. Bergles ed. New York: Hemisphere, pp. 3-39, 1990.

3. Hannemann, R., L. R. Fox and M. Mahalingham, “Thermal design for microelectronic components”, in Cooling Techniques for Computers, W. Aung, ed. New York: Hemisphere, pp. 245-276, 1991.

4. Guyennet, M. M. and P. Lecocq, “Boiling coupled with air cooling”, in Cooling of Electronic Systems, S. Kakac, H. Yuncu, and K. Hijkata ed. MA Norwell,: Kluwer, pp.623-641, 1994.

5. Kraus, A.D. and A. Bar-cohen, “Thermal analysis and control of electronic equipment” McGraw-Hill, 1983.

6. Kiley, R. F. and C. A Soule, “Engineering heat sinks”, Powertechnics Magazine, July, 1990.

7. Soule, C. A., “Air and liquid cooled techniques for high power density components”, Power conversions and intelligent motion, Vol. 19, No.11, 1993.

8. Kadle, D.S. and E. M. Sparrow,.“Numerical and experimental study of turbulent heat transfer and fluid flow in longitudinal fin arrays", ASME Journal of Heat transfer, Vol. 108, pp.16-24, 1986.

9. Heng, S. and J. Pei, “Air impingement cooled pin-fin heat sink for multichip unit” Proc. National electronic packaging and production conference, Vol. 2, Des Plaines, IL, 1991.

10. Sathe, S. B., K. M. Kelkar, K. C. Karki, C. Tai, C. R. Lamb, and S. V. Patankar, “Numerical prediction of flow and heat transfer in an impingement heat sink”, ASME Journal of Electronic Packaging, Vol. 119, pp. 58-63, 1997.

11. Dunn, R. M., M. Schulman and N. Timko, “Electronic circuit module cooling”, United States Patent No. 4,277186, Aug. 13, 1981.

12. Sathe, S. B., B. G. Sammakia, A. C. Wong, and H. V. Mahaney, “A numerical study of a high performance air-cooled impingement heat sink”, Proc. National Heat Transfer Conference, Portland, OR, ASME-HTD, Vol. 303, pp.43-53, 1995.

13. Chu, R. C. and R. E. Simons, “Evolution of cooling technology in medium and large scale computers- an IBM perspective”, in Heat Transfer in electronic and Microelectronic Equipment, A. E. Bergles, ed. New York: Hemisphere, pp. 41-60, 1990.

14. Antonetti, V. W., R. E. Simons, and G. R. Arent, “Cooling a hot computer”, Electro Mechanical Design, pp. 34-37, Sept. 1973.

15. Chu, R. C., U. P. Hwang and R. E. Simons,.“Conduction cooling for an LSI package: A one-dimensional approach”, IBM Journal of Research and Development, vol.26, pp.45-54, 1982.

16. Mouromtseff, I. E. and H. N. Kozanowski, “Comparative analysis of water-cooled tubes as class B audio amplifiers”, Proc. IRE, vol.23, pp. 1224-1251, 1935.

17. Chu, R. C., O. R Gupta, U. P. Hwang, , K P. Moran and R. E. Simons “Cooling system for data processing equipment”, US patent 3586101, 1971.

18. Simons, R.E., “The evolution of IBM high performance cooling technology”, IEEE Trans. Comp., Packaging, and Manufacturing Technology-Part A , Vol. 18, No. 4, pp. 805-811, December, 1995.

19. Xie, H., M. Aghazadeh, W. Lui, and K. Haley, “Thermal solutions to Pentium processors in TCP in notebooks and sub-notebooks”, IEEE Trans. Comp., Packaging, and Manufacturing Technology-Part A, Vol. 19, No. 1, pp. 54-65, March, 1996.

10 ULTRASONIC ACOUSTIC STREAMING COOLING EFFECT

Qun Wan
Ph.D. Student
Andrey V. Kuznetsov
Assistant Professor
Dept. Mechanical and Aerospace Engineering

The cooling effect of ultrasonic acoustic streaming of the air between two plates is being modeled. One plate is the fixed heat source from a chip on IC board, for example, and the other is a vibrating PZT plate with a frequency in the ultrasonic range. The fluid flow and energy equations are written in terms of perturbations on top of the harmonic solution. The first order (linear function of the perturbation term) equations have been solved and the results are shown. This solution will be used as a driving force term in the solution of the higher order equations. The cooling effect associated with steady acoustic streaming regime, the emphasis of this project, appears in the second order terms.

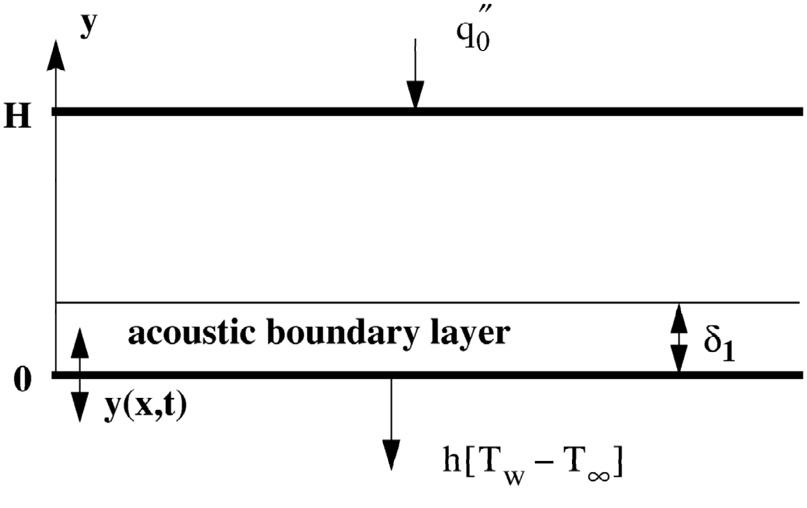

10.1 INTRODUCTION

The heat dissipation from an integrated circuit (IC) board becomes more and more important when the density of the IC components on the board increases rapidly. Various kind of cooling method has been invented and applied, such as heat sinks, fans etc. In this project, a novel cooling concept, ultrasonic acoustic streaming cooling, will be studied. This concept takes advantage of the unique micro-scale and high frequency properties of the fluid media. The problem will be modeled in a rectangular domain with proper boundary conditions and fluid mechanics equation will be used to compute the flow pattern and temperature distributions.

10.2 DETAILS OF THE PROJECT

This project concerns the cooling effect of a vibrating PZT at ultrasonic frequency over a heat source (generated from electric chips for example). Figure 1 shows the geometry:

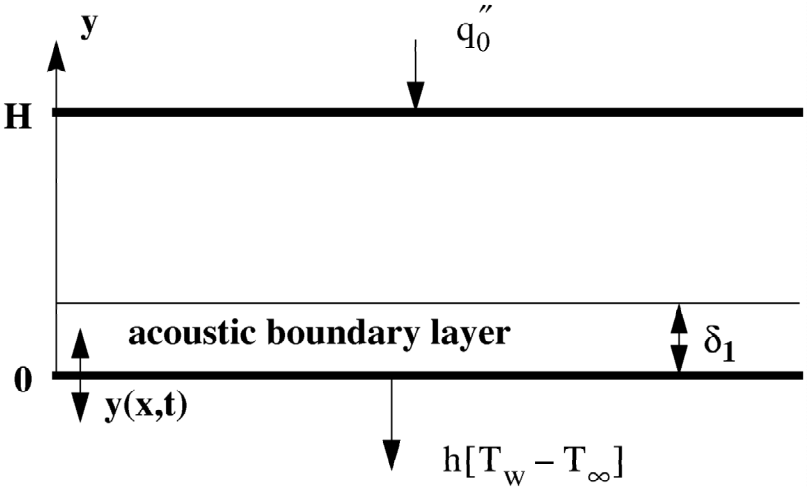

Figure 1. A Schematic Diagram for the Heat Transfer Analysis.

According to existing theory, some steady acoustic streaming is expected to form between two plates despite the harmonic oscillation of the PZT, which has zero displacement over one period. It is this steady acoustic streaming that carries away the heat from the heat source to two open ends. The magnitude of the acoustic streaming may depend on the system configuration, vibration parameters and others. Ultrasonic waves are thought to generate much greater acoustic streaming and hence have significant cooling effects. From the results of a similar system by Loh [1], the gap between two plates is in the range of 0.1~2mm. This property enables effective cooling in the compact environments such as a laptop computer.

10.2.1 THEORETICAL BACKGROUND

The theories of acoustic streaming are given by Bradley [2] and Nyborg [3]. Zhao et al [4] compared two theories and noted that Bradley and Nyborg derived the theories in a similar way. However, the difference is that Nyborg dealt with rectilinear fluid motion while Bradley extended the theory to non-rectilinear cases. Hence Bradley's theory will be used with a vibrating surface.

Bradley considered the conservation equations of mass, momentum, and entropy of compressible fluid with harmonically displace boundary. He further applied perturbation expansion of pressure, density, and velocity using a small parameter

$$\varepsilon = u_0 / c_0 \tag{1}$$

where u_0 is the characteristic acoustic particle velocity and c_0 is the small-signal sound speed. Expressions for velocity ($\mathbf{u}$), pressure (p) and density (ρ) can be written as

$$\begin{aligned} \mathbf{u} &= \mathbf{u}_0 + \varepsilon \mathbf{u}_1 + \varepsilon^2 (\mathbf{u}_{dc} + \mathbf{u}_2) + O(\varepsilon^3) \\ p &= p_0 + \varepsilon p_1 + \varepsilon^2 (p_{dc} + p_2) + O(\varepsilon^3) \\ \rho &= \rho_0 + \varepsilon \rho_1 + \varepsilon^2 (\rho_{dc} + \rho_2) + O(\varepsilon^3) \\ \varepsilon &= u_0 / c_0 , u_0 = f(\omega, A) \end{aligned} \tag{2}$$

with B.C.

$$\begin{aligned} &\frac{\partial}{\partial t}\mathbf{d}(\mathbf{r}_0, t) = \mathbf{u}(\mathbf{r}, t)\big|_{\mathbf{r}=\mathbf{r}_0+\mathbf{d}(\mathbf{r}_0,t)} \\ &= \mathbf{u}(\mathbf{r}, t)\big|_{\mathbf{r}=\mathbf{r}_0} + \mathbf{d}(\mathbf{r}_0, t) \cdot \nabla \mathbf{u}(\mathbf{r}, t)\big|_{\mathbf{r}=\mathbf{r}_0} + O(\varepsilon^3) \end{aligned} \tag{3}$$

The variables with subscript 'dc' are the acoustic streaming variables, which are non-harmonic. All others are harmonic. Digital subscripts denote the ranks of order of the variables. The high order solution is based on the low order results. Hence the first order equations must be solved since the zero order results are trivial in this case.

The equation for first order variables in Eqn (2) is given as below:

$$\begin{aligned} &\nabla\nabla \cdot \mathbf{u}_1 + \frac{\mu}{\rho_0 c_0^{\ 2}} \nabla^2 \frac{\partial \mathbf{u}_1}{\partial t} + \frac{\mu_B + \mu/3}{\rho_0 c_0^{\ 2}} \nabla\nabla \cdot \frac{\partial \mathbf{u}_1}{\partial t} - \frac{1}{c_0^{\ 2}} \frac{\partial^2 \mathbf{u}_1}{\partial t^2} = 0 \\ &\frac{\partial \rho_1}{\partial t} + \rho_0 \nabla \cdot \mathbf{u}_1 = 0 \\ &p_1 = c_0^{\ 2} \rho_1 \end{aligned} \tag{4}$$

with B.C.

$$\mathbf{u}_1(\mathbf{r}, t)\big|_{\mathbf{r}=\mathbf{r}_0} = \mathbf{u}(\mathbf{r}, t)\big|_{\mathbf{r}=\mathbf{r}_0} \tag{5}$$

Hence the acoustic stream equations can be written as:

$$\rho_0 \nabla \cdot \mathbf{u}_{dc} = \dot{m} \tag{6}$$

$$-\mu \nabla^2 \mathbf{u}_{dc} - \left(\mu_B + \mu/3\right)\nabla\nabla \cdot \mathbf{u}_{dc} + \nabla p_{dc} = \mathbf{f}_b \tag{7}$$

with B.C.

$$\mathbf{u}_{dc}\left(\mathbf{r},t\right)\Big|_{\mathbf{r}=\mathbf{r}_0} = \left\langle \left(\mathbf{d} \cdot \nabla\right)\mathbf{u}_1\left(\mathbf{r},t\right)\right\rangle\Big|_{\mathbf{r}=\mathbf{r}_0} \tag{8}$$

where < > denotes time-average over one period and

$$\dot{m} = -\frac{1}{{c_0}^2}\nabla \cdot \left\langle \mathbf{I} \right\rangle, \ \mathbf{I} = p_1 \mathbf{u}_1 \tag{9}$$

$$\mathbf{f}_b = -\frac{1}{{c_0}^2}\left\langle p_1 \frac{\partial \mathbf{u}_1}{\partial t}\right\rangle - \rho_0 \left\langle \left(\mathbf{u}_1 \cdot \nabla\right)\mathbf{u}_1 \right\rangle \tag{10}$$

To apply the above theory to this project, assume the gap between two plates is H in width and the length of the plates is L. The harmonic displacement at the vibrating boundary is

$$\mathbf{d}_1\left(t,x,0\right) = \mathbf{j}\sin\omega t \sin kx \ , \tag{11}$$

and the velocity at the boundary is

$$\begin{aligned} \mathbf{u}_1\left(t,x,0\right) &= \mathbf{j}\omega A \cos\omega t \sin kx \\ \mathbf{u}_1\left(t,x,H\right) &= 0 \end{aligned} \ . \tag{12}$$

The gradient for the 2D velocity components $\mathbf{u}_1\left(t,x,y\right) = \left(u\left(t,x,y\right), v\left(t,x,y\right)\right)$ at both left and right exits are zero.

$$\left.\frac{\partial u}{\partial x}\right|_{x=0} = \left.\frac{\partial v}{\partial x}\right|_{x=0} = 0, \left.\frac{\partial u}{\partial x}\right|_{x=L} = \left.\frac{\partial y}{\partial x}\right|_{x=L} = 0 \tag{13}$$

The first order variables in the complex number form are:

$$\begin{aligned} u\left(t,x,y\right) &= \hat{u}\left(x,y\right)\exp\left(i\omega t\right) \\ v\left(t,x,y\right) &= \hat{v}\left(x,y\right)\exp\left(i\omega t\right) \\ p\left(t,x,y\right) &= \hat{p}\left(x,y\right)\exp\left(i\omega t\right) \end{aligned} \tag{14}$$

The new variables indicate the amplitude and phase difference from the vibration at the boundary as well. The first order equations (4) in the form of new variables are

$$\begin{aligned} &\left[1 + i\omega\left(A_\mu + B_\mu\right)\right]\frac{\partial^2 \hat{u}}{\partial x^2} + i\omega A_\mu \frac{\partial^2 \hat{u}}{\partial y^2} + \left[1 + i\omega B_\mu\right]\frac{\partial^2 \hat{v}}{\partial xy} + \frac{\omega^2}{{c_0}^2}\hat{u} = 0 \\ &i\omega A_\mu \frac{\partial^2 \hat{v}}{\partial y^2} + \left[1 + i\omega\left(A_\mu + B_\mu\right)\right]\frac{\partial^2 \hat{v}}{\partial x^2} + \left[1 + i\omega B_\mu\right]\frac{\partial^2 \hat{u}}{\partial xy} + \frac{\omega^2}{{c_0}^2}\hat{v} = 0 \end{aligned} \tag{15}$$

$$\hat{p} = i\frac{{c_0}^2 \rho_0}{\omega}\left(\frac{\partial \hat{u}}{\partial x} + \frac{\partial \hat{v}}{\partial y}\right) \tag{16}$$

with B.C.

$$\begin{aligned} &\hat{u}(x,0) = 0, \hat{v}(x,0) = \omega A \sin kx \\ &\hat{u}(x,H) = 0, \hat{v}(x,H) = 0 \end{aligned} \tag{17}$$

$$\left.\frac{\partial \hat{u}}{\partial x}\right|_{x=0} = \left.\frac{\partial \hat{v}}{\partial x}\right|_{x=0} = 0, \left.\frac{\partial \hat{u}}{\partial x}\right|_{x=L} = \left.\frac{\partial \hat{v}}{\partial x}\right|_{x=L} = 0 \tag{18}$$

where

$$\begin{aligned} A_\mu &= \frac{\mu}{\rho_0 {c_0}^2} \\ B_\mu &= \frac{\mu_B + \mu/3}{\rho_0 {c_0}^2} \end{aligned} \tag{19}$$

Some of the terms in the acoustic streaming equations can also be expressed in the form of new variables:

$$\begin{aligned} \dot{m} &= -\frac{1}{{c_0}^2} \nabla \cdot \langle \mathbf{I} \rangle \\ &= -\frac{1}{2{c_0}^2} \left[\frac{\partial \operatorname{Re}\left(\bar{\hat{p}} \hat{u}\right)}{\partial x} + \frac{\partial \operatorname{Re}\left(\bar{\hat{p}} \hat{v}\right)}{\partial y} \right] \end{aligned} \tag{20}$$

$$\begin{aligned} \mathbf{f}_b &= -\frac{1}{{c_0}^2} \left\langle p_1 \frac{\partial \mathbf{u}_1}{\partial t} \right\rangle - \rho_0 \langle (\mathbf{u}_1 \cdot \nabla) \mathbf{u}_1 \rangle \\ &= -\frac{1}{2} \left[\begin{aligned} &\mathbf{i} \left(\frac{\omega}{{c_0}^2} \operatorname{Re}\left(i \bar{\hat{p}} \hat{u}\right) + \rho_0 \operatorname{Re}\left(\left(\bar{\hat{u}} \frac{\partial}{\partial x} + \bar{\hat{v}} \frac{\partial}{\partial y} \right) \hat{u} \right) \right) \\ &+ \mathbf{j} \left(\frac{\omega}{{c_0}^2} \operatorname{Re}\left(i \bar{\hat{p}} \hat{v}\right) + \rho_0 \operatorname{Re}\left(\left(\bar{\hat{u}} \frac{\partial}{\partial x} + \bar{\hat{v}} \frac{\partial}{\partial y} \right) \hat{v} \right) \right) \end{aligned} \right] \end{aligned} \tag{21}$$

$$\left.\langle (\mathbf{d} \cdot \nabla) \mathbf{u}_1 (\mathbf{r}, t) \rangle\right|_{\mathbf{r}=\mathbf{r}_0} = \frac{1}{2} A \sin kx \left[i \frac{\partial}{\partial y} \operatorname{Re}(i\hat{u}) + j \frac{\partial}{\partial y} \operatorname{Re}(i\hat{v}) \right] \tag{22}$$

10.2.2 NUMERICAL RESULTS

The acoustic streaming equations can be solved by numerical methods. A second order central difference scheme of the finite difference method was employed. The simulation method is tested at low frequency (ω=1000). The following graphs (Figure 2~12) show the flow pattern of the first order velocity $\mathbf{u}_1$ at different stages in one period. The fluid is air in standard state. Figure 2, 7, 12 show the flow patterns when the bottom boundary velocity reaches its maximum.

From the set of graphs, the velocity pattern at the end of one period is exactly the same as the one at the beginning. The phase difference between most points within the flow field and the vibrating boundary at the bottom is very small. This may be due to the small viscosity of air and the low frequency studied.

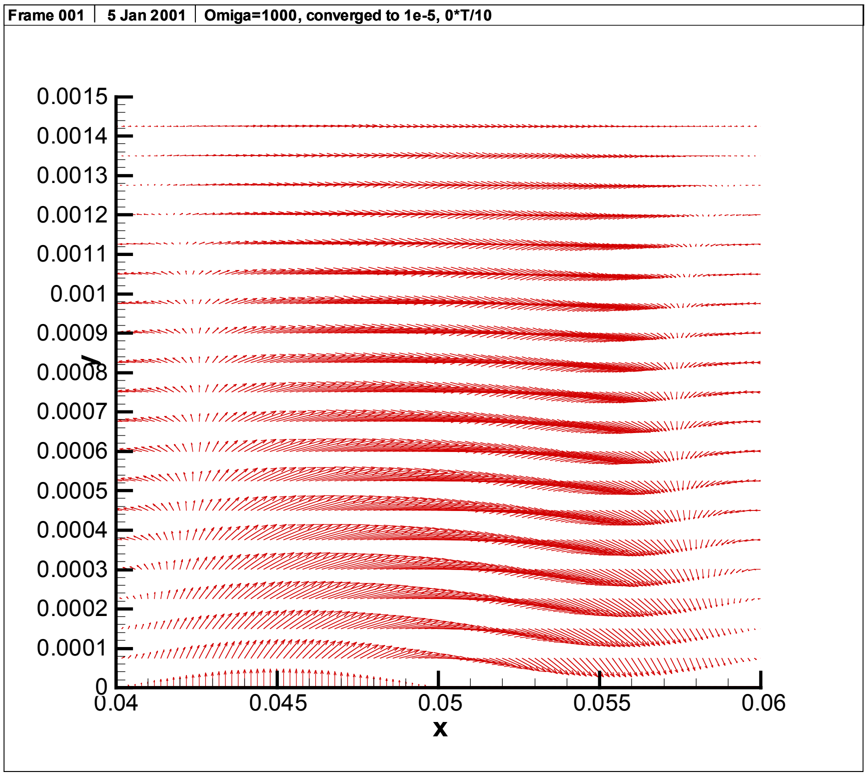

Figure 2. Flow Velocity Vector at t=0 (bottom sinusoidal vibration at ω=1000, air)

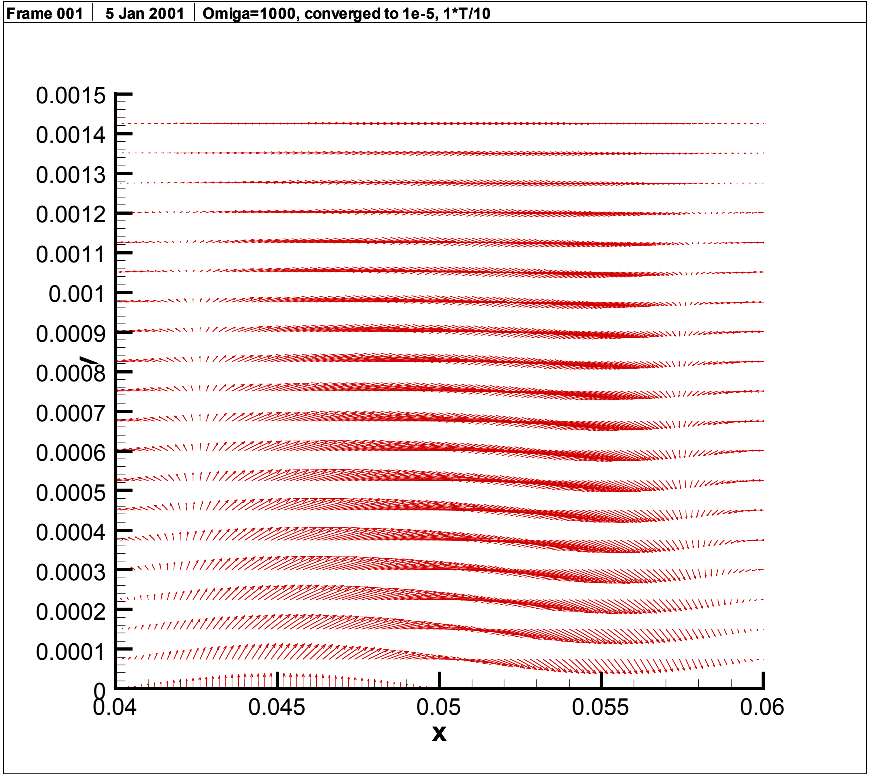

Figure 3. Flow Velocity Vector at t=0.1T (bottom sinusoidal vibration at ω=1000, air)

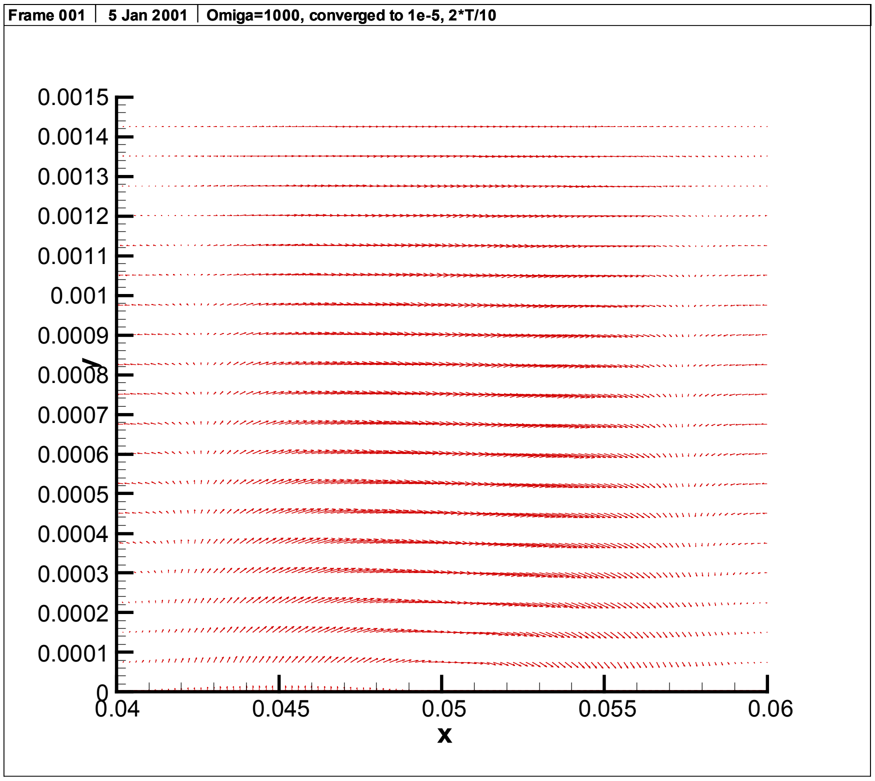

Figure 4. Flow Velocity Vector at t=0.2T (bottom sinusoidal vibration at ω=1000, air)

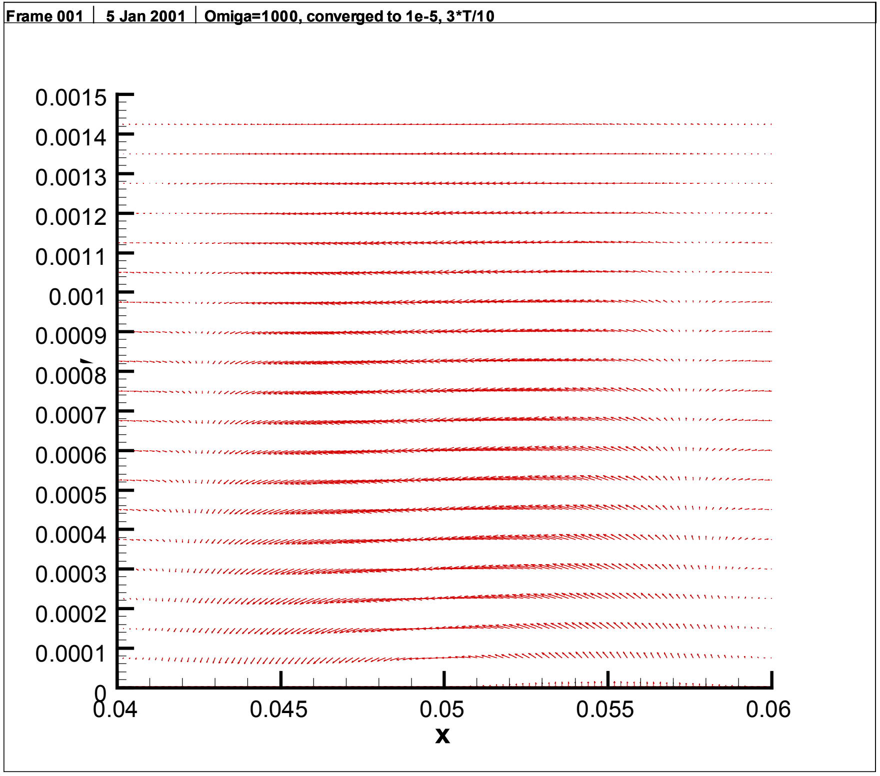

Figure 5. Flow Velocity Vector at t= 0.3T (bottom sinusoidal vibration at ω=1000, air)

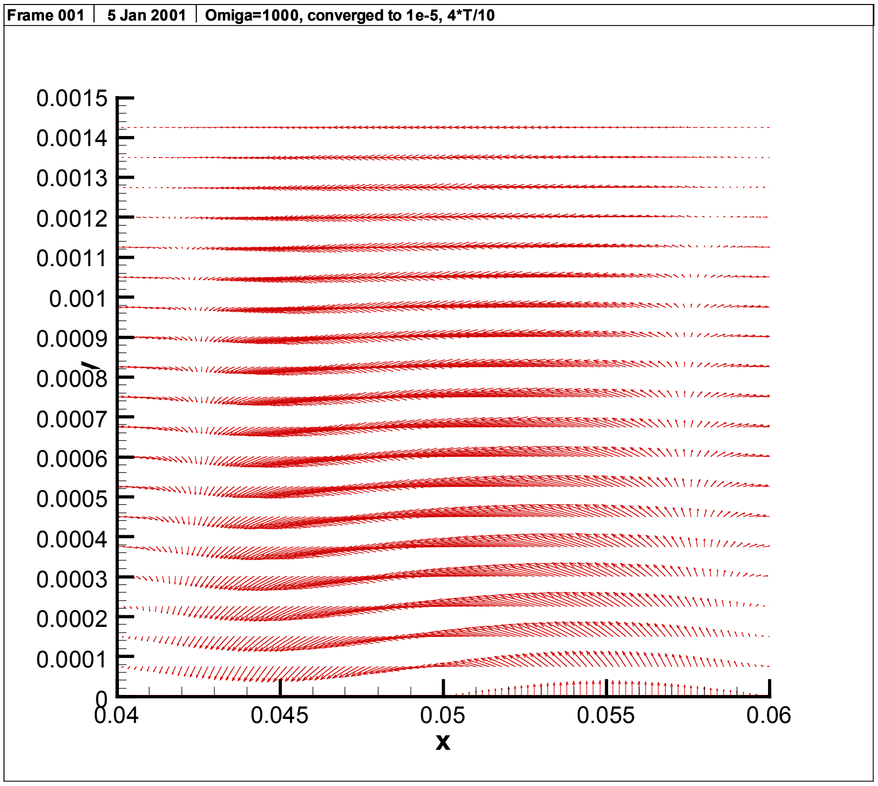

Figure 6. Flow Velocity Vector at t=0.4T (bottom sinusoidal vibration at ω=1000, air)

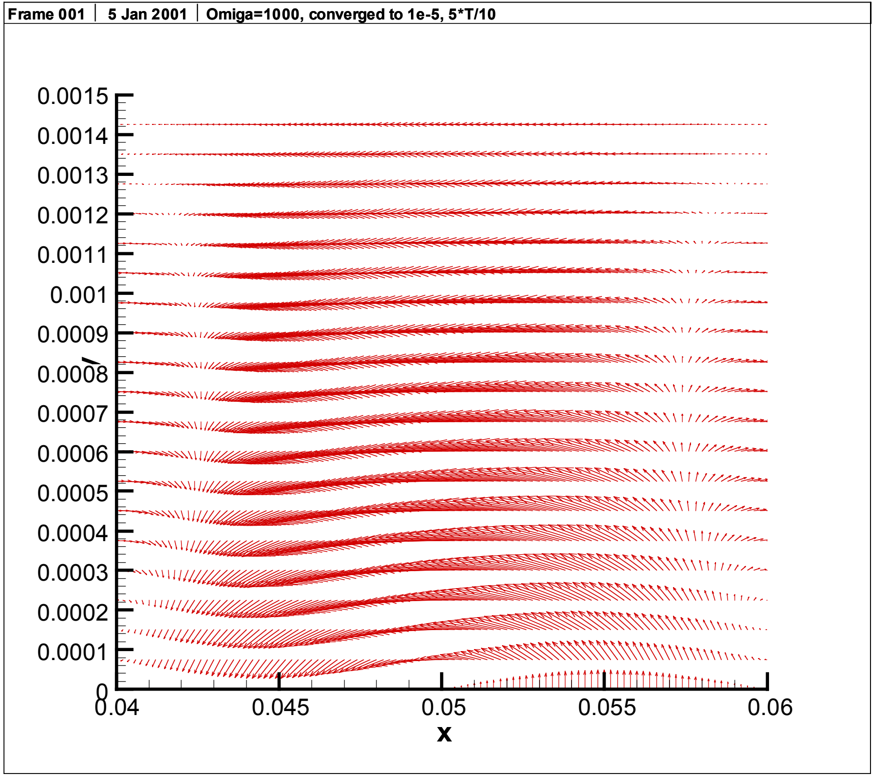

Figure 7. Flow Velocity Vector at t= 0.5T (bottom sinusoidal vibration at ω=1000, air)

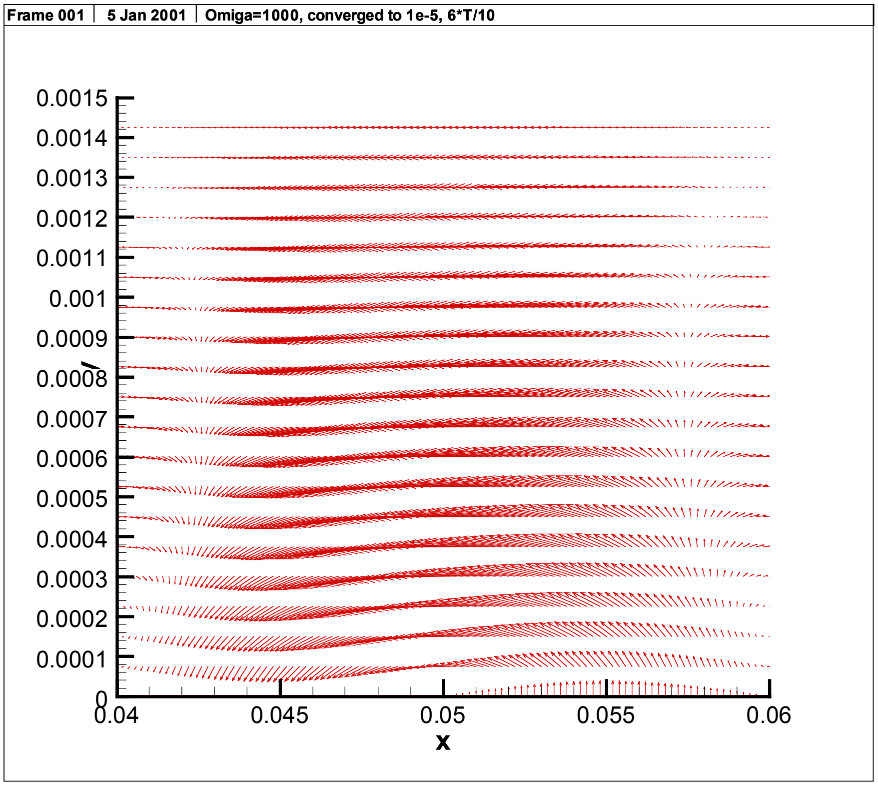

Figure 8. Flow Velocity Vector at t=0.6T (bottom sinusoidal vibration at ω=1000, air)

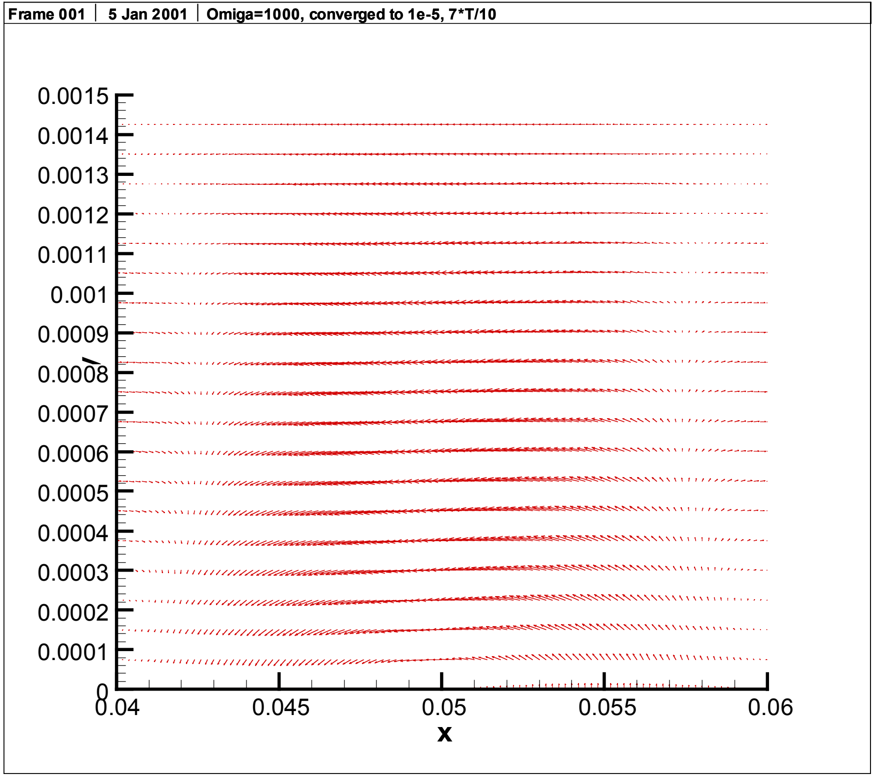

Figure 9. Flow Velocity Vector at t=0.7T (bottom sinusoidal vibration at ω=1000, air)

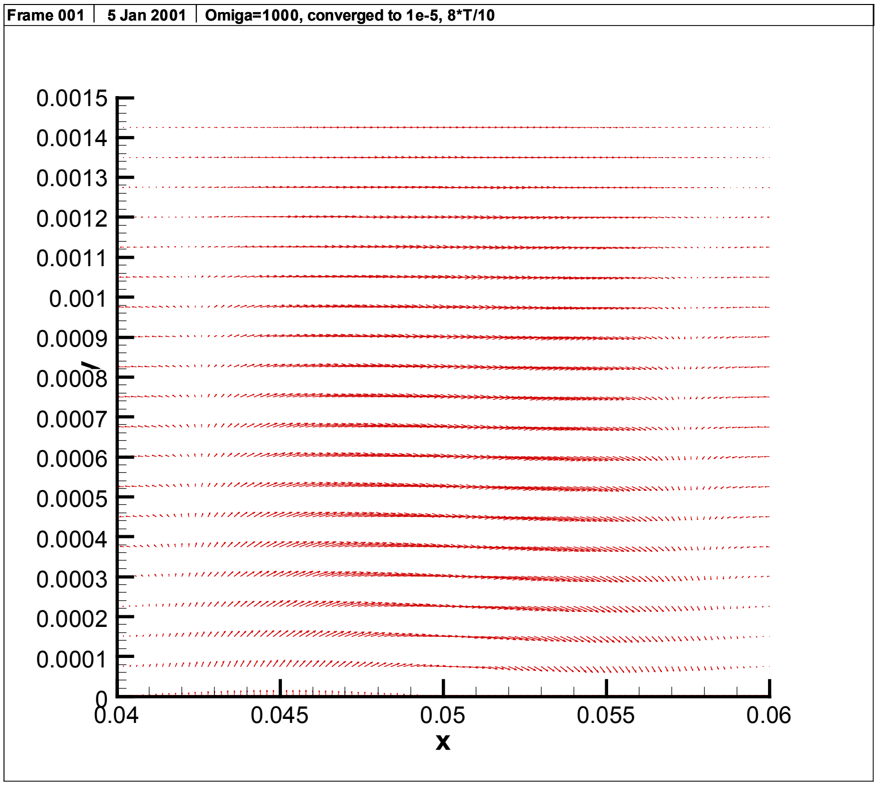

Figure 10. Flow Velocity Vector at t=0.8T (bottom sinusoidal vibration at ω=1000, air)

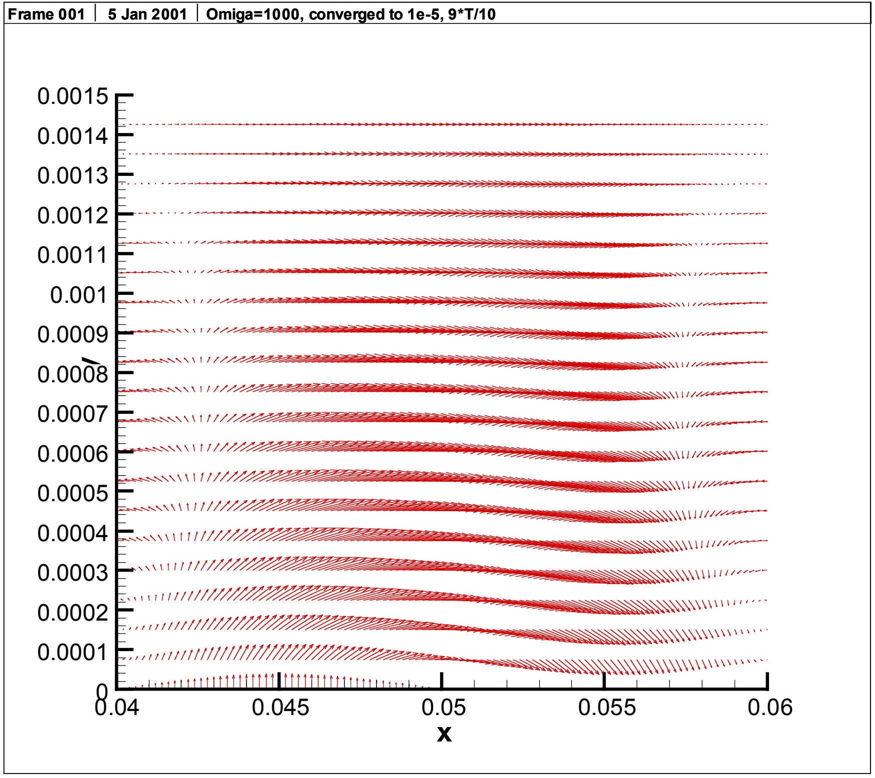

Figure 11. Flow Velocity Vector at t= 0.9T (bottom sinusoidal vibration at ω=1000, air)

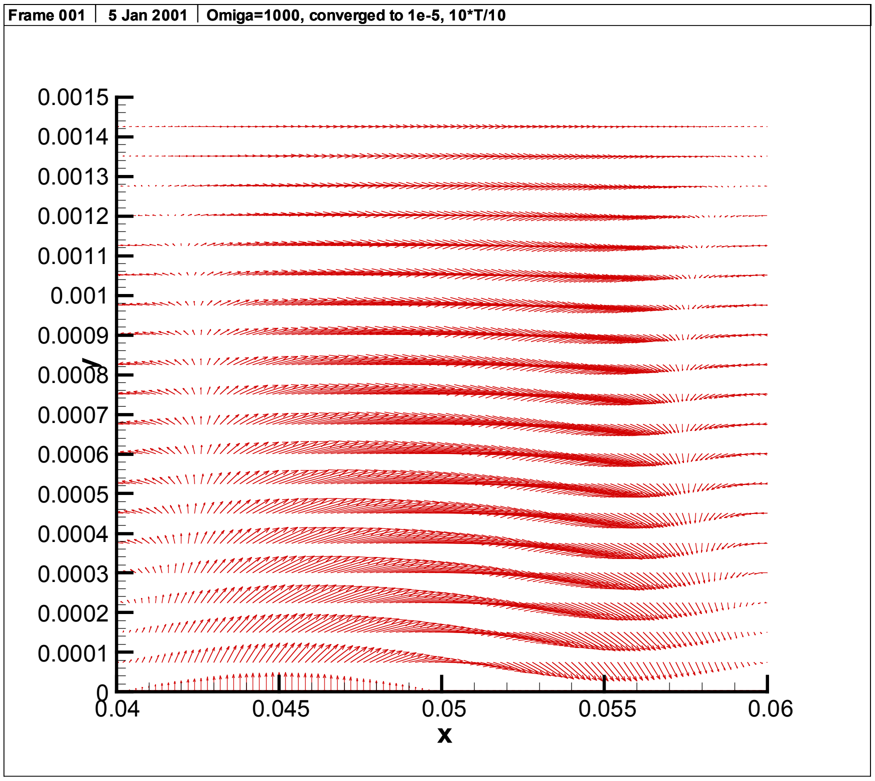

Figure 12. Flow Velocity Vector at t=T (bottom sinusoidal vibration at ω=1000, air)

10.3 FUTURE WORK

The first order equations will be solved for high frequency and the new variables defined in Eqn (20)-(22) will be evaluated. This information will define the acoustic streaming flow fluid. Based on the flow, the thermal problem can be solved to find the cooling effect.

REFERENCES

1. Loh, Byoung-Gook, "Industrial applications of ultrasonic flexural waves: Object transport and cooling of microelectronic components", Ph.D. dissertation, North Carolina State University, 2000

2. Bradley, C. E., "Acoustic streaming field structure: The influence of radiator" J. Acoust. Soc. Am. 100, 1399-1408, 1996.

3. Nyborg, W. L., in Physical Acoustics, edited by W. P. Mason (Academic, Ney York,), Vol 2B, pp. 265-331, 1965.

4. Zhao, Xiaoliang; Zhu, Zhemin; Du Gonghuan, A Note about acoustic streaming: Comparison of C. E. Bradley's and W. L. Nyborg's theories, J. Acoust. Soc. Am. 104 (2), Pt. 1, August 1998.

11 ACOUSTIC STREAMING INDUCED BY ULTRASONIC FLEXURAL VIBRATIONS AND ASSOCIATED ENHANCEMENT OF CONVECTIVE HEAT TRANSFER

Byoung G. Loh
Graduate Student
Paul I. Ro
Associate Professor
Mechanical and Aerospace Engineering

Acoustic streaming induced by ultrasonic flexural vibrations and associated enhancement of convective heat transfer are investigated. Two distinctive acoustic streaming patterns in half-wavelength of the flexural vibrations are observed, which agrees well with the theory. However, acoustic streaming velocity observed from computational fluid dynamics (CFD) simulation exceeds the theoretically estimated velocity by a factor ranging from 10 to 100, depending upon the location along the beam. Both CFD simulation and analytical analysis reveal that the acoustic streaming velocity is proportional to the square of the vibration amplitude and the wavelength of the vibrating beam that decreases with the excitation frequency. It is observed that the streaming velocity decreases with the excitation frequency. Also, with an open-ended channel, a substantial increase in streaming velocity is observed from CFD simulation

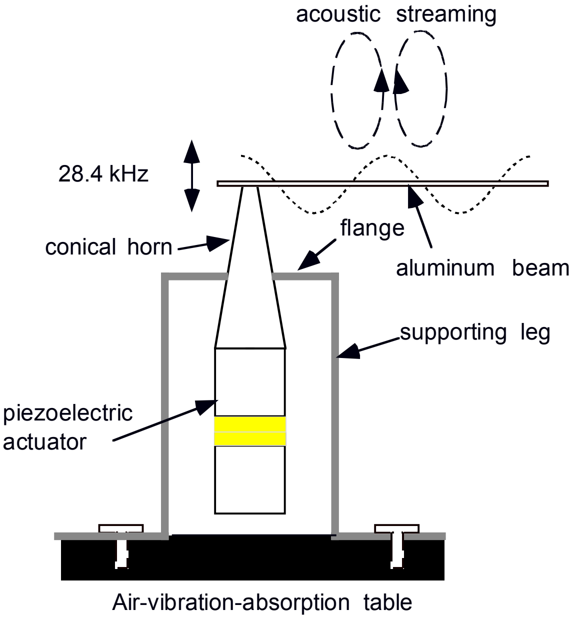

11.1 INTRODUCTION

Acoustic streaming is a steady circular airflow occurring in a high intensity sound field. Two factors have been known to induce acoustic streaming; spatial attenuation of a wave in free space and the friction between a medium and a vibrating object [1]. When sound waves propagate they are attenuated by absorption and scattered. This attenuation is in general insignificant in a short distance of propagation. However, the propagation of a high intensity sound wave results in the attenuation of pressure significant enough create a steady bulk airflow. This type of streaming is usually associated with a medium of high viscosity. The other type of acoustic streaming is attributed to the friction between a medium and a solid wall when the former is vibrating in contact with the latter or vice versa [2]. As long as there is an oscillating tangential velocity it is not important whether the source of the relative motion arises from either acoustic oscillations in the fluid or vibrations of the solid. Both cases lead to frictional dissipation within Stokes boundary layer. Unlike acoustic streaming resulting from spatial attenuation, this streaming has two components; inner and outer streaming. The inner streaming is created within the boundary layer due to the friction between the medium and the wall. Then, the inner streaming also induces relatively large scale steady streaming outside the boundary layer. This process can be compared to the generation of electromagnetic field by a surface current on a conductor [1]. It is reported that the acoustic streaming is especially effective in promoting certain kinds of rate process occurring on the solid and fluid interface including convective heat transfer, electrical effects, changes in biological cells, and removal of loosely adhering surface layers [2].

In [3], Faraday found currents of air to rise at displacement anti-nodes on plates, and to descend at the nodes. The first theoretical analysis of acoustic streaming phenomenon was performed by Rayleigh [4]. Further development of the theory was made by Schlichting, Nyborg, and Lighthill where emphasis was placed on the fundamental role of dissipation of the acoustic energy in the evolution of the gradients in the momentum flux [5,6]. In the study of Jackson & Nyborg, acoustic streaming induced by sonic longitudinal vibration is investigated [7]. Acoustic streaming induced by ultrasonic flexural traveling waves is studied for a micropump application and negligible heat transfer capability of acoustic streaming is reported [8]. Gould studied heat transfer across a solid-liquid interface in the presence of sonically induced acoustic streaming [9]. Gopinath & Mills investigated convective heat transfer due to acoustic streaming across the ends of a Kundt Tube [10,11]. Selected references gives an overview of the works done for investigating the heat transfer characteristics of acoustic streaming [12-14].

Most of previous studies concentrate on acoustic streaming induced by sonic longitudinal vibration in an enclosed space such as Kundt Tube. Not much research on acoustic streaming induced in an open space by ultrasonic flexural vibration has been carried out. Ultrasonic excitation significantly increases acoustic streaming velocity. As a result, convective heat transfer rates can grow to that of conventional fan-based cooling fans can offer. In addition, ultrasonic excitation permits silent operation. Employing flexural vibrations as a source of acoustic streaming allows for slim profile and low power operation because flexural impedance of an elastic beam is generally far smaller than longitudinal impedance. These merits make ultrasonically induced acoustic streaming an alternative to conventional convective cooling using a motor-driven fan. To take full advantage of this promising technology, it is imperative to understand the nature of formation of acoustic streaming, the transient characteristics, streaming velocity, and associated enhancement of convective heat transfer.

The objective of this work is to investigate the steady momentum and heat transfer due to outer acoustic streaming induced by ultrasonic flexural vibrations in an open environment. Primary focus is placed on experimental observation of the phenomenon, simulation employing computational fluid dynamics software (CFX) and comparison with the existing analytical solution by Nyborg (1958).

11.2 EXPERIMENTAL OBSERVATIONS

11.2.1. EXPERIMENTAL APPARATUS

The experimental setup shown in Figure 1 consists of a beam and modules that contain a piezoelectric actuator and a horn. The beam and horn are made of 6061-T6 aluminum because of the excellent acoustical characteristics of this material. The piezoelectric actuator is a bolted Langevin type transducer (BLT) designed to resonate at 28 kHz [15]. The conical horn is used to increase the amplitude of vibration provided by the actuator. A conical geometry was chosen because it not only gives a desired amplification ratio but also can be easily machined. A mounting flange was included in the design of the horn and is located at the nodal lines where the velocity of vibration of the horn goes to zero. This allowed the mounting of the horn and BLT assembly onto a supporting base plate that was in turn bolted to the surface of an air-driven vibration absorption table. The small end of the horn was threaded to connect the beam with the horn using a machine screw. The dimension of the beam is determined such that one of the natural frequency of the beam is located in the vicinity of the resonant frequency of the actuator, thereby maximizing the displacement of the beam for a given power supply. The determined dimension is 10 mm wide, 1 mm thick and 128 mm long. Frequency spectrum analysis of the system reveals that at an excitation frequency of 28.4 kHz, maximum vibration amplitude of the beam is achieved.

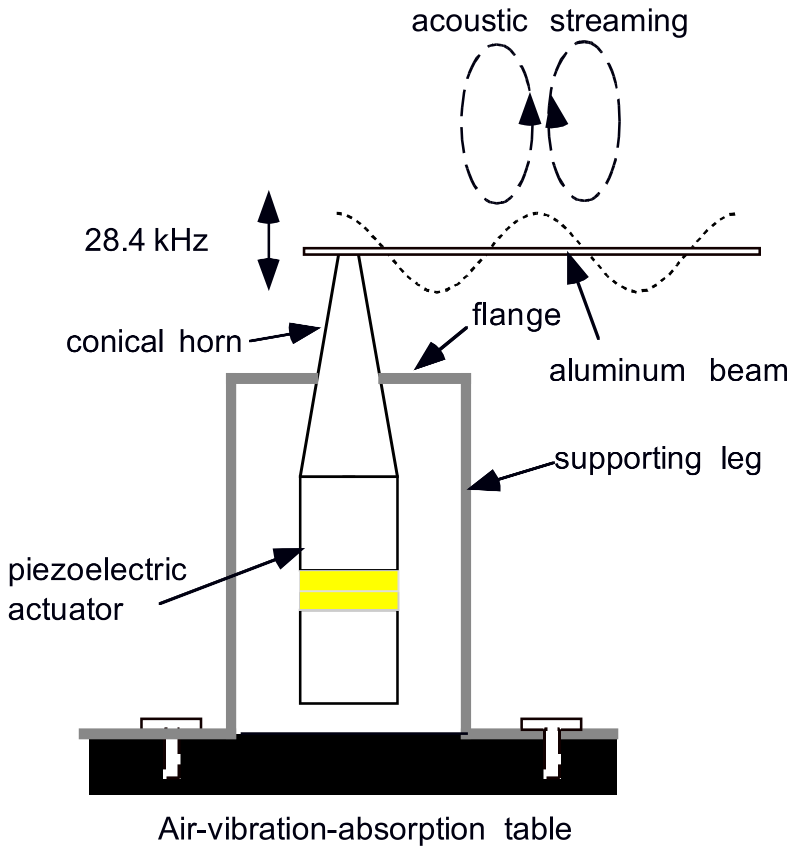

Figure 1. Experimental Setup

11.2.2 ACOUSTIC STREAMING NEAR THE VIBRATING BEAM

To visualize acoustic streaming near the beam, the beam is excited at 28.4 kHz with a vibration amplitude of 10 µm. Acetone is sprayed onto the vibrating beam. When Acetone comes in contact with the beam it becomes small droplets and follows airflow pattern near the beam until it completely evaporates. A fiber optic lamp locally illuminates the region near the vibrating beam. Light is reflected from only Acetone droplets and the beam, making ambient air appear black. The whole process is videotaped using a camcorder. Figure 2 shows a snapshot of the process and the unique features of acoustic streaming. First, air rises above the anti-nodes and descends toward the nodes. Since vibration amplitude is not uniform along the length of the beam, the maximum distance to which Acetone droplets rise above the anti-nodes are not uniform either. Second, there exist two distinctive circular airflows within each half wavelength, 1 cm for this case. Clearer acoustic streaming is observed with bigger vibration amplitude.

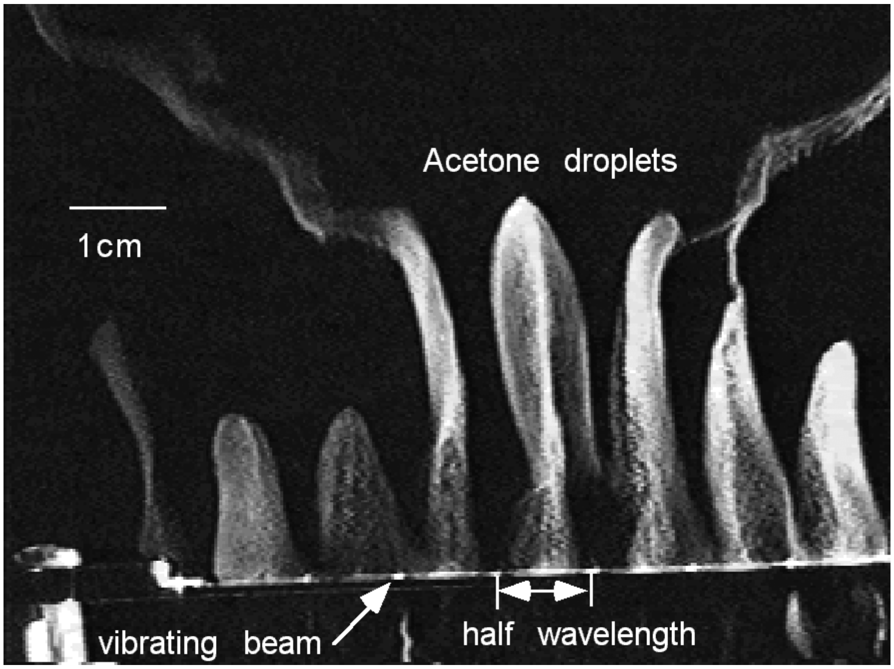

Figure 2. Acoustic Streaming over a Ultrasonically Vibrating Beam

11.2.3 STREAMING IN THE GAP

Primary application of acoustic streaming would be enhancement of convective heat transfer. To this end, it is possible to envision that a heated object is placed over a vibrating beam near which acoustic streaming is induced. Then, the temperature of the heated object will decrease due to forced convection caused by acoustic streaming. Therefore, for heat transfer application, it is more important to study how acoustic streaming pattern changes when there is a stationary upper beam. Specifically, the acoustic streaming velocity is a primary interest because convective heat transfer is proportional to the acoustic streaming velocity.

An aluminum beam that is 1 cm wide, 2.5 cm thick, and 11 cm long is placed 1 cm over the vibrating beam. The same visualization process used for the case without an upper stationary beam is performed at the gaps ranging from 2 mm to 1 cm. It is observed that acoustic streaming in the gap is strong enough to blow most of Acetone droplets out of the gap, making it almost impossible to perform visual observation of acoustic streaming pattern. Therefore, CFD simulation presented in Section 11.4 is used to estimate acoustic streaming pattern and velocity in the gap.

11.2.4 ENHANCEMENT OF CONVECTIVE HEAT TRANSFER

To measure the enhancement of convective heat transfer due to acoustic streaming, a heat source containing an aluminum plate, a resistor, and a thermocouple is made. The bottom of the plate is made of aluminum. The top is made of Plexiglas that contains a 600 Ω resistor and a thermocouple. The resistor is connected to a variable voltage power supply and serves as a heater. With the 600 Ω resistor, the temperature of the plate can be increased to 98 °C. During the experiment, the room temperature was kept at 20 °C. The heat source is placed 1.5 mm above the vibrating beam. As the temperature of heat source reaches a steady state value of 98 °C with a power supply of 3.4 Watt, acoustic streaming is generated by vibrating the beam at 28.4 kHz with a vibration amplitude of 10 μm. Then, the temperature changes of the plate are measured using the thermocouple. Due to the inherent noises in the voltage signal from the thermocouple, the signal is filtered through a low pass filter and sampled at 20 Hz using a data acquisition board. A temperature drop of 30 °C is achieved in 4 minutes and maintained as shown in Figure 3. As the vibration amplitude is further increased to 25 μm, a temperature drop of 40 °C is achieved and this value is the maximum temperature drop obtained.

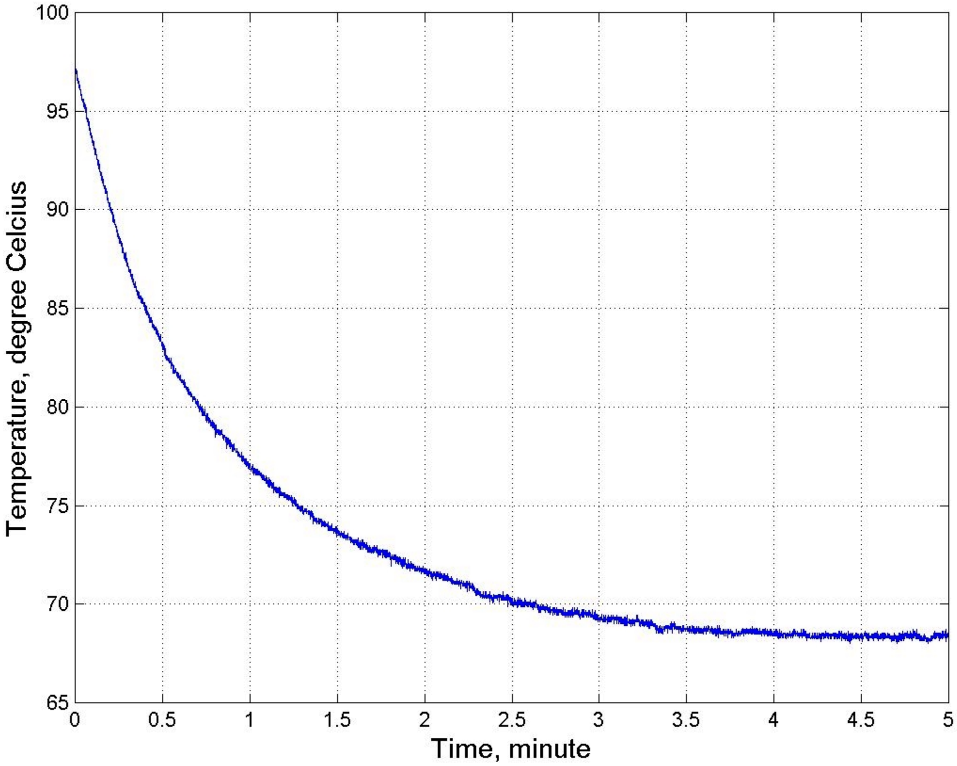

Figure 3. Measurement of Temperature Drop of Heat Source

11.3 THEORY

Nyborg (1958) formulated the equation for near boundary acoustic streaming using successive approximation method as

$$\mu\nabla^2 u_2 - \nabla P_2 + F = 0 \tag{1}$$

$$F \equiv -\rho_o < (u_1 \cdot \nabla)u_1 + u_1(\nabla \cdot u_1) > \tag{2}$$

where μ is kinematic viscosity, ρ_0 is constant equilibrium density, u_1 is oscillatory particle velocity, u_2 is acoustic streaming velocity, P_2 is a steady state "dc" pressure, F is nonlinear driving forcing term, and < > means a time average over a large number of cycles. Without averaging, F contains a dc part and harmonically varying terms. The former induces acoustic streaming. When averaged over a relatively long period of time, the effect of harmonically varying forcing terms disappears and only the contributions from the dc part appear in the solution. The acoustic streaming velocity, u_2 approaches a constant value as the distance from the vibrating beam approaches infinity. This time-independent limiting velocity, U_L, is given by

$$U_L = -\frac{3}{4\omega}U_0(\frac{dU_0}{dx}) \tag{3}$$

where ω is excitation frequency, U_o, is amplitude of the irrotational velocity tangent to the boundary [16]. To calculate outer acoustic streaming motion, the limiting velocity, U_L is used as a slip velocity at the solid surface by assuming Stoke boundary layer thickness negligible [6].

The amplitude of the tangential irrotational velocity, U_o, is obtained from the normal irrotational velocity, V, imposing the zero-divergence condition assumed in the Nyborg's formulation. For a relatively small gap, the normal irrotational velocity is assumed to be

$$V = A\omega \cos k_b x \left(\frac{h-y}{h}\right) \sin\omega t = V_0 \sin\omega t \tag{4}$$

where A is the peak vibration amplitude of an elastic beam, k_b is the bending wave number of the beam defined as $2\pi/\lambda_b$ where λ_b is the wavelength of the beam, h is the gap between the vibrating beam and the stationary beam as shown in Figure 4. Equation 4 satisfies the boundary conditions that V at $y = 0$ is equal to the velocity of the vibrating beam and V at $y = h$ is zero. By making use of the zero-divergence condition, $\frac{\partial U_0}{\partial x} + \frac{\partial V_0}{\partial y} = 0$, the amplitude of the tangential velocity, U_0, is given by

$$U_0 = \frac{A\omega}{2\pi}\left(\frac{\lambda_b}{h}\right)\sin k_b x \tag{5}$$

Upon substitution of Equation 5 into Equation 3, U_L, can be rewritten as

$$U_L = -\frac{3}{8} f\lambda_b \left(\frac{A}{h}\right)^2 \sin 2k_b x \tag{6}$$

where f is excitation frequency in Hertz Note that, in Equation 6, any explicit dependence of acoustic streaming velocity on μ disappears although it originates from the viscosity and that acoustic streaming velocity is a function of the wavelength of the beam and the gap in addition to the excitation frequency and the vibration amplitude.

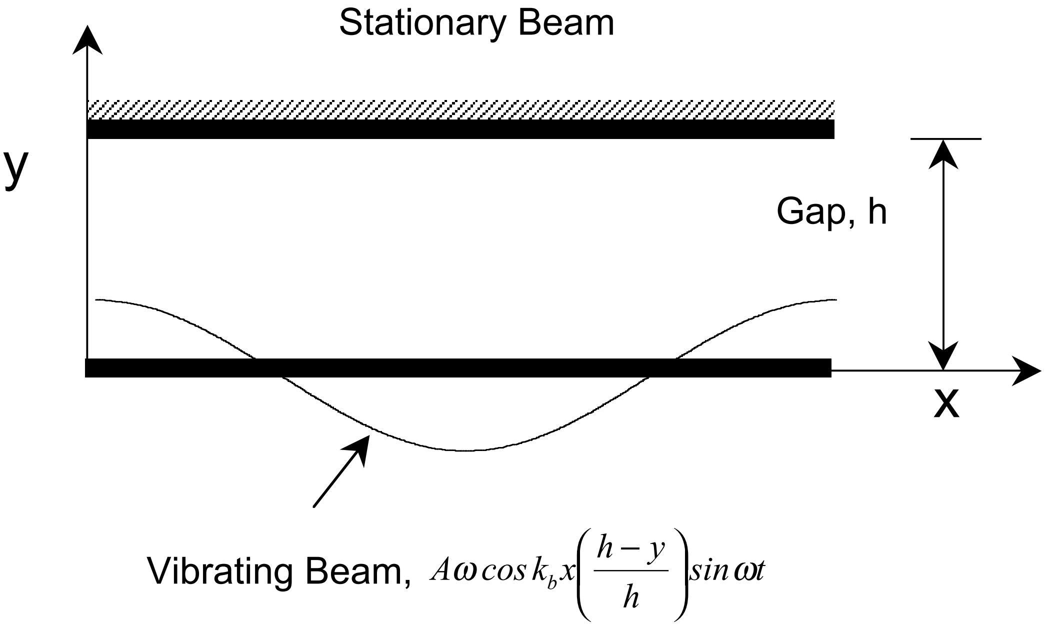

Figure 4. Simulation Schematic Drawing

11.4 COMPUTATIONAL FLUID DYNAMICS (CFD) SIMULATION

The Reynolds number based on the representative conditions, i.e., the thickness of the gap is 2 mm, A is 25 µm, λ_b is 2 cm, and f is 28.4 kHz, is less than 1800, which is in the range of laminar flow. The air speed in the gap is less than Mach 0.3 so that the incompressible fluid assumption can be applied. The governing equations for incompressible transient laminar Newtonian fluid flow are continuity:

$$\nabla \cdot \vec{v} = 0 \tag{7}$$

and linear momentum:

$$\frac{\partial \vec{v}}{\partial t} + (\vec{v} \cdot \nabla)\vec{v} = \frac{1}{\rho}\left(-\nabla p + \mu \nabla^2 \vec{v}\right) \tag{8}$$

The simulation covers more than 4000 periods with 16 time-steps each to get the quasi-steady state solution. The velocity $\vec{v}$, which contains harmonic terms and a "dc" term, is calculated from Equations 7 and 8. The acoustic streaming velocity ($\overline{v}_{a,i}$, i =1,2, and 3) is obtained by averaging $\vec{v}$ over a period as follows:

$$\overline{v}_{a,i} = \frac{1}{T_a}\int_0^{T_a} v_i dt \qquad i = 1,2, \text{ and } 3 \qquad (9)$$

where T_a is the period.

11.4.1 NUMERICAL ANALYSIS

The numerical analysis was carried out with a user-enhanced, validated program CFX 4.3 with the SIMPLEC algorithm for the pressure correction (AEA Technology, Bethel Park, PA), which is available on an SGI Origin 2000 at North Carolina Supercomputing Center (NCSC, RTP) or on a Sun Ultra 10 at North Carolina State University (Computational Fluid-Particle Dynamics Lab). The code is based on the Finite Volume Method (FVM) with multi-block structure and non-staggered grid. The algebraic equations are discretized with respect to the computational space coordinates with implementation of the boundary conditions. A time-dependent moving grid option is applied to solve the flow field induced by the ultrasonic flexural vibration (UFV) at the vibrating wall boundary. This option allows to specify time-dependent grid positions on the lower wall surface at each time step. The size of the computational mesh is about 4,000 control volumes and the required CPU hours to obtain the quasi-steady state flow field after more than 4000 periods of vibration is about 90 hours on the SGI Origin 2000.

11.4.2 CFD RESULTS

Figure 5 shows the time-evolution of vortices in the gap between a two infinite beams due to acoustic streaming. At time $t = 0$, no air flow exists in the gap, and then the lower beam starts to vibrate with the frequency $f = 28.4$ kHz, vibration amplitude $A = 20\ \mu m$ and wavelength $\lambda_b = 20$ cm in a 2 mm gap between two beams. Four vortices over a single wavelength emerge near the lower vibrating beam (cf. Figure 5-a). They appear between nodal points and anti-nodal points of the vibrating beam with two of them in the center moving closer (cf. Figure 5-a through l). The air flows upward at anti-nodal points and downward at nodal points, which is similar to the experimental visualization shown in Figure 2. After 610 pulses a steady streaming flow field is achieved (cf. Figure 5-f through l).

(a) after 20 pulses

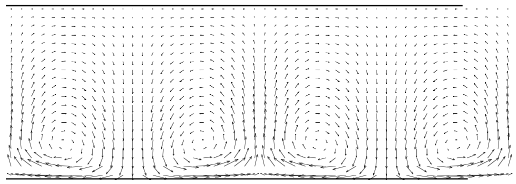

(b) after 60 pulses

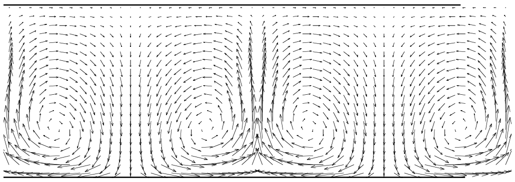

(c) after 110 pulses

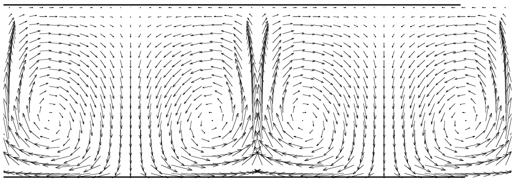

(d) after 210 pulses

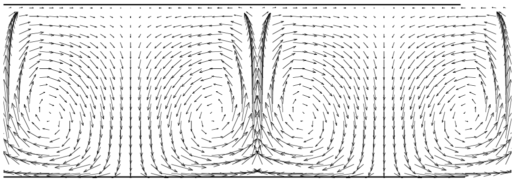

(e) after 410 pulses

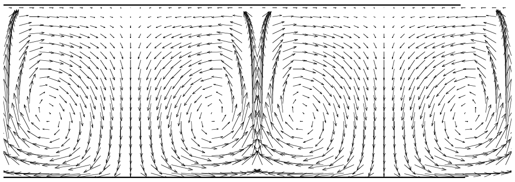

(f) after 610 pulses

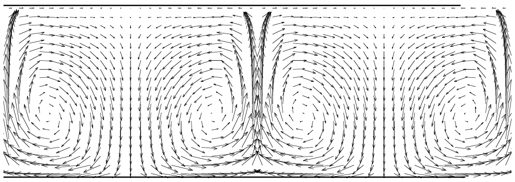

(g) after 1220 pulses

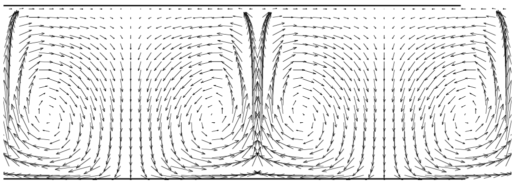

(h) after 3050 pulses

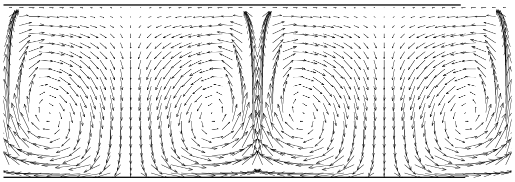

(i) after 6100 pulses

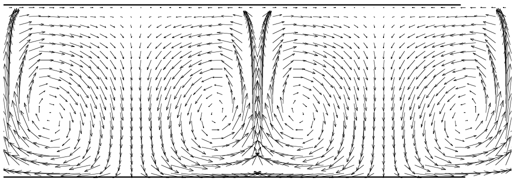

(j) after 12200 pulses

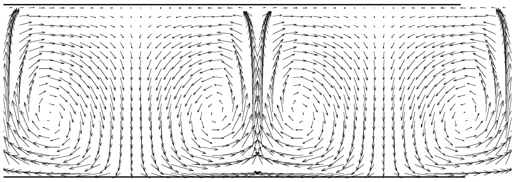

(k) after 18300 pulses

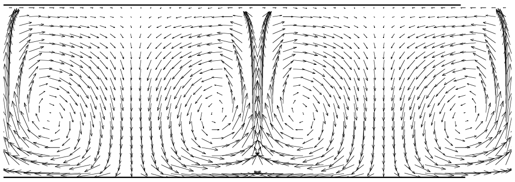

(l) after 24400 pulses

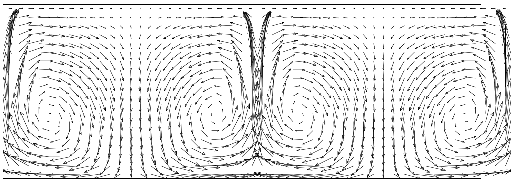

Figure 5. Development of Streaming Velocity

Figure 6 represents the acoustic streaming velocity tangent and normal to the beam along a fictitious vertical line passing through a vortex center. The tangential and normal velocities are zero at the vortex center (about y=0.072 cm). The tangential velocity reaches 70 cm/sec near the lower vibrating beam and 30 cm/sec near the upper beam. The normal velocity is significant only near the nodal and anti-nodal points, and near zero along the vertical line through the vortex center as shown in the flow field of the converged solution in Figure 5-l.

To observe the effect of changing excitation frequency, vibration amplitude, and gap on the streaming velocity and patterns, simulations were conducted. It is observed that the vortical flow patterns are not influenced by changing simulation conditions but the magnitude of the acoustic streaming velocity is strongly influenced. Therefore, for the following analyses only the variations of the magnitude of streaming velocity along a vortex center are compared and discussed except for the case of open ends in Section 4.2.3.

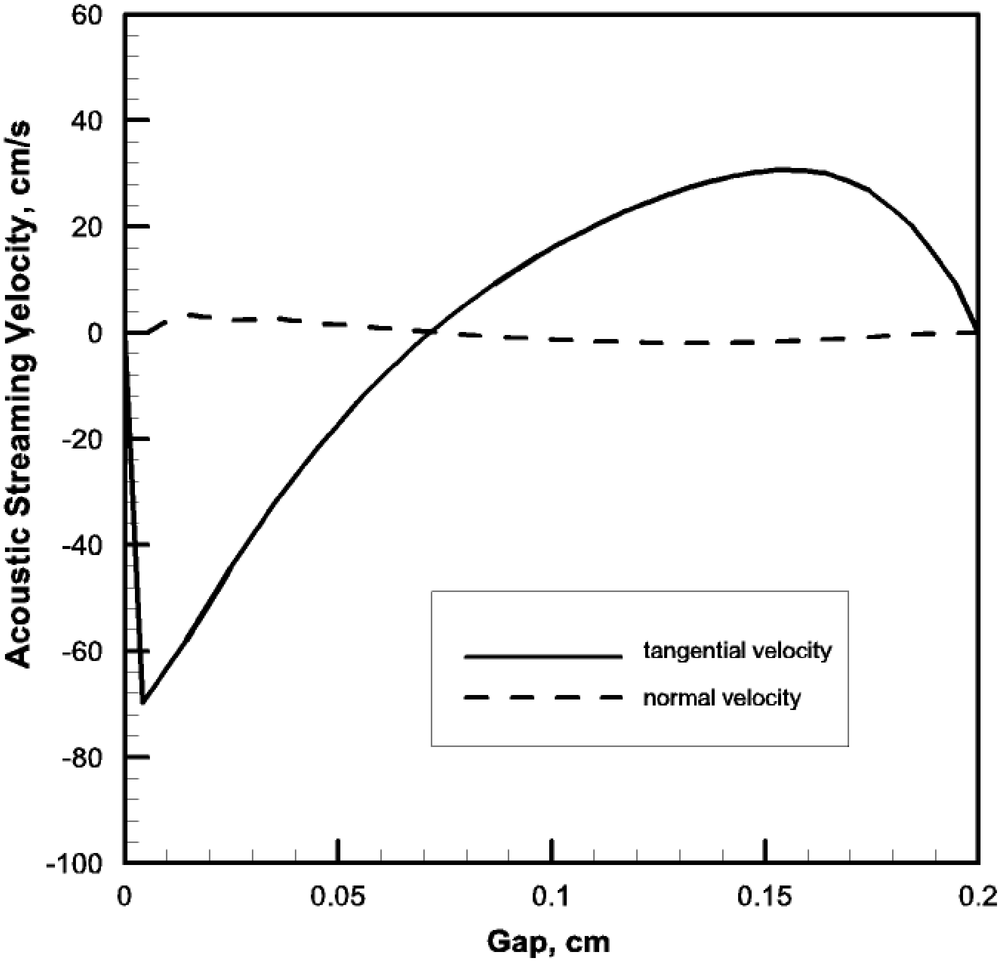

Figure 6. Streaming Velocity Through the Vortex Center

Effect of Vibration Frequency The effect of the excitation frequency on the acoustic streaming velocity is measured. Of particular interest is the change in acoustic streaming velocity when the excitation frequency becomes ultrasonic. If the excitation frequency of the beam increases with vibration amplitude constant, the irrotational velocity would also increase with the excitation frequency, resulting in an increase in acoustic streaming velocity because acoustic streaming velocity is proportional to the square of the irrotational velocity [2]. Therefore, the effect of excitation frequency can be properly measured only when the velocity of the vibrating beam is

maintained at a constant value as the excitation frequency increases by decreasing the vibration amplitude. Detailed test conditions are shown in Table 1.
9

Table 1. Simulation Condition

Frequency, kHz	Vibration amplitude, μm	Velocity of Vibrating Beam, m/s	Wavelength, mm
6.0	93.0	3.5	48.0
12.0	47.0	3.5	34.0
18.0	31.0	3.5	28.0
28.4	20.0	3.5	20.0
50.0	11.0	3.5	17.0

Figure 7 shows the maximum acoustic streaming velocity in the 2 mm gap at an excitation frequency of 6, 12, 18, 28.4 and 50 kHz with a vibration amplitude detailed in Table 1. The results are obtained from CFD simulation and the analytical solution based on Equation 6. It is observed that the maximum streaming velocities decreases with the excitation frequency. The maximum streaming velocities at 28.4 kHz near the lower and upper beams are 66.2 cm/sec and 30.6 cm/sec, respectively. The acoustic streaming motions near the lower beam are directly influenced by the motion of the lower vibrating beam while streaming motions near the upper beam are induced by the streaming flow near the lower beam. In the process of inducing streaming motions near the upper beam, airflow is attenuated. As a result, the maximum streaming velocities are observed near the lower beam. As shown in Equation 6, the acoustic streaming velocity is proportional to the square of the vibration amplitude and the wavelength of the vibrating beam that decreases with the excitation frequency. Although the excitation frequency grows, a decrease in the wavelength and the vibration amplitude offsets an increase in the acoustic streaming velocity resulting from the growth of the frequency. As a result, both CFD simulation and the analytical solution indicate that the maximum streaming velocity decreases with excitation frequency. Moreover, no significant change in acoustic streaming velocity is observed as the excitation frequency becomes ultrasonic. The analytical solution does not include the attenuation of flow, resulting in uniform streaming velocities across the gap. Therefore the analytical solution can be compared to the streaming velocity near the lower beam obtained from CFD simulation. It is noted that an analytical solution formulated following Nyborg's theory underestimates acoustic streaming velocity compared to the CFD results.

Effect of Vibration Amplitude and Gap Figure 8 shows the maximum streaming velocities near the beams for a vibration amplitude of 5, 10, 15, 20, 25, 30 and 40 μm with a gap of 2 mm at an excitation frequency of 28.4 kHz. The wavelength is 20 mm. The maximum streaming velocity increases as the vibration amplitude increases due to increase in the irrotational velocity. The maximum irrotational velocity near the lower vibrating beam can be calculated with the excitation frequency, the vibration amplitude and wavelength of the beam, and the gap.

For a vibration amplitude of 25 µm, the maximum streaming velocities near the lower and upper beams from CFD simulation reach 100 cm/sec and 45 cm/sec, respectively. For the same vibration amplitude, a maximum streaming velocity of 3.3 cm/sec is obtained from the analytical solution. It is observed that as the vibration amplitude grows, maximum streaming velocity from both CFD simulation and the analytical solution increase in a similar trend, an increase with the square of the amplitude but the analytical solution predicts significantly smaller acoustic streaming velocity. An explanation for this difference is being investigated by the authors. Figure 9 represents the maximum acoustic streaming velocity as a function of the gap between the vibrating beam and the upper stationary beam. The maximum streaming velocity decreases with the growth of the gap for both CFD simulation and the analytical solution. It is also observed that the analytical solution underestimates acoustic streaming velocity as opposed to CFD simulation result. The disagreement between the analytical solution and CFD simulation result grows as the gap increases because the analytical model is developed with an assumption that the gap is small enough to presume a linear variation of the normal irrotational velocity across the gap.

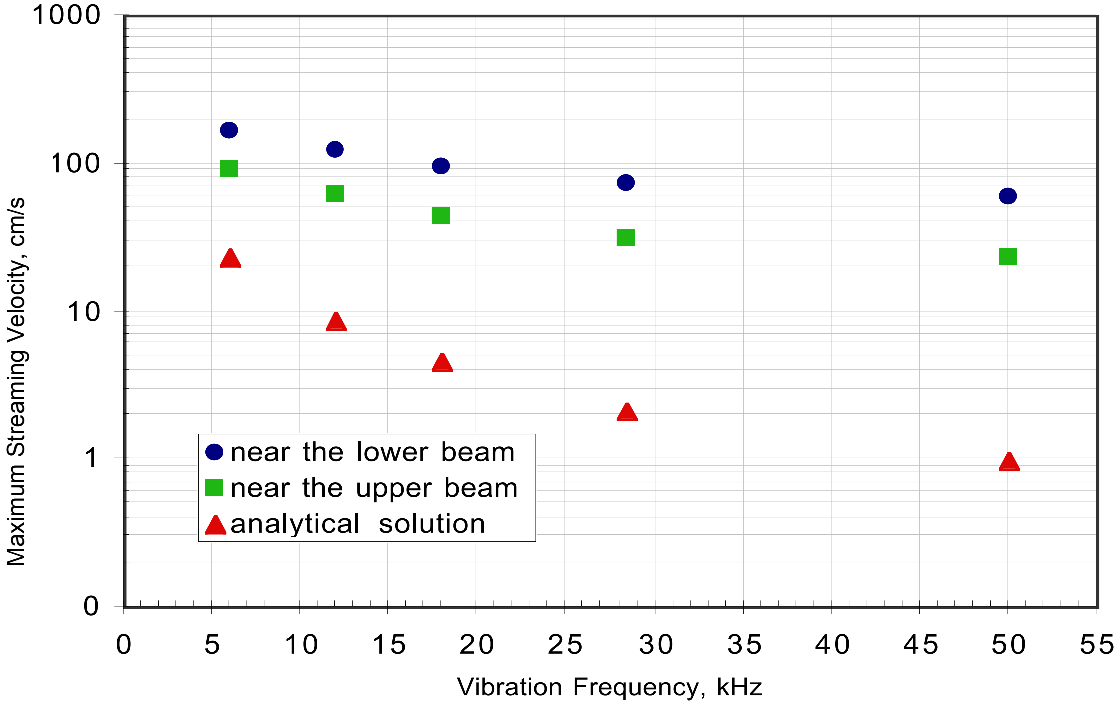

Figure 7. Theoretical Maximum Streaming Velocity versus Vibration Frequency

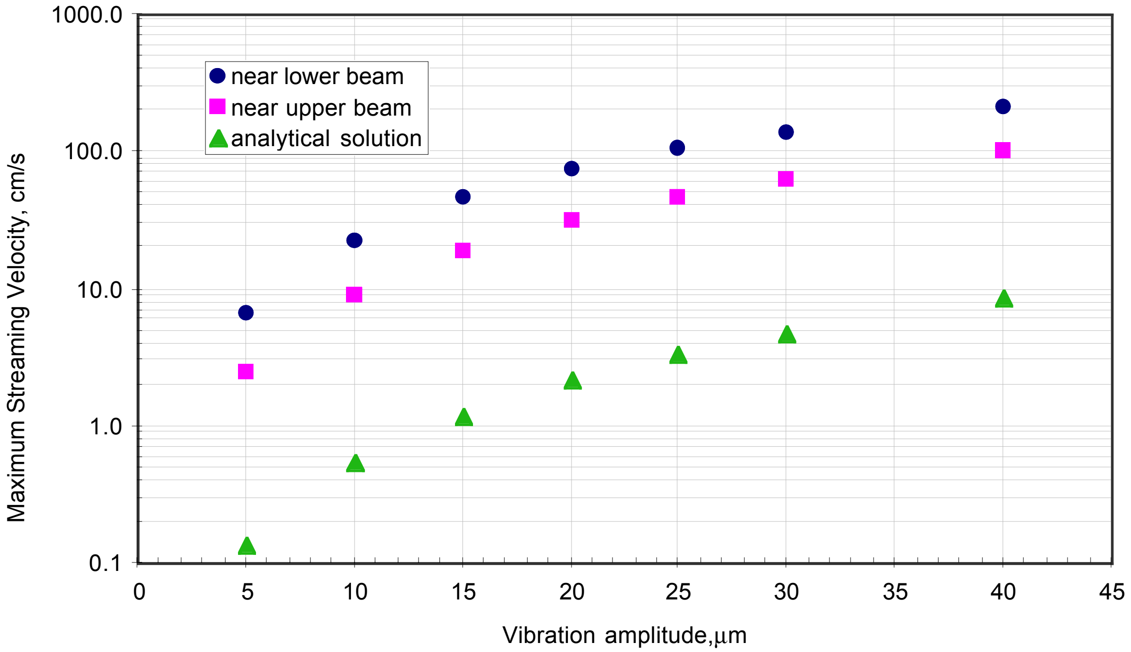

Figure 8. Theoretical Maximum Streaming Velocity versus Vibration Amplitude

Effect of Beam End Openings Figure 10 shows the streaming velocity fields for the 2 mm gap case considering the entire system, i.e., a one-and-a-half-wavelength long vibrating beam (3 cm) and a one-wavelength long stationary upper beam (2 cm) to observe the effect of an open-ended channel. Vortical flow and flow entrainment are observed near the ends of the upper beam. The vortex centers in the channel are located at x = 0.3 and 0.65 cm with a symmetry condition at x = 1 cm. Due to air entrainment, the flow field near the end is disturbed, forming a small vortex (cf. enlarged Figure 11). Figure 12 shows the magnitude of the acoustic streaming velocity in the gap from a three-dimensional perspective. A maximum streaming velocity occurs at the openings of the gap near the upper beam, which enhances the mixing of flow between inside and outside the gap. The streaming velocities near the lower beam are generally greater than those near the upper beam except for the maximum streaming velocity that occurs at the openings. The velocities observed with an open-ended channel are greater than those without an opening (cf. Figure 9). The velocity near the lower beam reaches up to 130 cm /sec due to the flow entrainment and is almost twice that of the 2 mm gap case without flow entrainment. Flow entrainment enhances the flow speed and changes the flow pattern, resulting in enhanced cooling capability.

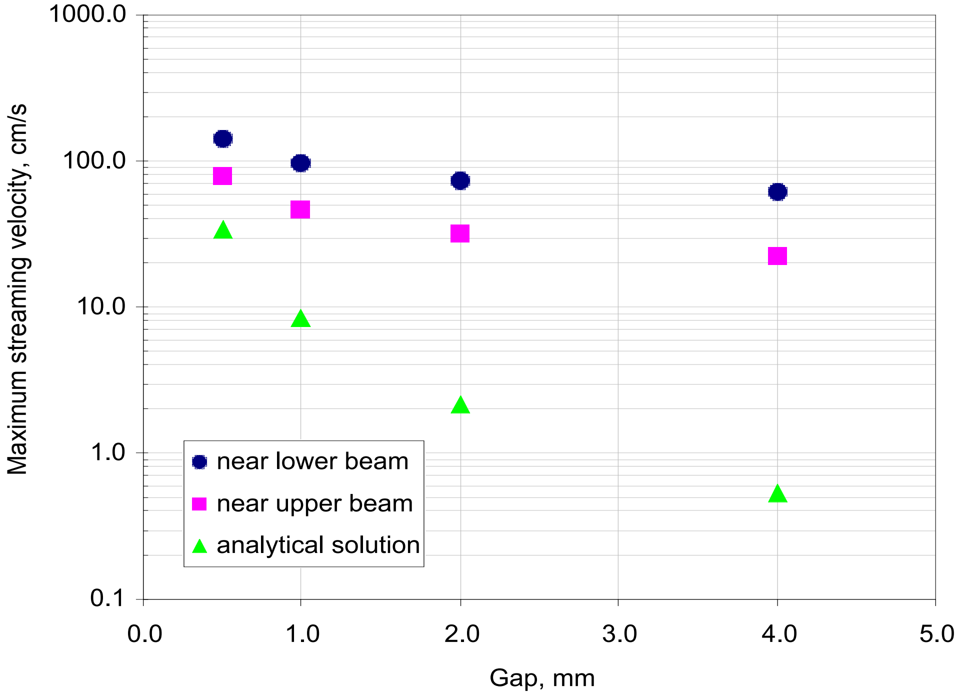

Figure 9. Theoretical Maximum Streaming Velocity versus Gap

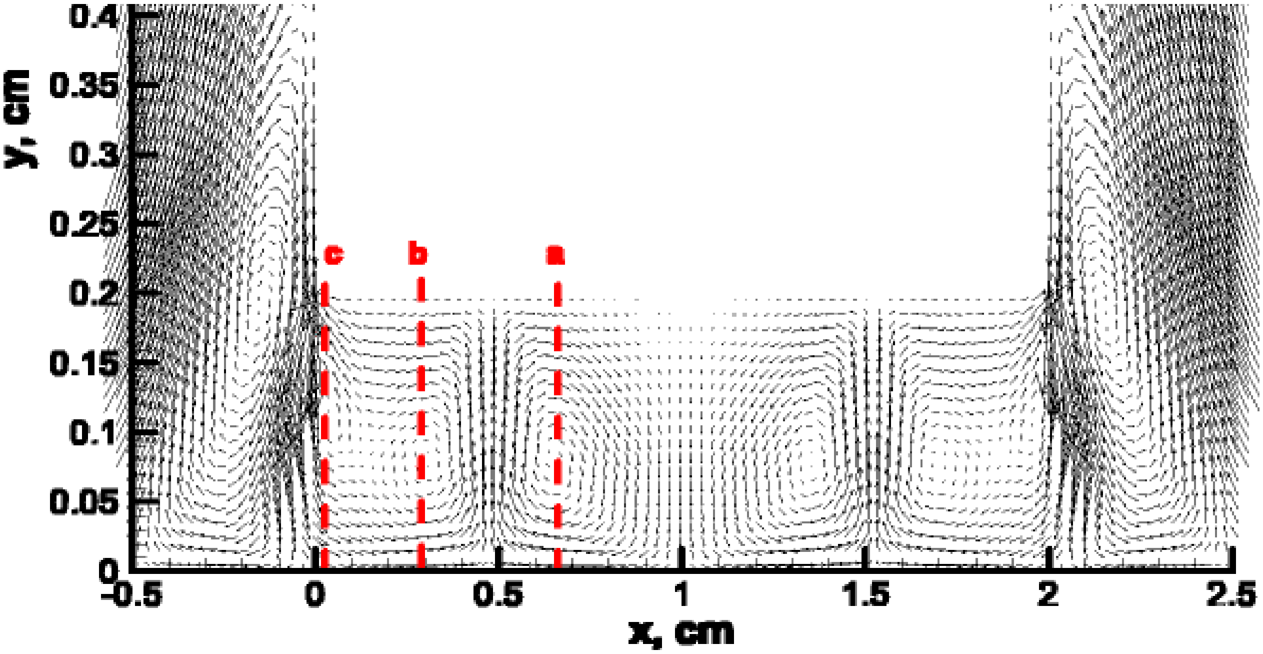

Figure 10. Streaming Velocity for the Entire System

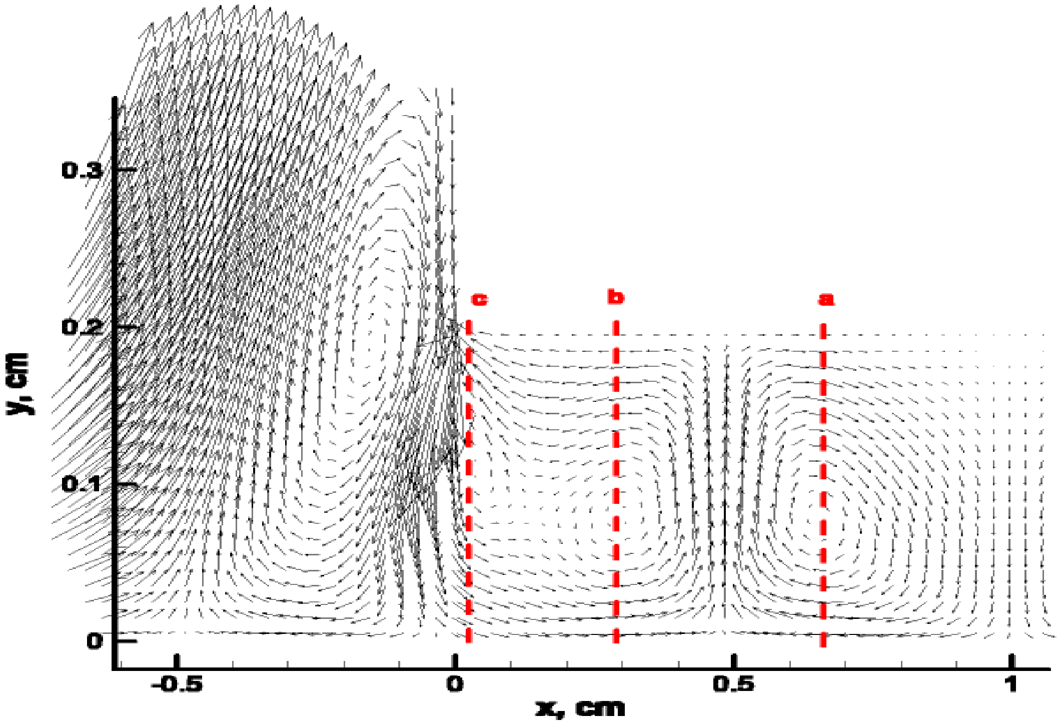

Figure 11. A Close-up View of Figure 10

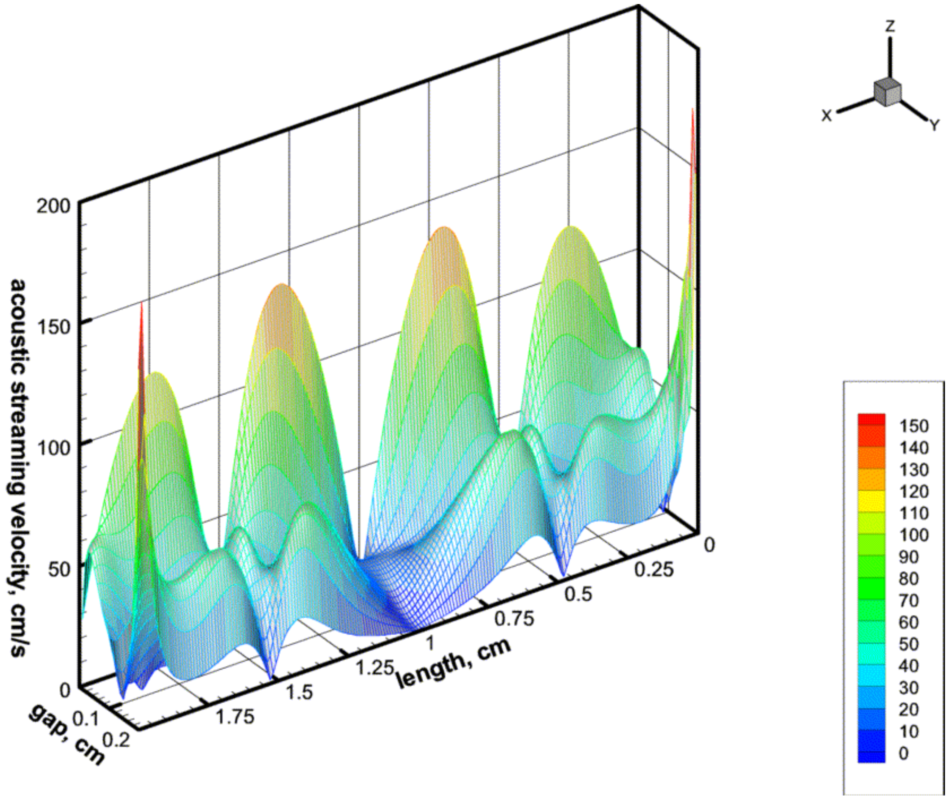

Figure 12. Three-Dimensional Velocity Contour inside the Gap

11.5 CONCLUSIONS

An investigation of acoustic streaming induced by the ultrasonic flexural vibration is presented. The investigation includes acoustic streaming pattern, velocity, and associated heat transfer characteristics. Acoustic streaming patterns visualized using Acetone correspond well with the prediction by Nyborg. Using acoustic streaming, a notable temperature drop of 40 °C was obtained in 4 minutes and maintained. Employing CFD simulation, it was shown that the vortical flows, observed by experiment and predicted by acoustic streaming theory, could be reproduced. Also, it was found that the streaming velocity from simulation is far greater than the estimation from the analytical solution based on sonically induced acoustic streaming assuming inviscid flow [2,13]. This result proves that the theoretical calculations based on sonically induced acoustic streaming may not be extended to estimating ultrasonically induced acoustic streaming velocity. With an open-ended channel, simulation revealed the existence of large flow entrainment at the channel ends, which enhances convective heat transfer and can not be captured with the analytical solution due to the complexity of boundary conditions. With a computational control volume mesh of 2000, the CFD simulation of the flow field induced by a beam vibrating at an ultrasonic frequency is computationally very intensive. It takes almost 10 CPU hours on the Cray T-90 supercomputer and 90 CPU hours on SGI Origin 2000 to obtain a fully developed acoustic streaming flow field. Although the CFD simulations are expensive, more accurate and realistic results can be obtained including a three-dimensional effect of acoustic streaming and the open-ended channel.

REFERENCES

1. Lee, C. P. and T. G. Wang, “Outer Acoustic Streaming,” J. of Acoust. Soc. Am., 88 (5), pp. 2367-2375, 1990.

2. Nyborg, W. L., “Acoustic Streaming near a Boundary,” J. of Acoust. Soc. Am., 30(4), pp. 329-339, 1958.

3. Faraday, M., "Phil.Trans." 121, p. 229, 1831.

4. Rayleigh, Theory of Sound, Dover Publication, New York, 1945.

5. Schlicting, H., Boundary Layer Theory, McGraw-Hill Book Company, Inc., New York, 1955.

6. Lighthill, J., “Acoustic Streaming,” J. of Sound and Vib., 61(3), pp. 391-418, 1978.

7. Jackson, F. J. and W. L. Nyborg, “Sonically-Induced Microstreaming near a Plane Boundary. I. The Sonic Generator and Associated Acoustic Fields,” J. of Acoust. Soc. Am., 32(10), pp. 1243-1250, 1960.

8. Nguyen, N. T. and R.M. White, “Design and Optimization of an Ultrasonic Flexural Wave Micropump using Numerical Simulation,” Sensors and Actuators, 77, pp. 229-236, 1999.

9. Gould, R. K., “Heat Transfer across a Solid-Liquid Interface in the Presence of Acoustic Streaming,” J. of Acoust. Soc. Am., 40(1), pp. 219-225, 1966.

10. Gopinath, A. and F. Mills, “Convective Heat Transfer From a Sphere Due to Acoustic Streaming”, J. of Heat Transfer, 115, pp. 332-341, 1993.

11. Gopinath, A. and F. Mills, “Convective Heat Transfer Due to Acoustic Streaming across the Ends of Kundt Tube,” Journal of Heat Transfer, 116, pp. 47-53, 1994.

12. Uhlenwinkel, V., R. Meng, K. Bauckhage, P. Schreckenber, and O.Andersen, “Heat Transfer to Cylindrical Bodies and Small Particles in an Ultrasonic Standing-Wave Fields of Melt Atomizer,” Multiphase-Flow and Heat Transfer in Materials Processing ASME, FED- Vol.201/HTD-Vol 297, pp. 19-24, 1994.

13. Vainshtein, P., M. Fichman and C. Cutfinger, “Acoustic enhancement of heat transfer between two parallel plates,” Int. J. Heat & Mass Transfer, 38(10), pp. 1893-1899, 1995.

14. Chen, Z. D., and M. P. Taylor and J. J. Chen, “Heat Transfer on a Surface Affected by an Air/Water Interface Undergoing Wave Motion,” The Minerals, Metals & Materials Society, pp. 429-435, 1998.

15. Sashida, T, An Introduction to Ultrasonic Motors, Clarendon Press, Oxford, 1993.

16. Andres, J. M. and U. Ingard, “Acoustic Streaming at High Reynolds Numbers,” J. of Acoust. Soc. Am., 25(5), pp. 928-937, 1953.

12 MODELING AND SLIDING MODE CONTROL OF FRICTION-BASED OBJECT TRANSPORT USING TWO-MODE ULTRASONIC EXCITATION

Witoon Panusittikorn
Graduate Student
Min C. Lee
Associate Professor, Pusan National University
Paul I. Ro
Associate Professor
Department of Mechanical and Aerospace Engineering

This section introduces the modeling and sliding mode control of an object transport system whic employing friction force to drive an object on an ultrasonic flexural vibrating beam. The mechanism of a friction drive is analyzed, and its potential to automate the object transport prototype is described. The characteristic of the friction drive is expressed in a mathematical model. Hertzian contact theory and a modified spring model were used to estimate the effective contact area and normal force. Coulomb friction theory was used to apply the normal force to the effective friction driving force in the positive and the negative slip regions. The nonlinear relationship between the output estimated friction drive and the input voltage is described. The model is linearized approximately and applied to feedback control simulation. Simulation results of the estimated slider displacement verify the accuracy of the friction model. A sliding mode controller is designed for the object transport prototype in order to observe implementation problems. Problems of noise and low sampling frequency of the hardware were exposed. Adding analog and digital lowpass filters were encountered to reduce the noise problem. Results of sliding mode control (SMC) at a low sampling frequency of 10 Hz is compared with the result of PID control. It is shown that the trajectory performance of the sliding mode control is superior to that of PID control.

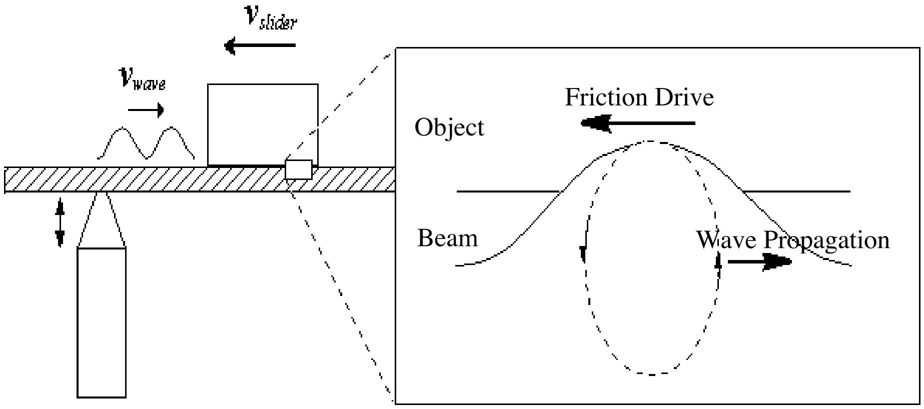

12.1 INTRODUCTION

An ultrasonic motor is a type of actuator that uses mechanical vibrations in the ultrasonic range and generates the friction forces to drive a rotor/slider instead of magnetic driving forces as in conventional electro-magnetic motors. Since Sashida invented the ultrasonic motor in 1982 [1], it has been widely investigated in various fields including physics, mathematics, dynamics and control due to its unique advantages over conventional electro-magnetic motors such as silent operation, use of a simple structure, and the absence of transmission components and lubricants [2-13]. Especially, the ultrasonic motors are ideal for a clean-room environment such as manufacturing wafers and for electric parts assembly line to handle products sensitive to magnetic fields, such as semiconductors because the motors have less maintenance, compact size, high output power at low speed and are not influenced by magnetic fields. The precision controllability also enables ultrasonic motors to address more sophisticated tasks.

In this study, the motors are applied to the transportation system of electric parts in a clean-room. To control the transport system, a friction model of this driving mechanism should be developed. The contact friction is described as a Coulomb friction force, which is a product of a friction coefficient and normal contact force. In traveling wave type ultrasonic motor design, a simple spring model was used to represent the normal contact force [14-15]. To improve the accuracy of this model, the normal force of a linear ultrasonic motor was expressed in terms of a Fourier Series to solve this nonlinear contact force problem [16]. The results showed a strong nonlinear dependence on the parameters characterizing the contact force. In this study, a mathematical model of the friction drive is derived using the Hertzian contact theory and a modified spring model to estimate the effective contact area and normal force [17].

A linear beam-type ultrasonic motor is investigated. In its design, a finite-length beam serves as a stator while the transported object functions like a slider. The beam is excited to produce elliptical motions on the surface of the beam that drive the slider. In a previous study, two principles have been developed to generate the progressive waves without reflecting waves in a finite beam. One utilizes the theory of impedance matching in a transmission line [18,19]. The other principle employs an excitation frequency between two adjacent flexural modes to induce the progressive wave with the same frequency, but 90° out of phase [20,21]. In this study, two-mode excitation method is selected because the method shows better performance over impedance matching in terms of robustness with respect to a varying slider mass. To optimize transport performance, the direction of travel and transport speed must be automatically controlled. In this respect, the two-mode excitation provides the necessary capability for feedback control implementation because it can alternate slider speed and direction by magnitude and phase modulation of the supplied voltage. The modulation is accomplished by a computer-controlled function synthesizer. As a result, this implementation does not require manual switching, which is the case for impedance matching [21]. An open loop control was demonstrated in [21], but the performance leaves much room for improvement and indicates a need for closed-loop control. In the literature, the closed loop control for friction-based object transport has not been almost investigated [22]. In this study, a sliding mode controller (SMC) [23-26] was designed and tested on the transport system

12.2 DESCRIPTION OF OBJECT TRANSPORT SYSTEM

Friction-based object transport employs the energy transfer principle of ultrasonic motors to drive objects on a vibrating beam. Supplied electric power causes the actuator to vibrate in the longitudinal direction. As shown in Figure 1, the vibration is transmitted to a orthogonally connected beam, which, in turn, induces flexural beam vibration. The beam is designed such that the flexural waves can propagate along the length of the beam. When traveling waves are induced on the beam, the particles on the surface of the beam move along an elliptical path. This elliptical motion, when it comes in contact with the slider surface, drives the slider via friction force. The direction of the moving slider opposes the direction of the propagating progressive waves [21]. An elliptical motion of the beam particle is exemplified in traveling waves where both time and space are of 90° out of phase. Two-mode excitation is used to generate the progressive waves. The waves propagate in a finite-length beam due to the contribution of two major natural frequencies. The waves of two-mode excitation propagate, but the wave contour is not consistent, which is in contrast to the contour of traveling waves. The complicated beam surface motion of the two-mode excitation contributes to a difficult modeling problem. To simplify the flexural motion of the two-mode excitation waves, the equations of motion for the conventional traveling waves are approximated as propagating along an infinite beam.

Figure 2 shows the control layout of the transport system. The system consists of an aluminum beam supported by ultrasonic excitation actuators. The actuator employs a piezoelectric stack to induce the harmonic input voltage with an ultrasonic frequency to generate vibration displacement. The frequency is chosen between two neighboring natural frequencies [21, 22].

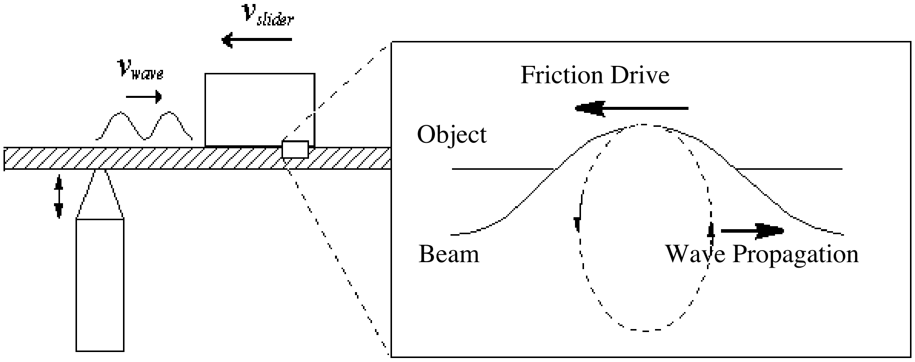

Figure 1. Direction of propagating wave and moving object

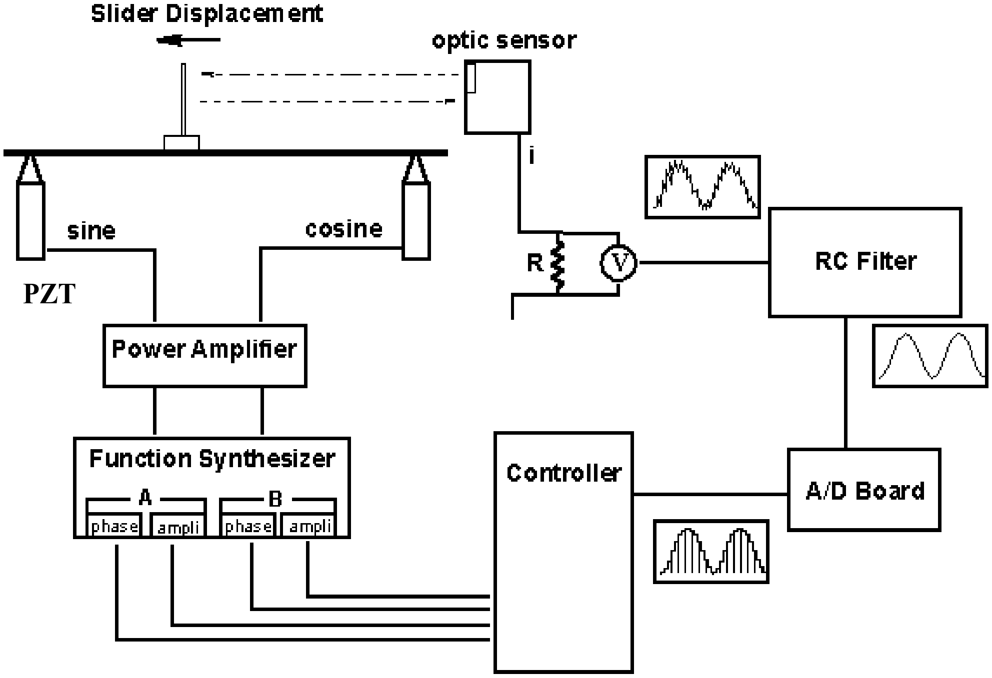

Figure 2. Feedback control layout of object transport

The displacement is amplified by a conical horn. These two actuators are excited with a phase difference of 90° to generate the progressive waves. A steel box is the test slider. To integrate a viscoelastic friction layer between the two metallic parts similar to conventional ultrasonic motors, a piece of duct tape is attached under the slider.

When progressive waves drive the slider along the beam, the displacement of the slider is observed by an optical sensor. The sensor output is a small electric current that is transformed to a voltage by a resistor. The voltage drop across the resistor is sampled using an A/D board connected to a PC. The PC utilizes the control algorithm to generate the appropriate phase and amplitude commands for the object transport system. Then, the phase and amplitude commands are sent to a function synthesizer, which generates the voltage signal for the piezoelectric actuators. The resulting voltage of the function synthesizer has to be amplified to excite the actuator.

12.3 FRICTION DRIVE MODEL BASED DYNAMIC EQUATION

Friction-based actuation of the ultrasonic object transport is a non-linear problem [14-16] characterized by Coulomb's friction law. The law expresses the force as a product of a constant friction coefficient and normal contact force. The normal contact problem can be explained by

Hertzian contact theory where two bodies having curved surfaces are pressed together. Line contact, then, changes to area contact [17]. When no traveling waves are generated, the weight of the slider is uniformly distributed over the interface area between the beam surface and friction layer of the slider. When the traveling waves propagate, the small vibration amplitude of the beam holds the slider up. Due to an elastic friction layer interposed between the slider and beam surface, the slider weight distributes normally over the interface area. Most of the weight is intensely distributed on the peak of the wave crest. The weight distribution gradually decreases away from the peak. This contact can be illustrated by pressing a thin rubber plate on a small metal cylinder. The effective friction drive occurs where the distributed weight is large enough to deform the shape of the friction layer. In other words, the effective friction drive is made only in the contact area of the traveling wave crest. By trial and error, one-eighth of the slider weight was determined to be a constant force pressed on the crest. According to Hertzian Contact Theory, the area contact of two-curved surface is transformed to a narrow rectangle of width $2b$ and length L as illustrated in Figure 3. The half-width b of a flat surface pressing on a cylinder is given by the equation between the width b and force pressed on the slider and beam [17]. The friction layer is assumed to be an elastic material. The normal contact force is expressed by Equation(1).

$$\begin{aligned} N &= \sigma_{friction} Area_{contact} \\ &= E_{friction} \varepsilon_{friction} Area_{contact} \end{aligned} \tag{1}$$

where

$\sigma_{friction}$ = normal stress of friction layer in the contact area

$Area_{contact}$ = contact area

$\varepsilon_{friction}$ = strain in friction layer

$E_{friction}$ = friction layer’s modulus of elasticity

Strain is a result of deformation in contact area divided by thickness of friction layer

$$\varepsilon_{fiction} = \frac{w(x) - w_0}{h_{friction}} \tag{2}$$

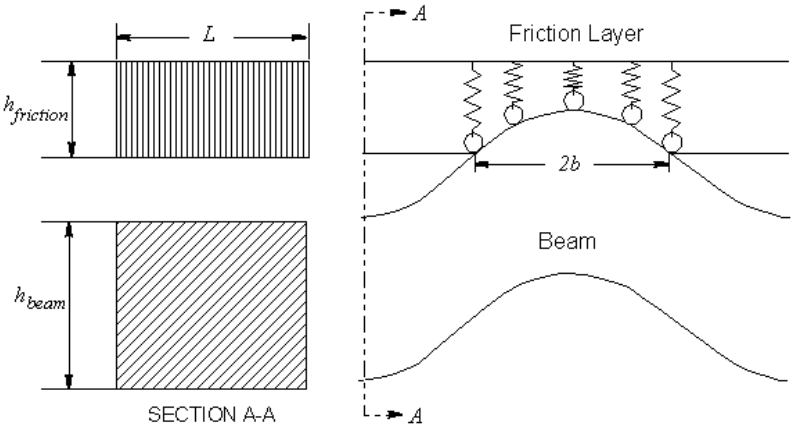

Figure 3. Parameter definition for estimated friction model

where

$w(x)$ = transverse motion in the contact area, $A\cos(\frac{2\pi x}{\lambda})$
w_0 = transverse displacement at the starting contact point, $A\cos(\frac{2\pi b}{\lambda})$
$h_{friction}$ = cross-sectional thickness of friction layer, 1mm.
wave length of traveling waves, 33mm

In Figure 4, the shape of deformation in the contact area can be described as a parabola. As a result, the normal contact force varies from point to point. The total normal force is the sum of those forces at every point in the contact zone:

$$N = \frac{E_{friction} L}{h_{friction}} \times 2\int_0^b [A\cos(\frac{2\pi x}{\lambda}) - A\cos(\frac{2\pi b}{\lambda})]dx \qquad (3)$$

When traveling waves propagate, every particle on the beam surface moves in an elliptical motion. The longitudinal velocity increases rapidly as the point moves higher up to the crest and decreases as the point passes behind the crest. This elliptic motion allows the friction layer and the beam to slip in the contact region as shown in Figure 5. At the point where the velocity is larger than that of the slider, the beam moves faster than the friction layer. Positive slip motion occurs in this case, and friction forces drive the slider. On the other hand, at the point where the longitudinal velocity is less than that of the slider, negative friction force impedes the slider. The effective friction drive force is calculated as the sum of the positive and negative friction force in the contact area.

$$\begin{aligned} F_d &= \mu N \,\mathrm{sgn}[V_{longitudinal} - V_{slider}] \\ &= \frac{\mu E_{friction} L}{h_{friction}} \times 2\int_0^b [A\cos(\frac{2\pi x}{\lambda}) - A\cos(\frac{2\pi b}{\lambda})]\times \mathrm{sgn}[V_{long}\cos(\frac{2\pi x}{\lambda}) - V_{slider}]dx \end{aligned} \tag{4}$$

Where

F_d = friction drive

μ = estimated friction coefficient, 0.25

V_{long} = longitudinal-vibration velocity amplitude of traveling waves, $\frac{d}{dt}u(x,t)$

V_{slider} = measured slider velocity

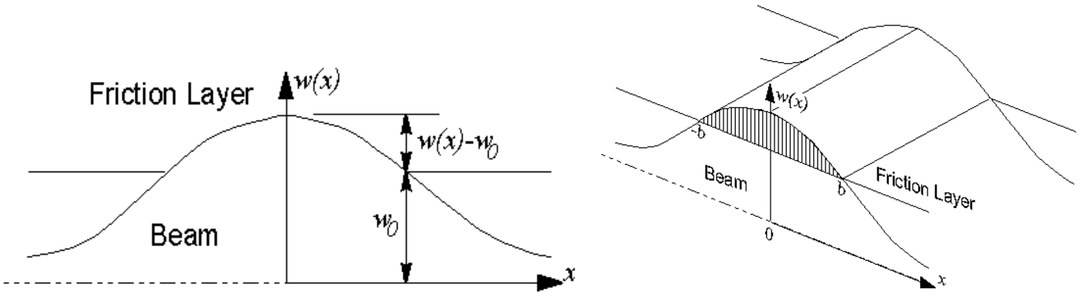

Figure 4. Normal force due to deflection of friction layer

The friction driving force can be described in terms of amplified input voltage according to the following equation.

$$F_d = 0.0515732 \times Vt \left\{ 10.1584e-3 + \left[\frac{0.20444}{\sqrt{Vt}} - 0.0138 \right] \cos\left(\frac{38.9253}{\sqrt{Vt}} \right) - 5.2521e-3 \times \sin\left(\frac{38.9253}{\sqrt{Vt}} \right) \right\} \tag{5}$$

The force shows a strong nonlinear characteristic with respect to amplified input voltage *Vt*. A comparison of the estimated and measured friction drive is shown in Figure 6. The measured friction data was obtained from Kircher's experiment [22], where the driving force was evaluated by a spring gauge attached at the end of the slider. The friction model represents a similar profile to the actual friction drive. Yet, the estimated friction drive was 0.03 N greater than the measured results. This is the result of imprecise properties of the friction layer, a piece of duct tape. In addition, the duct tape may wear after running for many experiments such that the tape surface is rippled. Consequently, it is no longer a smooth contact and the actual friction drive deviates from the results of the friction model.

Figure 5 illustrates the nonlinear relationship between the driving force and input voltage. The force gradually grows as the voltage approaches 200 V. Then, it accelerates and slowly approaches saturation at 500 V. The profile of estimated friction drive is similar to an S-shape. In the voltage range of 100-500 V, the relationship between the amplified input voltage and friction drive can be linearized to construct the estimated feedback control model. The linear equation of the model can be represented as

$$F_d = 0.0282 \times \left(\frac{Vt}{100} \right) \tag{6}$$

Figure 6 demonstrates the measured open loop responses of the slider displacement as a function of amplified input voltages. Each slider begins slowly and then the steady state speed after 0.3 s. In steady state, the velocities are kept constant. The velocity at the low input voltage is slow, as expected. When the voltage increases, the velocity also increases until the amplified input voltage is close to 500 V. At 500 V, the slider velocity is barely different from that of the amplified input voltage (400 V). These velocity profiles correspond to the S-shape friction drive evolution in Figure 5. The length of the slider is 35 mm, which is close to the wavelength of the traveling waves, 33 mm, only one wave crest contacts the slider in each cycle. The slider slowly speeds up at the start and then reaches the constant velocity. At the steady state, the behavior would be characterized as a damping force where the force is proportional to velocity. When the slider changes direction, the system moves from rest before progressing into the steady state.

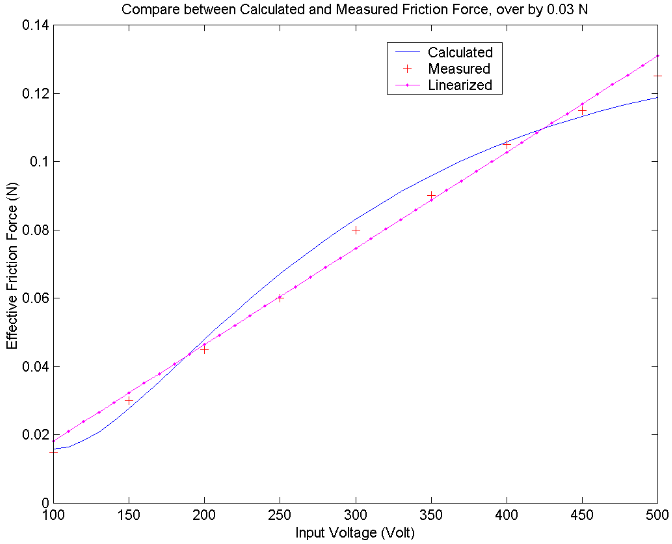

Figure 5. Comparison of estimated friction drive and measured force with linearized model

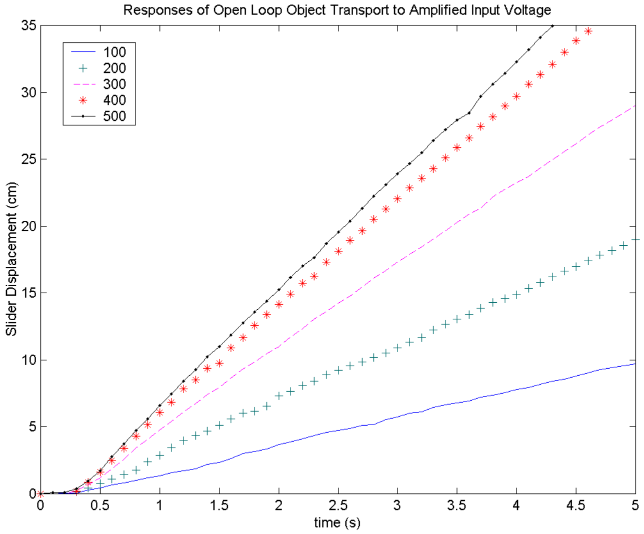

Figure 6. Measured responses of object transport

According to the linearized model of the amplified input voltage, the relationship of the voltage and slider displacement can be described by the following equation.

$$\begin{aligned} F_d &= 0.0282\left(\frac{Vt}{100}\right) = m\ddot{x} + c\dot{x} \\ &= 0.0282 \times U = m\ddot{x} + 1.8\dot{x} \end{aligned} \tag{7}$$

where U is the control law and the damping coefficient 1.8 was obtained by trial and error to match the estimated results with the observed data. As a matter of fact, this relationship is obtained from the simplification of the nonlinear friction drive. The model contains the parametric imprecision and unmodeled dynamics. Incorporating terms that represent those uncertainties results in

$$U = (\hat{m} + \tilde{m})\ddot{x} + (\hat{c} + \tilde{c})\dot{x} \tag{8}$$

where

$\hat{m}$ = estimated slider mass, $m/0.0282$
$\tilde{m}$ = imprecise term of slider mass
$\hat{c}$ = estimated damping, $\hat{c} = 1.8/0.0282$
$\tilde{c}$ = imprecise term of damping

12.4 SLIDING MODE CONTROL AND SIMULATION

12.4.1 DESIGN OF SLIDING MODE CONTROL

Sliding mode control (SMC) is a systematic approach to robust control that allows a general n^th^ order system to be replaced by an arbitrary parametric 1st order system. The equivalent 1st order system, called sliding surface *S*, represents the performance of the feedback control. For an example tracking problem, when the slider tracks the desired trajectory, the system is on the desired surface *S*=0. On the contrary, when the slider loses the desired position, the sliding surface *S* falls off the surface *S*=0. The control law is then re-evaluated. The inverse control law with a restricted stability condition is given in such a way that *S* returns to the desired surface and the nth order system remains stable. In the presence of modeling uncertainties, the inverting control law method has to be discontinuous. Specifically, the control law will reverse the sign as the sliding surface crosses zero. Even though the sliding surface returns back to the surface *S*=0, it may not be constantly maintained on the surface because the value of the control law is not known precisely. The value of *S* may fall to the other side of surface *S*=0. Then, the control law is re-evaluated. As a result, a good tracking performance of SMC has to compensate for high control activities. SMC consequently, requires a fast operating system for implementation.

The fundamental notion about conventional SMC with a fixed switching gain is described in [23]. Fixed-gain methods, however, may not assure stability in the presence of large parametric uncertainties and unmodeled nonlinear dynamics [24-26]. SMC with variable switching gain shows the capability to compensate for the uncertainties and imprecise parameters of friction models [27-31]. According to the friction drive model of equation(8), the state-space representation using slider displacement x, velocity $\dot{x}$, and acceleration $\ddot{x}$ and the input voltage U is expressed as

$$(\hat{m}+\tilde{m})\begin{bmatrix}\dot{x}\\ \ddot{x}\end{bmatrix}=\begin{bmatrix}0 & 1\\ 0 & -(\hat{c}+\tilde{c})\end{bmatrix}\begin{bmatrix}x\\ \dot{x}\end{bmatrix}+\begin{bmatrix}0\\ 1\end{bmatrix}U \tag{9}$$

The tracking motion problem, where the slider follows the desired trajectory x_d, is of interest. Position error e is given by

$$e(t)=x_d(t)-x(t) \tag{10}$$

The equivalent 1st order system, the surface *S*, is expressed in terms of an arbitrary constant λ and the tracking error *e*.

$$S=\left(\frac{d}{dt}+2\lambda+\lambda^2\int dt\right)^{n-1} e \tag{11}$$

Consequently, when the feedback algorithm is used to move a slider on the desired trajectory, sliding surface *S* is retained at zero. If the slider is off track, then the surface *S* takes on a value other than zero. As a result, sliding surface S represents the performance of feedback tracking motion control [32]. To maintain S at zero such that the slider tracks the desired trajectory, the equivalent control law U_{eq} is introduced. The equivalent control law U_{eq} is estimated to achieve the condition

$$S=0 \qquad \text{and} \qquad \dot{S}=0 \tag{12}$$

The derivative of S is given as

$$\dot{S}=\hat{m}(\ddot{e}+2\lambda\dot{e}+\lambda^2 e) \tag{13}$$

where $\dot{e}=\dot{x}_d-\dot{x}$ and $\ddot{e}=\ddot{x}_d-\ddot{x}$

Rearranging the Equation(13) yields,

$$\begin{aligned}\dot{S}&=\hat{m}(\ddot{x}_d-\ddot{x})+\hat{m}(2\lambda\dot{e}+\lambda^2 e)\\ &=\hat{m}\ddot{x}_d-\left\{U-\tilde{m}\ddot{x}-(\hat{c}+\tilde{c})\dot{x}\right\}+\hat{m}(2\lambda\dot{e}+\lambda^2 e)\end{aligned} \tag{14}$$

The equivalent control U_{eq} that achieves $\dot{S}=0$ is

$$U_{eq}=\hat{m}\ddot{x}_d+\hat{c}\dot{x}+\hat{m}(2\lambda\dot{e}+\lambda^2 e) \tag{15}$$

However, the equivalent control U_{eq} may not consistently maintain the sliding surface S=0 in the face of imprecise dynamics modeling and disturbances. A discontinuity across the surface S=0 is added to bound the effects of those uncertainties. Sliding mode control law U is,

$$U=U_{eq}+K\,\mathrm{sgn}(S) \tag{16}$$

where K is a variable switching gain; an arbitrary positive number that guarantees S=0.

The derivative of S including the switching term is given as

$$\begin{aligned}\dot{S}&=\hat{m}\ddot{x}_d-\left\{\hat{m}\ddot{x}_d+\hat{c}\dot{x}+\hat{m}(2\lambda\dot{e}+\lambda^2 e)+K\,\mathrm{sgn}(S)-\tilde{m}\ddot{x}-(\hat{c}+\tilde{c})\dot{x}\right\}+\hat{m}(2\lambda\dot{e}+\lambda^2 e)\\ &=\tilde{m}\ddot{x}+\tilde{c}\dot{x}-K\,\mathrm{sgn}(S)\end{aligned} \tag{17}$$

To guarantee the bounded sliding surface, the variable switching gain K must satisfy the stability condition

$$\frac{1}{2}\frac{d}{dt}S^2=S\dot{S}\le 0 \tag{18}$$

By substituting terms of $\dot{S}$, the condition is expanded to

$$\begin{aligned}S\dot{S}&=S\left\{\tilde{m}\ddot{x}+\tilde{c}\dot{x}-K\,\mathrm{sgn}(S)\right\}\\ &=(\tilde{m}\ddot{x}+\tilde{c}\dot{x})S-K|S|\le 0\end{aligned} \tag{19}$$

Thus,

$$(\tilde{m}\ddot{x}+\tilde{c}\dot{x})S\le K|S| \tag{20}$$

$$(\tilde{m}\ddot{x}+\tilde{c}\dot{x})\,\mathrm{sgn}(S)\le K$$

The switching gain must be greater than the bounds on modeling imprecision and dynamic uncertainties to guarantee the stability of the feedback control system.

$$K \geq \left|\tilde{m}\ddot{x} + \tilde{c}\dot{x}\right| \tag{21}$$

The nominal control law based on the estimated parameters and the measured displacement is determined as

$$U_m = \hat{m}\ddot{x} + \hat{c}\dot{x} \tag{22}$$

where x is the measured slider displacement. Through Equations(16) and (22), the bound on the modeling imprecision can be effectively calculated as

$$U - U_m = \tilde{m}\ddot{x} + \tilde{c}\dot{x} \tag{23}$$

The variable switching gain is then chosen as

$$K = a\left|U - U_m\right| \geq \left|U - U_m\right| \tag{24}$$

where a is an arbitrary positive constant, $a \geq 1$

Thus, the sliding control law U in the time domain is

$$U(t) = U_{eq}(t) + K(t)\,\mathrm{sgn}\big(S(t)\big) \tag{25}$$

which can be implemented in the digital control environment as

$$U(k) = U_{eq}(k) + a\left|U(k-1) - U_m(k)\right|\mathrm{sgn}\big(S(k)\big) \tag{26}$$

Variable switching gain K is obtained from the difference of the preceding control law $U(k-1)$ and the nominal $U_m(k)$ to prevent an algebraic loop. This calculation should be performed at a high rate to decrease the effect of delay.

12.4.2 SIMULATION

The mathematical model of the friction-based object transport and the feedback control algorithm were developed in SIMULINK, a simulation module of MATLAB. The desired trajectory assigned as a reference path was compared with the measured slider displacement to evaluate the displacement error. The error was then transferred to the controller to generate the control law based on the algorithm. The control law was supplied to the object transport system to correct the position error. To evaluate a trajectory tracking performance of sliding mode control, the performance is compared with that of PID control. The resulting slider displacement was fed back and compared to the reference path. Then the control cycle was repeated. The simulated control cycle time was 100 ms. Figure 7 shows the SIMULINK diagram of both control algorithms tested in the simulation. PID controller gains, a proportional K_p of 3.0, an integral K_i of 0.0 and a derivative gain K_d of 0.3, were obtained from Kircher's experiment [22].

SMC parameters such as sliding surface S, equivalent control law U_{eq}, and nominal control law U_m were implemented. By trial and error, the arbitrary constant λ was selected such that the tracking performance was favorable (λ=0).

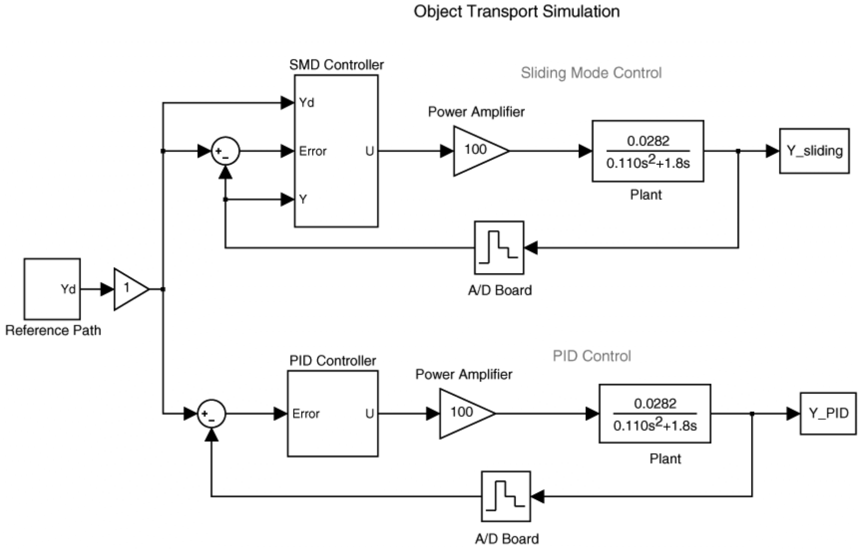

Figure 7. Diagram of closed loop control, PID and SMC

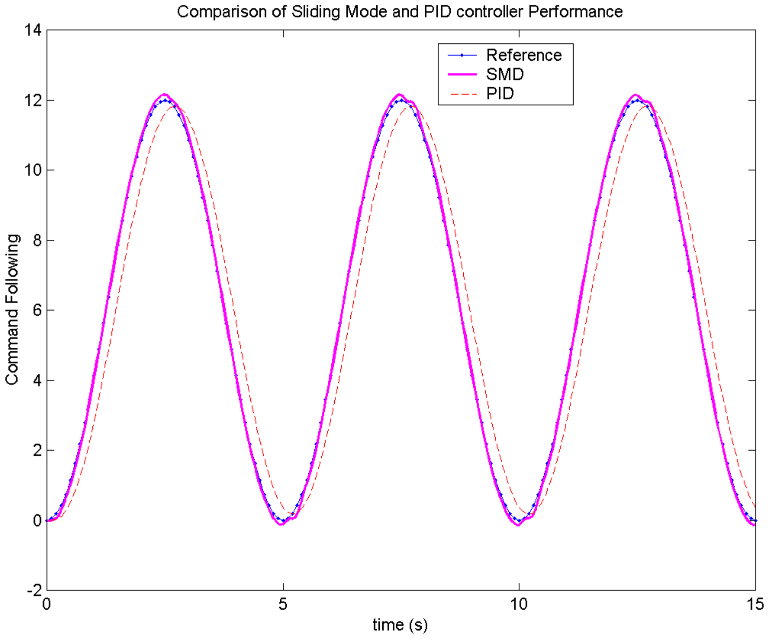

Figure 8. Trajectory tracking performance of SMC and PID

A sinusoidal reference path was simulated to observe the performance of the control law. Due to the limitation of slider velocity as shown in Figure 6, the amplitude and frequency of the sine wave were selected such that the velocity of reference path did not exceed the capacity of slider.

A comparison between the reference trajectory and the resulting path of the control algorithms, PID and SMC, is shown in Figure 8. The figure shows that both control algorithms have the potential to solve the tracking problem but SMC exhibits better tracking. The SMC slider path is exactly overlaid on the reference trajectory except near the crest of the trajectory, while PID shows a delay. The errors near the crest are due to slow sampling time, 100 ms. Figure 8 shows that the values of λ and switching gain a were favorably selected. No significant tracking error or chattering was observed.

12.5 EXPERIMENTAL IMPLEMENTATION

12.5.1 EXPERIMENTS

To test the performances of the algorithms experimentally, the object transport module was connected to the feedback control system as shown in Figure 2, which included an optical sensor, an A/D board, a controller (PC), a function synthesizer and a power amplifier. The excitation frequency of the PZT from the function synthesizer is 26 kHz. Noise in the measured slider displacement was displayed on the controller scope while running the object transport experiment. In experiment, a low-pass RC filter was included to remove high frequency noise. To eliminate the remaining noise, a digital low-pass Infinite Impulse Response (IIR) filter was integrated into the control algorithm[33]. A sixth-order IIR filter was designed for implementation. The optical sensor needs 5 ms to produce an output. The communication between the controller (PC) through a cable to function synthesizer consumes 25 ms per instruction. Two-mode excitation requires a pair of voltage amplitude and phase instructions to be supplied to the actuators. Four instructions were relayed to the function synthesizer in every sampling cycle. As a result, the sampling period can not be reduced below 100 ms.

Based on the simulation results, a PID control was implemented with gains K_p of 3.0, K_i of 0.0, and K_d of 0.3. A SMC was constructed with a constant λ of 8 and switching gain a of 1.05. Sinusoidal waves were used as reference trajectories to observe the performance of the controllers. Due to the limitation of slider velocity, the amplitude and frequency of the sine wave were selected such that the velocity of the reference path did not exceed the capability of slider. Similar to the simulated responses of the reference sine wave, both control algorithms directed the slider to follow the path. PID again showed a noticeable delay, while SMC barely deviates from the desired path. However, the experimental SMC response was not as smooth as that of the simulation. Some roughness and significant position errors near the crest were observed. Similar to the simulation results, measured control activities of SMC were higher than that of PID for both reference paths. Figure 9 shows the responses and control activities of each controller. An additional mass of 100 g was added to the slider to observe the robustness of the control algorithm. As shown in Figure 10, the PID responded with a longer delay while maintaining a smooth path. The SMC showed good tracking performance even though the response showed a position error near the crest due to low sampling time.

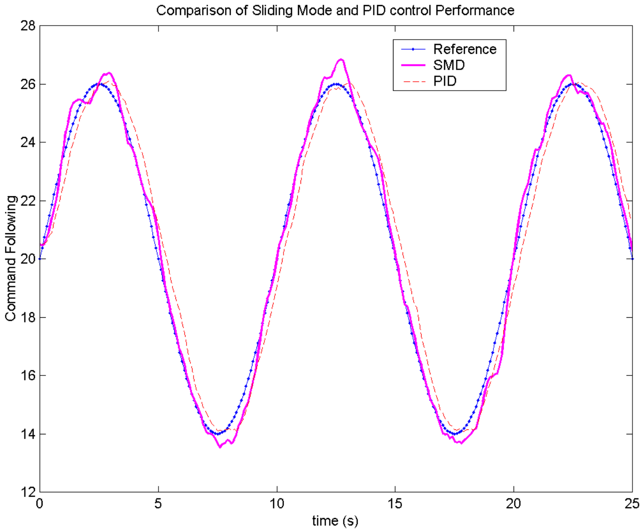

Figure 9. Performances of SMC and PID from the experiment

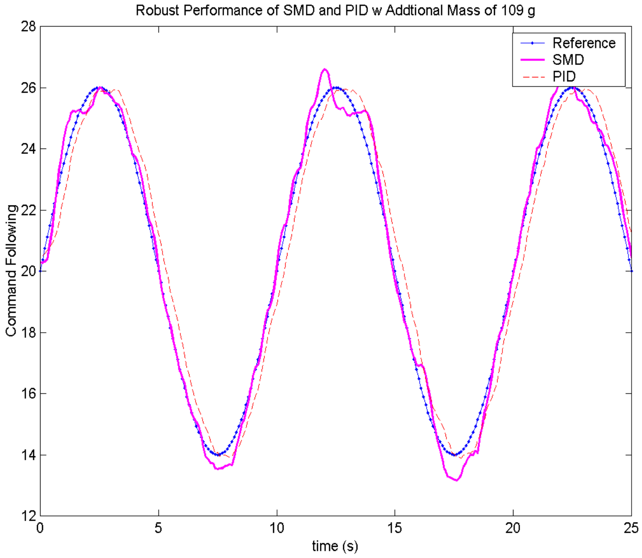

Figure 10. Robustness test of SMC and PID control

To improve the trajectory tracking performance of sliding mode control, the controller was re-parameterized to increase the SMC sensitivity to tracking error. The new set of the SMC parameters is shown in Table 1. The estimated mass $\hat{m}$ and switching gain a are increased. The higher switching gain a contributed to tracking error reduction. Meanwhile, this adjustment increases the chattering in the response because SMC more aggressively penalizes any deviation away from the surface *S*=0. Consequently, the constant λ and damping coefficient were reduced to compromise the effect of those increasing parameter values. With this set of gains, the SMC is expected to be more sensitive to the tracking error without increasing the chattering. The response shows a smoother profile as shown in Figure 11. Reduced tracking error near the crest of the desired path was observed. Again, no significant delay was observed in the responses. However, the resulting response is not perfect as described in the simulation due to hardware limitations.

Table 1. New set of SMC parameters

SMC Parameters	Previous Set	New Parameters
Estimated mass $\hat{m}$ (g)	0.110	0.152
Switching Gain *a*	1.05	1.48
Constant λ	8.0	7.8
Damping coefficient	1.8	1.28

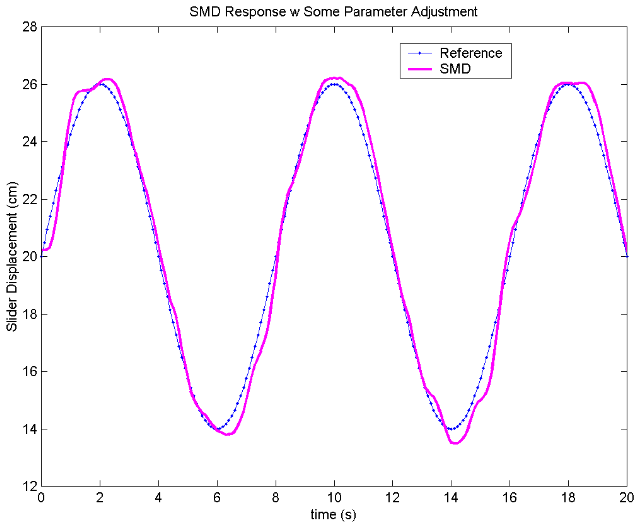

Figure 11. SMC responses with parameter adjustment

12.5.2 DISCUSSION

The experimental results showed the performance of PID and SMC control algorithms in the presence of imprecise parameters and uncertainties. Both algorithms could position the slider on the reference trajectory. Experimental PID and SMC results corresponded well with the predicted behavior in simulation. PID presented a delayed response, whereas SMC could track desired path with negligible error. However, experimental SMC response was less than the predicted in simulation in the terms of tracking performance. The rough response may be the result of the nonlinear friction drive. The simulation employed a linearized model to estimate the controller performance, but in the experiment, the controller faced the nonlinear environment. In addition, the noise residue of the IIR filter can affect the derivative values that show up as ripples in the control law U. If the sampling frequency of controller is increased to 1000 Hz, SMC was expected to deal with unmodeled nonlinearities and uncertainties more efficiently. However, this high sampling frequency is beyond the capability of the present system.

According to the result of robustness test with an additional mass, the response of the SMC was quite smooth. The position response, however, showed a bigger error near the crest. Another run was made by lowering the estimated mass value while increasing the switching gain a to reduce the error. With this run, an increase in chattering was expected. When tested, SMC achieved neither the smooth profile nor reduced tracking error. It seemed that more parameters might be adjusted. By observation, the tracking error was largest near the crest of the reference path where the slider was commanded to change direction.

12.6 CONCLUSIONS

Sliding mode control for a friction-based object transport system using two-mode ultrasonic excitation is presented. A friction drive mechanism was analyzed by applying Hertzian contact and Coulomb's friction theory. An assumption to simplify the modeling of progressive waves generated by two-mode excitation was made. Sliding mode control (SMC) schemes were designed to solve the position-control problem. Simulations verified the algorithm performance. The trajectory tracking performance of SMC was compared with that of PID control by simulation. The result was superior to that of PID. Experimental results at a low sampling frequency of 10 Hz showed that the control algorithms provided a good command following. The good performance can be attributed in part to an accurate friction drive model that was able to predict the nonlinear friction drive close to the measured driving force. The profile of the friction drive with respect to an increasing input voltage agreed with the object transport's behavior. The estimated value, however, was a bit higher than the measured driving force. The causes of the higher estimated friction drive came from the model simplification, imprecise properties of a friction layer, and a worn friction layer.

The feedback control responses of the simulation showed that the SMC slider path was exactly overlaid on the reference trajectory while the linear PID showed a significant delay. The delay was a result of the limitation of the algorithm capability. Implementation problem was a time delay of each hardware process. The feedback control system had to operate at a low sample frequency of 10 Hz, which obstructed the SMC performance. In accordance with the simulation, the experimental PID provided a delay response, while SMC barely deviated from the desired path except near the crest of the path. However, experimental SMC response was less than expected from the simulation in the terms of tracking performance. Significant tracking error and fairly rough response, which were the result of long time delay of the function synthesizer, were observed. SMC was re-parameterized to be more sensitive to the error without increasing a chattering. By increasing an estimated mass $\hat{m}$, and switching gain a and decreasing a constant λ, and damping coefficient, the slider path was quite smooth and significantly reduced a tracking error.

Based on the experimental implementation, the present controller system leaves room for improvement. However, the good performance of the re-parameterized SMC, indicates that a new SMC algorithm that can intuitively change the gains to compensate for the uncertainties is required. Future work would test the potential of an adaptive gain SMC in presence of a low sampling frequency. Another recommendation for future work would be controller hardware development. The controller could not only generate the control law, but also synthesize a signal by itself. With this capability, increasing the sampling frequency from 10 Hz up to 1000 Hz could be achieved. As a result, the present SMC scheme would provide the high- performance feedback control response.

REFERENCES

1. Sashida, T., “Trial construction and operation of an ultrasonic vibration driven motor”, Jpn. J. Appl Phy., vol. 51, pp. 713, 1982 (in Japanese).

2. Kenjo, T. and T. Sashida, “Introduction to Ultrasonic Motors”, Oxford Science Publications, Claredon Press, Oxford, 1993.

3. Ueha, S., Y. Tomikawa, M. Kurosawa and N. Nakamura, “Ultrasonic Motors: Theory and Applications”, Oxford Science Publications, Claredon Press, Oxford, 1993.

4. Hosoe, K., “An application of an ultrasonic motor to automatic focusing lenses”, Proc. 25th Tohohu Univ. Tsuuken Symp., pp. 117-122, 1989.

5. Kurosawa, M. *et al.*, “An ultrasonic motor using bending vibration of a short cylinder”, IEEE Trans. Ultrason., Ferroelec., Freq. Contr., vol. 36, pp. 517, 1989.

6. Uchino, K., K. Kato and M. Tohda, “Ultrasonic linear motors using a multilayered piezoelectric actuator”, Ferroelect., vol. 87, pp. 331-334, 1988.

7. Inoue, T., S. Takahashi and M. Suga, “Application to ultrasonics to paper

transport mechanisms", Techno, pp. 47-49, May 1989 (in Japanese).

8. Kumada, A., "A piezoelectric ultrasonic motor", Japanese J. Appl. Physics, vol. 24 (Supplement 24-2), pp. 739-741, 1985.

9. Zemella, R., "Design and development of a linear traveling wave motor", M.S. thesis in Aeronautics and Astronautics, Massachusetts Institute of Technology, May 1990.

10. Kuribayashi, M., S. Ueha, and E. Moru, "Excitation conditions of flexural traveling waves for a reversible ultrasonic linear motor", J. Acoust. Soc. Japan, vol. 77, no. 4, April 1985.

11. Inaba, R., A. Tokushima, O. Kawasaki, Y. Ise, and H. Yoneno, "Piezoelectric ultrasonic motor", Proc. IEEE Ultrason. Syp., pp. 747-756, 1987.

12. Ultrasonic Motor, Panasonic Industrial Co. (Division of Matsushita Electric Corporation of America), Secaucus, NJ, 1987.

13. Yamaguchi, M., "Vibrator and ultrasonic motor employing the same", U.S. Patent 4 983 874, Jan. 8, 1991.

14. Hirata, H., and S. Ueha, "Design of Traveling wave type ultrasonic motor", IEEE Trans Ultrason., Ferroelec. and Freq. Contr., vol. 42, no. 2, pp.225-231, 1995.

15. Hirata, H., and Ueha, S., "Characteristics estimation of a traveling wave type ultrasonic motor", IEEE Trans Ultrason., Ferroelec., and Freq. Contr., vol. 40, no.4, pp.402-406, 1993.

16. Schmidt, J., P. Hagedorn, and M. Bingqi, "A Note on the Contact Problem in an Ultrasonic Travelling Wave Motor". Int. J. Non-linear Mechanics, vol. 31, no. 6, pp. 915-924, 1996.

17. E. Shigley and C. Mischke, "Mechanical Engineering Design 5th Edition", McGraw-Hill Inc., 1989.

18. Kuribayashi, M., Ueha, S., and Mori, E., "Excitation Conditions for Flexural Traveling Waves for a Reversible Ultrasonic Liner Motor", J. Acoust. Soc. America, vol. 77, no. 4, pp.1431-1435, 1989.

19. Kurasawa, M. and S. Ueha, “High Speed Ultrasonic Linear Motor with Transmission Efficiency”, Ultrasonics, vol, 27, pp.39-44, January 1989.

20. Tomikawa, Y. *et al.*, “Excitation of Progressive wave in a Flexurally Vibrating Transmission Medium”, Proc. 10th Sym. Ultrason. Elect., vol. 29, no.1, pp.179, 1989.

21. Loh, B. and P. Ro, “An Object Transport System Using Flexural Ultrasonic Progressive Waves Generated by Two-Mode Excitation”, IEEE Trans On Ultrson., Ferroelec., *and Freq. Contr.*, vol. 47, no. 4, pp.994-999, July 2000.

22. Kircher Wolfgang, and P. Ro, “A PID Closed Loop Control for an Object Transport System using Flexural Ultrasonic Progressive Waves”, MS. Thesis, North Carolina State University, Spring 2000.

23. Slotine, J., “Sliding Controller Design for Non-linear Systems”, Int. J. Control, vol. 40, no. 2, pp.421-434, 1984.

24. Dunnigan, M. *et al.*, “Position Control of a Vector Controlled Induction machine using Slotine’s Sliding Model Control Approach”, IEE Proc.: Elec. Power Appl., vol. 145, no. 3, pp.231-238, May 1998.

25. Sharaf, E. *et al.*, “Nonlinear Robust Control of a Vector Controlled Synchronous Reluctance Machine”, IEEE Trans. Power Elect., vol. 14, no. 6, pp.111-1121, 1999.

26. Gajdar, T. *et al.*, “Multi-Model based Gain-Scheduling Sling Mode Control Design for an Intelligent Railway Vehicle System”, IEEE Int. Conf. Intel. Eng. Sys., Proc., INES, pp.553-558, 1997.

27. Korondi, P. *et al.*, “Sliding Mode based Disturbance Observer for Motion Control”, Proc. IEEE Conf. *Decision and Contr.*, vol. 2, pp. 1926-1927, 1998.

28. Song, G. *et al.*, “Sliding Mode based Smooth Adaptive Robust Controller for Friction Compensation”, Int. J. Robust and Nonlin. Contr. Vol. 8 no. 8, pp. 725-739, July 1998.

29. Kawabe, T. *et al.*, “Sliding Mode Control for Wheel Slip Ratio Control System”, Vehicle Sys. Dynamics, vol. 27, no. 5-6, pp.393-408, June 1997.

30. Shim, W., and P. Ro, “Robust Friction Compensation of Submicron Positioning

and Tracking for a Ball-screw Driven Slide System", Precision Engineering, J. Int. Soc. Precision Eng. and Nanotech., vol. 24, no. 2, pp.160-173, April 2000.

31. Phillips, A., and M. Tomizuka, "Robust Wide-Range Controller using Multirate Estimation and Control for Velocity Reguation and Tracking", Adv. Info. Storage and Proc. Sys. Amer. Soc. of Mech. Eng., vol. 1, pp 189-196, 1995.

32. Slotine, J., and L., Weiping, "Applied Nonlinear Control", Prentice Hall, 1991.

33. Mitra, S., "Digital Signal Processing A Computer-Based Approach", McGraw Hill Inc., 1998.

13 TOOL DEFLECTION COMPENSATION

Edward L. Miller
Graduate Student
Thomas A. Dow
Professor, Mechanical and Aerospace Engineering
Ken P. Garrard
PEC Staff Member

A technique to compensate for deflection of small milling tools (diameter < 1 mm) has been demonstrated during the past year. This open loop technique involves predicting the cutting and thrust forces, applying these forces to the tool, calculating the tool deflection, finding the magnitude of the error and creating a new tool path to eliminate this error. The tool force model has evolved from a decade of research to predict the forces in diamond turning. This model was modified to include the effects of tool rotation in milling as well as the changes in contact area and force direction using a ball end mill on a free form surface. An extensive set of experimental measurements were made to corroborate the components of the tool forces in the cutting and thrust directions. The force model was then combined with tool stiffness to calculate the deflection of the tool as a function of the depth of cut, the upfeed per revolution and the geometry of the part. Two experiments were used to demonstrate the effectiveness of this compensation technique; a slot and a large circular groove. Each experiment reduced the error due to tool deflection from by an order of magnitude from 20-50 µm to 2-5 µm.

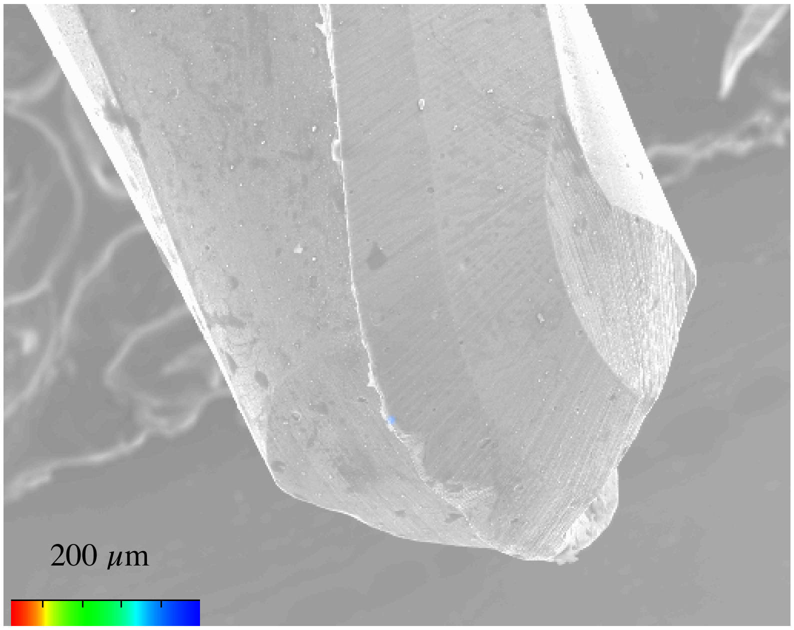

13.1 BACKGROUND

Minor [1], a graduate of the Precision Engineering Center (PEC), developed a model for predicting the cutting forces on straight end milling cutters in both the cutting and radial directions. This model grew out more than a decade of involvement at the PEC by Arcona [2], Drescher [3,4] and Carroll [5]. Using such a model, the process can be better controlled and more precise parts can be machined.

The application of the model to milling cutters [1] had a similar goal; that is, predicting the magnitude of the force and the change due to tool wear, then using that information as a control input for the machining process. Position control becomes an increasingly important problem as the features required for new designs become smaller and the concomitant accuracy becomes higher. This problem takes on a different dimension when applied to miniature end mills (diameters < 1mm). The forces associated with cutting can produce significant deflection in these long thin tools. Ball end mills compound the problem because cutting can take place at different points and directions around the radius of the ball end. The resulting forces are applied in different directions and because the tool stiffness is significantly different in the radial vs. axial direction, different deflections are produced for the same applied load. Since such tools are required for small features, compensation for the tool deflection is an important goal.

The objective of this section is to describe the application of the cutting model to the geometry of a miniature ball end mill and to develop a open loop technique to compensate for the resulting tool deflection. With knowledge of the shape of the part from the CAD model, the tool geometry and the predicted tool forces, a compensation technique to modify the part program for the machine controller has developed. The result of this work is an integrated compensation technique that will account for tool deflection due to cutting forces, reduce the overall errors and improve the accuracy of the machined part.

13.1.1 MINIATURE MILLING TOOL DESCRIPTION

Dies and injection molds have small features and three-dimensional free form surfaces to meet specific functional specifications. Because of the nature of this application, the mold surfaces must be reproduced in hard steel. Until recently, such dies were manufactured by grinding and polishing, a process requiring long lead time and often lacking the required accuracy. Increasingly, these dies are being fabricated using high-speed ball end mills. Several toolmakers currently manufacture miniature ball end milling tools in a range of diameters down to 0.2 mm. The supplier of the tools selected (Jabro Tools) makes tools with diameters from 0.2 to 1.5 mm and three different flute lengths - short (0.8 mm), long (2.5 mm to 7.5 mm) and extra long (4 mm to 12 mm). Figure 1 is a photograph of the short, long and extra long milling tools.

The tools are made from Tungsten carbide coated with titanium aluminum carbide to improve wear resistance. The workpiece material is S7 tool steel (Hardness = 52-55 Rc). Under these conditions, the tool force compensation technique cannot be applied.

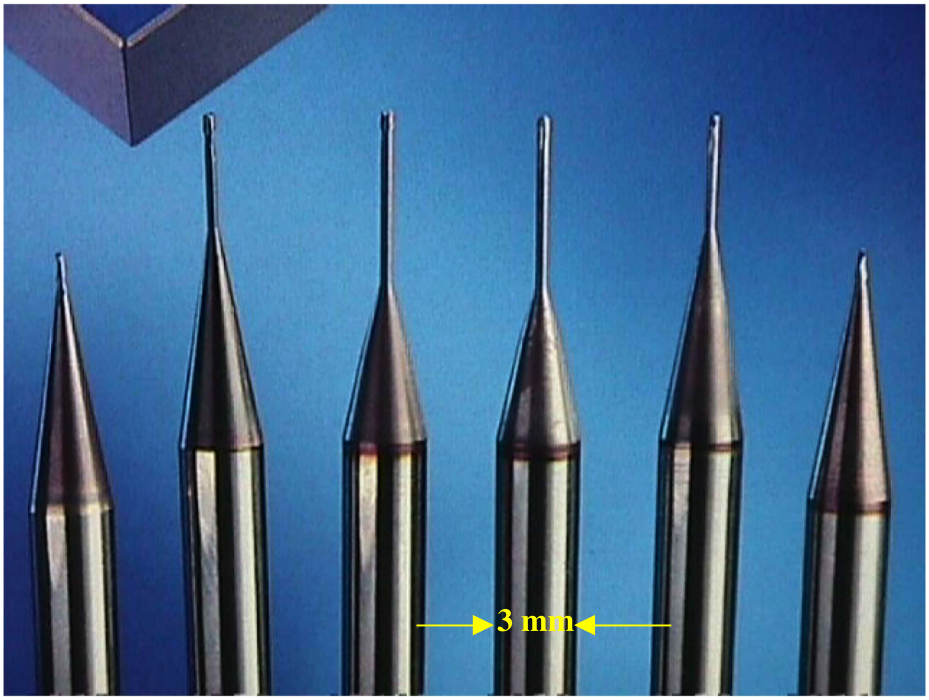

Figure 1. Photograph of miniature milling tools. Short tools at the ends, long inside them and extra long tools at the center.

13.2 TOOL FORCE MODEL

13.2.1 MODEL BACKGROUND

Drescher was the first student at the PEC to investigate cutting forces developed in a diamond turning operation in an MS program funded by Kodak. Drescher continued his work as a PhD student and developed a model for tool forces based on experimental measurements of cutting and thrust forces in diamond turning. Arcona continued Drescher's work and added an elastic component to the analysis resulting in the following equations for the cutting and thrust forces in a diamond turning operation.

$$F_c = \frac{HA_c}{3}\left(\frac{\cot(\gamma)}{\sqrt{3}}+1\right)+\mu_f A_f\left(0.62H\sqrt{\frac{43H}{E}}\right) \tag{1}$$

$$F_t = \frac{\mu HA_c}{3}\left(\frac{\cot(\gamma)}{\sqrt{3}}+1\right)+A_f\left(0.62H\sqrt{\frac{43H}{E}}\right) \tag{2}$$

where

H = hardness of workpiece material
E = elastic modulus of the workpiece material
A_c = face area of chip (~ depth of cut times the feed distance per revolution)
A_f = flank area of the tool (width of worn region on flank face)
μ = friction coefficient at the interface between the rake face of the tool and the workpiece
μ_f = friction coefficient at the interface between the flank face of the tool and workpiece
γ = shear angle of the chip (the value used in the model for S-7 steel was 50°).

Arcona's tool force model was used to predict the cutting forces developed in a ball end milling operation for this project. Because the milling process involves a tool that rotates, it was necessary to modify the chip geometry in a manner similar to Minor [1]. Two areas of tool contact are important; the face area of the chip and the flank area of the chip. The face area changes with the depth of cut and the flank area changes with wear of the tool.

13.2.2 CHIP FACE AREA

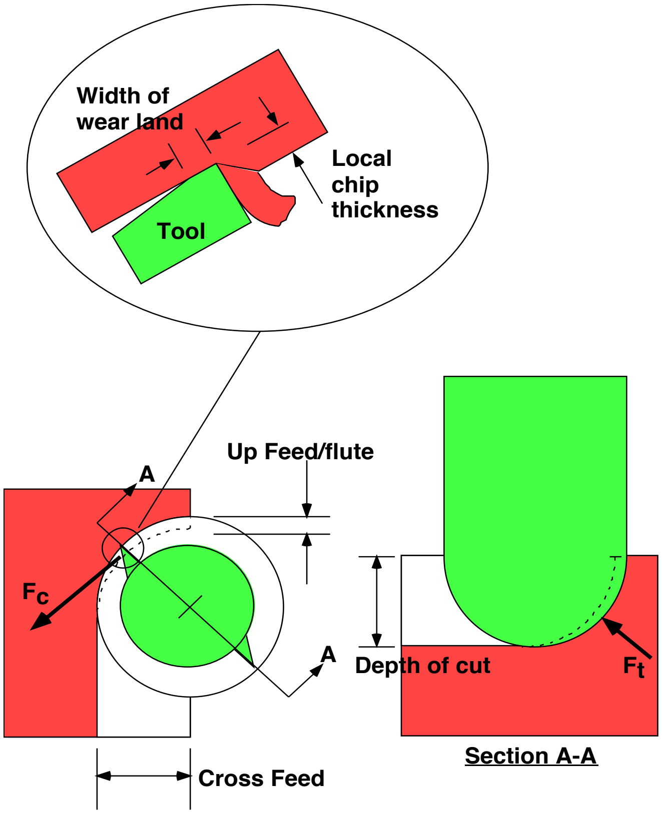

Figure 2. Sketch of chip geometry and tool forces in a ball end milling process.

In an orthogonal cutting process, the chip area is simply the cross-feed multiplied by the depth of cut. However the ball end milling process illustrated in Figure 2 is more complicated. As the tool rotates it also translates (feeds) through the workpiece and the chip area changes as a function of tool rotation. Figure 2 shows how the chip area changes and the forces developed during the cutting process. The change in chip area can be approximated by

$$A_c = df \sin\theta(1 \pm \zeta) \tag{3}$$

where d is the depth of cut, f is the cross-feed per flute of the tool, θ is the rotational position of the tool, and ζ is the offset of one flute with respect to the other. If the tool has runout (due to centering or tool fabrication error), then one flute will cut a larger chip than the other flute. Hence, the cutting forces will increase some percentage for one flute and decrease that same percentage for the other flute during each revolution of the tool.

13.2.3 TOOL FLANK AREA

The second chip area term in the force model is the flank area of the tool. This area can be described as the interface between the flank of the tool and the workpiece material and is illustrated in the inset of Figure 2. In orthogonal machining the flank area is simply the width of the wear land times the length of the tool in contact with the workpiece. As with the face chip area, A_c, the flank area for a ball end milling operation is more complicated due to the geometry of the tool. The flank area in a ball end milling process will be a function of tool radius, wear land width, contact angle, and tool rotation. The approximation for the flank chip area is,

$$A_f = \left(\frac{R_t * W_L * \phi}{2 - sin\theta}\right) = \left(\frac{L_c * W_L}{2 - sin\theta}\right) \tag{4}$$

where R_t is the radius of the tool, W_L is the width of the wear land, ϕ is the contact angle between the tool and the workpiece defined by the tool radius and the depth of cut and θ is the rotational position of the tool. The length of contact, L_c, is shown in Figure 2 and is equal to R_t times ϕ. Using these two chip area calculations, Arcona's tool force model can now be applied to a ball end milling operation. Experimental measurements of the forces using ball end mills will be compared to the forces calculated using the tool force model. The wear land values used in the force model were measured experimentally using the method described next.

Tool Wear Land Measurement Technique A wear land is a flat region worn on the flank face of the tool (see Figure 2) as it rubs against the previously machined portion of the workpiece. As sliding increases over time, the size of the wear land increases, which in turn causes the forces to increase. Therefore, it is important to know the width of the wear land on the tool to correctly predict the force.

A scanning electron microscope (SEM) image of a used tool is shown in Figure 3. The average wear land width for this tool is approximately 15 μm. The measured width of the wear land is used in the tool force model.

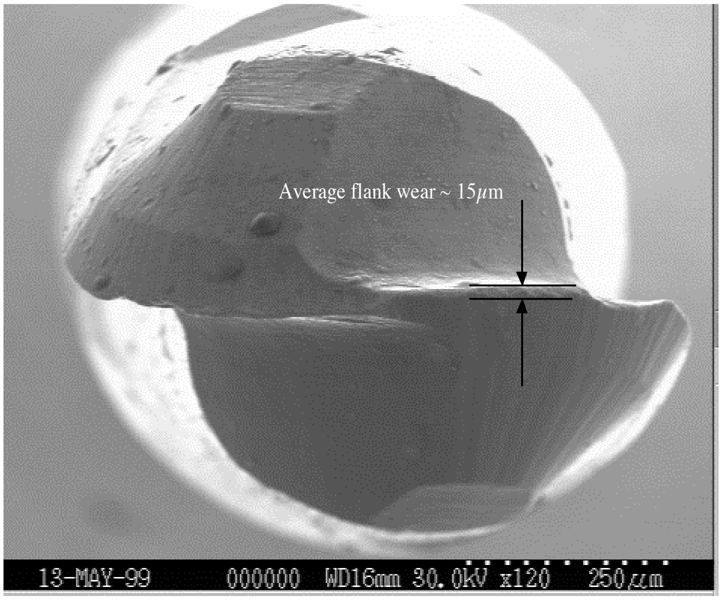

Figure 3. SEM image of a worn ball end mill.

While the SEM provides a high quality image of the tool, it is time consuming to set up and use. A more practical approach is to use a light microscope to measure the wear land on the milling tools. Since the wear land is flat it will appear as a bright region in the field of view as the tool is rotated and the wear land becomes parallel with the objective lens of the microscope. Since the flutes of the ball end mill are straight in the cutting region, a fixture was built to position the tool under the microscope. Figure 4 is a sketch of the tool fixture. The tool is held at the focus of the objective lens by the fixture and it can be rotated such that the entire length of each flute can be carefully examined and measured.

The width of the wear land was quantified using a calibrated video micro-scaler. The tool is placed in the fixture and the wear land is located. The image of the tool and the calibrated lines are projected onto the monitor to read the width of the wear land.

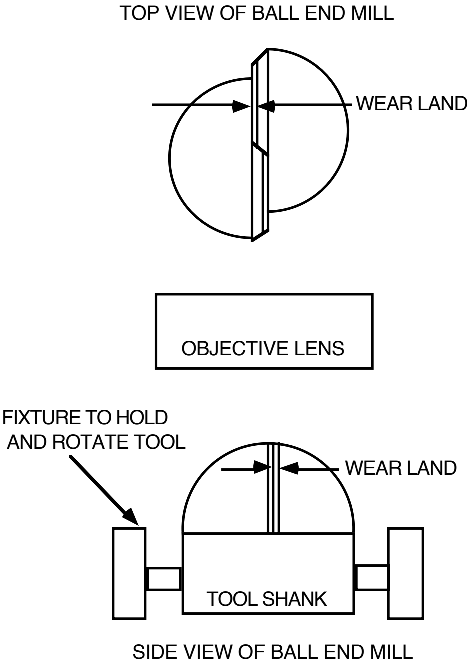

Figure 4. Apparatus used to view flank wear.

13.3 TOOL FORCE MEASUREMENT EXPERIMENTS

13.3.1 EXPERIMENTAL SETUP

A cutting experiment was developed such that the tool forces could be measured using a Kistler 9255A three-axis load cell. The forces were generated during slot cutting with a ball end mill. The experiment was to collect data while cutting the slot in a piece of S-7 steel at a fixed up-feed and depth of cut using new short and long 0.8 mm diameter ball end mills. The force data was acquired for several different cutting conditions.

Figure 5 is a photograph of the experimental force measurement system. The three-axis load cell is mounted in a specially designed mount on the X-axis of the Nanoform 600 diamond turning machine. A piece of S-7 steel that has been ground flat on both sides is used as the test specimen. It is secured through the top of the load cell with a bolt preloaded to 30 N-m. The milling tool is mounted in a Westwind D1090-01 air bearing turbine spindle capable of speeds up to 60,000 rpm. This spindle is attached to the Z-axis of the Nanoform 600.

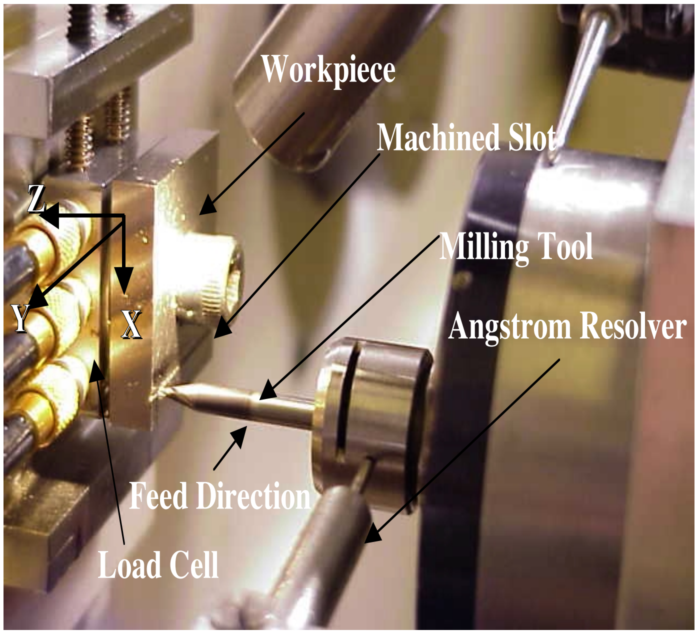

Figure 5. Photograph of experimental force measurement system.

To determine the speed of rotation of the tool, an optical detector was used to measure the time for a single rotation of the spindle. A section of the spindle collet was marked with black ink that produced a change in reflectivity on the collet that could be detected with an optical displacement gage (Angstrom Resolver) mounted perpendicular to the spindle collet. The output from the gage was connected to an oscilloscope and the square wave produced was used to measure the spindle speed. This mark was also used to set the angular orientation of the tool during the tool installation in the spindle.

Experimental Procedure During the cutting experiments, a four-channel digital oscilloscope simultaneously recorded the tool rotation speed and the cutting forces in the x, y, and z directions. After the data was captured in the HP 54501A digitizing oscilloscope, it was transferred to a personal computer for further analysis using a software package called HP 34810B BenchLink Scope. The software was used to transfer an image of the screen with the captured waveforms as well as 500 time and voltage data values for each trace. This data could then be transferred to another software application for further analysis.

Figure 6 is a plot of the data acquired from an experiment. The graph shows the data collected over 20 ms. Each period of the square wave represents one revolution of the tool rotating at 10,000 rpm. Hence, three and one third revolutions of data (500 points) were acquired from all four channels of the oscilloscope. This figure shows the repeatability of the forces in each direction from one revolution of the tool to the next.

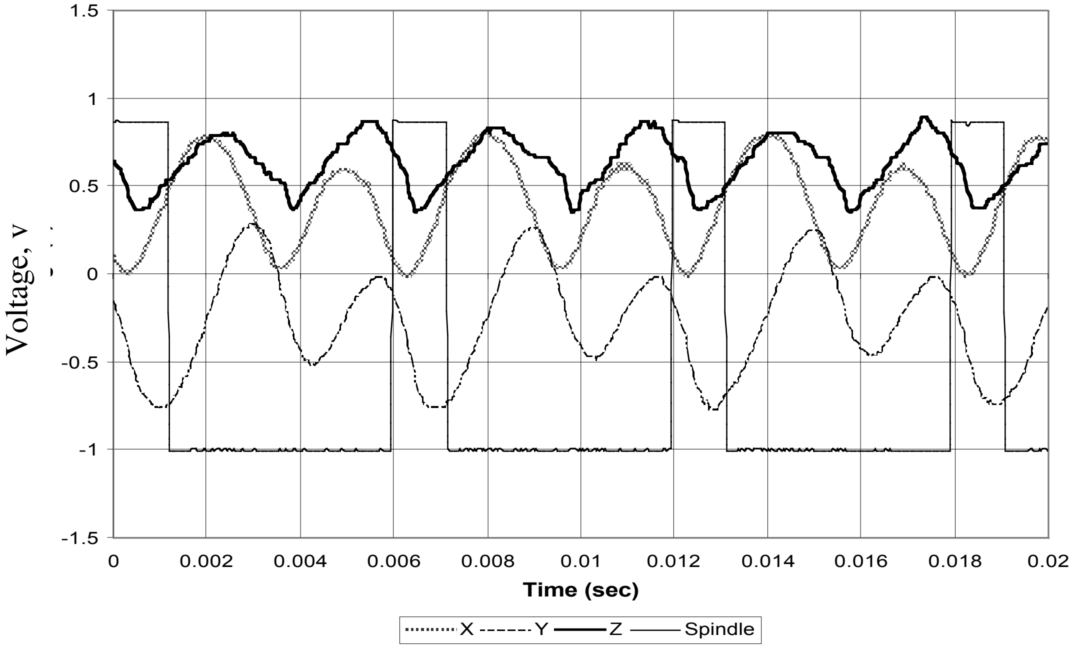

Figure 6. Graph of experimentally measured cutting forces and once-per-revolution output from the optical detector of spindle rotation.

13.4 COMPARISON OF TOOL FORCE MEASUREMENTS AND MODEL

The data acquired during the experiments can be compared to that predicted by the model for similar machining conditions. First, the force in each direction is averaged over the number of spindle rotations recorded and then converted from volts to force in Newtons. This conversion is based on the calibration of voltage vs. force performed on each channel of the load cell.

The forces predicted in Equations (1) and (2) are in the cutting and radial directions to the tool motion. To compare these forces to the experiments, the forces predicted with the model (cutting and thrust) are transformed into Cartesian (x,y and z) forces using the following transformation.

$$
\begin{aligned}
F_x &= F_c \cos\alpha \sin\theta - F_t \sin(0.5\phi)\cos\theta \\
F_y &= -F_c \cos\alpha \cos\theta - F_t \sin(0.5\phi)\sin\theta \\
F_z &= F_c \sin\alpha \cos\theta + F_t \cos(0.5\phi)\sin\theta
\end{aligned}
\tag{10}
$$

where

$F_c =$ cutting force from Equation (1)
$F_t =$ thrust force from Equation (2)
$\alpha =$ sweep angle (angle between the rotation axis of the tool and a line normal to the workpiece surface)
$\phi =$ contact angle between the tool and workpiece from Equation (11)
$\theta =$ rotational position of the tool

Figure 7 shows a sketch of the tool tilted and defines the sweep angle α and the contact angle ϕ associated with the transformation Equation (10). The contact angle is defined as follows:

$$\phi = cos^{-1}\left(1 - \frac{d-\delta}{R_t}\right) \tag{11}$$

where

$d =$ programmed depth of cut
$\delta =$ tool deflection (sum of components in radial and axial directions)
$d-\delta =$ actual depth of cut

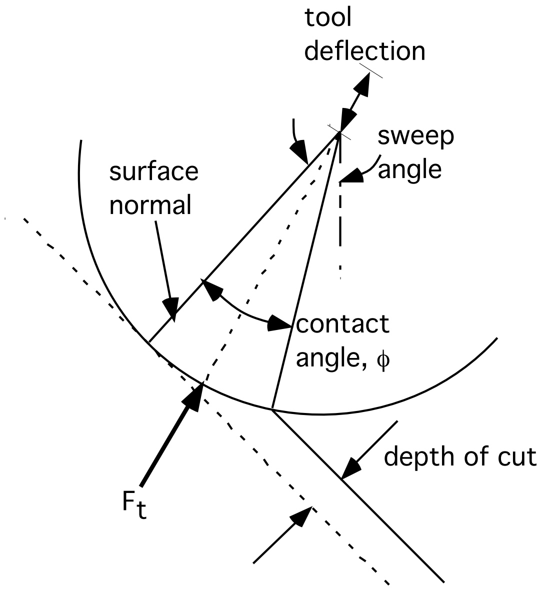

Figure 7. Sketch of ball end mill contact geometry.

The force measurements were conducted for several different cutting parameters to demonstrate the validity of the cutting model. In addition, the reproducibility of the force measurements was investigated by repeating one high force and one low force experiment using a different cutting tool. The experiment involved cutting a series of single grooves using a constant depth of cut, a constant feed rate and the tool normal to the surface (α=0). A list of the cutting parameters investigated in this series is given in Table 1.

The data from four of the experiments listed in Table 1 were compared with the forces predicted using the tool force model of Equations (1) and (2) with the transformations in Equation (10). The results are shown in Figures 8 through 11. Each graph shows the measured force in the x, y and z directions averaged over 3+ revolutions of the tool compared with the forces predicted from the model. Figures 8 and 9 show a low up-feed and high up-feed respectively using a small depth of cut, while Figures 10 and 11 show low and high up-feeds respectively using a larger depth of cut.

Table 1. Cutting parameters for force measurement experiments. Repeated experiments are denoted with (*).

Up-feed (μm / rev)	**Spindle Speed (rpm)**	**Depth of Cut (μm)**
18.75	40,000	25 (*)
18.75	40,000	100
18.75	10,000	25
18.75	10,000	100
75	10,000	25
50	10,000	100 (*)

Figure 8 is a graph of the forces in the x, y and z direction for a single rotation of the milling tool as it cuts a slot in the hardened S-7 steel. The definition of the x, y and z directions are set by the orientation of the load cell and are shown in Figure 5. The spindle speed is 40,000 rpm so the time scale associated with each revolution is 1.5 ms. The cutting conditions are a depth of 25 μm, an up-feed of 18.75 μm, a tool with two flutes and an average wear land of 7 μm. The three lines are the output of the model for these cutting conditions and the dots are the average measured values of the force over the 3+ revolutions of the tool.

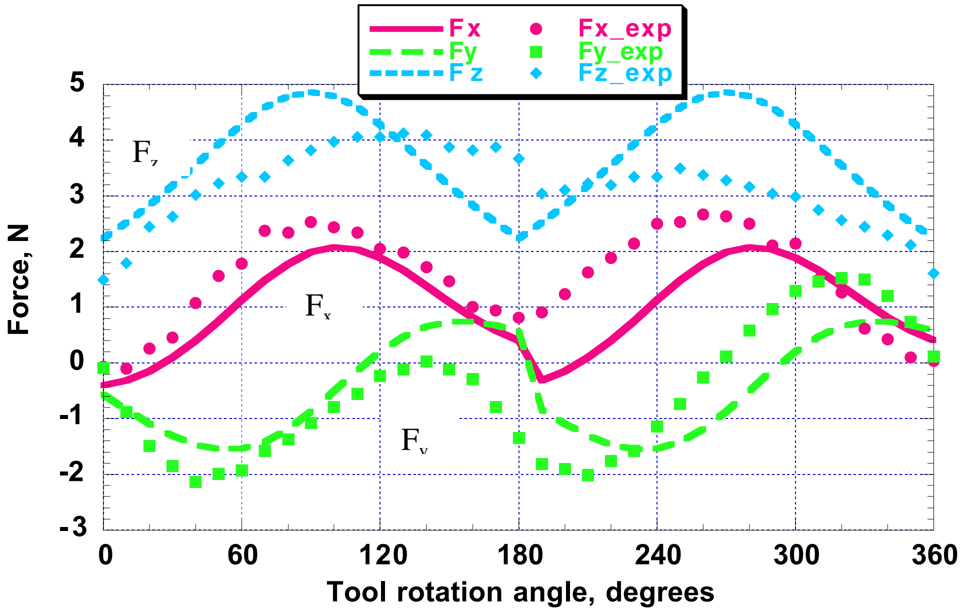

Figure 8. Experimentally measured cutting forces and predicted cutting forces.

Cutting parameters: Up-feed = 18.75 μm/rev; Spindle = 40,000 rpm; Depth of Cut = 25 μm.

Z-Force The general trend of the data is to repeat at 180° intervals because of the two flutes. The top curve is the z force which is always positive; that is, in a direction to push the workpiece away from the tool. There is some disagreement between the numerical value of the force between the model and the measurements but both start at 2 N as flute 1 enters the cut at 0°, peak near 90° at 5 N and repeat for the flute 2. Notice that the peak force associated with the flute 2 is less than for flute 1. This is most probably due to runout in the tool making the chip size different for each flute. The model applied to Figure 8 did not consider runout but this effect was included in Figure 9 using Equation (3).

X-Force The middle curve in Figure 8 is the force measured in the x direction. In this case the force measured as the flute enters the cut is nearly zero, it rises to a peak of 2 N near 90° and returns to zero at 180°. The tool is perpendicular to the z direction in these experiments so the cutting force (Equation (1)) has a dominant effect on the forces measured in the x and y directions. Here flute 1 enters the slot at zero depth of cut which increases to a maximum at 90° of rotation when the flute is horizontal; that is, the cutting force points down or in the positive x direction in Figure 5. The second half of the motion of flute 1 is the inverse of the first half. The model shows a discontinuity at 0° and 180° because of the influence of the thrust force, which in this case is small. The model for thrust force in Equation (2) shows that the second term does not depend on the depth of cut so it will remain at a constant value. When flute 1 leaves the workpiece and flute 2 enters at 180°, there is a component of the thrust force that reverses. This effect is sometimes measured in the experiments but does not exactly match the model.

Y-Force The bottom curve in Figure 8 is the force in the y direction – opposite to the feed direction of the workpiece. In the y direction, the force changes sign; for the first quarter revolution, the force is negative or opposite to the feed direction. It then changes sign as the flute begins moves in the +y direction. The second flute shows the same behavior. The forces measured in the y direction are about 45° out of phase with the x forces as a result of the transformation equations.

In Figure 9, F_x and F_y are approximately 20% higher for the cut made by the first flute (0° - 180°) than for the cut made by the second flute (180° - 360°). The reason for the difference between the force is likely the effect of tool runout; the magnitude of which is ±5 μm for the high-speed spindle. The runout of the tool is also evident in Figure 11 where the first flute cuts approximately 35% more than the second flute. The effect of tool runout for the high-speed spindle can be minimized. This was accomplished by using a Federal gage to measure the runout of the tool in the spindle. The tool can then be rotated in the spindle collet and re-measured; this was repeated until the runout was minimized. This technique was used on the later experiments shown in Figures 8 and 11, but was not used earlier for the data shown in

Figures 9 and 10. For the spindle and tools used in these experiments the runout could be reduced approximately 60% by using this technique.

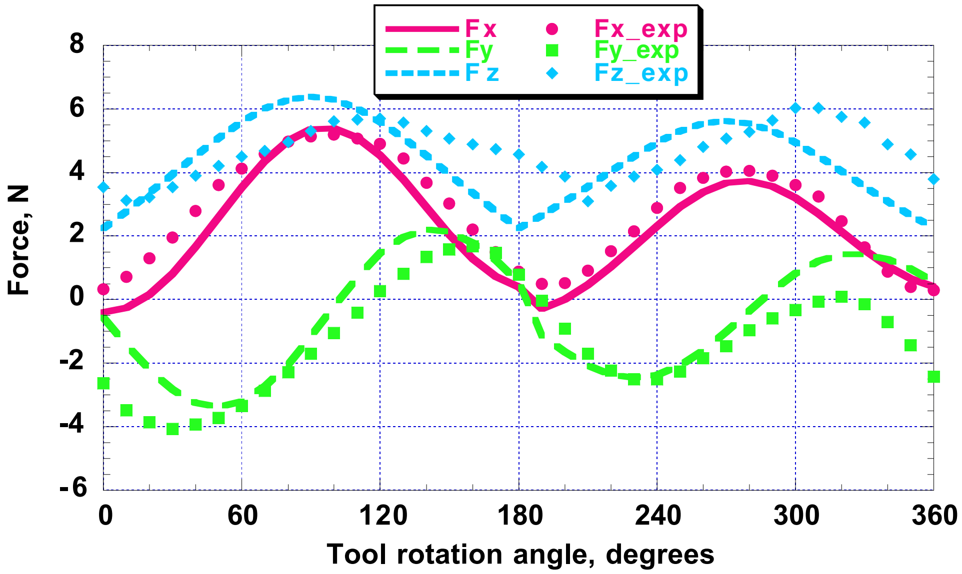

Figure 9. Experimentally measured cutting forces and predicted cutting forces. Cutting parameters: Up-feed = 75 μm/rev; Spindle = 10,000 rpm; Depth of Cut = 25μm.

Figures 8 and 9 show the effect of changing the up-feed of the tool while holding the depth of cut constant. Since Figure 8 represents an experiment with a lower up-feed (smaller chip removal rate), the forces are expected to be lower than those shown in Figure 9 where the up-feed is four times higher. The maximum forces for the higher up-feed experiment in the F_x and F_y directions are approximately twice that for the lower up-feed experiment. The maximum force in the F_z direction is approximately 50% more for the higher up-feed experiment. The model does a good job of following the experimental measurements. The expected increase in force for this change in up-feed is 50% (as measured) in the z direction and double (as measured) in the x and y directions.

Figures 10 and 11 can be compared in a similar manner to Figures 8 and 9; however in this case, the up-feed is increased while holding the depth of cut constant. Notice that the forces (both measured and predicted) in the x, y and z directions in Figure 11 are double the values measured in Figure 10. Also notice in Figure 10, the runout is much higher and the model has been compensated to include this effect.

One other comparison to be made for this data is to contrast the results in Figures 9 and 10. In Figure 9, the depth of cut is 75 μm and the up-feed is 25 μm for a product of 1875. In Figure 10, the depth of cut is 100 μm and the up-feed is 18.75 μm for a product of 1875. If the force was simply proportional to the amount of material removed, these two cases should be equivalent.

However, a comparison of the two figures shows a significant difference. The larger depth of cut and smaller feed rate exposes a greater length of the tool to contact with the workpiece and leads to larger forces. The P-P value of the x, y, and z forces in Figure 9 are approximately 60% of those measured for the conditions of Figure 10.

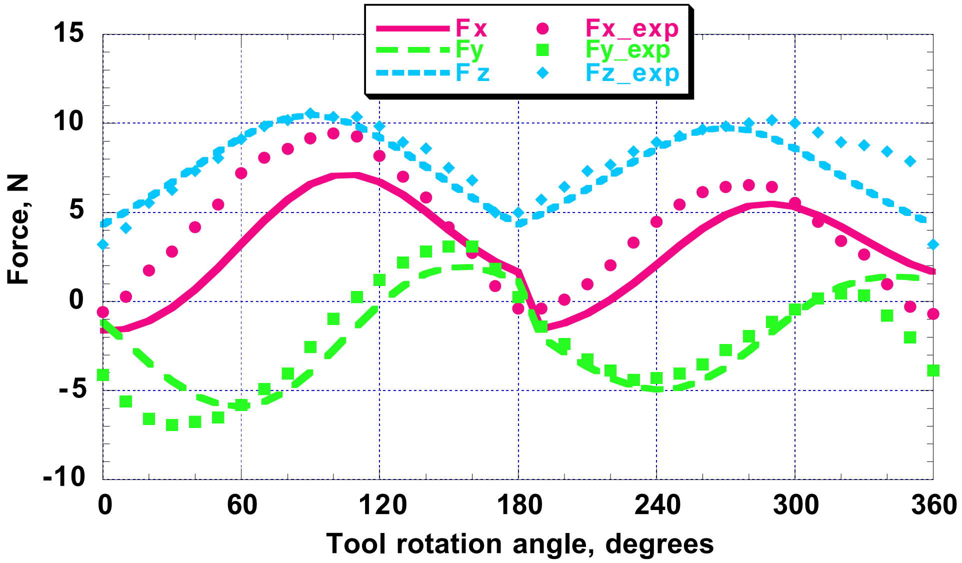

Figure 10. Experimentally measured cutting forces and predicted cutting forces. Cutting parameters: Up-feed = 18.75 μm/rev Spindle = 10,000 rpm Depth of Cut = 100μm.

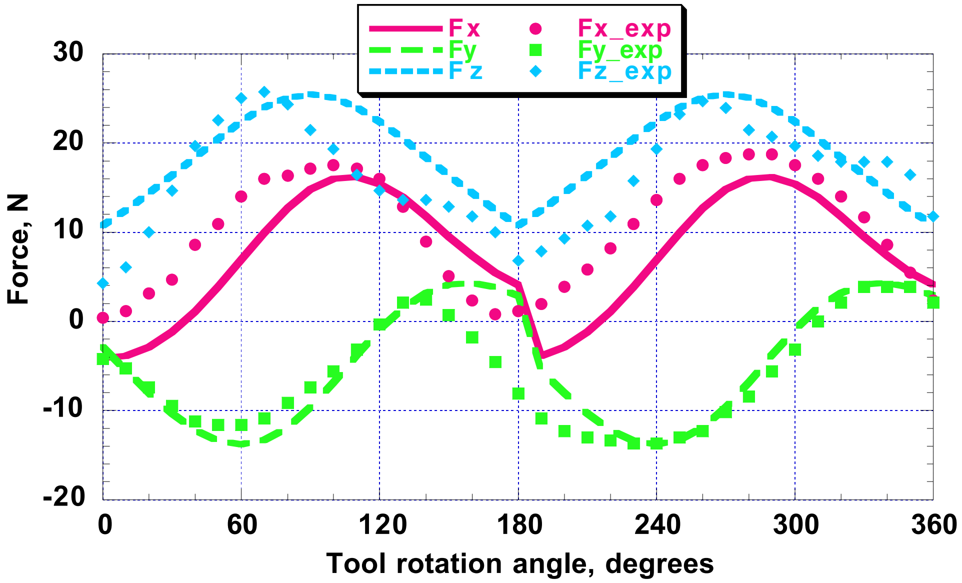

Figure 11. Experimentally measured cutting forces and predicted cutting forces. Cutting parameters: Up-feed = 50 μm/rev Spindle = 10,000 rpm Depth of Cut = 100 μm.

The forces measured in the experiments ranged over an order of magnitude from 2 to 20 N. The model appears to provide a good estimate of the cutting and thrust forces and proved useful in the compensation experiments.

13.5 TOOL STIFFNESS

The tool force model predicts the cutting and thrust forces. To find the tool deflection caused by these forces, however, it is necessary to know the stiffness of the tool. The stiffness of the small ball end mills have been estimated analytically and experimentally measured.

13.5.1 TOOL STIFFNESS MEASUREMENTS

The radial deflection of the tool was measured with the tool mounted in the spindle. A wire was glued to the end of the tool and different weights were suspended from the wire. An electronic indicator was positioned on the tool where the wire was attached. The experiment involved suspending a weight from the wire, zeroing the electronic indicator, removing the weight and reading the indicator. This procedure was repeated several times for a range of loads from 20 to 200 grams. A force-deflection curve was plotted using the average deflection calculated for each set of data. The slope of the curve yields the stiffness of the tool. The experiment was performed on the short, long and extra long 0.8 mm diameter ball end mills illustrated in Figure 1. A similar procedure was followed to measure the axial stiffness of the spindle except that the force was applied along the axis of the spindle.

13.5.2 STIFFNESS CALCULATION

Since measurement of tool stiffness is a time consuming task, the idea of estimating the stiffness based on the tool geometry is attractive. The stiffness was calculated using simple beam theory based on the diameter and length of the tool. The radial deflection was calculated by modeling the tool as a cantilever beam mounted to a rigid support loaded at the end. The assumption of a rigid support was inaccurate and measurements of the spindle stiffness were necessary to reconcile the results. The axial deflection was calculated by modeling the tool as an axially loaded beam mounted to a rigid support and again the spindle stiffness was important. The tool is much stiffer in the axial direction and therefore it will deflect more in the radial direction for the same applied loads. Equations (12) and (13) were used to calculate the tool deflection.

$$K_r = \frac{F}{\delta_r} = \frac{3EI}{L^3} \tag{12}$$

$$K_a = \frac{F}{\delta_a} = \frac{EA}{L} \tag{13}$$

K_r = radial stiffness of the tool
F = force applied to the tool
δ_r = radial deflection of the tool
E = elastic modulus of the tool
I = area moment of inertia of the tool
L = length of tool
K_a = axial stiffness of the tool
δ_a = axial deflection of the tool
A = cross sectional area of the tool

Spindle Stiffness The radial stiffness, axial stiffness and tilt of the spindle will have an impact on the measured tool stiffness as well as the deflection during a cutting operation. To determine the spindle stiffness, measurements of the deflection of a 3 mm diameter cylinder mounted in the spindle were made at different points along the length. This data was fit to the model in Equation (14) and the radial and tilt deflection of the spindle (α_0 and δ_0) as a function of load were determined.

$$\delta(x) = -\frac{F}{EI}\left(\frac{Lx^2}{2} - \frac{x^3}{6}\right) + \alpha_0 x + \delta_0 \tag{14}$$

where

α_0 = tilt of the tool at the face of the spindle
δ_0 = radial deflection of the tool at the face of the spindle

The axial stiffness of the spindle was measured by hanging a weight from the tool end with the spindle mounted in a vertical direction. A Federal gage was used to measure the displacement of the collet. Using the measured displacement the axial stiffness of the spindle was determined to be 850,000 N/m at an air pressure of 40 psi and 980,000 at 80 psi. Milling experiments up to this point have been run with the spindle air bearing pressure set to 40 psi. The axial stiffness of the tool itself was not measured.

13.5.3 COMPARISON OF MODEL AND MEASUREMENTS

Table 2 is a list of the measured tool stiffness for the short, long and extra long milling tools and the calculated stiffness of the tool with the effect of the spindle stiffness. The predicted stiffness of the long tool is quite close to the measurements but the short tool stiffness is much larger than the predicted value. This difference is due to the unmodeled shape of the reduced section of the tool as a result of grinding the ball end mill geometry. This change will reduce the calculated stiffness toward the measured value. While this comparison indicates that calculations could be used to find the stiffness, the measured values were used for the experiments.

Table 2. Measured and calculated stiffness of ball end mills.

Tool Length (Stiffness Direction)	Measured Stiffness, N/m	Calculated Stiffness Including Spindle Stiffness, N/m
Short (Radial)	406,200	557,000
Short (Axial)	$2.6x10^6$	$2.6x10^6$
Long (Radial)	198,500	208,000
Long (Axial)	$2.6x10^6$	$2.6x10^6$
Extra Long (Radial)	77,290	78,190
Extra Long (Axial)	$2.6x10^6$	$2.6x10^6$

13.6 TOOL DEFLECTION COMPENSATION

13.6.1 SLOT WITH LINEARLY VARYING DEPTH

An experiment was developed to show that the deflections of the tool could be predicted and compensated. The experiment involved cutting slots in the hard steel workpiece with the tool tilted at three different angles (α = 10°, 25°, and 50°). The depth of cut varied linearly from 0 to 75 μm over a 20 mm length. Figure 12 is a sketch of the experimental set up. First, a slot was cut at the three different tool tilt angles (α) without compensation. Since the tool will deflect due to the cutting forces, the desired (i.e., programmed) depth of cut will not be reached. Next, the three more slots were cut at the same tool tilt angles but changing the programmed depth based on tool deflection calculations.

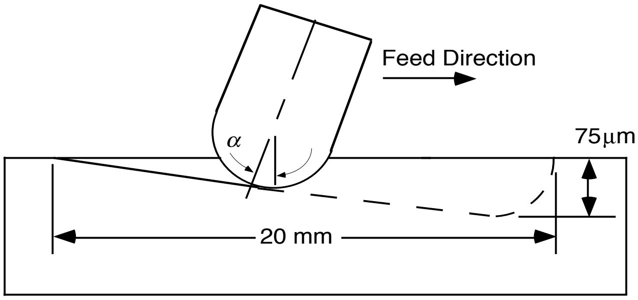

Figure 12. Sketch of linearly varying depth of cut experiment.

Force/Deflection Relationship There is a non-linear relationship between the machining force and the tool deflection. A cutting and thrust force will be generated for any given depth of cut and feed rate. These forces will produce a deflection of the tool and a reduction in the depth of cut and/or cross-feed that will lower these forces. Because of this interaction between force and deflection, the force equation must be solved iteratively. For example, if the angle of interest for the tool deflection is the flute just entering the cut (tool rotation angle $\theta=0$), the thrust force (F_t) on the tool can be written as the second term in Equation (2).

$$F_t = K_2 \;\; W_L \;\; R_t \;\; cos^{-1}\left[1-\frac{d-\dfrac{F_t}{K_t(\alpha)}}{R_t}\right] \tag{15}$$

where

K_2 = material constant $= 0.62H\sqrt{\dfrac{43H}{E}}$

W_L = width of the wear land

R_t = radius of the milling tool ball end

d = programmed depth of cut

$d-\dfrac{F_t}{K_t(\alpha)}$ = actual depth of cut including tool deflection

$K_t(\alpha)$ = tool stiffness which is a function of the direction of the force

If the forces must be calculated for another rotational angle of the tool, both cutting and thrust forces are involved. The complication in Equation (15) is that the thrust force is on both sides of the equation. This force changes the depth of cut and therefore the contact length between tool and workpiece. Because the thrust force is inside the inverse cosine on the right, it cannot be easily extricated. As a result, an iterative program was written to calculate the force as a function of the operating conditions and tool geometry. The tool stiffness plays an important role in the tool force expression. If the tool were infinitely stiff ($K_t = \infty$), the force would not effect the depth of cut and would only be a function of the depth of cut. If, on the other hand the tool were infinitely compliant ($K_t = 0$), then the angle of contact would be zero and no force could be applied because the tool would bend away from the part. This equation can also be solved for the force necessary to produce a desired depth of cut including the effects of tool deflection.

There is a value of force that will satisfy Equation (15); and once that force is known, the deflection can be calculated using the tool stiffness. With this knowledge, an algorithm can be created to find a commanded depth of cut that will produce the desired depth. In other words, since the tool deflection has been predicted, the depth of cut in the part program can be changed (increased) to compensate for that deflection and achieve the desired depth of cut.

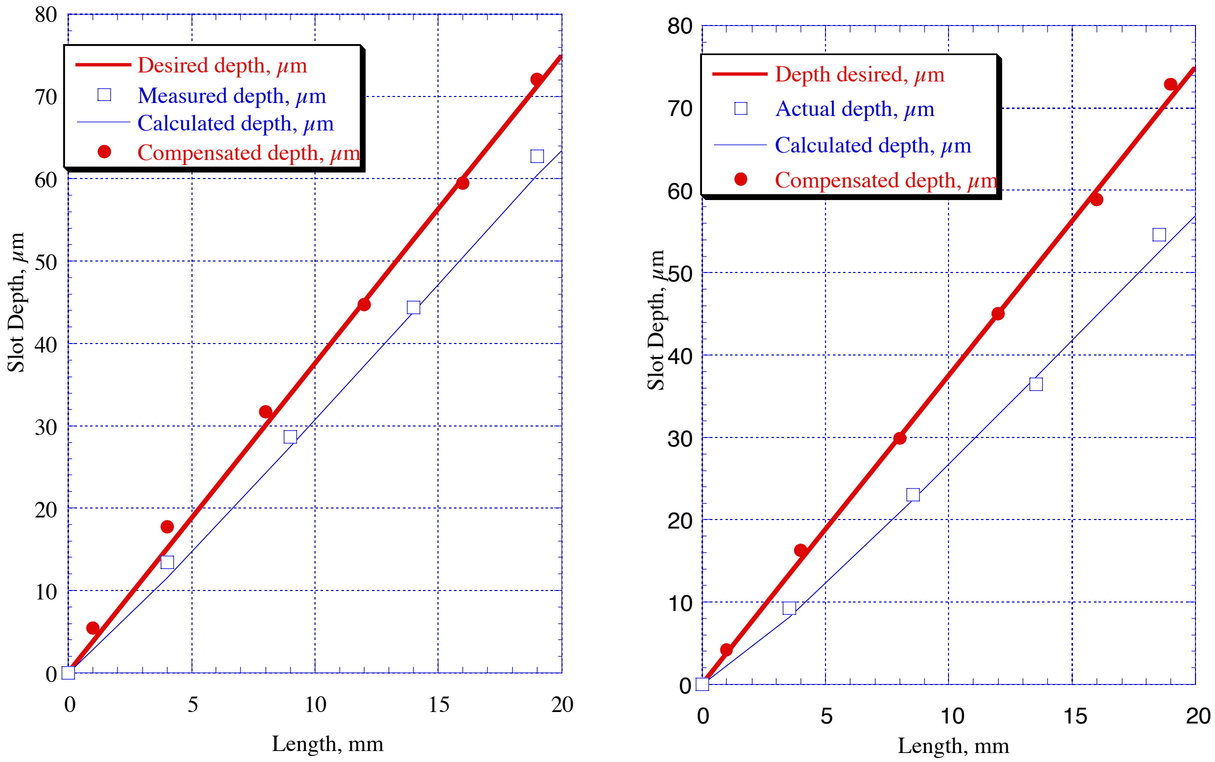

Figure 13. Geometry of slots cut with tool tilted at 25° (left) and 50° (right)

Compensation Experiment The results of the experiments to test this algorithm are shown in Figure 13. Each graph shows the experimentally measured depth of the groove as a function of length. The results of the experiment performed with the tool tilted at 25° are shown in the left side of Figure 13. When the part is cut without compensation, the depth was about 62 μm when the commanded depth was 75 μm. The uncompensated depth of cut from the model (lower line) correlates well with the measured depth of cut. When the tool deflection is included in the model and a new tool path is calculated, the compensated depth is much closer to the desired value (within about 2 μm) over the entire slot. The graph on the right shows the results for the tool tilted at 50°. The added tilt puts the forces more along the softer radial direction and the uncompensated results are nearly 20 μm from the desired values. However, the compensated depth eliminates the error.

13.6.2 CIRCULAR GROOVE

The deflection experiments discussed above involved a single, fixed tool angle with an increasing depth of cut. The results show that the compensation strategy worked well. Unfortunately, the situation for most machining is more complicated – the force on the tool is at a variety of angles and the depth of cut and cross-feed are changing. To verify that tool force/deflection model is effective in predicting and compensating the tool deflections, a more comprehensive experiment was devised.

The goal of this experiment is to create a surface with the small mill where the forces on the tool vary in direction. The experiment involved machining a shallow groove with a 3 mm diameter ball end mill and then enlarging that groove by 100 μm using the 0.8 mm ball end mill. There were several advantages to this technique: first, the large and small tool were held in the same spindle and so alignment was not necessary; second, the initial groove was created with a stiff tool, the shape of which could be measured prior to the experiment; third, the groove was easy to fabricate with a few passes of the large diameter mill; and finally the small width of the groove produced a nearly constant up-feed. The only downside of this experiment was the large relative size of the small mill with respect to the larger mill that produced the groove, an issue that created larger edge effects than expected.

Groove Fabrication A block of S-7 tool steel was mounted on the spindle of the ASG 2500 DTM with the center of the groove at a radius approximately equal to 80 mm. The large mill was mounted in the high-speed spindle and the 1.5 mm radius groove was machined to a depth of 0.5 mm. The small 0.8 mm mill replaced the larger mill and the tool motion was reprogrammed to enlarge the radius of the groove to 1.6 mm; that is, remove 100 μm from the surface. The geometry is shown in Figure 14.

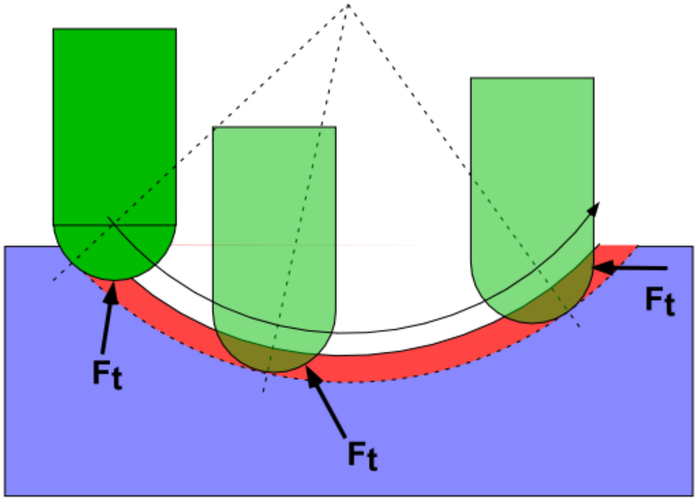

Figure 14. Experiment to measure the influence of tool deflection on fabricated shape of a groove.

In these experiments, the sweep angle of the small tool is approximately ±50˚. The sweep angle is defined as the angle between vertical and the normal to the point of contact between the tool and part. The magnitude of the cutting force will depend on the depth of cut and the up-feed (the tool moves into the page in Figure 14) but the direction will depend on where the tool contacts the workpiece. The depth of cut defines the extent of the contact between tool and the workpiece shown in Figure 14. The thrust force on the tool is assumed to act along the bisector of this contact angle. The force will deflect the tool to a new position dependent upon the axial and radial stiffness of the tool and spindle. As shown earlier in this report, the axial stiffness is much larger than the radial stiffness; so the radial component of force will produce the bulk of the tool deflection. Also note that the direction of the thrust force depends on the direction of the tool feed. Because the contact is in front of the sweep angle, the direction of the force is not symmetrical even if range of the sweep angles is symmetrical. At the maximum sweep angle on the left, the thrust force is nearly vertical whereas on the right it is almost horizontal. This change in angle has a profound effect on the tool deflection because of the lower stiffness in the radial compared to the vertical direction.

Force/Deflection Relationship Once the magnitude and direction of the thrust force is calculated, the tool deflection in the radial and axial directions can be found from the stiffness values. These displacement components can be used to offset the tool path and compensate for the tool deflection. The components of the tool deflections can be written as:

$$\delta_x = \frac{F_t}{K_R}\sin\left(\alpha + \frac{\phi}{2}\right)$$
$$\delta_y = \frac{F_t}{K_A}\cos\left(\alpha + \frac{\phi}{2}\right) \tag{16}$$

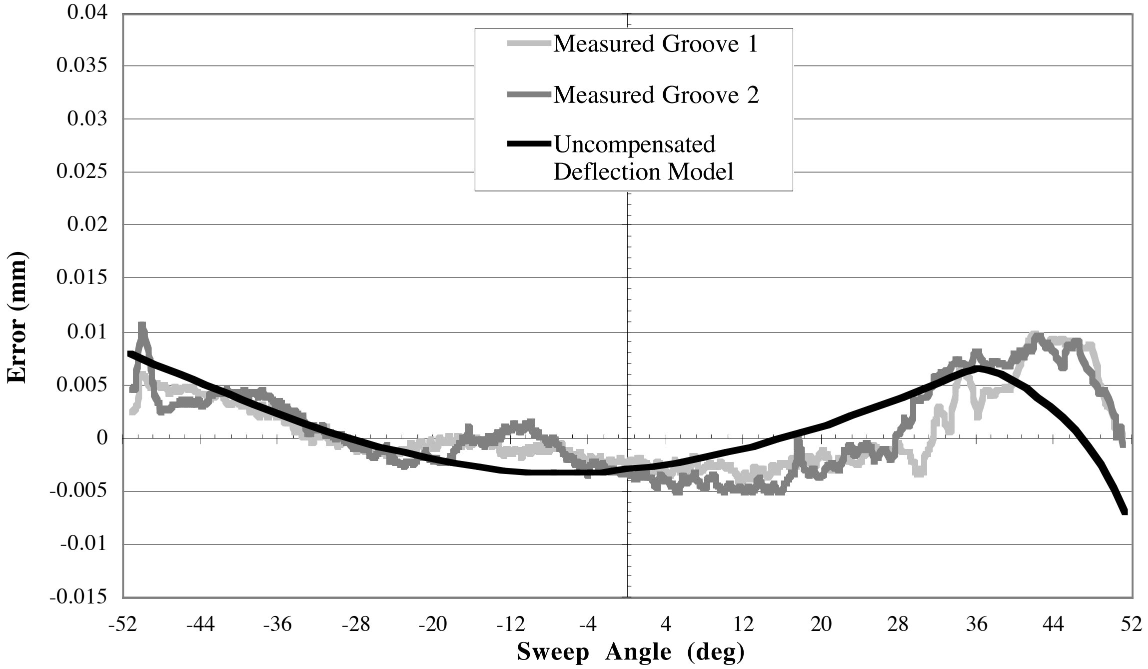

Figure 15. Uncompensated shape of groove using short tool – Experiments and theory. Error is difference between the shape of the groove and the best fit circle of 1.6 mm radius.

Uncompensated Groove Shape Equation (16) can be used to calculate the distortion that should occur if the tool path of the small tool is not compensated for the tool deflection and the result can be compared with the experiments. The Form Talysurf[1] was used for the measurement of the groove shape and the data was analyzed by finding the best fit to the desired radius of 1.6 mm. The results for the short tool are shown in Figure 15.

---

[1] The Talysurf provides data in the form of radial error versus width of the groove. To compare this data to the analysis, the width of the groove must be turned into a sweep angle or visa versa. To produce the width value on the Talysurf traces, the desired groove radius is multiplied by the sine of the sweep angle.

The data for the experimental results are scaled so that the average error is zero. A perfect surface, that is, one with a 1.6 mm radius, would appear as a horizontal line. The fact that the data in Figure 15 is high at the edges and low at the middle indicates that the actual radius cut is less than the 1.6 mm radius desired. To produce corresponding data from the analysis, the tool deflection along the normal to the groove at each sweep angle was calculated. This value can be written as:

$$\delta_n = \delta_x \sin\alpha + \delta_y \cos\alpha \qquad (17)$$

Figure 15 compares the calculated and measured error as a function of the sweep angle. Measurements of two grooves cut with different tools (but the same type) are shown and the results are quite repeatable. The model also fits the measured data very well and the shape of the curve is characteristic of all of the uncompensated experiments. The relative error is largest on the left where the tool enters the part, is a minimum near the center and grows until the tool senses the edge of the part at about 36° after which the error drops to zero. Without this edge effect, the error would continue to grow and become much larger on the right than on the left because the force becomes more horizontal. However, the tool also approaches the edge of the part and runs out of material to cut. The location of the peak is a function of the radii of the part and tool as well as the depth of cut. The overall error for the short tool is small, less than 15 μm, but the predicted error matches both the shape and magnitude measured.

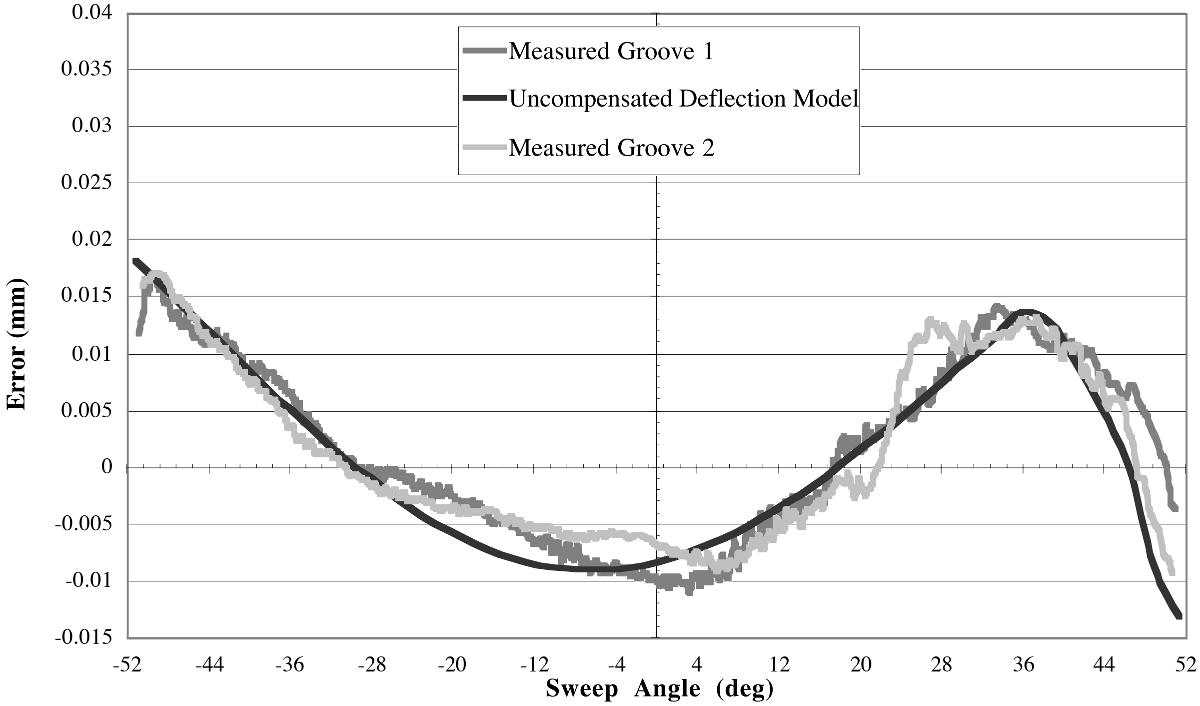

Figure 16. Uncompensated shape of groove using long tool – Experiments and theory. Error is difference between the shape of the groove and the best fit circle of 1.6 mm radius.

Figure 16 shows a similar error plot except that the results were obtained using the long tool. The stiffness of this tool is about half that of the short tool. As in the short tool results, the two grooves cut and measured are very similar in magnitude and shape and the calculated shape provides a good estimate of the error. The error for the long tool is nearly twice that for the short tool, a peak-to-valley magnitude of approximately 25 μm. Figure 17 is the error plot for grooves cut with the extra long tool. The characteristic shape of this error plot is similar to the previous uncompensated experiments but the magnitude has grown to nearly 50 μm. There is more variation in the experimental measurements but the analytical predictions still indicate a reasonable estimate of the experimental results.

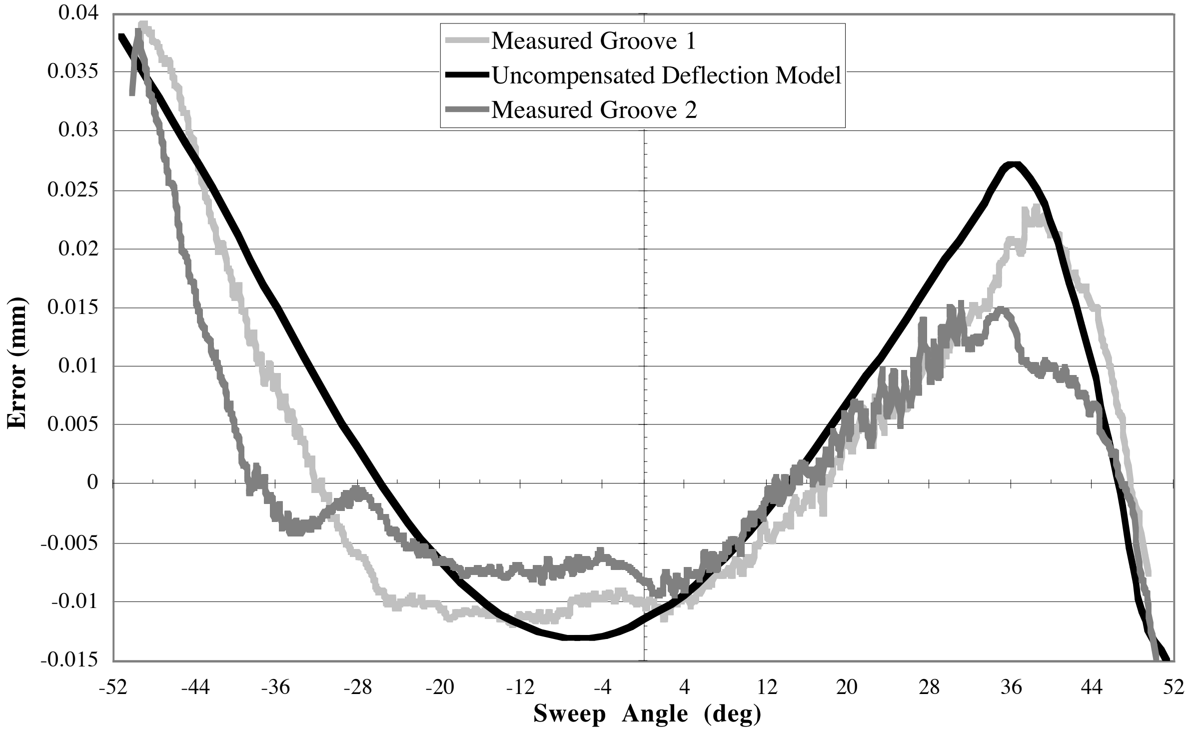

Figure 17. Uncompensated shape of groove using extra-long tool – Experiments and theory. Error is difference between the shape of the groove and the best fit circle of 1.6 mm radius.

Compensated Groove Shape The results of the uncompensated grooves shown in Figures 15 through 17 indicate that the model does a good job of predicting the shape of the groove resulting from tool deflection. The next step was to use this information to compensate for the deflection and create a "perfect" groove; that is, one that has the correct depth (0.6 mm) and the correct radius (1.6 mm). Only the error plot for the extra long tool is discussed but this is characteristic of that measured for the shorter, stiffer tools.

Figure 18 shows the error in shape that results from applying the model and producing a corrected tool path that will compensate for the effects of tool deflection. The tool force calculation in this case is simplified when compared to the uncompensated case because the actual depth of cut is known, it must be 100 μm to produce the desired shape. So rather than a interative solution, the force can be calculated directly. Then, knowing the contact angle, the components of the deflection can be calculated and the compensation values are simply the magnitude of the deflections with a reversed sign.

The results of a compensation experiment superimposed on the uncompensated shape of the groove in shown in Figure 18. Notice that the error in the surface shape is much lower for the compensated experiment (by a factor of 5) but seems to be limited to the order of ±5 μm. This difference is also the order of the difference between the two test grooves. This result points to a fundamental limit to this open loop technique; that is, knowing the tool geometry including any tool wear or fracture that occurs during the cut. Because the workpiece is hardened steel, wear of the tools is a fact of life and this technique will be limited. However, for long thin tools, the potential is still impressive.

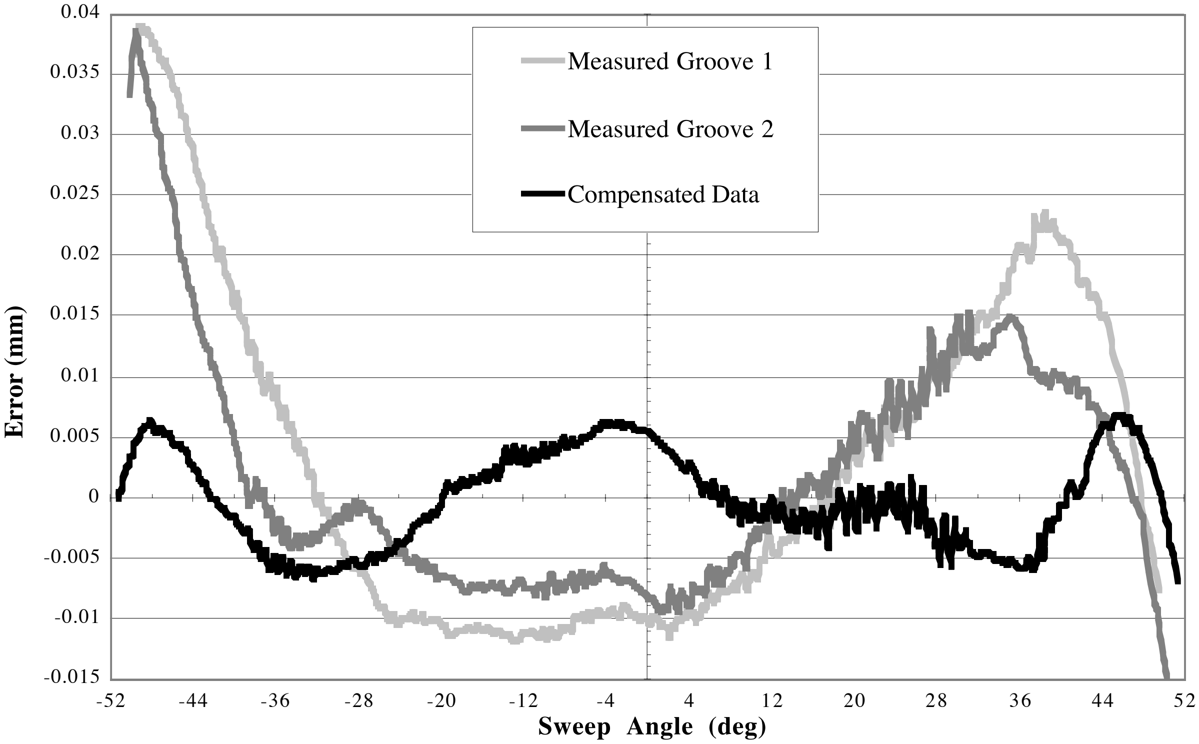

Figure 18. Effect of compensation on error using extra-long tool.

Machined Radius of Curvature Another way to portray the results of the measurements is to compare the best fit radius of curvature of the machined part rather than the error at each point on the surface as was done in Figure 18. The plot in Figure 18 shows the error in magnitude but also the trend in the fabricated shape. The uncompensated plots show that when compared to the desired 1.6 mm radius that the sides were not cut deep enough with respect to the middle resulting in a smaller radius of curvature than desired. The compensated plot, while it does not match the desired radius everywhere, does constrain it all the way across the groove.

Instead of looking at the error from the desired radius, the data analysis program can find the best fit radius to the groove. This result provides a more general evaluation of the error in the fabrication process. Figure 19 shows the error in the radius of the groove as a function of the radial stiffness of the tool for uncompensated grooves (solid) and compensated grooves (dotted). On the left is the extra long tool with a radial stiffness of about 80,000 N/m. The two uncompensated grooves made with this style tool have a radius error of –0.06 and –0.1 mm respectively; that is, the radius cut is too small because the tool deflects in at the sides. These are the two uncompensated grooves shown in Figures 17 and 18. The long tool has a radial stiffness of 200,000 N/m and the two uncompensated grooves cut with this style tool each have a radius error of –0.05 mm. Finally the short tool is shown at right and the uncompensated radius error is –0.025 mm. Note that the uncompensated error seems to be both smaller and have less variation as the tool becomes stiffer. When these uncompendated grooves are compared to the compensated groove results (dotted top line), the power of this technique is apparent. Note that the error in the radius is less than ±10 μm for any of the tools.

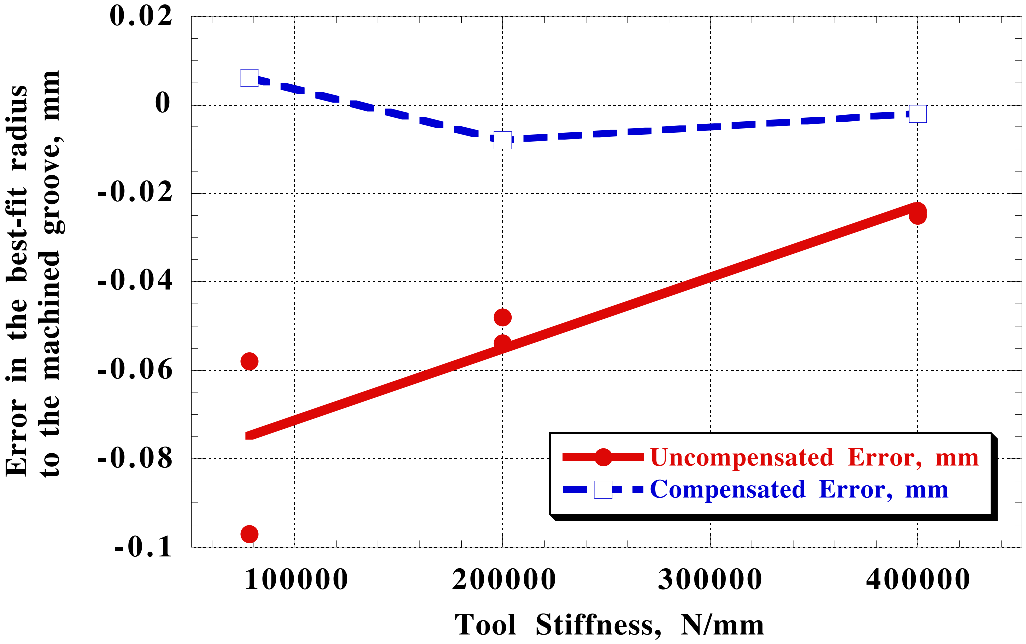

Figure 20. Summary of the compensation experiments

13.7 FUTURE WORK

The ability to compensate the deflection of small milling tools using an open loop technique based on a force and deflection model has been demonstrated. Significant improvements in the geometry of both slots and circular grooves cut in hard steel substrates are shown. However, this is not a completed problem. The next step is to build such a system into the CAD and CAM models for a manufacturing process to generate a new tool path that will correct the tool deformation errors. Unfortunately this is not a easy task because of the complexity of the CAD programs and the lack of access to the information needed.

To implement the correction scheme described above, the location of the tool and the part are needed as well as the location of the tool/workpiece interface and the shape of the part at that location. The shape of the part means the curvature in the plane of motion of the tool as well as the curvature in a plane normal to this path. This information can be used to find the depth of cut, the cutting and thrust forces, the direction of these forces and the deflection of the tool. This information can then be used to find the errors and the corresponding corrections to the tool path to correct these errors. This open loop compensation technique will be limited by a knowledge of the geometry of the tool and the change in that geometry with wear during the machining process.

The implementation of this technique will require a concentrated effort between the PEC with an industrial partner interested in this capability.

REFERENCES

1. Minor, P., “Tool Wear and Tool Forces in High Speed Machining of Aluminum”, MS Thesis, North Carolina State University, 1998.

2. Arcona, C., “Tool Force, Chip Formation, and Surface Finish in Diamond Turning”, Ph.D. Dissertation, North Carolina State University, 1996.

3. Drescher, J.,”Tool Force Measurements in Diamond Turning”, MS Thesis, North Carolina State University, 1989.

4. Drescher, J., “Tool Force, Tool Edge and Surface Finish Relationships in Diamond Turning” Ph.D. Dissertation, North Carolina State University, 1991.

5. Carroll, J., “A Numerical and Experimental Study of Single Point Diamond Machining”, Ph.D. Dissertation, North Carolina State University, 1986.

14 PRECISION REPLICATION OF OPTICS

David D. Gill
Graduate Student
Thomas A. Dow
Professor
Mechanical and Aerospace Engineering

The fields of optical communication, photonics, and display technologies require the development of high volume, high precision production methods. These applications require components that are thin, highly transmissive, and environmentally stable presenting uniform properties throughout a range of temperature and humidity conditions. Molded polymer optics fulfill many of the requirements for these parts, but still present challenges. The effect of individual molding variables on the replication of precision features in optics is not well understood. Means of minimizing the effects of environmental changes on polymer optics are needed before these optics will truly be able to replace their more expensive glass and silicon counterparts. The objective of this research is an investigation into the replication of features in precision optics and the co-molding of these optics onto thermally stable substrates. Results during the past year have shown that nanometer size features can be successfully replicated in polymer optics by both ultraviolet cure photopolymer molding and injection molding. An injection molding machine has been delivered and injection molding process variables have been investigated and key variables identified and studied for their effects on feature replication. Optimization of these variables has produced significant reduction in the form error of replicated optics. In addition, work has begun on a molding system that will allow the co-molding of polymer optics onto glass substrates to reduce the sensitivity of polymer optics to environment changes.

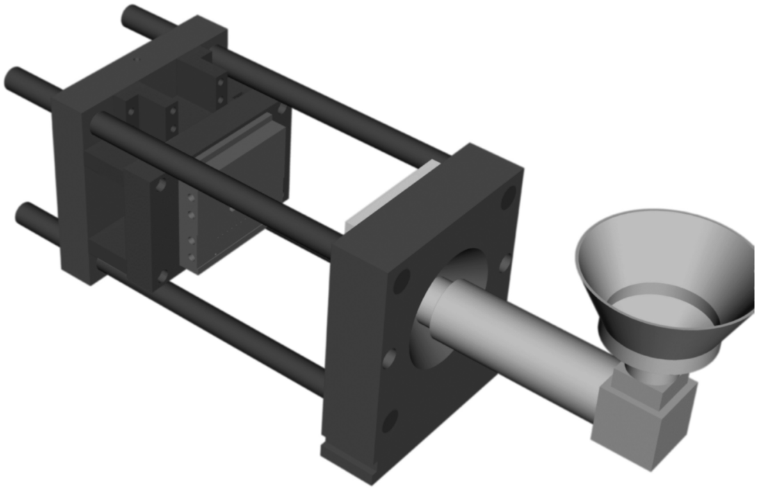

14.1 INTRODUCTION

Advancements in the fields of optical communication, photonics and display technologies require the development of high volume, high precision production methods. As signal traffic continues to increase on fiber optic networks, there is a need to perform switching without converting the optical signal to an electric signal. These switches, often called Micro Optical Electro-Mechanical Systems (MOEMS), must be fast, durable, highly transmissive, and thermally stable. Video displays on laptop computers and personal assistants are increasing in quality and there is a constant demand for wider viewing angle and screens with increased brightness and clarity. Display applications also require components that are thin, precisely located over a large area, and highly transmissive. Both fields require high-volume, low-cost fabrication and assembly techniques.

Molded polymers fulfill many of the requirements for these parts, but still present challenges. For example current production methods for MOEMS rely on integrated circuit technologies such as lithography and flip-chip construction. These methods require many steps with precision alignments of successive masks to produce the desired features. The components are built up from silicon in the z dimension and then separated from the substrate and rotated to produce in-plane optical networks on the substrate [1]. Replicated polymer optics would serve well in this application if they could be thermally stable throughout the wide temperature operating range and provide long service life. One potential solution is to mold the polymer optics in a thin layer on a thermally stable substrate [2]. Such optics could be cast in a UV curable polymer [3] (low volume production, low capital investment) or injection molded (high volume production, high capital investment). The application of thin polymer optics on a thermally stable substrate would also benefit the field of display technology where laptop and personal assistant screens require microlenses and optical waveguides on the glass screen substrate.

The goal of this research involves the development of processes capable of accurately reproducing sub-micrometer optical features over small and large areas as well as rapidly co-molded features on thermally stable substrates.

14.2 REPLICATION TECHNIQUES

14.2.1 UV CURE MOLDING

UV cured polymers have been extensively used for creating soft contact lenses and also for replicating thin optical surfaces on top of glass and plastic substrates [7, 8]. This process was studied to evaluate the capability to reproduce nanometer sized features and to assess the speed and repeatability of the process.

The experimental setup, shown in Figure 1, consists of an aluminum mold that was diamond turned to a mold cavity depth of 350 μm. This cavity is considered deep for UV molding and the available monomer is normally intended for use as a bonding agent between lenses. The monomer was poured into the aluminum mold and the mold placed in a vacuum chamber to remove entrained air bubbles. Upon removal from the vacuum chamber, a glass plate was placed over the cavity. Vacuum pressure pulled the glass tight against the mold and helped to remove any air from the glass placement process. UV illumination cross-linked the monomer and it adhered to the glass plate because of adhesion promoters present within the monomer.

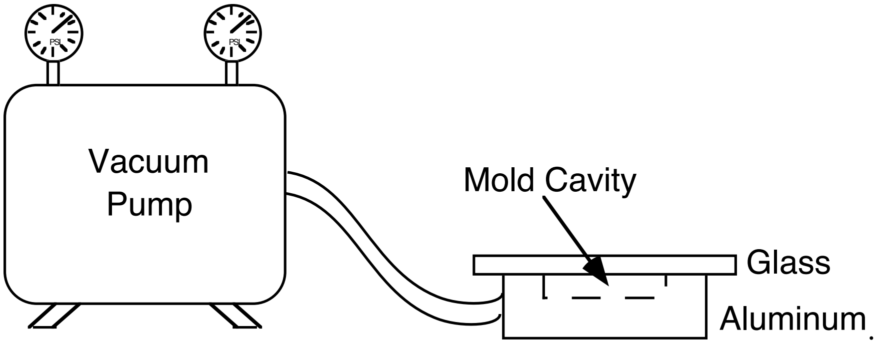

Figure 1. UV Cure Experimental Setup

Different radiation intensities were obtained by changing the distance between the light and the mold. Different cure times were also investigated to find the best conditions for cure of this thick lens section. While features were accurately replicated within a few nanometers, this process is quite slow. Current industrial uses of UV cure monomer require either a massively parallel operation with many parts being cured at the same time, or production a lens array every 1 to 2 hours. The speed of the curing process can be increased by using higher intensity UV radiation, but the high rate of cure introduces additional stresses and promotes the inclusion of air bubbles in the part. The results of the UV cure tests are given in 14.3.1.

14.2.2 INJECTION MOLDING

The long cycle time of UV cure optic replication prompted research into injection molding. To achieve the goal of precision replication of sub-micrometer features in thin lenses over a large substrate in injection molding, the research has been divided into four stages:

1. The first stage investigated the transfer of feature and form from the mold to the molded part. Previous research [4, 5, 6] reported the molding variables that affect feature transfer, but further study is warranted for optical components. Tests were conducted using a diamond-turned mold producing a 25 mm diameter plano-convex lens with center thickness of 3.5 mm. The plano mold half had features ranging between 0.5 and 16 μm width with depths less than 21 nm.

2. The second stage will investigate the injection molding of part geometries onto thermally stable substrates such as glass, and quartz using the convex half of the mold in conjunction with a plano substrate located in the fixed side of the mold base. Research in this project is currently studying the challenges of this second stage.
3. The third stage of the project will combine the molding of very thin parts onto thermally stable substrates.
4. The fourth stage will investigate the transfer of micrometer and sub-micrometer features within the very thin parts on thermally stable substrates, possibly incorporating precision slides to produce in-plane optics.

Concave-Plano Lens A Van Dorn, 75 ton hydraulic injection molding machine was used to fabricate test lenses. Two mold halves, one plano (fixed half) and the other concave (to make a convex lens) were diamond turned from aluminum and installed in the mold bases on the machine (See Figure 2).

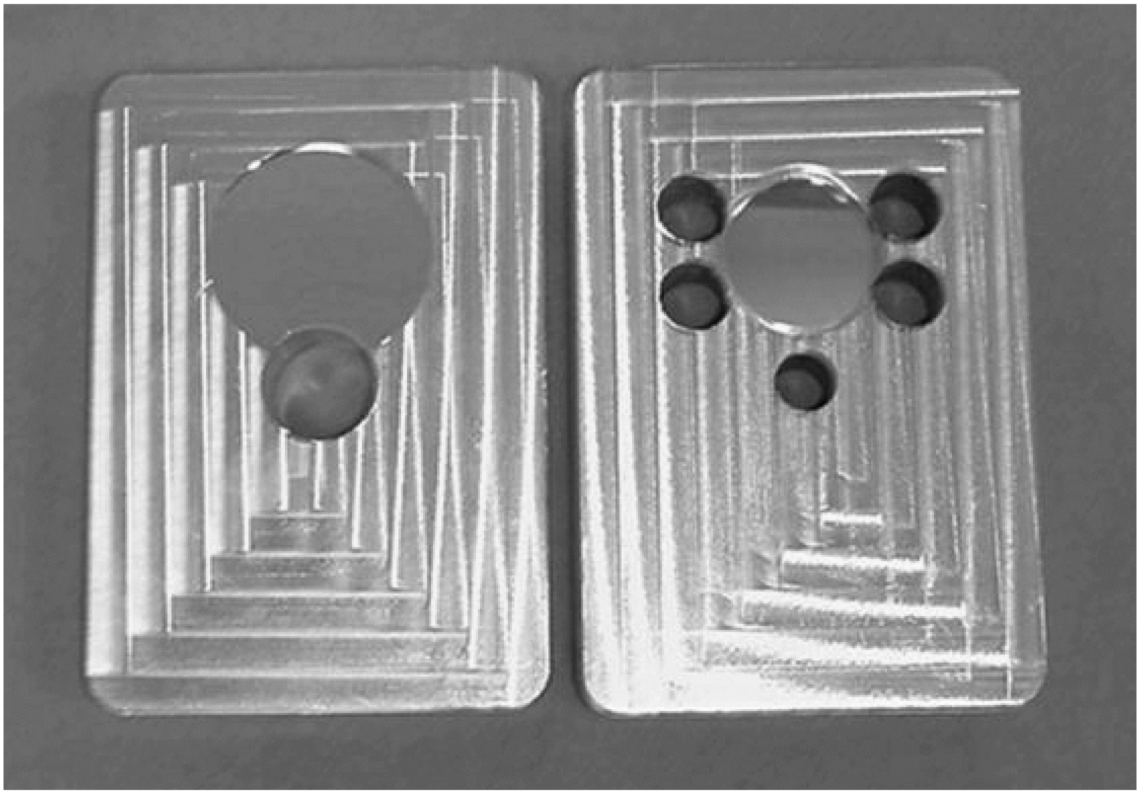

Figure 2. Diamond Turned Mold Halves with Plano (left) and Convex (right) Mold Cavities

VEREX 1301 polystyrene (Nova Chemicals) was injection molded with varying hold times, cooling times, and barrel temperature profiles to determine the optimum parameters for form and feature replication. An injection pressure of 11.4 MPa was held constant for all trials. The hold time was varied between 2 and 20 seconds while maintaining a constant injection pressure, barrel temperature profile, and cooling time. Subsequently, the in-mold cooling time was varied between 4 and 20 seconds while maintaining a constant barrel temperature profile, holding time, and injection pressure.

The barrel temperature test varied the temperatures at three control locations along the injection barrel. The machine controls the temperature using a PID controller that monitors the temperature at the front and rear of the barrel and at the injection nozzle. Electric heater bands at each location maintain the desired temperature. The temperatures at the three locations were varied between 215°C and 265°C. The process temperature range published for the polystyrene is between 190°C and 274°C, but the entire range was not available using the other molding parameters as set due to the melt and flow characteristics of the polymer. The results of these tests are presented in section 14.3.2.

A New Injection Molding Machine Due to the lack of repeatability found with lenses made using the Van Dorn 75 machine (see Results and Discussion for explanation), a new injection molding machine was needed for use in photonics fabrication. A Nissei HM7-C injection molding machine was purchased. The Nissei is a 7 ton hydraulic machine that is more properly sized for investigating precision photonics. This benchtop machine has a 6.2 cm^3 shot size which allows the use of small single cavity molds. A common guideline is to use 25-50% of the maximum shot volume per shot so that the barrel residence time (the amount of time that is required for a given polymer molecule to traverse the injection barrel) allows the polymer to melt adequately, but not overheat or burn. A new mold base, mounting plates, and preliminary mold inserts have been built for this machine. The insert design clamps directly on the glass substrate which is possible because of the lower tonnage of this machine. The mold design concept is shown below in Figure 3 with the mold plates and molding inserts shown in Figure 4.

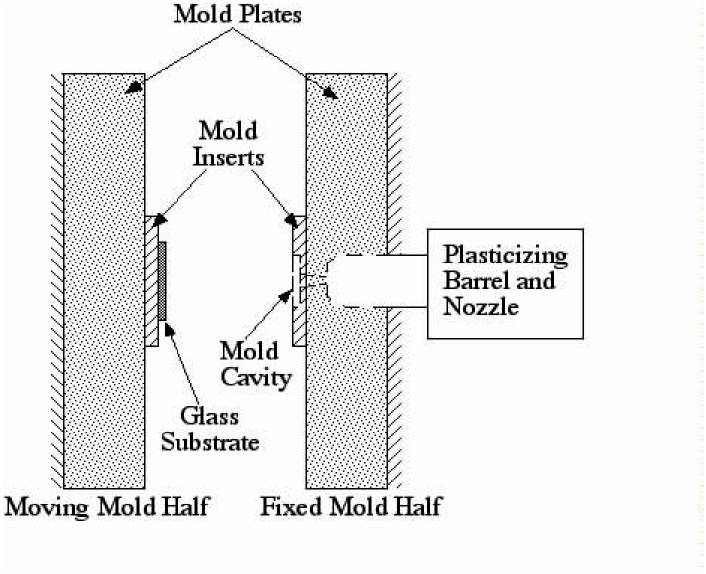

Figure 3. Side View of Mold Design Concept for Injection Molding on Glass Substrates

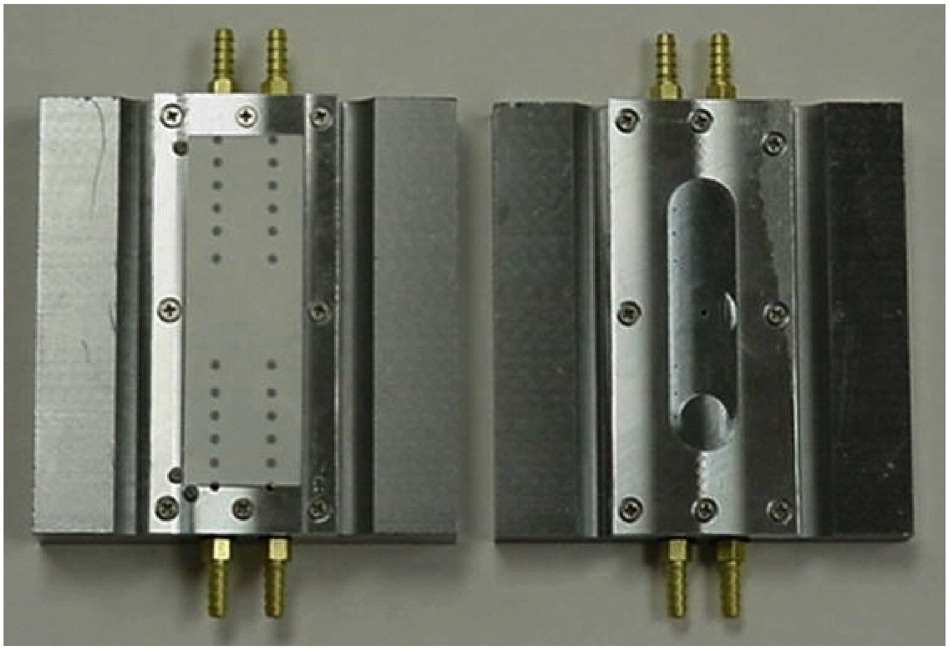

Moving Mold Half Fixed Mold Half

Figure 4. Top View of Mold Plates and Inserts for Co-molding on a Glass Substrate

The mold plates and mold base are steel for strength, but the mold inserts are aluminum to allow diamond turning or diamond vibration assisted machining of the mold cavity. In addition, the moving side of the mold where the substrate is positioned must be diamond turned so that the glass substrate will be evenly supported and will not crack when the mold is closed and the 7 tons of clamping force are applied to the substrate. This force is necessary to seal the mold cavity against the glass. To achieve the goal of injection molding on a glass substrate, the system must incorporate a means of securing and releasing those substrates as each lens will require a new substrate. The glass substrate is held in the mold using vacuum pressure and the part is ejected from the mold using compressed air. The use of vacuum reduces the likelihood of fracturing the glass while positioning the substrate and offers the additional advantage of reducing the pressure in the mold which is a common strategy to help mold features fill. Figure 4 shows the pressure/vacuum ports on the faces of the mold inserts as well as the connections for the supply hoses on the sides of the mold plates. The glass substrate is also shown in position on the moving half of the mold (on the left in Figure 4).

The substrate introduces several challenges that require innovative methods of mold design. In traditional molds, the plastic is injected into the mold through a sprue that then feeds a runner system that distributes the polymer melt to the mold cavity. The point at which the runner meets the cavity often has a narrow cross section and is called a gate. The gate is the point at which the plastic "freezes" which stops the filling of the mold and prevents the mold from being overpacked with polymer. The gate also acts as a pressure reducer which helps to smooth pressure changes in the mold cavity. After the part has cooled in traditional molds, the mold is opened and the part remains in the moving half of the mold where it is ejected by some mechanical means. Because of the need to seal the mold cavity directly on the substrate, the mold cavity is in the fixed side of the mold and that is where the cooled part will stay as well. This requires that ejection of the part be by air as the fixed side of the mold has no capabilities for mechanical ejection of the part. The uncommon placement of the mold cavity in the fixed side of the machine allows the polymer to be injected directly in the center of the cavity which should decrease dimensional variations across the polymer lens because of a more even pressure distribution than is found in side gated molds. Injecting the polymer directly into the mold without first going through runners and gates, called direct injection, requires a very short sprue so that hardened plastic can be removed from the mold and sprue using only air pressure. Direct injection may cause the pressure fluctuation to be somewhat higher in the mold cavity during the molding cycle as there is no pressure reducing gate in this design.

An initial mold, shown in Figure 5, was created by conventionally machining a mold cavity in steel. The cavity was then hand polished and scribe marks were added to the cavity using a hardness indenter to study the fidelity of replication. The scribe marks were created using different application forces to create different depth features, but all with the same feed rate. The scribing action used to create these features caused the material from the groove to be ploughed to the sides creating both peaks and valleys that proved to be useful for analysis of feature replication in molding. Unfortunately, this ploughing action also created a non-uniform scribe edge.

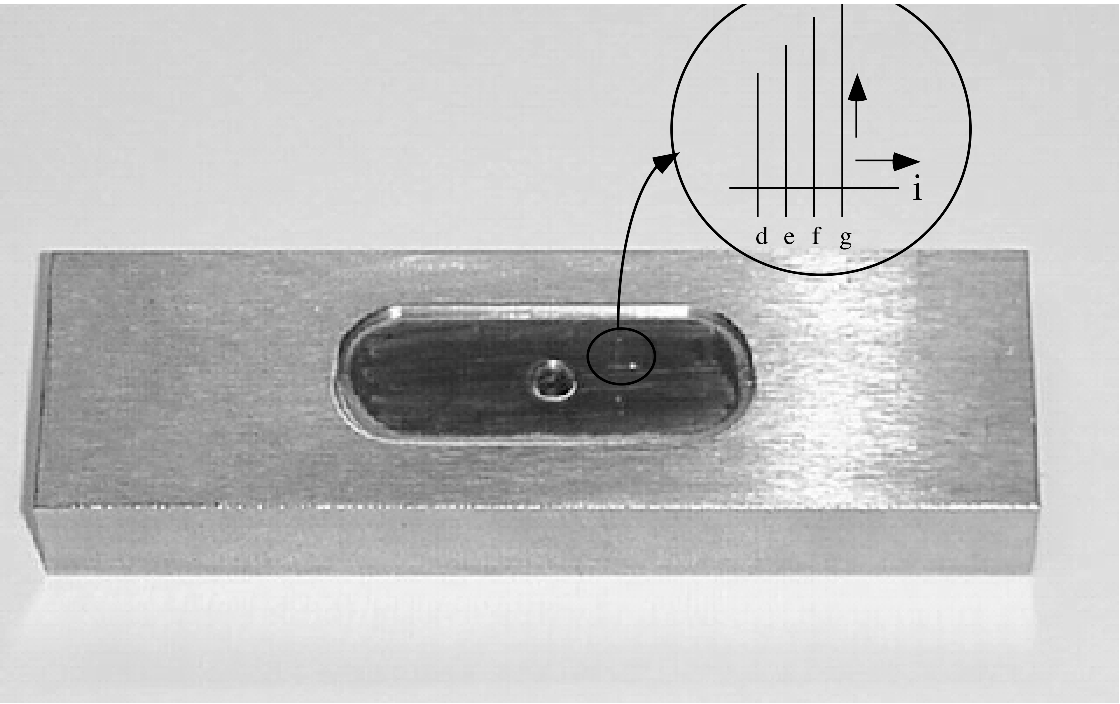

Figure 5. Hand Polished Injection Mold with Scribe Pattern as Shown

The scribe marks can be seen in Figure 5 as very light lines to the upper right of center (circled in the figure) in the oval mold cavity. These scribes were labeled as d,e,f,g, and i for identification purposes. Scribes d,e,f,g were produced with the Vickers pyramidal indenter loaded with 150, 100, 50, and 200 grams respectively scribing in the direction shown by the vertical arrow. The scribe labeled i was created by dragging the indenter sideways in the direction shown by the horizontal arrow. The indenter load for scribe "i" was 100 grams.

14.3 RESULTS AND DISCUSSION

14.3.1 UV CURE MOLDING

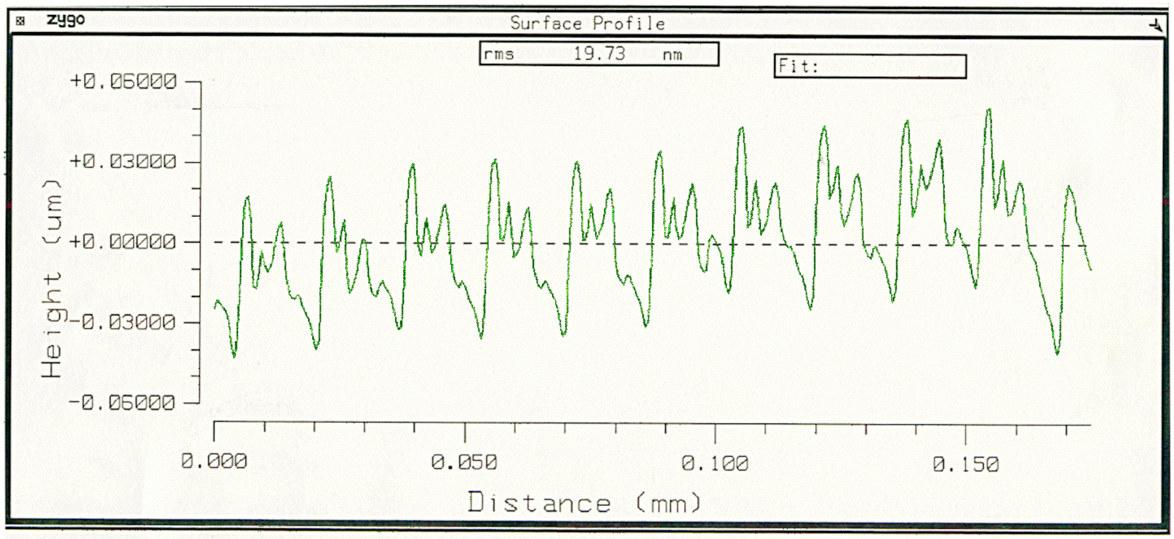

Figure 6(a). White Light interferometer trace of diamond turned aluminum mold surface

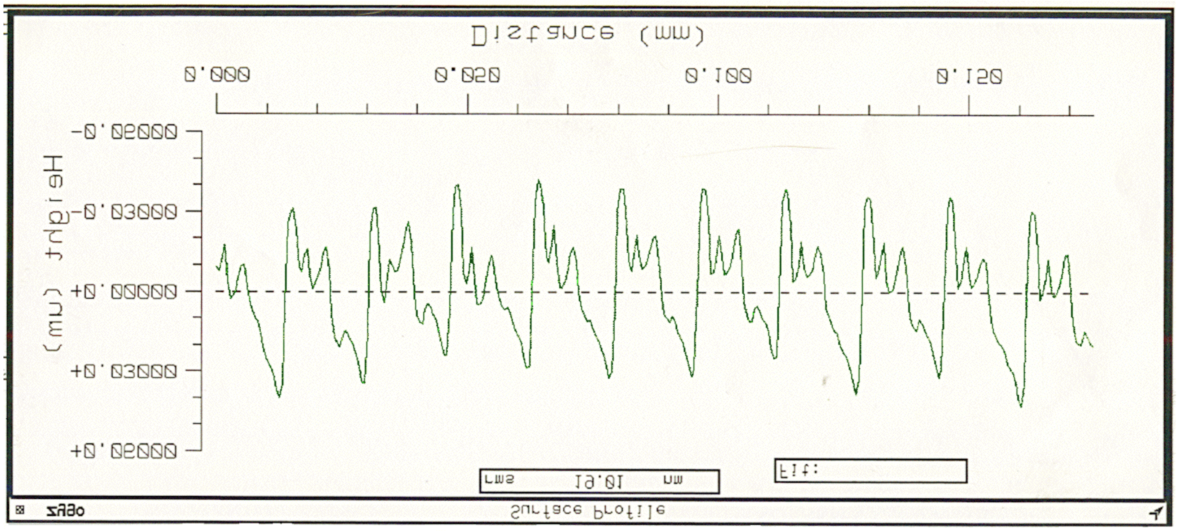

Figure 6(b). Inverted white-light interferometer trace of UV cured polymer replica.

Figure 6 illustrates the quality of the UV polymer replication. Figure 6(a) is a white-light interferometer trace of a diamond turned mold and Figure 6(b) is an inverted trace of the plastic replica. The surface has the characteristic features of diamond turning with a slightly-damaged tool resulting in a rms roughness of 20 nm. The feed rate for this surface is about 20 μm per revolution. The replicated surface is inverted to make it easy to compare the mold and replica. The small features of the tool (some less than 10 nm) are copied with impressive fidelity using UV cure polymers.

Figure 7(a) shows a top-down view of the center of a mold and Figure 7(b) is a UV replicated lens created in the diamond turned mold. In this case the feed rate was 20 μm using a 3 mm tool radius. The theoretical height of the features is 15 nm. The replicated lens on the right again shows the ability of UV replication to accurately reproduce optical features.

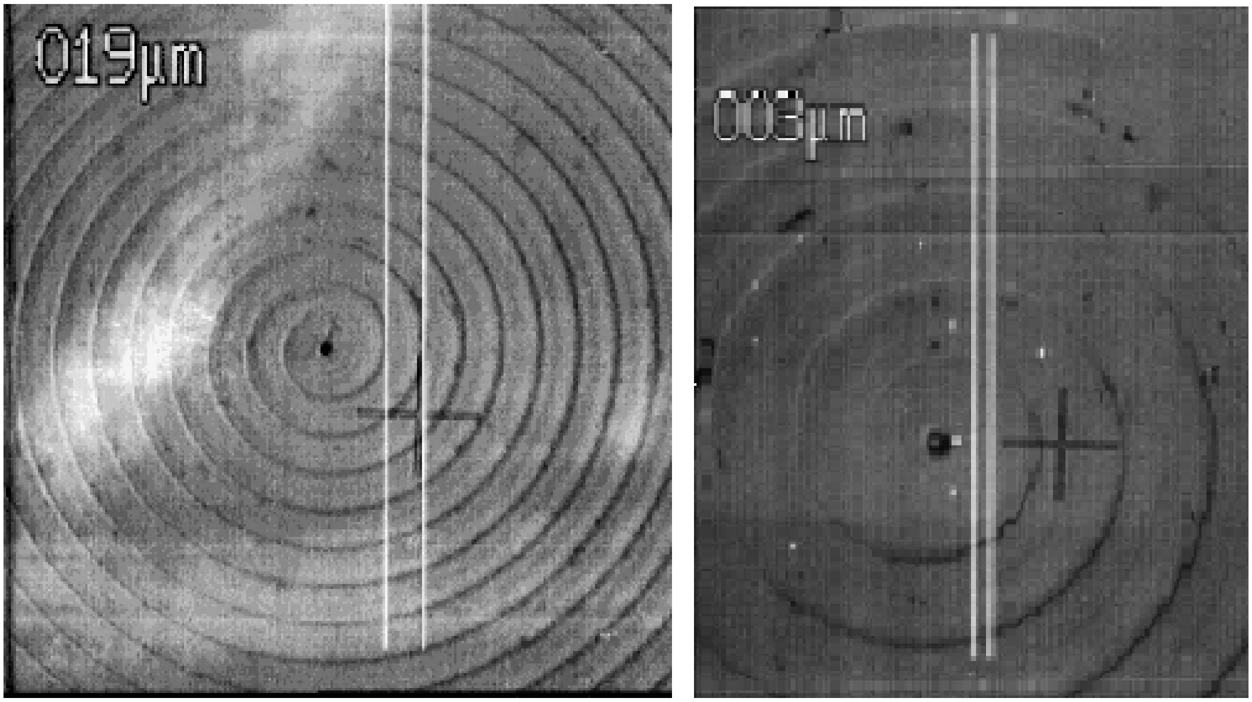

(a) Mold (b) Replicated Lens

Figure 7. 200x Micrograph of Mold Center and 500x Micrograph of UV Replicated Lens

14.3.2 INJECTION MOLDING

Van Dorn Investigation of the transfer of features from the mold to a part requires an understanding of the variables of that transfer process and their effect on the accuracy of the process. A literature search revealed widely varying opinions as to the relative effects and importance of the different molding variables. To help quantify this information, a large number of test lenses were molded with varying packing time, cooling time, and barrel temperature, three variables often attributed with much influence over the molding process.

The figure of merit selected was the peak-to-valley error on the flat side of the molded lens. Flat features are difficult to mold so this measurement was deemed a useful comparison. A significant reduction in form error (on the order of 75%) was observed as the packing time was increased from 1 to 10 seconds. The influence of cooling time was less apparent. While a slight downward trend was observed (increased cooling time reduced form error), more scatter in the data also existed for these tests. The results of the barrel temperature profile tests showed similar scatter. The tests did show the ability of the injection molding process to accurately replicate shallow features with widths of 5 to 50 μm. Figure 8 shows two lenses created from the same mold. The lens in Figure 8(a) was UV replicated while the lens in Figure 8(b) was injection molded. The same features, seen in both lenses, were created by changing feedrates during diamod truning of the mold. The features are approximately 2 μm wide with very low aspect ratios and 16 μm and 50 μm spacings between features. The features in both lenses, created by different processes, are replicated with equal accuracy. The injection molded lens does not meet the level of surface finish achieved in the UV cured lens. This difference is thought to be due to a low mold temperature during injection.

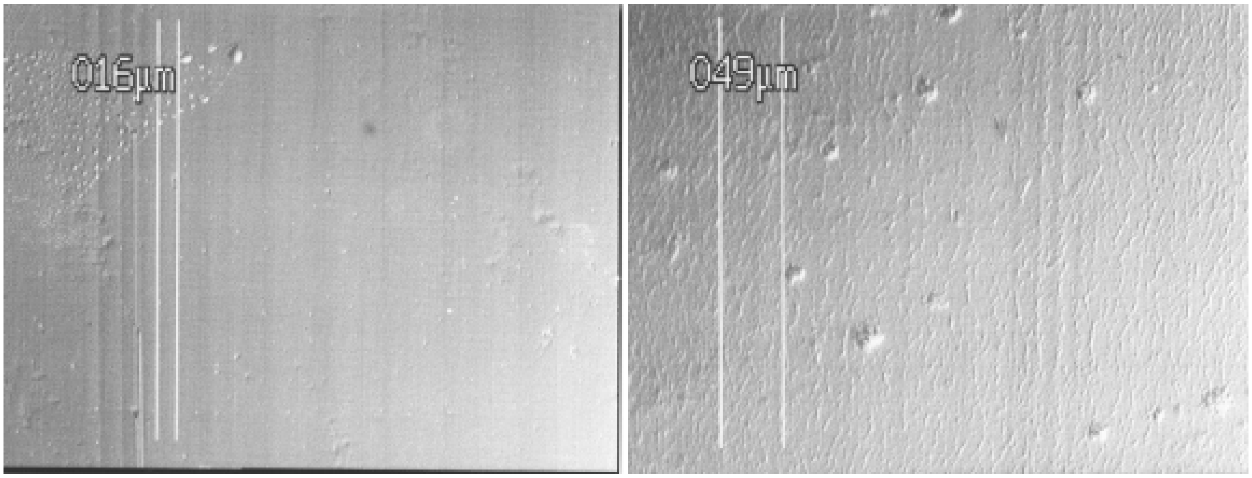

(a) UV Photopolymer Lens (b) Injection Molded Lens

Figure 8. 200x Micrograph of UV Cured and Injection Molded Lenses from Same Mold

The tests of the effects of barrel temperature and cooling time on the replication of features were inconclusive because of a lack of repeatability. The tests showed possible trends, but the data was not repeatable and trends seemed unstable. Analysis of the process showed that the most likely cause of the problems was a lack of repeatability in the machine. The machine PLC was prone to crashes and hangups causing temperatures to oscillate and preventing process equilibrium.

Nissei Because of this lack of control on the Van Dorn 75, a Nissei HM-7C machine was purchased. Though this machine has only had a few parts created on it to date, the accuracy of the replication and the control of the process appear to be much better. Figure 9 shows a stylus profilometry trace of the scribes on the mold and Figure 10 shows the accompanying measurement of the polystyrene part shot in this mold. The scribe marks are of a much higher aspect ratio than that of the tool cusps shown in Figure 8, and feature replication does not appear to be as accurate as in the low aspect ratio features. The peaks in the mold replicated well as valleys in the replicated lens, but the valleys in the mold did not fill. Nearly 95% of the feature height was transmitted from the mold peaks compared to approximately 30% of the feature depth for the mold valleys. There are several factors that may contribute to this including low mold temperature, air trapped in the valleys, and high viscosity polymer. Additional trials will be conducted in the near future to improve feature transmission and to isolate the effects of the individual molding variables as much as is possible in the new molding machine.

14.4 CONCLUSIONS

The research has shown the capabilities of both ultraviolet cure photopolymer and injection molded polystyrene for application to photonics. UV photopolymer parts were created with feature replication varying by only nanometers from the original mold. This was true of features with both medium and low aspect ratios. The photopolymer parts were slow to create and took painstaking effort regarding the removal of tiny bubbles from the polymer before exposing to UV light. Additionally, UV photopolymer has only been formulated for thick sections (above 100 μm) in research applications. Injection molding promises high volume production of optics with good feature transmission as well. Low aspect ratio features were transmitted with high accuracy as were features that were protrusions on the mold. In the testing completed to date, cavities in the mold of medium aspect ratio were only transmitting 30% of the feature height. The effect of the individual molding variables on optical feature transmission is ongoing with preliminary results showing a 75% increase in part feature quality with increased packing time. All other variables tested showed mixed results due to machine problems. Future work will extend the understanding of these molding variables and investigate the processes which will cause the polymer to firmly adhere to rigid glass substrates. Environmental testing of the co-molded optics will then show the effectiveness of the co-molding approach.

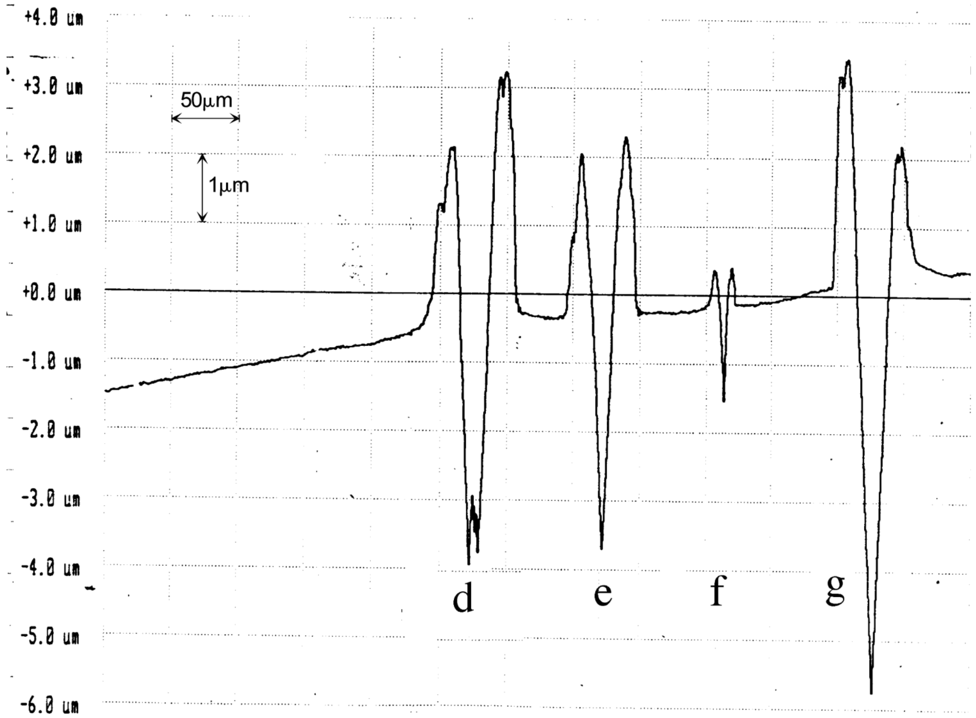

Figure 9. Stylus Profilometer Measurement of Scribes d,e,f,g on Mold Surface

Figure 10. Stylus Profilometer Measurement (Inverted) of Scribes d,e,f,g as Replicated in a Polystyrene Lens

REFERENCES

1. Zhou, G., et al., “New Approach for Nonsilicon Micromachined Three-Dimensional Multilevel Diffractive Optical Elements,” SPIE proc., vol. 3879, pp. 88-95, 1999.

2. Baraldi, L. and R.E. Kunz, “High Precision Molding of Integrated Optical Structures,” SPIE Proc., vol. 1992, pp. 21-29, 1993.

3. Tanagami, M., et al., “Low-Wavefront Aberration and High-Temperature Stability Molded Micro Fresnel Lens,” IEEE Photonics Tech. Letters, vol. 1, pp. 384-385, Nov. 1989.

4. Chou, S.Y., P.R. Krauss, P.J. Renstrom, “Imprint of Sub-25nm Vias and Trenches in Polymers,”, Applied Physics Letters, vol. 67, n.21, pp. 3114-3116, 1995.

5. Kemmann, O., C. Schaumburg, L. Weber, “Micro Moulding Behaviour of Engineering Plastics,” SPIE Proc., vol. 3680-1, pp. 464-471, 1999.

6. Yoshii, M., H. Kuramoto, Y. Ochai, “Experimental Study of the Transcription of Minute Grooves by Injection Molding (II)”, Polym. Eng. Sci., V38, n. 9, pp. 1587, Sept. 1998.

7. Blough, G., et. al., “Single-point diamond turning and replication of visible and near-infrared diffractive optical elements”, Applied Optics, Vol 36, No 20, p. 4648, 1997.

8. Anagnostis, J, et.al., “Replication of high fidelity surface relief structures”, ASPE Spring Topical Meeting, Vol 19, p. 29, 1999.

15 VIBRATION ASSISTED MACHINING (VAM): ELLIPTICAL DIAMOND MILLING

Matthew A Cerniway
Graduate Student
Thomas A Dow
Professor
Mechanical Engineering Department

Turning has been the precision manufacturing method of choice over milling due to its combination of relatively short machining time and high-quality surface finish with single crystal diamond tools. However, one advantage that milling has over turning is the ability to uncouple the cutting speed from the material feed rate. The research underway at the Precision Engineering Center (PEC) is the development of a hybrid system that combines the advantages of milling and turning via a cyclic elliptical cutting motion. To this end, the Ultra Mill (UM), an in-plane (linear) elliptical tool servo, has been designed and built. Falling under the classification of Vibration Assisted Machining (VAM), UM research is also exploring the tool-chip interaction effects relating to duty cycle based cutting. A percentage quantity, the duty cycle is the fraction of the time per cycle that the tool is in contact with the material. Midway through its development, testing has shown that elliptical cutting has several advantages over standard cutting under identical machining parameters in the areas of surface finish and cutting force. As theorized, the ability both to uncouple part and tool speeds and to increase the projected tool cutting area, resulted in a 19% improvement in surface finish at part centers. The second advantage associated with the elliptical motion of the UM comes via a reduced cutting force. Closely following a PEC developed theoretical model of generated cutting forces, workpiece forces were reduced by as much as 50% verses standard cutting without any increase in surface roughness. The next step is the development of a high-speed version of the UM, ~8 kHz or 480,000 rpm equivalent. The effects of tool wear in elliptical milling and the potential of diamond milling of non-typical materials, i.e. steel and ceramics, will be investigated.

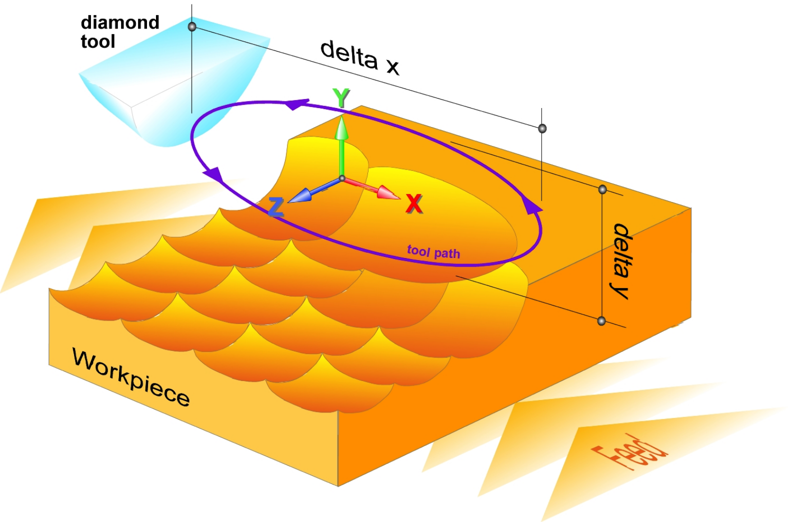

15.1 PRECISION MANUFACTURE OF OPTICAL SURFACES

In the current state of technology, the manufacture of optical components, whether mirrors, transmission optics or the like, requires the use of one of three primary machining techniques: turning, planning or milling. Due to its combination of relatively short machining time and high-quality surface finish, turning has established itself as the preferred method in the precision community. But despite all its benefits, it does have one major drawback, the coupling of part rotational speed with cutting speed. It is in this regard that milling and the ability to vary the two independently has an advantage.

A new class of machining, Vibration Assisted Machining (VAM), has been suggested as the next step in the evolution of optics manufacturing. Research performed by Brinksmeier at the Univ. of Bremen has suggested that VAM may extend the use of diamond tools to materials that destroy the diamond due to heat induced chemical abrasion [1]. It has also been hypothesized that a cyclic cutting motion possessing both a vertical and horizontal component may reduce tool forces by helping to lift the chip from the workpiece [2]. Brittle material such as ceramics and silicates, low-carbon steels and certain plastics stand to benefit from VAM.

The Precision Engineering Center (PEC) at North Carolina State University has developed a hybrid vibration assisted machining servo that combines the advantages of both milling and turning. Achieved through a unique linkage system, this servo or UltraMill produces an in-plane (linear) elliptical cutting motion.

15.2 THE ULTRAMILL

15.2.1 DESCRIPTION

To study the linkage dynamics, a low-speed (LS) prototype with an operational bandwidth of DC to 400 Hz was designed and built. Figure 1 illustrates the primary components of this servo variant.

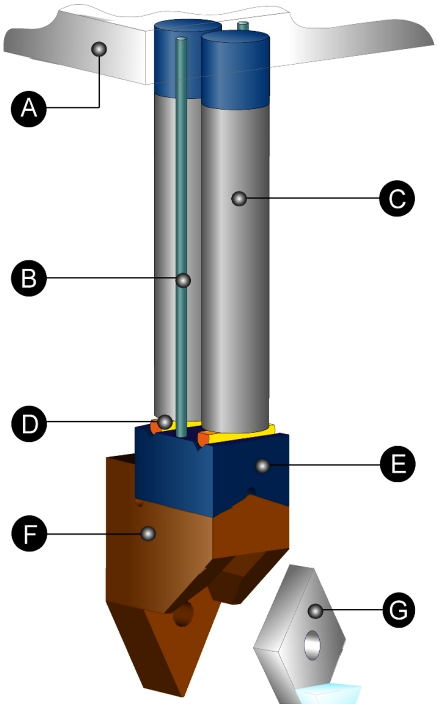

Figure 1. Low Speed Prototype

A steel frame (A) capable of mounting on both a vacuum chuck and micro-height adjustable tool post forms the base of the UltraMill-LS. Enclosed within the base is a cam mechanism *(not shown)* used to apply approximately 10 lbs of tension to a 0.010” diameter music wire (B) that serves a two-fold purpose: one to preload the piezo ceramic stacks and two to keep the head firmly seated on the stack ends while it undergoes the rapid acceleration changes associated with the UM-LS motion. Two 44-layer piezoelectric actuators (C) form the engine of this tool servo. These 6.35 mm diameter stacks measuring 25.4 mm in overall length are each capable of producing 22 µm of displacement. Seated on the end of each piezo stack is a 6 mm long, 1.58 mm diameter half round hardened steel pivot pin (D), that mates to a V-notched groove in the tool head mount (E). Utilizing a kinematic design for precise realignment, the mount connects to the tool head (F). Machined out of 6061-T6 Aluminum, the tool head accepts diamond shaped tool inserts (G).

15.2.2 THEORY OF MOTION

The UltraMill produces a cyclical elliptical cutting motion. This motion is referred to as linear because the ellipse resides in the 2D space of the x and y axes. The basis of the ellipse can be found in the makeup of the UM's linkage system shown in Figure 2.

Assuming the linkage arms "a", "b" and "c" are equal in length, driving the piezo stacks 90° out of phase with respect to each other will result in the tool traversing a circular path. By varying the relationship between the arms, the path can be modified. Referred to as a "T" shaped linkage, holding the trunk of the "T" or arm "c" constant and adjusting the relationship between arms "a" and "b" will result in tilting the path. Equating the lengths "a" and "b" while elongating arm "c" generates a level elliptical path.

The direction of the travel shown in Figure 2 is counter-clockwise or forward. However, forward or reverse is controlled by which piezo actuator receives the +90° phase addition to its supply voltage. In the case of forward motion, the second stack, denoted "Piezo Two" in Figure 2, receives the phase adjustment.

Since piezoelectric ceramics vary almost linearly with voltage, the end stack position can be modeled with a cosine function.

$$P_1 = A\cos(wt) \qquad (1)$$

$$P_2 = A\cos(wt + \phi) \qquad (2)$$

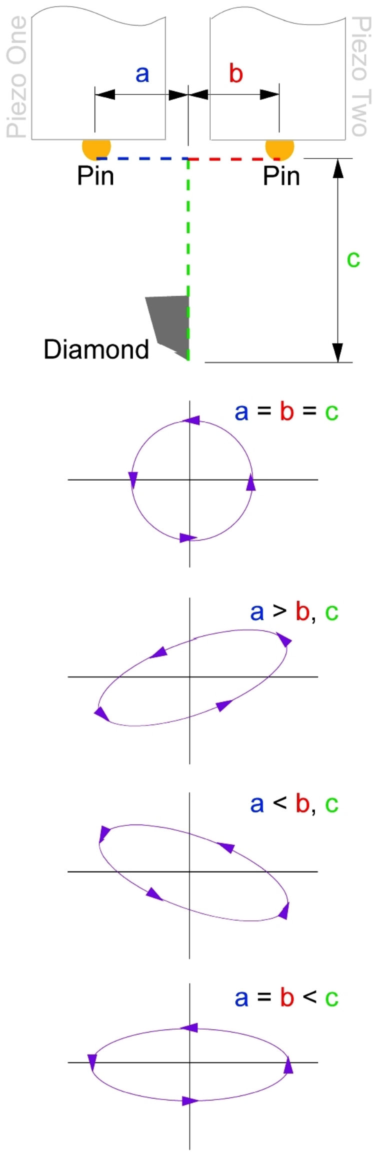

Figure 2. Linkage and Path Shapes

Coupled with the "T" linkage, the component position location *Δx* and *Δy*, can be calculated. β describes the amount of tilt between the two stacks.

$$\beta = \frac{P_2 - P_1}{a + b} \tag{3}$$

$$\Delta x = c \times \beta \tag{4}$$

$$\Delta y = \frac{P_1 \times b + P_2 \times a}{a + b} \tag{5}$$

Figure 3a reveals the tool path of the UM-LS with a = b = 3.150 mm and c = 22.962 mm. Due to the phase shift, only 70% of the piezo stack elongation is exhibited in the y-axis displacement. This varies from 100% at 0° phase separation to 0% at 180° separation. This relationship becomes evident when y-axis displacement is plotted on top of the stack end movement (Figure 3b).

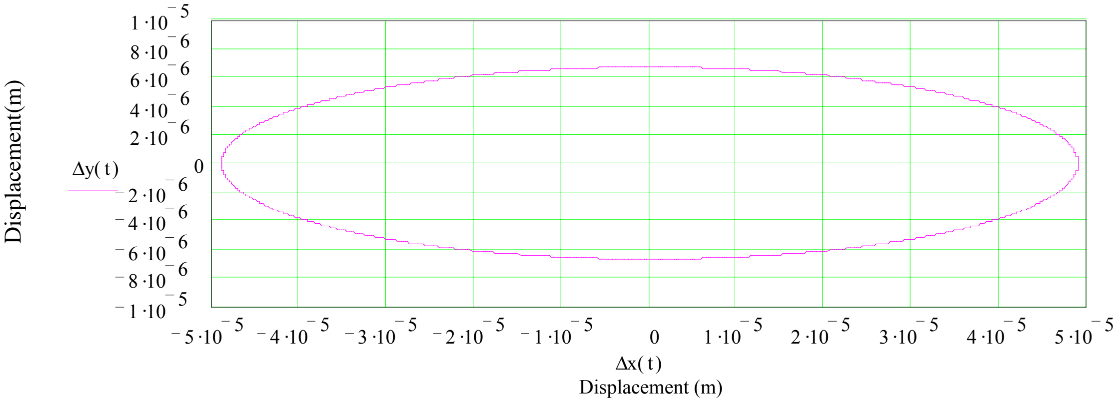

Figure 3a. Tool Path

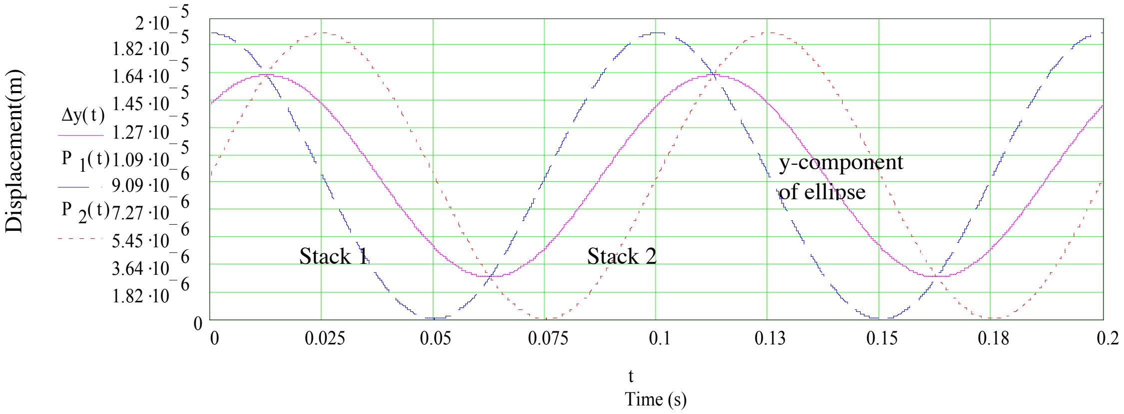

Figure 3b. Y-Axis Relationship to Phase Separation (freq = 10Hz)

15.2.3 OPERATION

The 8-volt ac actuator supply voltage is generated using a HP® 8904 multi-function synthesizer, which is capable of not only supplying a uniform sine wave to each channel but also providing the 90° phase shift. Using a Kepco® PCX 40-0.5 voltage regulator, a 4-volt offset is provided to the synthesizer thus allowing the supply signal to avoid negative voltage that would damage the stacks. The supply voltage is then amplified 100x by routing the signal through a Trek® model 50/750 amplifier.

15.2.4 SYSTEM BEHAVIOR

System behavior is broken into two categories: natural frequency and motion. Using a StanfordResearch Systems® Model 780 Spectrum Analyzer, a swept sign wave is generated. Once amplified, it is feed into one of the two stacks. Initial comparative testing showed less than a 1% deviation in system response for excitation of either piezo stack. As seen in Figure 5, a reflective insert of equal weight to a 1mm radius diamond tool insert is used in conjunction with a dual channel fiber-optic displacement gage (Opto-Acoustics® Angstrom Resolver®). This gage has nanometer resolution and is used to decompose the tip motion into its x and y components. The results of this testing, listed in Table 1, put the first natural frequency at 525 Hz. To operate under the first natural frequency, the operational bandwidth is dc to 400 Hz.

Table 1. Operational parameters of low-speed UltraMill

UltraMill-*LS*		
Bandwidth	0 - 400	hz
Drive Voltage	0 - 8	Vac
Mass	7.2	grams
Natural Frequency		
1st (out of plane)	525	hz
2nd (rotational)	700	hz
Motion		
Major Axis	47.501	µm
Minor Axis	7.295	µm
Tilt	-2.411	°
Axis Ratio	6.51	--

Using the same data collection equipment discussed above, the tip motion was measured by driving the stacks with their normal 800-volt signal. After processing the fiber-optic output with the spectrum analyzer the path shown in Figure 4 resulted.

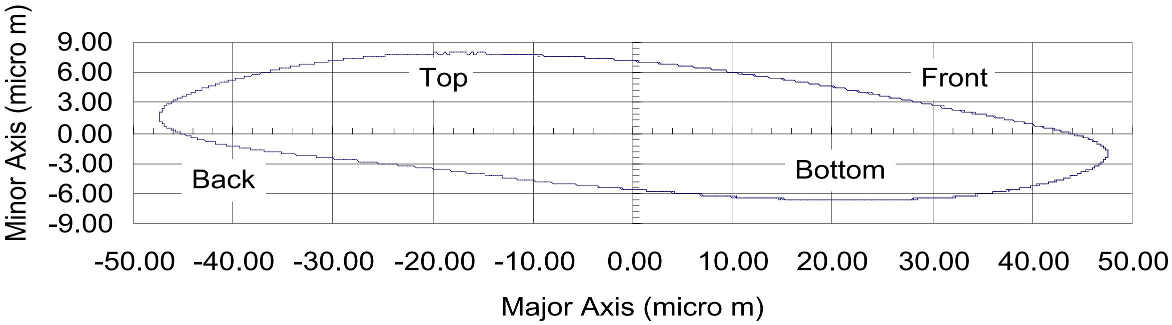

Figure 4. Cutting Motion of Low-Speed UltraMill

The shifted minor axis peak of this particular assembly is due to a slight difference in the stack properties: elongation and hysterisis. The tilt is a result of small differences (1-10µm) in the overall lengths of the two stacks. Despite the minor variation from the ideal waveform, the cutting zone, labeled “Bottom” is acceptable for cutting purposes.

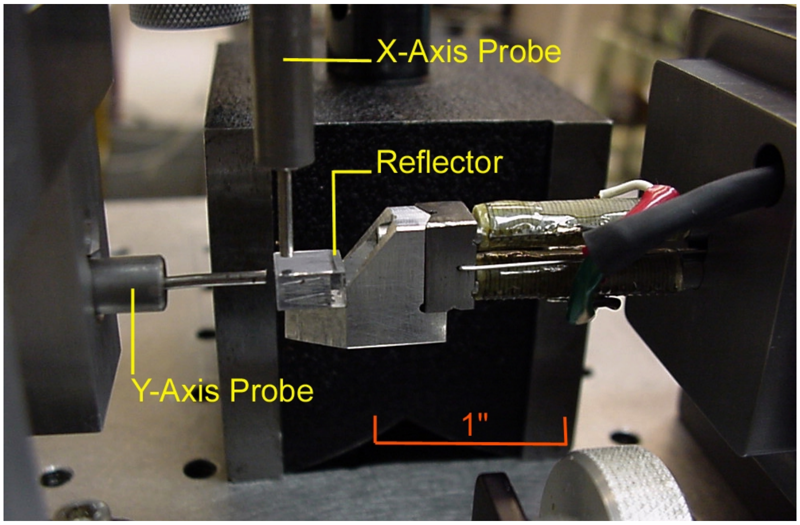

Figure 5. Motion Testing Arrangement

15.3 SURFACE FEATURES

15.3.1 SURFACE FINISH

The peak-to-valley surface roughness in the x-y plane of an elliptically driven tool is:

$$PV_{ellipse} = \frac{b f_{index}^{2}}{8a^{2}} \qquad (6)$$

where f_{index} is the distance indexed per cycle and a and b are the respective major and minor axes of the ellipse. With a large axis ratio (a/b), very low surface roughness can be achieved.

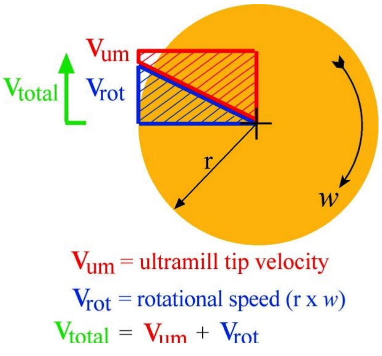

Figure 6. Uncoupled Speeds

When used as a replacement for a stationary tool in a turning operation, the advantage of uncoupled part rotational speed and cutting speed can be exploited. As illustrated in Figure 6, the tool moves from the outside of the part to the inside of the part. During standard turning the tool tip velocity decreases from maximum velocity equal to the rotational speed times the radius of the part to a velocity of zero at the center of thepart. This non-uniform cutting speed can have deleterious effects on the surface finish.

Instead of changing the rotational speed of the lathe's air bearing spindle which could vibrate during adjustment, the UM's tip velocity can be adjusted to compensate for the rotational velocity decrease. The result should be an improved surface finish at the interior of the part.

The UM operates on the principal of a duty cycle, the percentage of time per elliptical cycle that the diamond is in contact with the workpiece. The duty cycle influences both the amount of force exerted on the material (covered in a later section) and the surface roughness described earlier by Equation(6). Duty cycle is adjusted by varying the distance indexed between cycles, f_{index}. Figure 7 plots the duty cycle for all the ratios of workpiece velocity(V) to critical (maximum) tool velocity(V_{crit}) cases. During the bottom half of the elliptical cycle, the tool is moving towards the workpiece. During the top half, the tool is in retreat. Figure 7 shows that as the workpiece velocity matches or exceeds the tool velocity, the tool can not retreat fast enough and thus cutting is always taking place, i.e. $V/V_{crit} = 1.0$ or 100% Duty Cycle.

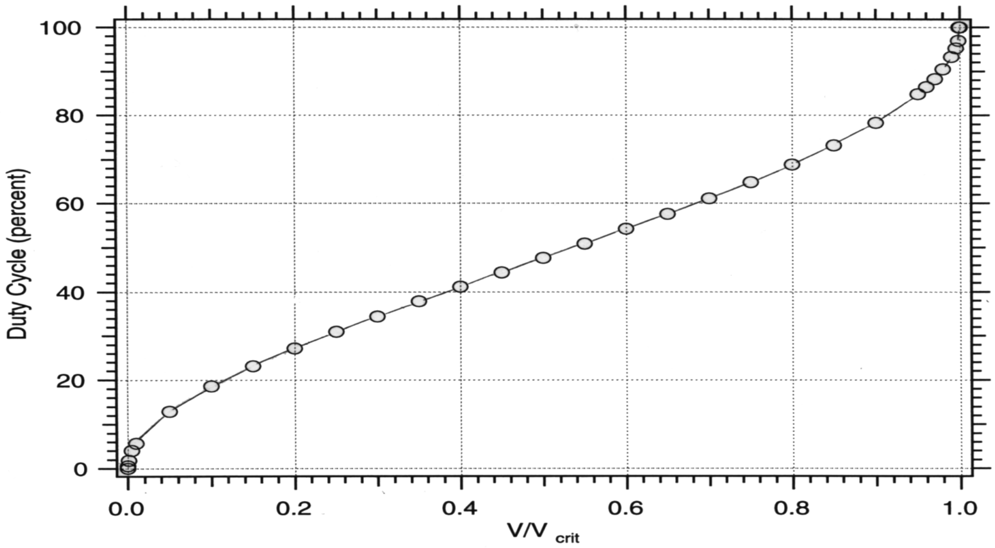

Figure 7. Duty Cycle Chart for Elliptical Cutting

Table 2. Surface Finishes

Theoretical Surface Finishes @ 10hz		
Duty Cycle	f_{index} (µm)	P-V (nm)
5%	2.985	3.601
10%	10.446	44.099
15%	21.638	189.219

Previous research into vibration cutting used duty cycles on the order of 10 – 20%. Based partially on these earlier trials and on the as yet to be discussed cutting force model, duty cycle percentages of 5, 10 and 15 were chosen. Reading these values from Figure 7 as 0.010, 0.035 and 0.0725 respectively, the per cycle index distance is calculated,

$$f_{index} = 2\pi \times DutyCycle_{\%} \times axis_{major} \qquad (7)$$

The index values and theoretical x-y plane surface finish are compiled in Table 2.

15.3.2 PHASE EFFECTS

The last surface feature created by elliptical milling is referred to as phase. Note the phase shift between the features at the left side of Figure 8 compared to those at the right for the next pass of the tool. Phase alignment is analogous to the phase between two sinusoidal signals. They are said to be in-phase at 0° and out of phase between 1° and 359°. And like signals, in-phase surface features sum to produce a greater amplitude or surface roughness. For the best surface finish, each row's cuts should be 180° out of phase with the next. In other words, a 180° phase shift would result in each successive row removing the peaks left by the previous pass of the tool. Figure 9, borrowed from earlier PEC work into the development of a theoretical grinding model shows how surface roughness is reduced as phase shift approaches 180° or 0.5 in normalized form [4].

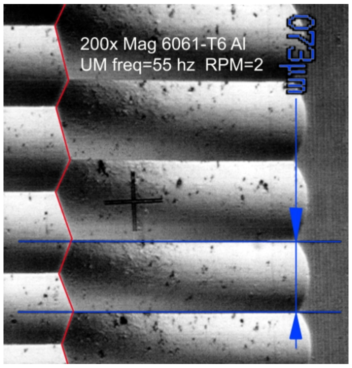

Figure 8. 200x Magnification 6061-T6 Al, UM Freq.= 55 Hz, Spindle Speed = 2 rpm

For turning applications, phase can be calculated by the following equation,

$$Phase = \frac{N_w}{N_p} - Int\frac{N_w}{N_p} \tag{8}$$

where N_w is the tool rotational speed or UM frequency and N_p is the part rotational speed or up-feed. So, like the UM's tip generated velocity, control of phase alignment can be used to improve part surface finish.

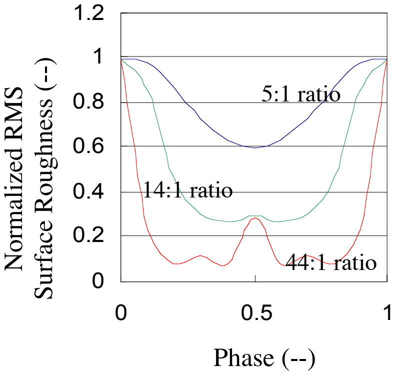

Figure 9. Surface Improvement with Increased Upfeed: Crossfeed Ratio.

15.3.3 EXPERIMENTAL RESULTS

Surface Finish As hypothesized in the preceding section, turned copper and aluminum alloys have shown reduced roughness for elliptical cutting. Figures 11 compares typical results of these trials. Mounted on an ASG-2500 Diamond Turning Machine, copper (c11000 alloy) and aluminum (1000 Series) plugs, 12mm in diameter, were turned using the same spindle speed, cross feed and depth of cut parameters. Comparing the surface roughness and form error of 14 turned plugs (7 standard turning and 7 with UM) showed a 19% reduction in radial peak to valley surface roughness and a 74% reduction in angular peak to valley surface roughness, defined in Figure 10. Form error over the sampling group showed no improvement with the UltraMill active.

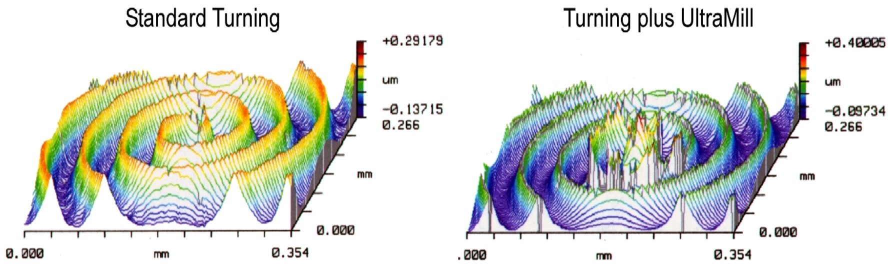

Figure 11. Oblique Plots of Turned Copper Flats. Reduced Peak Height of UM Sample vs. Standard.

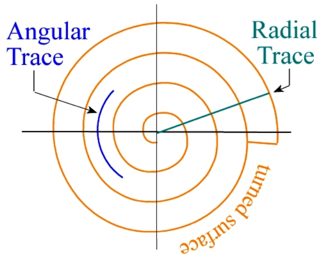

Figure 10. Surface Roughness Trace Definitions

The improved surface finish is a result of an effective increase in tool size caused by the elliptical motion of the tool. Illustrated in Figure 12, the summation of the cords spanning the contact points on the diamond tool bit form a 2D elliptical cross-section. This increases the cutting zone in every cycle compared with that of a stationary tool. The result is most pronounced as the part radius decreases, i.e. towards the center of the part. As with phase, the peaks of the preceding row's cuts are clipped off by each subsequent pass of the tool.

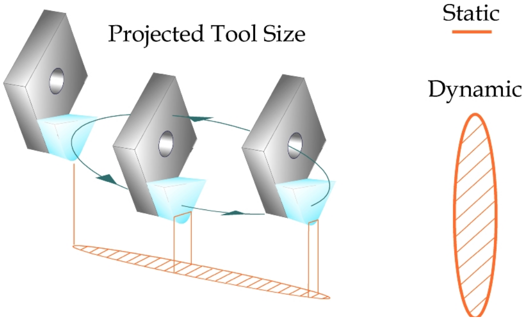

Figure 12. Dynamic Tool

Phase

The surface of each turned sample was mapped and phase alignment was tabulated. Phase is controlled by the ratio of the up-feed to the cross feed assuming a constant cut width. Figure 13 is the surface map of a turned part with the up-feed and cross-feed parameters indicated. Note how the cut widths in Figure 13 are not uniform. Thus the actual phase from one row to the next varied from the theoretical value established by Equation (8). To assess why, the length of each cut was measured and adjusted for the differences in radii. For a constant rpm, the further away the tool is from the center of the part (increasing radius) the greater the distance (circumference) that must be traversed per spindle rotation. With a fixed number of cuts per second (UM operational

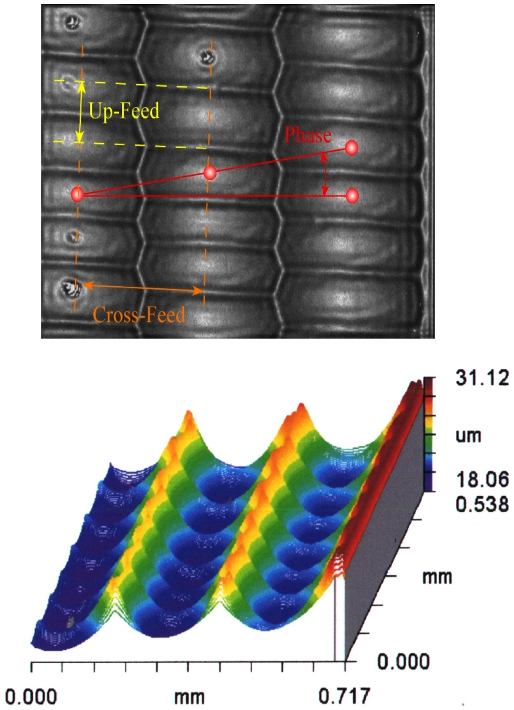

Figure 13. Turned Aluminum Flat

frequency), this increasing circumference results in the UM cutting a longer chip per elliptical cycle as the radius from the part center increases. It was found that the variance from one cut to the next was on the order of 6.3%. Data from a representative sample is plotted in Figure 14. Taken with the radius of the particular cut, the cut length is an indirect measure of phase. Once the theoretical value was adjusted by the given percentage, the accuracy fell to within ± 0.3°.

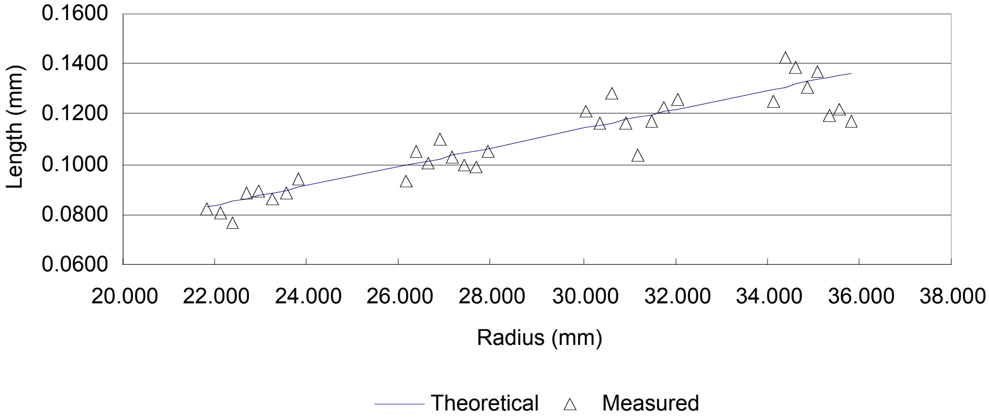

Figure 14. Chip length variation from theoretical

15.4 CUTTING FORCES

15.4.1 THEORETICAL MODEL

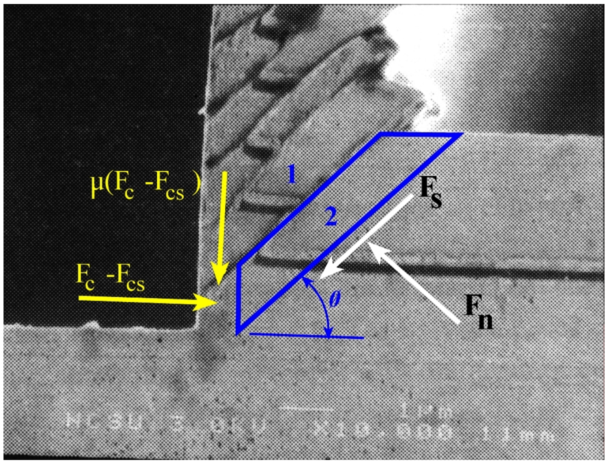

Figure 15. Cross section of plated copper chip w/ next section overlaid

The elliptical cutting model is base on a linear model developed by Dr. Christopher Arcona while at the Precision Engineering Center [3]. Figure 15 is a SEM image of the root of the chip. Segment 1 is the chip just created, while segment 2 is the chip that will form when the tool is indexed another 0.5μm forward. Overlayed on this image are the forces acting on cross section 2. The total cutting force acting on the tool is F_c. F_{cs} is the force associated with the sliding of the tool over the workpiece. F_s and F_n are the component forces acting at a shear angle of ϕ on the shear zone. Lastly, μ is the coefficient of friction between the diamond face and the chip. Performing a force balance on element 2 results in equations for the cutting force and thrust force.

$$F_c = F_s \cos(\phi) + F_n \sin(\phi) + F_{cs} \tag{9}$$

$$F_t = \mu(F_c - F_{cs}) + Ft_{sliding} \tag{10}$$

The coefficient of friction at the tool/chip interface, μ, can be calculated from the summation of forces in the vertical direction. The result of which is Equation (11),

$$\mu = \frac{\cos(\phi) - \dfrac{\sin(\phi)}{\sqrt{3}}}{\dfrac{\cos(\phi)}{\sqrt{3}} + \sin(\phi)} \tag{11}$$

If the material hardness and either the shear angle or the coefficient of friction is known, the tool forces can be calculated. Written in terms of cutting conditions and material data, the tool forces are given by,

$$F_c = \frac{HA_c}{3}\left(\frac{\cot(\phi)}{\sqrt{3}} + 1\right) + \mu_f \sigma_f A_f \tag{12}$$

$$F_t = \mu\left[\frac{HA_c}{3}\left(\frac{\cot(\phi)}{\sqrt{3}} + 1\right)\right] + \sigma_f A_f \tag{13}$$

$$\sigma_f = 0.62H\sqrt{\frac{43H}{E}} \tag{14}$$

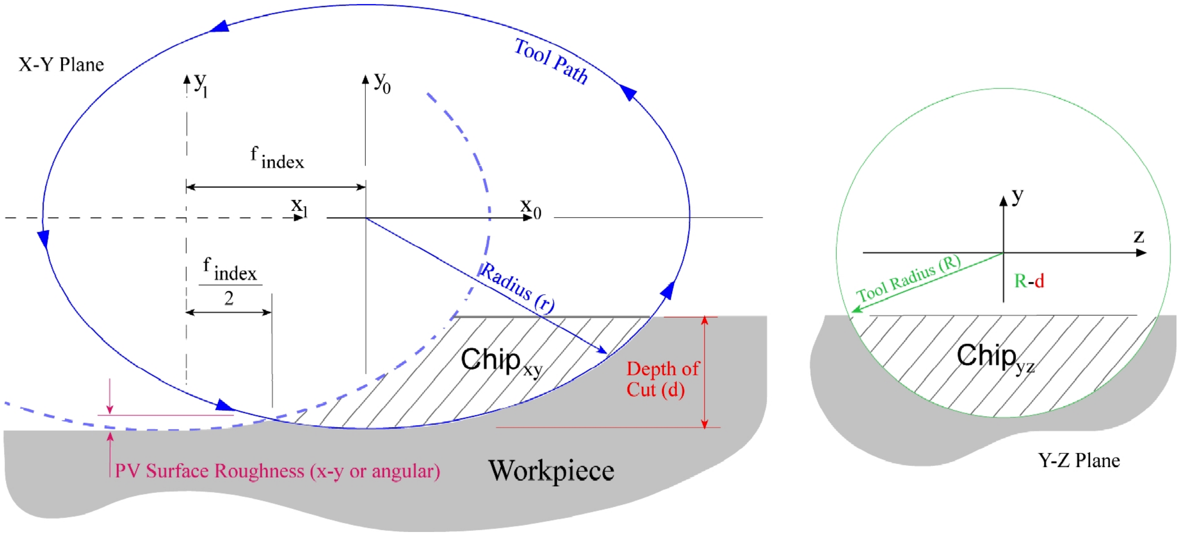

Figure 16. Basic chip geometry in 2D (straight line) elliptical milling

Elliptical cutting differs from standard cutting for which the preceding force model was developed in two respects. The first is varying chip thickness as illustrated in Figure 16. The point of initial contact is half the index distance also referred to as the duty cycle index distance. Between this point and the time when the tool leaves the workpiece, the chip thickness varies as shown in Figure 17.

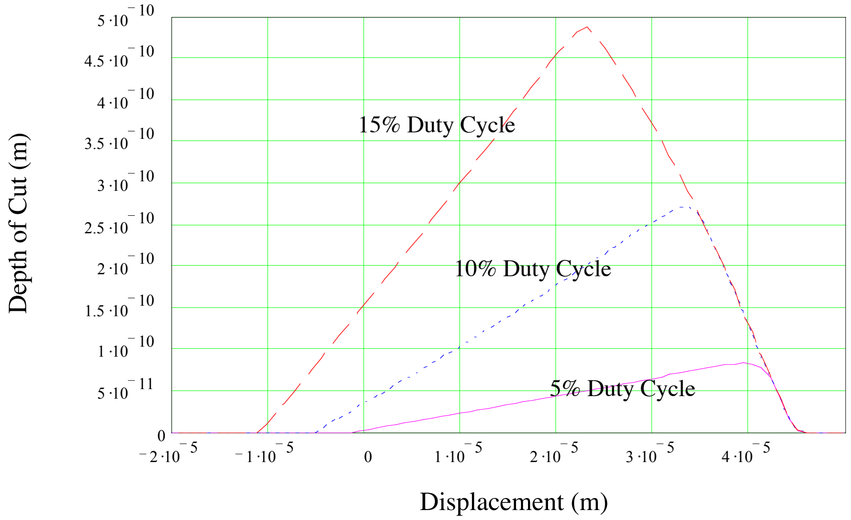

Figure 17. Chip thickness for different duty cycles (1 mm tool edge radius, 5 µm depth of cut major axis = 47.5 µm, minor axis = 7.3 µm)

The second and most interesting departure from the standard model concerns the relationship between the tool and the chip velocities. For standard cutting of a material such as copper with a shear angle of ~ 45°, the vertical velocity of the chip will be equal to the cutting speed. Thus for standard cutting, the chip velocity and tool edge velocity are functions of the shear angle.

The elliptical milling velocity relationship is not as simplistic. No longer is the cutting velocity constant. It changes in magnitude and direction as a result of the elliptical motion of the tool. This change in cutting direction has an effect on two parameters in the model, the shear angle and the frictional Area, A_f. Figure 18 disassembles the velocity and shear angles into their

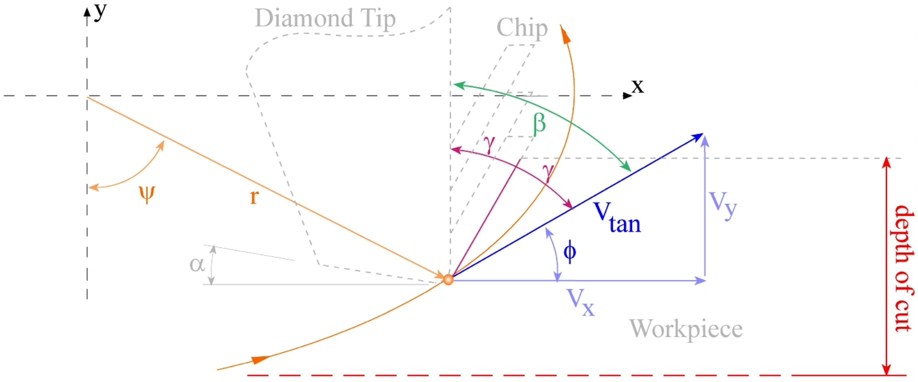

Figure 18. Tool Velocity Components

component parts. Note, that while still under investigation, shear angle, γ, is assumed to be the bisector of the angle between the workpiece tangent and the tool face, β. The validity of this assumption and several others are currently being evaluated in light of the force test results.

Proceeding with the given model, knowing the x and y components of the tool motion, the velocity components can be calculated by differentiation,

$$V_x = \frac{d}{dt}x(t) + V_{workpiece} \tag{15}$$

$$V_y = \frac{d}{dt}y(t) \tag{16}$$

The tangential velocity, $V_{\tan}$, is then calculated.

$$V_{\tan} = \sqrt{V_x^{\ 2} + V_y^{\ 2}} \tag{17}$$

The angle, ϕ, between the path tangential velocity and the x-axis is given by,

$$\phi = \tan^{-1}\left(\frac{V_y}{V_x}\right) \tag{18}$$

Finally the shear angle and chip velocity are determined,

$$\gamma = \frac{\pi}{4} - \frac{\phi}{2} \tag{19}$$

$$Velocity_{chip} = V_{\tan}\tan(\gamma) \tag{20}$$

Figure 19 plots $V_{\tan}$ for one cycle of an operational frequency of 10 Hz. The tangential velocity is shown bounded by the minimum and critical velocities used in determining the duty cycle index, f_{index}.

$$V_{critical} = 2\pi \times f \times axis_{major} \tag{21}$$

$$V_{minimum} = 2\pi \times f \times axis_{minor} \tag{22}$$

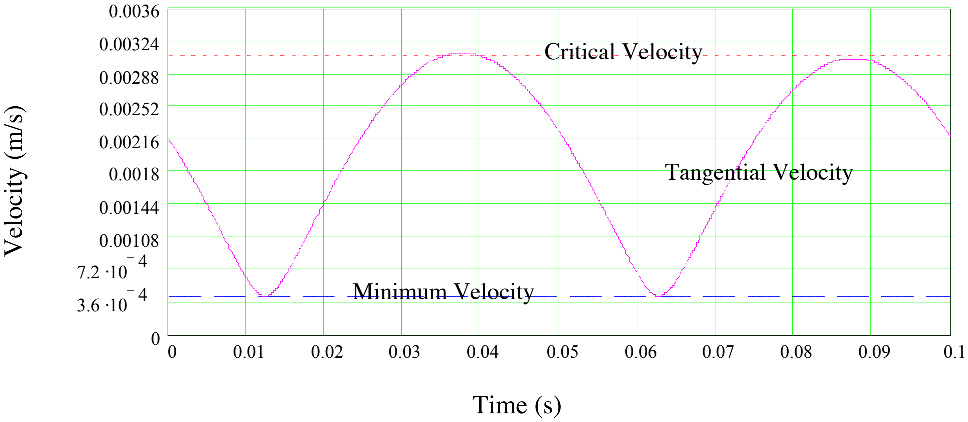

Figure 19. Path Tangential Velocity Change Over One Cycle (operational freq. = 10 hz)

The length of time during which cutting is taking place is simply,

$$time_{\%} = \frac{DutyCycle\%}{f} \tag{23}$$

For a cutting frequency of 10 Hz and with duty cycles of 5, 10 and 15%, contact times are 0.005, 0.010 and 0.015 seconds respectively. These numbers are useful when looking the plot of chip/tool velocity interaction shown in Figure 20. Note that for the given cutting frequency, the fourth quadrant (Figure 22), or primary cutting quadrant, starts at 0.04 seconds and continues to 0.0625 seconds.

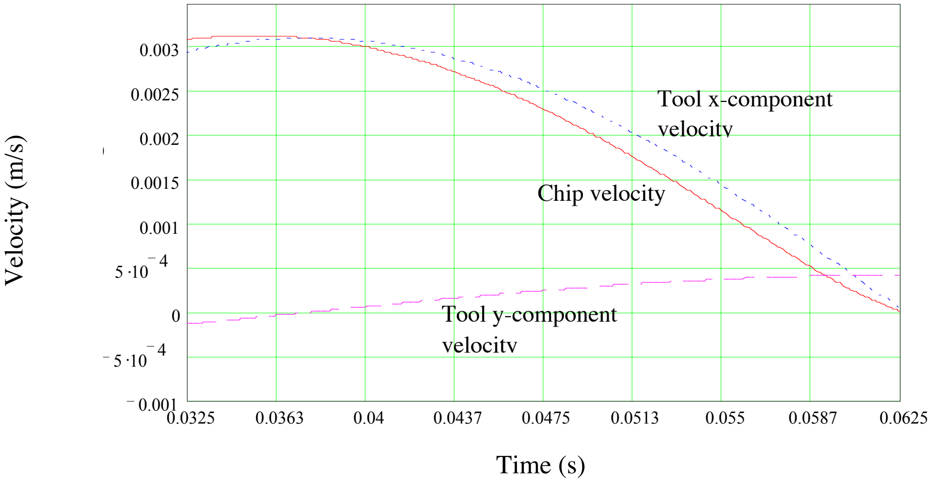

Figure 20. Chip and Tool Component Velocities

What is interesting is the cross over point at which the vertical component of the tool becomes greater than that of the chip velocity. For the given parameters, this takes place around 0.06 seconds. Figure 21 provides a close-up look at that section.

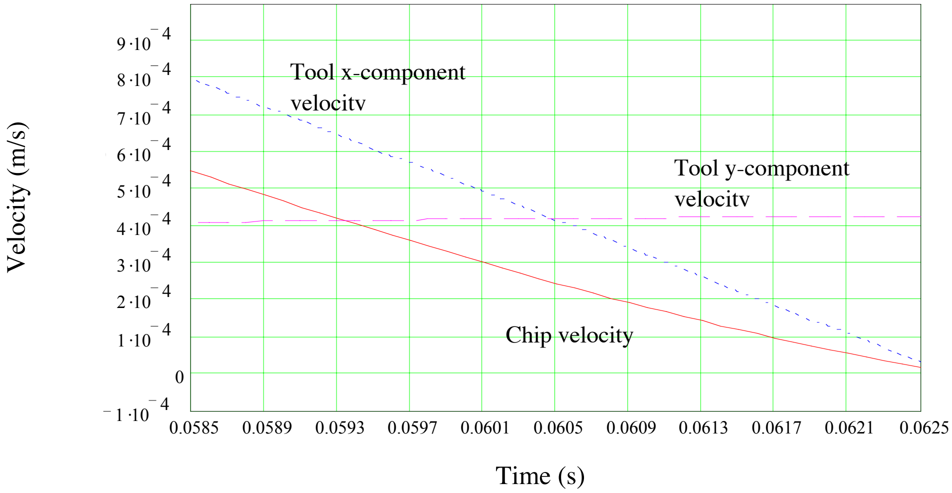

Figure 21. Zoomed View of Velocity Relationship Plot (Figure 20)

Assuming a depth of cut equal to the minor axis, Figure 21 shows that during the last 0.00185 seconds (0.42μm of cutting) the velocity of the tool is greater than that of the chip. This is a significant finding, because this lifting of the chip by the tool results in a sign change in the force equation, thus reducing the force exerted on the workpiece. This lifting effect opens up the possibility of machining materials that were too brittle to machine.

Although presented for a specific case, this lifting phenomenon can be predicted for any set of cutting velocities. The portion of the cycle involved in lifting the chip from the workpiece is increased as the phase separation of the driving piezoelectric stacks is decreased. However, changing this separation would result in a higher peak to valley surface roughness as calculated by Equation (6).

Changing the duty cycle offers even a greater reduction in force. As defined earlier in the discussion of elliptical milling surface features, duty cycle is the percentage of time that the tool is cutting over one cycle. In physical terms, it is the distance (Equation 7) the tool is indexed before the next cut is made.

15.4.2 EXPERIMENTAL RESULTS

Based on the cutting model, the point at which duty cycle cutting no longer exhibits a reduction in force over standard cutting is approximately 30%. Therefore 5, 10 and 15% duty cycles were selected for this test. The experiment was also limited to straight in-line cutting by locking the rotating spindle and using the cross slide to move the tool. Figure 22, a test sample of 6061-T6

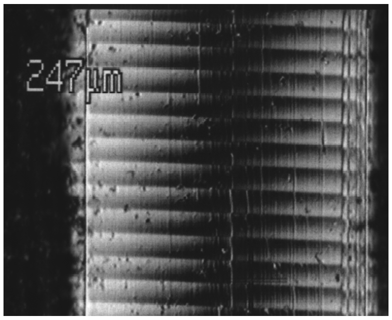

Figure 22. In-Line Cutting

Aluminum cut with a 15% duty cycle at an operational frequency of 10 Hz, illustrates the typical surface features produced during these experiments. The effects of cross-feed and phase are left for future experiments.

The ASG-2500 Diamond Turning Machine (DTM) was utilized for this experiment. Mounted on the DTM was a specially designed sample holder containing a Kistler® 9251A 3-axis force gage (Figures 23 and 24). The gage output voltage was recorded with a data acquisition module and fed to a G3 iMac for data analysis.

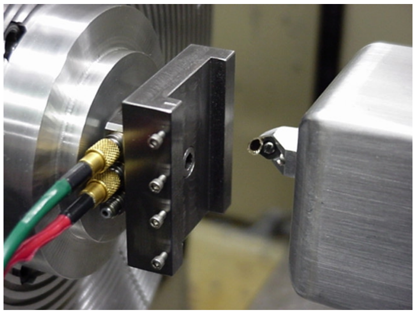

Figure 23. Force Gage on ASG-2500

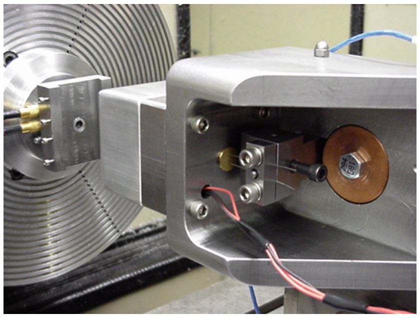

Figure 24. UltraMill Base w/ Preload Cam

The experiments were divided into two classes: Class A and Class B.

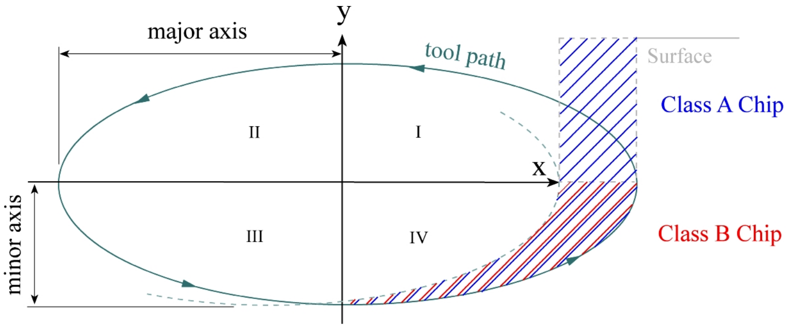

Figure 25. Depth of Cut Classification

As shown in Figure 25, Class B cutting occurs when the depth of cut is “below” the centerline x-axis of the elliptical path. Conversely, Class A cutting is when the depth of cut puts the surface of the workpiece “above” the centerline.

The materials used in this experiment were c11000 copper and 6061-T6 aluminum. The nose radius of the diamond tool varied from 1 to 3 mm. Measurements of the diamond edge radii were made on an atomic force microscope (AFM) and the findings implemented into the force model. Figures 26 and 27 report the predicted forces seen by the workpiece.

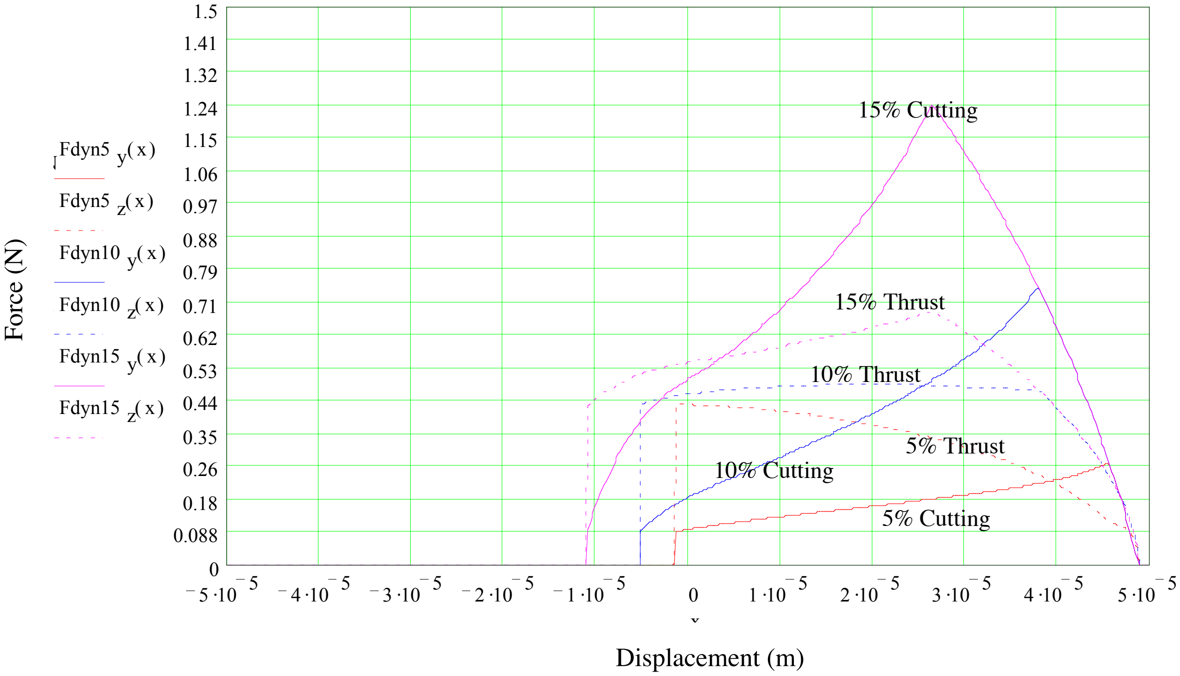

Figure 26. Cutting and Thrust Force for a Class B Chip
(copper, 3mm diamond, 6 μm depth of cut)

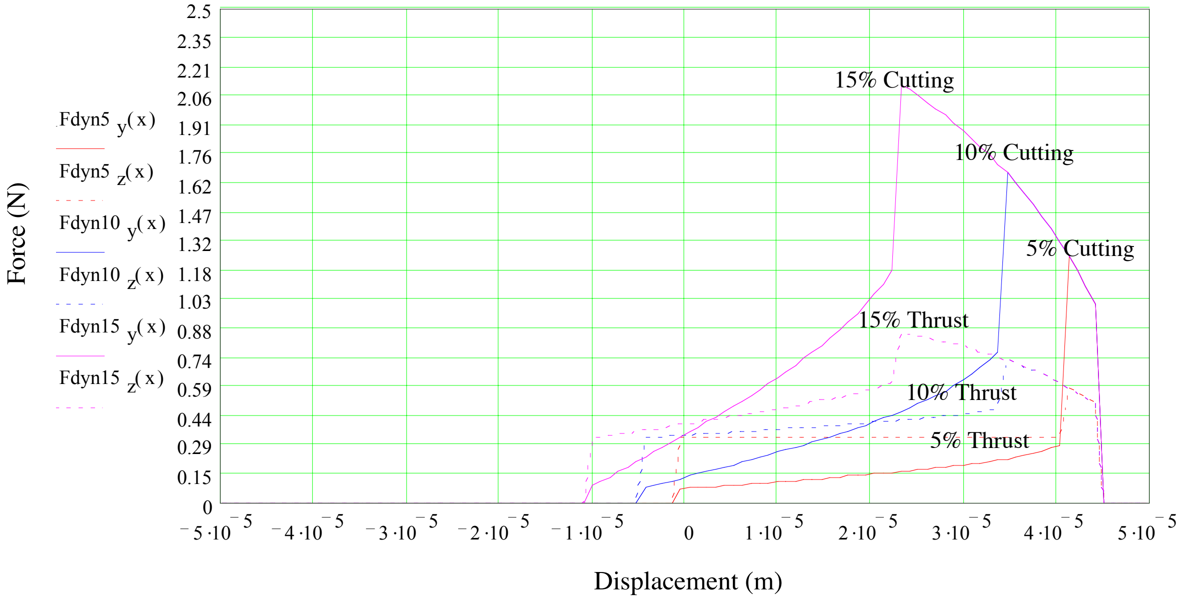

Figure 27. Cutting and Thrust Force for a Class A Chip
(copper, 1mm diamond, 10 μm depth of cut)

The cutting and thrust forces are shown as solid lines while thrust forces are shown as dotted lines of the same color (also labeled). Items not plotted on these two graphs are the forces generated by standard cutting. For the case shown in Figure 26, the standard cutting and thrust forces would be 1.839 N and 0.869 N respectively. The standard tool force for the second case, Figure 27, are 2.935 N in the cutting direction and 1.096 N in the thrust direction. In both cases, the duty cycle forces are lower than in standard cutting. The reason for the reduced forces is the amount of chip volume cut per cycle. Standard cutting removes the whole chip at all times, while elliptical milling removes just a fraction of that volume per cycle. But when summed over time, the volumes are equal. Comparing the duty cycles, the forces get progressively smaller as the duty cycle is reduced.

The key features to note when comparing the model to the test data are:

1. The crossover point between the cutting and thrust force.
2. The shape of the back slope.
3. The starting point of the cut.
4. The steep angle change with the 10µm depth of cut trail (Due to the transition from Class B cutting to Class A cutting, see Figure 25).

Figure 28 shows the results of the cutting trails for a Class B in-line chip.

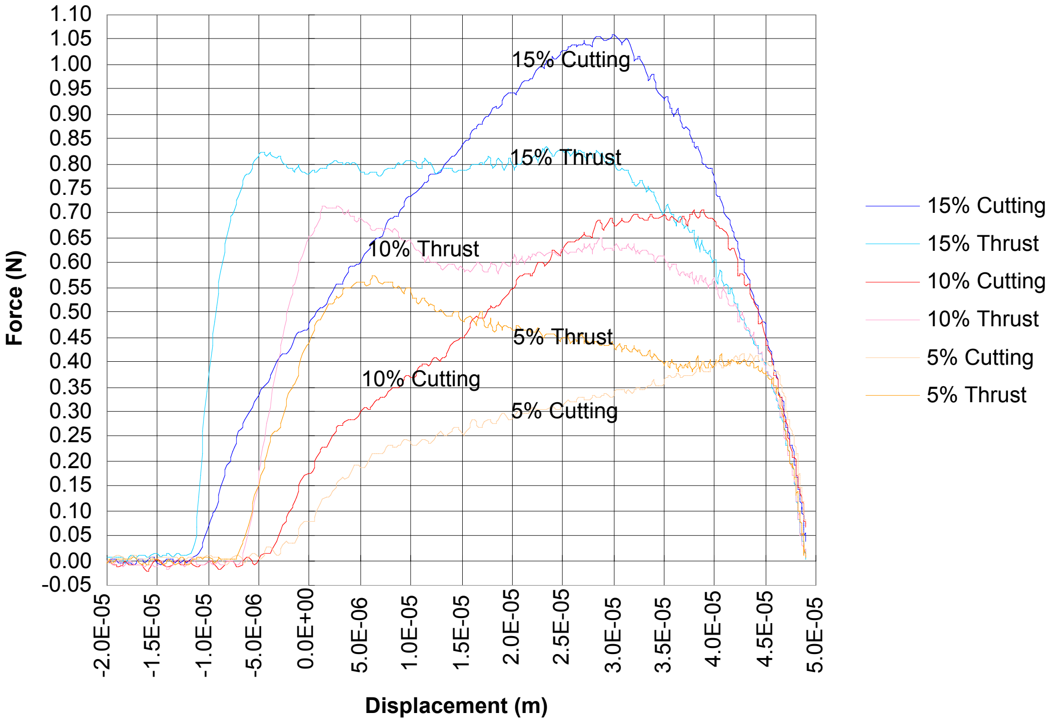

Figure 28. Duty Cycle Force Data for 110 Copper @ 6 µm Depth of Cut
3mm diamond / UM Freq = 10 Hz / DAQ Sampled @ 10 kHz per channel

For comparison purposes, Figures 29 through 31 combine the predicted and measured forces for each duty cycle.

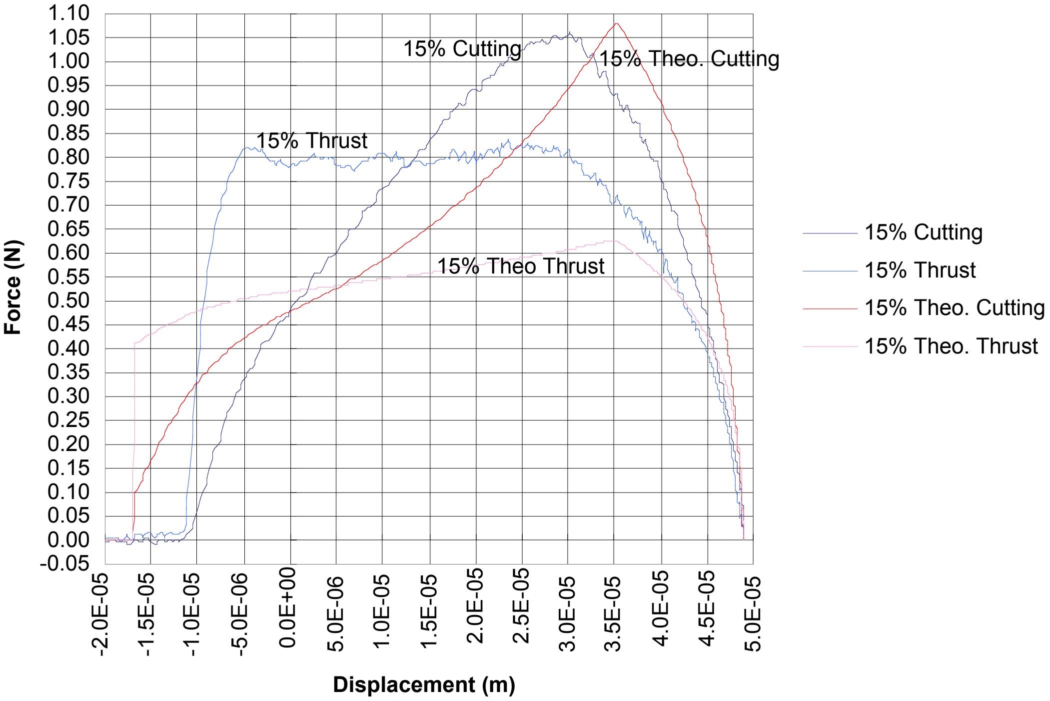

Figure 29. Experimental Data Overlaid with Predicted Values for 15% Duty Cycle

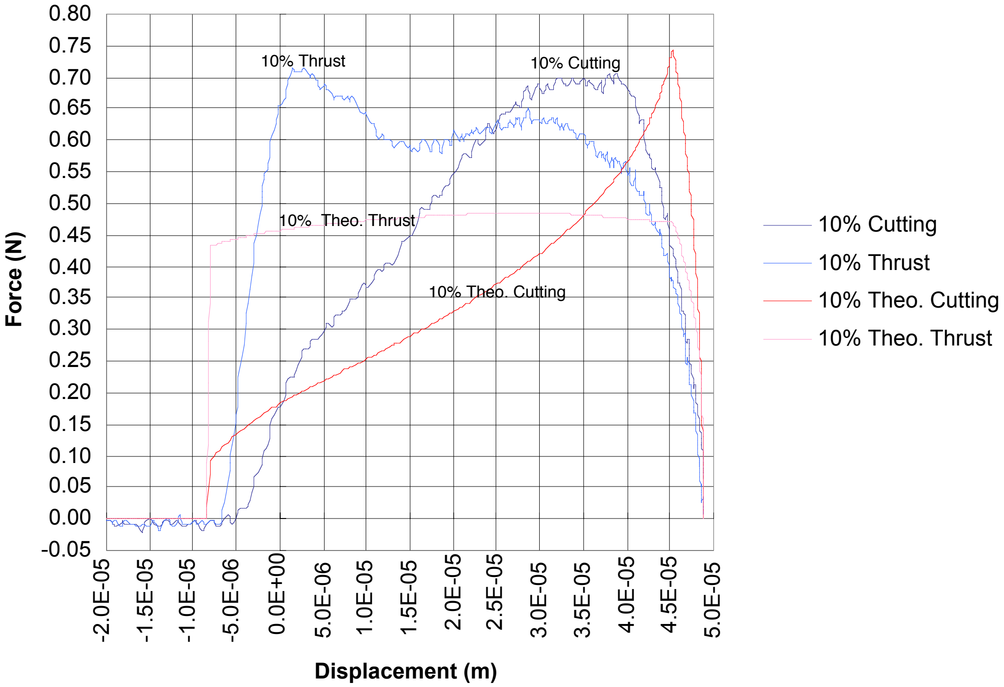

Figure 30. Experimental Data Overlaid with Predicted Values for 10% Duty Cycle

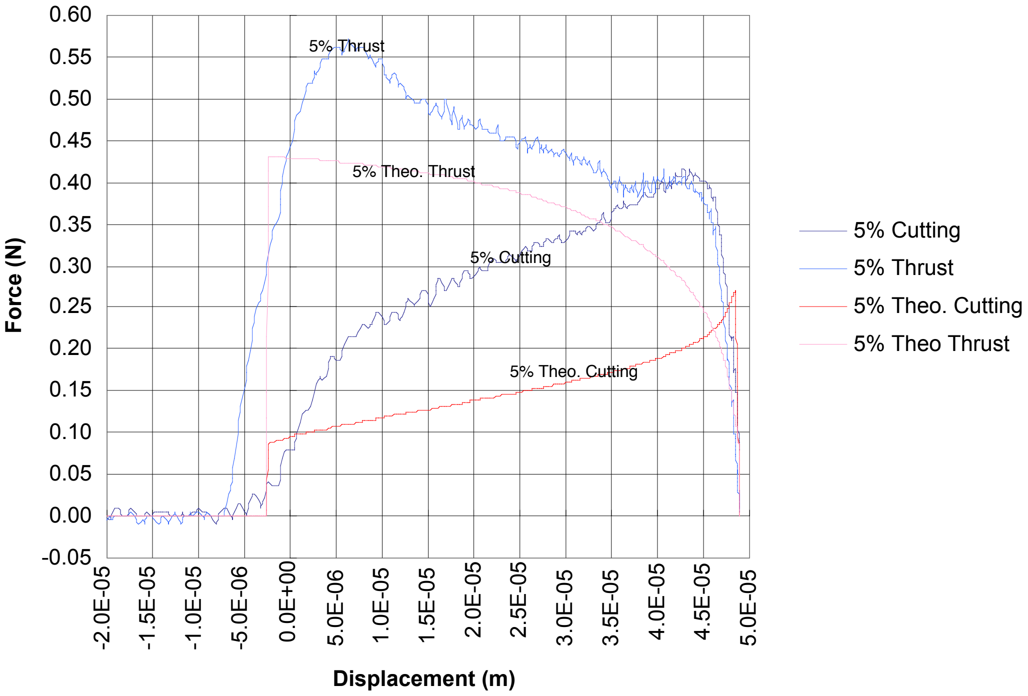

Figure 31. Experimental Data Overlaid with Predicted Valuesfor 5% Duty Cycle

The cutting force model closely predicted the shape of the back slope and relative magnitude of the cutting and thrust forces. The cutting force prediction accuracy ranged from 97.7% of actual for the 15% duty cycle case to 65.5% for the 5% duty cycle case. While predicting the overall shape and relation to the cutting force, the thrust force deviated somewhat from the test data. This is most likely a result of the shear angle assumption and/or the change in the tool's wear land over the elliptical path. Lastly, the model performed extremely well in the area of chip width, predicting it to within 8% of the actual width.

Force comparisons for Class A chips track similarly to those of the Class B chips just described. Figure 32 shows the forces recorded for one Class A chip cut on a 10% duty cycle. Note the increase in the front side slope. This is due to the depth of cut being greater than the minor axis. Also, the forces generated are greater than those of the 10% duty cycle case for a Class B chip due to the increased thickness of the chip.

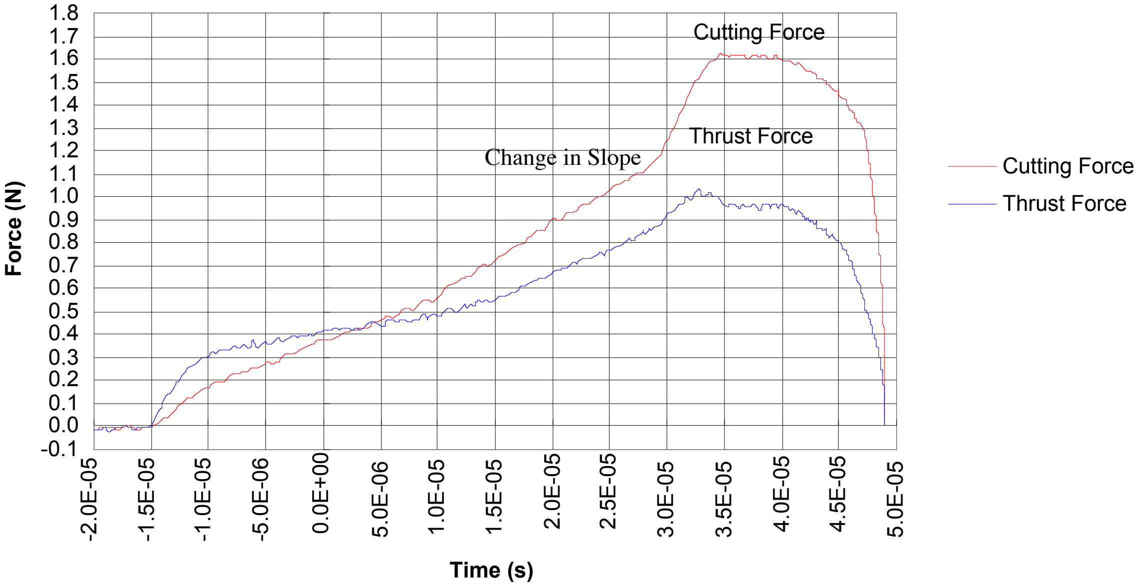

Figure 32. Experimental Data for 10% Duty Cycle
110 Copper / UM Freq. = 10 Hz / 1.02 mm radius diamond /
12.5 µm depth of cut / DAQ sampled @ 10kHz per channel

The ideal surface roughnesses listed in Table 2 are compared in Table 3 with the surface measurements on the test samples from the force trials. The measured values represent an average over all the samples.

Table 3. Surface Roughness Comparison

Duty Cycle	Theoretical		Measured			
	PV		PV		Ra	
5%	3.6	nm	17	nm	3	nm
10%	44.1	nm	45	nm	13	nm
15%	189.2	nm	244	nm	68	nm

The results trend closely with those of the theoretical roughness values. The difference between the two sets of PV numbers is attributable to the FFT taken on an rms voltage signal used in determining the UM's elliptical path. Also noted from these values was that while the forces increased from Class B to Class A cutting, no deterioration was seen in the end surface quality. This was expected because the surface finish is purely a function of the ellipse and not the depth of cut.

15.5 CONCLUSION

Elliptical diamond milling has been shown to produce lower tool forces than those of standard machining due to the reduced chip volume removed per cycle, while still maintaining excellent surface finish quality. If used in a turning application, an additional advantage of lower surface roughness at the interior of a part can be realized.

Chip size and surface finish resulting from elliptical cutting can be readily predicted. Despite slight discrepancies, the general agreement between the test data and force model is also encouraging.

Future work entails refining of the 2D cutting model and extending it to more realistic 3D cases. With reduced forces, the use of the UM on brittle materials will be investigated as will the feasibility of elliptical cutting of carbon steel. Current PEC efforts are focused on the development of a high-speed version of the UM capable of operational frequencies in the 5 to 10 kHz range.

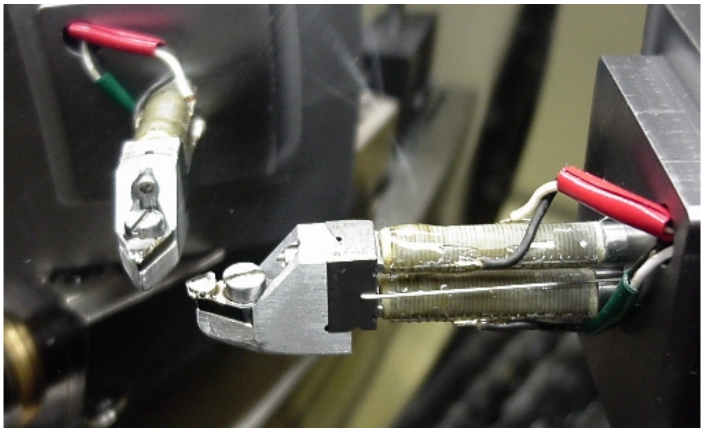

Figure 33. Image of the UltraMill-LS Reflected of a Turned Aluminum Sphere

REFERENCES

1. Brinksmeier, E. and Glabe, R., “Elliptical Vibration Cutting of Steel with Diamond Tools,” ASPE 1999 Annual Meeting, Vol. 20, pp 163-166, 1999.

2. Ahn, Jung-Hwan; Lim, Han-Seok:; Son, Seong-Min, “Improvement of Micro-machining Accuracy by 2-Dimensional Vibration Cutting,” ASPE 1999 Annual Meeting, Vol. 20, pp 150-153, 1999.

3. Arcona, Christopher, “Tool Force, Chip formation and Surface Finish in Diamond Turning,” Doctorial Thesis, North Carolina State University, Department of Mechanical and Aerospace Engineering. Raleigh NC, 1996.

4. Storz, Gene E. and Dow, Thomas A., “Control of Fracture and Damage in Precision Contour Grinding,” Precision Engineering Center 1995 Annual Report, Vol. 13, pp 177-196, 1995.

FACULTY, STAFF AND STUDENTS OF THE PRECISION ENGINEERING CENTER

Standing (L to R): J. Eischen, A. Sohn, T. Dow, R. Scattergood, M. Heinrich, M. Bauer, K. Garrard

Sitting: T. Wu, M. Cerniway, P. Ro, E. Meng, D. Gill

On Floor: M. Gou, B. Love, M. Lee, D. Kametz and Q. Wan

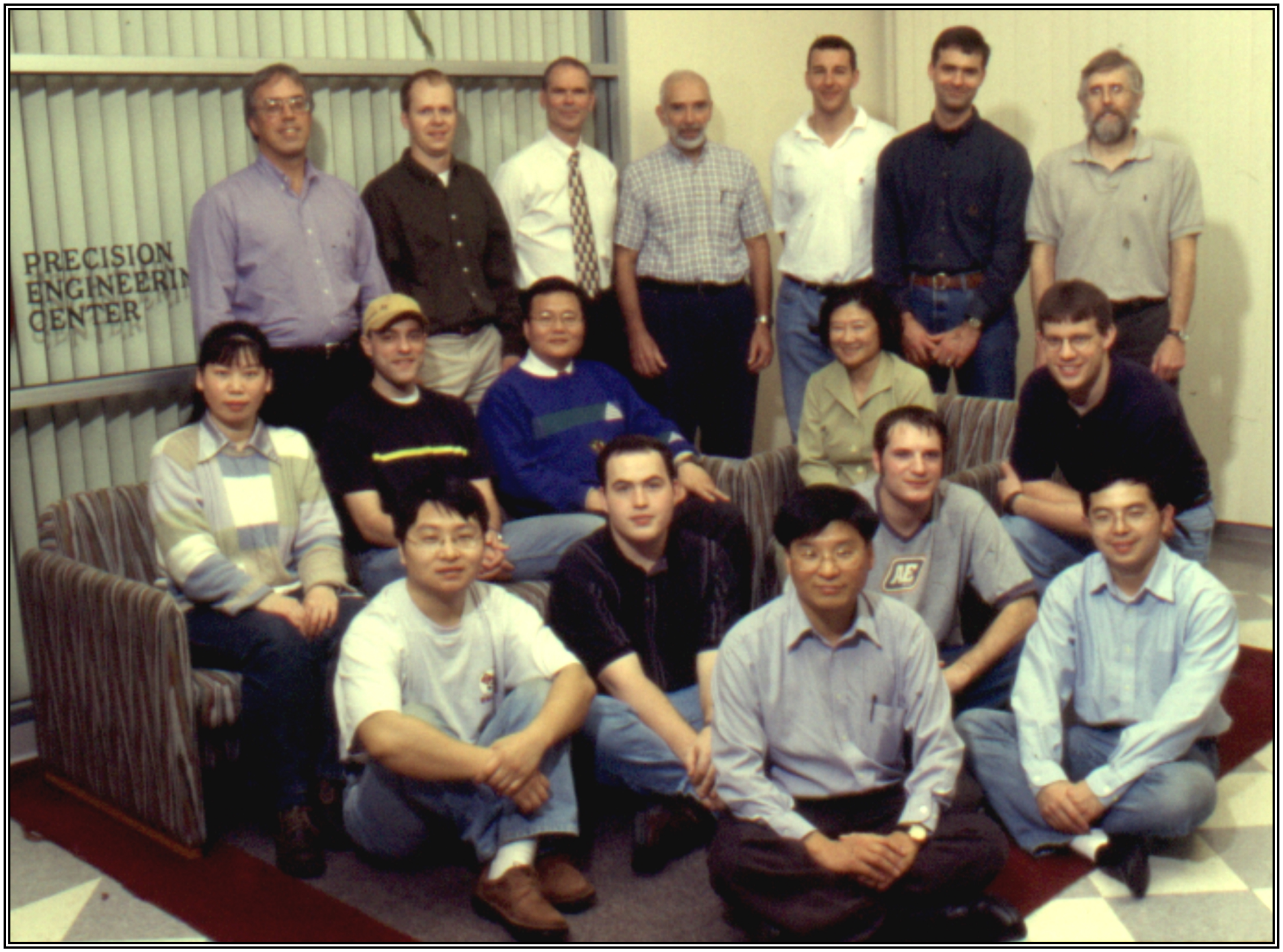

FACULTY, STAFF AND STUDENTS OF THE PRECISION ENGINEERING CENTER

Standing (L to R): J. Eischen, A. Sohn, T. Dow, R. Scattergood, M. Heinrich, M. Bauer, K. Garrard

Sitting: T. Wu, M. Cerniway, P. Ro, E. Meng, D. Gill

On Floor: M. Gou, B. Love, M. Lee, D. Kametz and Q. Wan

FACULTY

THOMAS A. DOW

Director, Precision Engineering Center
Professor, Department of Mechanical and Aerospace Engineering

BS, Mechanical Engineering, Virginia Polytechnical Institute, 1966
MS, Engineering Design, Case Institute of Technology, 1968
PhD, Mechanical Engineering, Northwestern University, 1972

After receiving his PhD degree from Northwestern University in 1972, Dr. Dow joined the Tribology Section of Battelle Columbus Laboratories and worked there for ten years. His research interests were in the areas of friction and wear and included studies on a wide variety of topics from lubrication of cold-rolling mills using oil-in-water emulsions to wet braking effectiveness of bicycle brakes to elastohydrodynamic lubricant film generation in ball and roller bearings. He developed experimental apparatuses, established analytical models, and corroborated those analyses with experimental measurements. Dr. Dow joined the faculty at North Carolina State University in 1982 and was instrumental in developing the academic and research program in precision engineering. His current research interests include the design of precision machining systems, real-time control, and metrology. He was one of the founders of the American Society for Precision Engineering and currently acts as the Executive Director.

GREGORY D. BUCKNER

Assistant Professor, Department of Mechanical and Aerospace Engineering

BS, Mechanical Engineering, Louisiana State University, 1986
MS, Mechanical Engineering, Virginia Polytechnic Institute, 1987
PhD, Mechanical Engineering, University of Texas at Austin, 1996

After receiving his PhD degree from the University of Texas at Austin in 1996, Dr. Buckner joined the University of Texas Center for Electromechanics (UT-CEM), where he served as a research engineer until 1999. His research at UT-CEM focused on the design and implementation of advanced controllers for electromechanical systems. Applications included self-learning control systems for active vehicle suspensions, magnetic bearings for flywheel systems, and manufacturing processes. Dr. Buckner joined the faculty at North Carolina State University in 1999 as an Assistant Professor of Mechanical and Aerospace Engineering. Dr. Buckner's research and teaching interests focus on the design and control of electromechanical systems, with an emphasis on self-learning algorithms. Current research topics include electromechanical actuators for system identification of milling processes, and magnetic bearings for flywheel and milling applications.

JEFFREY W. EISCHEN

Associate Professor
Department of Mechanical and Aerospace Engineering

BS, Mechanical Engineering, UCLA, 1978
MS, Mechanical Engineering, Stanford University, 1981
PhD, Mechanical Engineering, Stanford University, 1986

Dr. Eischen has been with N.C. State since 1986 and his research areas of interest include computational solid mechanics, elasticity, fracture mechanics and structural dynamics. Dr. Eischen worked with Failure Analysis Associates from June 1978 - June 1986 as a Mechanical Engineer. His primary responsibilities included analysis and prevention of industrial equipment failures.

KARL J. FALTER

Senior Development Engineer, Eastman Kodak Company
Adjunct Assistant Professor, Department of Mechanical and Aerospace Engineering

BS, Mechanical Engineering NC State University, 1988
MS, Mechanical Engineering NC State University, 1990
PhD, Mechanical Engineering NC State University, 1992

Prior to joining Eastman Kodak's Manufacturing Systems Technology Division in 1997, Dr. Falter was a Research Engineer for Rank-Pneumo, a division of Rank-Taylor Hobson. He also assisted the Rank-Taylor fellows in their research at the Precision Engineering Center. Dr. Falter previously worked as a post graduate researcher at the Precision Engineering Center on a variety of projects. These projects ranged from study of the acoustic disturbance of a diamond turning machine to finite element analysis of diamond tools. Dr. Falter's PhD dissertation concerned simplifications of finite element models used in the shock response analysis of electronic assemblies. His MS thesis, which concerned a laboratory technique used to measure power flow in vibrating structures, was completed as a student in the Precision Engineering Center.

HANS HALLEN

Assistant Professor
Department of Physics

BS, Engineering Physics, Cornell University, 1984
MS, Applied Physics, Cornell University, 1986
PhD, Applied Physics, Minor: Mathematics, Cornell University, 1991

Hans Hallen is a member of the Precision Engineering Center in addition to being on the Physics faculty, and has had considerable experience applying scanning proximal probes in a variety of environments, including ambient, ultra high vacuum, and low temperature. His emphasis has been on developing and applying probes with spectroscopic and subsurface analysis capabilities at the nanometer level. Hallen was the first to develop a submicron resolution scanning Hall probe instrument, and among the first to use ballistic electron emission microscopy to study electron transport and defect behavior in thin metallic films. He has built an extremely stable near-field scanning optical microscope (NSOM) instrument for high resolution spectroscopic use at room and low temperature and used it for NSOM-Raman studies that identified its several differences from far-field Raman and produced the first NSOM-Raman images. He has adapted NSOM for time-resolved optical studies and quantitatively measured and mapped excess carrier lifetimes on silicon with nanometer-scale resolution. Current NSOM efforts include using pulsed laser techniques for diffusion mapping and studies of exciton droplets in silicon, and a sub-100nm-resolution method of identifying dopant concentrations and surface passivation with a near-UV NSOM. Other collaborative efforts include improving wireless communications by predicting the channel far into the future (a few fades) using propagation physics, studies of particulates from the air, and evaluation of the optical properties of single point diamond turned optics.

PAUL I. RO

Associate Professor
Mechanical and Aerospace Engineering Department

BS, Mechanical Engineering, University of Minnesota, 1982
MS, Mechanical Engineering, Massachusetts Institute of Technology, 1985
PhD, Mechanical Engineering, Massachusetts Institute of Technology, 1989

Dr. Ro joined the faculty of North Carolina State University in January 1989, as an Assistant Professor in the Mechanical & Aerospace Engineering Department. He became an Associate Professor in July 1994. Dr. Ro has developed two graduate courses in the department (multivariable Control and Robotics) and has taught undergraduate Automatic Control and Dynamics courses. His research covers a wide range of controls and various applications of control theories in the following three areas: Precision Engineering, Robotics and Intelligent Vehicle Control.

In precision engineering, Dr. Ro's research concentrates on the characterization and control of microdynamic behaviors of precision slide systems (ball-screw, traction drive, piezo-electric drive, electrostatic drives and magnetic servo levitated drive) to enhance their nano-motion capabilities, development of advanced control schemes and experimental verifications to improve diamond turning process using force and position sensory feedbacks, design of a long-range fast tool servo system using magnetic servo levitated actuators, and active control of precision slide vibration using piezo-electric drives. In robotics, some of the on-going projects include design and implementation of free-floating non-holonomic space robot and a planar passive-joint robot for fuel consumption minimization, neural-fuzzy hybrid scheme for mobile robot path planning, and two-arm coordinated motion control for fixtureless assembly. In intelligent vehicle control, on-going projects include nonlinear tire model identification by Artificial Neural Network, hybrid neural-sliding mode control of 4 Wheel steering for robust handling, semi-active suspension control using energy based Fuzzy Logic scheme, and others.

PHILLIP E. RUSSELL

Professor
Department of Materials Science and Engineering

BS, Physics, Appalachian State University, 1975
MS, Physics, West Virginia University, 1977
PhD, Materials Science and Engineering, University of Florida, 1982

After graduate work at the University of Florida, Dr. Russell joined the Solar Energy Research Institute (a DOE lab) in Golden Co. in 1980. There he developed a photovoltic materials and device characterization laboratory with emphasis on electron and ion beam analytical instrumentation. After three years at SERI, Dr. Russell joined JEOL, Inc. in Boston, Massachusetts, an electron optical instrumentation company where he led the technical and application groups. One of his major projects was the development of an electron beam based integrated circuit metrology system. He was also involved in the development and application of focused ion beam systems and electron beam lithography systems, as well as numerous analytical instrumentation projects.

On joining North Carolina State University, Dr. Russell took on the role of Director of the Analytical Instrumentation Facility and has established graduate level courses in electron optics and electron optical instrumentation techniques. He was awarded the NSF Presidential Young Investigator Award in 1987. His research at NCSU and the Precision Engineering Center are in the areas of Scanned Probe Microscopy, Focused Ion Beam Technology, Scanning Electron Microscopy, Lithography metrology and beam testing of integrated circuits.

RONALD O. SCATTERGOOD

Professor
Materials Science and Engineering Department

BS, Metallurgical Engineering, Lehigh University, 1961
MS, Metallurgy, Massachusetts Institute of Technology, 1963
PhD, Metallurgy, Massachusetts Institute of Technology, 1968

R.O. Scattergood is a Professor in the Department of Materials Science and Engineering. He received BS degrees in Mining Engineering and Metallurgical Engineering from Lehigh University. His MS and PhD degrees were obtained in Metallurgy from M.I.T. In 1968 he became a member of the basic research staff in the Materials Science Division at the Argonne National Laboratory. In 1981, he joined the faculty as a Professor of Materials Engineering at North Carolina State University.

Professor Scattergood's major research interests have been focused on the mechanical behavior of solids. He has worked in the areas of strengthening mechanisms in solids, continuum theory of defects, radiation effects, wear and fracture processes in ceramics, and precision engineering with emphasis on machining processes. He has expertise in both analytical and computer modeling as well as in mechanical testing methods and microscopy. He has published over 140 technical papers, books and reports.

ALBERT J. SHIH

Associate Professor
Mechanical and Aerospace Engineering

BSME, National Cheng Kung University, Taiwan, 1984
MSME, National Cheng Kung University, Taiwan, 1986
PhD, Purdue University, 1991

Before joining N.C. State University in 1998, Dr. Shih worked in the Fuel Systems and Technical Center of Cummins Engine Company for seven years. He developed innovative and cost-effective manufacturing processes for sub-micron precision grinding of ceramic and hardened steel diesel engine components. He also worked in teams to implement the sub-micron precision ceramic plungers for diesel fuel systems. He led a team of three companies, Cummins Engine Co., Milacron, Inc. and Goldcrown (part of the UNOVA) to win a NIST ATP (Advanced Technology Program) grant on "Sub-micron Precision Grinding of Advanced Engineering Materials" in 1997. At Cummins, he continued to conduct basic research and publish results in the broad area of mechanical engineering.

DAVID YOUDEN

Technical Associate, Eastman Kodak Company
Adjunct Lecturer, Department of Mechanical and Aerospace Engineering

ASME, Central New England College, Worcester, MA, 1965

Prior to joining Eastman Kodak's Manufacturing Systems Technology Division in 1997, Mr. Youden was Research and Development Manager at Rank Pneumo, a division of Rank Taylor Hobson Inc. for ten years. Before that, he was Director of Engineering at the Cone Blanchard Machine Company. He has also worked at Ocean Systems, Inc. of Reston, Virginia and the Heald Machine Company, a division of Cincinnati Milacron. During his professional career, Mr. Youden has been granted numerous patents in the field of machine tools, and he has published and presented technical papers on the design and testing of ultra-precision machine tools in the US, Japan, and Germany.

Mr. Youden graduated from Central New England College and attended Worcester Polytechnic Institute and Clark University. He is a charter member of the American Society for Precision Engineering.

STAFF

KENNETH P. GARRARD

Research Assistant
Precision Engineering Center

BS, Computer Science, North Carolina State University, 1979
MS, Computer Studies, North Carolina State University, 1983

As a full-time research assistant, Mr. Garrard is studying the design of systems software that supports the development of high-speed real-time applications for special purpose multiprocessor computer systems. He has several years experience in academia and industry designing and implementing real-time systems. As a Precision Engineering Center staff member, Mr. Garrard's current activities include the design and implementation of software for Diamond Turning Machine and Fast Tool Servo controller projects.

ENA MENG

Administrative Assistant
Precision Engineering Center

BS, English, Taiwan University, 1963
MS, Library Science , Vanderbilt University, 1965

Ms. Meng became a member of the PEC Staff in November 1999. Previously she was a professional librarian at Michigan State University, East Lansing MI and a Business planner and financial analyst at IBM Corp., Cary, NC. Ms. Meng brings to the Center many years of financial and personnel management experience, as well as office administration skills. In addition to her accounting responsibilities, Ms. Meng provides the overall administrative support for the Center.

ALEXANDER SOHN

Research Assistant/Lecturer
Precision Engineering Center

B.S., Physics, University of Texas at Arlington, 1992
M.S., Physics, University of Texas at Arlington, 1994

Mr. Sohn joined the Precision Engineering Center in August, 1997 as a member of the technical staff. His current research interests range from machine design and metrology to the design and fabrication of nonimaging optics. Mr. Sohn's varied research activities began in microwave optics and atomic physics as a student at the University of Texas at Arlington and later progressed to precision machine design, design and fabrication of plastic optics as well as automation and machine vision at Fresnel Technologies, Inc. in Fort Worth, Texas.

GRADUATE STUDENTS DURING 2000

BRAD AUSTIN received his BS degree in Materials Science and Engineering from NC State University in 1998. During his undergraduate work, he worked in the Materials Engineering Laboratory at IBM in the Research Triangle. He is currently pursuing his MS degree in Materials Science and Engineering. His research involves studying the mechanical effects from the scribing of brittle materials.

MARKUS BAUER received his MS degree in Mechanical Engineering (Diplom-Ingenieur) in March 1998 at RWTH-Aachen (Technical University of Aachen, Germany). For his Master's thesis he designed a computer-controlled robotic manipulator arm using PZT actuators to control joint impedance and incremental angular encoders for position feedback. He is currently pursing a PhD degree in Mechanical Engineering. His research involves the design and implementation of an ultrasonic piezoelectric motor.

MATTHEW A. CERNIWAY received his BS degree in Mechanical Engineering from NC State University in 1996. Matthew's professional experience covers a wide range of engineering fields. Ranging from facility design and management with Nan Ya Plastics to equipment design with II-VI Inc and most recently as a field advisor to the Polar Ice Coring Office on the NSF's '99 Drilling season in Siple Dome, Antartica. Matthew is currently working towards his MS degree in Mechanical Engineering. His on going research is the "Ultra-Mill", a high speed piezo-actuated mill, sponsored by Kodak.

DAVID GILL received his BS degree in Mechanical Engineering from Texas Tech University in 1994. He completed a MS degree in Mechanical Engineering from Purdue University in 1997 in the area of Computer Aided Design and Manufacturing. Prior to coming to N. C. State in 1999, he worked in Manufacturing Engineering and Product Engineering at Caterpillar, Inc. Currently he is working towards a Ph.D. in Mechanical Engineering. His specific area of study and research is precision replication of optics.

MATIAS HEINRICH received his BS degree in Mechanical Engineering from NC State University in December of 1998. After working on the development of a third axis for the Nanoform 600 Diamond Turning Machine, he returned full time to pursue his MS degree at the PEC in the Summer of 1999. His research focuses on the development of a Piezoelectric Motor for use in Cryogenic environments of space. Design specifications are based on those for the Next

Generation Space Telescope (NGST) that will utilize such motors for the fine adjustment of a large flexible optical mirror.

DAVID KAMETZ received his BS degree in Mechanical Engineering in August of 2000 at Clarkson University in Potsdam, NY. David had a second major in Aeronautical Engineering while at Clarkson, but did not complete the program in order to enroll in graduate school. While at Clarkson he was the team leader of his senior design group in both his mechanical engineering and aeronautical engineering programs. His first semester at NCSU was spent as a teaching assistant in the machine shop, where he taught welding, machining and fabrication. David's research for IBM involves the improvement of both manufacturing lapping plates and the lapping process.

BYOUNG-GOOK LOH received his BS in Mechanical Engineering from Korea University in 1993 and his MS in Mechanical Engineering from North Carolina State University in 1995. Before coming the N.C. State, he spent 1 1/2 years working for POSCO Engineering & Construction Company in Seoul, Korea as an assistant project coordinator. Currently he is pursuing a Doctorate in Mechanical Engineering. His research involves the design and implementation of an ultrasonic material handling device.

MICHAEL LONG is a PhD student in Mechanical Engineering studying new designs for stiff high resolution load cells. Mr. Long received his BS and MS in Mechanical Engineering from Bucknell University in 1981. He is a full time employee of Eastman Kodak and has been awarded an Eastman Kodak Graduate Fellowship to pursue a PhD degree at North Carolina State University.

BRYAN LOVE received his BS degree in Mechanical Engineering from NC State University in May of 1999. After working in the product development group at Controls Southeast, Incorporated this past summer, he returned to NC State to work on his MS degree in Mechanical Engineering. His specific area of study and research is stress analysis and finite element modeling.

EDWARD MILLER began his post-secondary education at Central Virginia Community College where he earned an associate degree in Mechanical Engineering Technologies in 1995. He then transferred to the University of Virginia's School of Engineering and Applied Sciences. In 1998 he received a Bachelor of Science degree in Mechanical Engineering. Currently, Mr. Miller is pursuing a Master's of Science degree in Mechanical Engineering at N.C. State University. His research involves an investigation of deflections of high-speed miniature milling tools and the ability to compensate for tool deflections.

GANG MOU received his BS and MS degree in Mechanical Engineering from Sichuan Institute of Technology, China, in 1992 and 1995 respectively. Prior to come to NC State University in Fall 1999, he worked in an engineering company at Chinese Academy of Sciences. He is currently pursuing a PhD degree in Mechanical Engineering. His specific area of study and research is control technology and its application.

JUN QU received his BS and Master's degrees in Precision Instrument Engineering from Tianjin University in People's Republic of China in 1995 and 1998. He received his second Master's degree in Mechanical Engineering from Iowa State University in 1999. Currently he is pursuing a Ph.D. degree in Mechanical Engineering. His specific area of study and research is Precision Engineering.

QUN WAN received his B.S. degree in Thermophysics from University of Science and Technology of China in 1996. After working as manufacturing engineer in Teling (TRANE CHINA) Air-Conditioning Co. Ltd for one year, he came to the National University of Singapore, where he received his M.S. degree in Mechanical and Production Engineering in 2000. Prior to come to NC State University in Fall 2000, Qun had worked as software engineer in Vector Technology Co. Ltd (Singapore). Currently, he is a PhD student under Dr. Andrey Kuznetsov and his research focuses on Numeric Simulation on Cooling Effect of Ultrasonic Acoustic Streaming.

TAO WU received her BS and MS degree in Electrical Engineering from Northwestern Polytechnic University, China in 1993 and 1996. Prior to coming to NCSU in August 2000, She also received her PhD degree in Electrical Engineering in Shanghai Jiaotong University, China in 1999 and studied in University of Virginia for one year. Currently she is a PhD student in Mechanical and Aerospace Engineering and her research focuses on the development of a novel ultrasonic cooling concept for microelectronics.

GRADUATES OF THE PRECISION ENGINEERING CENTER

Student	Degree	Date	Company/Location
Jeffrey Abler	PhD	December 1994	ETEC Systems, Inc. Tucson, AZ
William Allen	PhD	December 1994	North Carolina State Univ. Raleigh, NC
Kelly Allred	MS	June 1988	
Christopher Arcona	PhD	May 1993	Norton Worcester, MA
Bradford Austin	MS	June 2000	IBM Corporation Fishkill, NY
Tom Bifano	PhD	June 1988	Boston University Boston, MA
Scott Blackley	MS	May 1990	Motorola Austin, TX
Peter Blake	PhD	December 1988	NASA Goddard Greenbelt, MD
Mark Cagle	MS	June 1986	NASA-Langley Norfolk, VA
John Carroll	PhD	January 1986	Cummins Engine Co. Columbus, IN
Damon Christenbury	MS	June 1985	Michelin Tire Co. Spartanburg, SC
James Cuttino	PhD	December 1994	UNC – Charlotte Charlotte, NC
Bob Day	PhD	July 1998	Los Alamos National Lab Los Alamos, NM
Joseph Drescher	PhD	May 1992	Pratt & Whitney East Hartford, CT
William Enloe	MS	December 1988	ITT Roanoke, VA
Karl Falter	MS	December 1989	Eastman Kodak Company Raleigh, NC

Peter Falter	PhD	May 1990	Lockheed-Martin Orlando, Florida
John Fasick	MS	May 1998	Burleigh Instruments Fishers, NY
Steven Fawcett	PhD	June 1991	MicroE Natick, MA
Andre Fredette	PhD	May 1993	IBM Research Triangle Park, NC
Jim Gleeson	MS	June 1986	Battelle Columbus Labs Columbus, OH
Mary Smith Golding	MS	May 1990	Harris Corporation Melbourne, FL
David Grigg	PhD	August 1992	Zygo Corporation Middlefield, CT
Hector Gutierrez	PhD	October 1997	Florida Inst. Of Tech. Melbourne, FL.
Christian Haeuber	MS	December 1996	Harris Corporation Melbourne, FL
Gary Hiatt	PhD	May 1992	Caterpiller Zebulon, NC
Peter Hubbel	MS	December 1991	Delco Electronics Kokomo, IN
Konrad Jarausch	PhD	December 1999	Intel Corporation San Jose, CA
Bradley Jared	PhD	December 1999	Corning Inc. Corning, NY
Jerry Kannel	PhD	June 1986	Battelle Columbus Labs Columbus, OH
Byron Knight	MS	May 1990	Harris Corporation Melbourne, FL
Mark Landy	MS	June 1986	Battelle Columbus Labs Columbus, OH
Mike Loewenthal	MS	December 1988	Cummins Engine Co. Columbus, IN
Michael Long	PhD	June 2000	Eastman Kodak Rochester, NY

Michael Hung-Tai Luh	MS	June 1989	Proctor and Gamble Cincinnati, OH
Dan Luttrell	MS	1987	Corning, Inc. Corning, NY
Edward Marino	MS	September 1999	Pratt Whitney Hartford, CT
Edward Miller	MS	December 2000	General Electric Greenville, SC
Michele Miller	PhD	December 1994	Michigan Tech. University Houghton, MI
Paul Minor	MS	September 1998	Pratt & Whitney Palm Beach, FL
Gary Mitchum	MS	June 1987	Harris Corporation Melbourne, FL
Charles Mooney	MS	December 1994	JEOL Peabody, MA
Larry Mosley	PhD	June 1987	Intel Corporation Chandler, AZ
Patrick Moyer	PhD	May 1993	UNC-Charlotte Charlotte, NC
Ayodele Oyewole	MS	October 1997	Pratt & Whitney East Hartford, CT
Hakan Ozisik	PhD	December 1989	Aerospace Corporation Long Beach, CA
John Pellerin	MS	May 1990	Sematech Austin, TX
Ganesh Rao	MS	December 1994	Oak Ridge National Lab Oak Ridge, TN
John Richards	MS	September 1997	Intel Corporation San Jose, CA
Walter Rosenberger	MS	May 1993	The East Group Kinston, NC
Alex Ruxton	MS	December 1996	Pratt &Whitney Palm Beach, Florida
Anthony Santavy	MS	August 1996	3M Corporation Petaluma, California

Keith Sharp	PhD	May 1998	Morganite Wales, England
Gordon Shedd	PhD	March 1991	Burleigh Instruments Fishers, NY
Wonbo Shim	PhD	May 2000	Seagate Inc. Oklahoma City, OK
Robert Skolnick	MS	September 1997	Chemtronics, Inc. San Diego, CA
Denise Skroch	MS	May 1989	IBM Corporation Raleigh, NC
Elizabeth Smith	MS	April 1989	
Stanley Smith	PhD	May 1993	Komag, Inc. Santa Clara, CA
Ronald Sparks	PhD	May 1991	Alcoa Corporation Pittsburg, PA
Brent Stancil	MS	December 1996	Harris Corporation Melbourne, FL
Gene Storz	MS	May 1994	
Anand Tanikella	PhD	August 1996	Norton Industrial Ceramics Northboro, MA
Donna Thaus	MS	May 1996	Northern Telecom Research Triangle Park, NC
John Thornton	MS	December 1993	Digital Instruments Santa Barbara, CA
Michael Tidwell	MS	December 1991	
John Tyner	MS	June 1995	Naval Depot - Cherry Point

ACADEMIC PROGRAM

Problems and limitations associated with precision manufacturing can originate in the machine, the process, or the material. In fact, most problems will probably be caused by a combination of these factors. Therefore, improvement of current processes and development of new manufacturing methods will require knowledge of a multi-disciplinary array of subjects. The educational goal of the Precision Engineering Center is to develop an academic program which will educate scientists and engineers in metrology, control, materials, and the manufacturing methods of precision engineering.

The graduate students involved in the Precision Engineering Center have an annual stipend as research assistants. They can take up to 3 classes each semester while spending about 20 hours per week on their research projects. These students also work in the Center full-time during the summer months.

The Precision Engineering Center began in 1982 with an emphasis on the mechanical engineering problems associated with precision engineering. As a result, the original academic program proposed was biased toward courses related to mechanical design and analysis. However, as the research program has developed, the need for complementary research in sensors, materials, and computers has become obvious. A graduate student capable of making valuable contributions in the computer area, for example, will require a significantly different academic program than in mechanical engineering. For this reason, the Center faculty have set a core curriculum and each student in the program is required to take at least 3 of these core courses. The remainder of the courses for the MS or the PhD degree are determined by the university or department requirements and the faculty committee of the student.

The required courses are:

- MAE 545 Metrology in Precision Manufacturing
- PY 516 Physical Optics
- MAT 700 Modern Concepts in Materials Science
- CSC (ECE) 714 Real Time Computer Systems

PhD DEGREE PROGRAM

The PhD program in Precision Engineering has been set up as a multi-disciplinary program, drawing upon courses throughout the University to provide background and expertise for the students. It should contain required courses to insure solid grounding in the fundamentals plus electives to prepare the student in his area of specialization. Because Precision Engineering is concerned with an integrated manufacturing process, students interested in computer control, materials, machine structure, and measurement and actuation systems are involved in the program. Student research projects include the wide variety of topics addressed in this report. Each student's thesis should have an experimental component because Precision Engineering is basically a hands-on technology.

MS DEGREE PROGRAM

The Master of Science degree will have a higher percentage of application courses than the PhD degree. The emphasis will be to develop the foundation for involvement in precision engineering research and development. A total of 30 credits including 6 credits for the MS thesis is required. The thesis, while less comprehensive than the PhD dissertation, will be directed at important problems in Precision Engineering. Typically the MS program will take four semesters plus one summer.

UNDERGRADUATE PROGRAM

The undergraduate degree broadly prepares an engineering student for industrial activities ranging from product design and engineering sales to production implementation. Because a large share of engineers only have the BS degree, these will be the people who must implement the new technology developed in research programs like the Precision Engineering Center. Therefore, a way must be found to acquaint engineers at the BS level with the techniques, problems, and potential of precision manufacturing.

In most undergraduate degree programs only limited time is available for technical electives. However, these electives offer the student the opportunity to expand his knowledge in many different directions. Beginning graduate courses (such as metrology) can be used as undergraduate electives.

Undergraduate projects and summer employment have also been utilized to include undergraduate students into the research program of the Center. During the 1998-1999 academic year, four undergraduate students in Mechanical Engineering were involved various projects at the PEC.

STUDY PLANS

Study plans for several example students are given below both for the MS and the PhD degree. Because of the breadth of the field and the wide range of thesis topics, few if any study plans will be exactly the same. The plan will depend upon the student's background, his interests, his thesis topic, the department, and the chairman and members of his committee.

PhD PROGRAM IN MECHANICAL ENGINEERING

Major Courses:

•	MAE	740	Advanced Machine Design I
•	MAE	741	Advanced Machine Design II
•	MAE	706	Heat Transfer Theory & Applications
•	MAE	713	Principles of Structural Vibration
•	MAE	760	Computational Fluid Mechanics and Heat Transfer
•	MAE	545	Metrology in Precision Manufacturing
•	MAE	715	Nonlinear Vibrations
•	MAE	716	Random Vibration
•	MAE	714	Analytical Methods in Structural Vibration
•	MAE	742	Mechanical Design for Automated Assembly
•	MAE	895	Doctoral Dissertation Research

Minor Courses:

•	MA	511	Advanced Calculus I
•	MA	775	Mathematical Methods in the Physical Sciences I
•	CSC	780	Numerical Analysis II
•	PY	516	Physical Optics
•	ECE	716	System Control Engineering
•	MAT	700	Modern Concepts in Materials Science
•	ECE	726	Advanced Feedback Control
•	ECE	764	Digital Image Processing

PhD PROGRAM IN MATERIALS ENGINEERING

Major Courses:

MAT	710	Elements of Crystallography and Diffraction
MAT	700	Modern Concepts in Materials Science
MAT	556	Composite Materials
MAT	715	Transmission Electron Microscopy
MAT	795	Defect Analysis/Advanced Materials Experiments
MAT	753	Advanced Mechanical Properties of Materials
MAT	712	Scanning Electron Microscopy
MAT	895	Doctoral Dissertation Research

Minor Courses:

PY	414	Electromagnetism I
ST	502	Experimental Statistics for Engineers I
MAE	740	Advanced Machine Design I
MAE	741	Advanced Machine Design II
MAE	545	Metrology in Precision Manufacturing
PY	516	Physical Optics
MA	401	Applied Differential Equations II

PhD PROGRAM IN ME (FOR STUDENT WITH MS DEGREE)

ECE	716	System Control Engineering
ECE	791	Gate Array Design
MAT	700	Modern Concepts in Materials Science
PY	516	Physical Optics
MA	502	Advanced Mathematics for Engineers and Scientists II
MA	775	Mathematical Methods in the Physical Sciences I
MA	780	Numerical Analysis II
MAE	732	Fundamentals of Metal Machining Theory
MAE	740	Advanced Machine Design I
MAE	741	Advanced Machine Design II
MAE	545	Metrology in Precision Manufacturing
MAE	716	Random Vibration

MS PROGRAM FOR ME STUDENT

MAE	713	Principles of Structural Vibration
MAE	740	Advanced Machine Design I
MAE	545	Metrology in Precision Manufacturing
MAT	700	Modern Concepts in Materials Science
PY	516	Physical Optics
MA	501	Advanced Math for Engineers and Scientists I
MA	502	Advanced Math for Engineers and Scientists II
MAE	695	Master's Thesis Research

MS PROGRAM FOR COMPUTER SCIENCE STUDENT

CSC	501	Operating Systems Principles
CSC	506	Architecture of Parallel Computers
CSC	512	Compiler Construction
ECE	521	Computer Design and Technology
CSC	715	Concurrent Software Systems
MAE	545	Metrology for Precision Manufacturing
MAE	789	Digital Control Systems
ECE	764	Digital Image Processing

MS PROGRAM FOR MATERIALS SCIENCE STUDENT

MAT	700	Modern Concepts in Material Science
MAT	710	Elements of Crystallography and Diffraction
MAT	715	Transmission Electron Microscopy
MAT	712	Scanning Electron Microscopy
MAT	722	Advanced Scanning Electron Microscopy and Surface Analysis
MAE	545	Metrology for Precision Manufacturing
PY	516	Physical Optics
ECE	738	IC Technology and Fabrication
MAT	695	Master's Thesis Research

MS PROGRAM FOR PHYSICS STUDENT

- PY 516 Physical Optics
- PY 552 Introduction to Structure of Solids I
- PY 753 Introduction to Structure of Solids II
- PY 781 Quantum Mechanics I
- PY 782 Quantum Mechanics II
- PY 783 Advanced Classical Mechanics
- PY 785 Advanced Electricity and Magnetism I
- PY 786 Advanced Electricity and Magnetism II
- MAT 700 Modern Concepts in Material Science
- MAE 545 Metrology for Precision Manufacturing
- PY 695 Master's Thesis Research

SHORT COURSES AND TV COURSES

Six graduate level courses: Scanning Electron Microscopy (MAT 712), Advanced SEM Surface Analysis (MAT 722), Modern Concepts in Material Science (MAT 700), Mechanical Properties of Materials (MAT 705), and Metrology (MAE 545) have been offered as video courses nationwide via National Technological University. In a typical year, approximately 120 students from industry and national laboratories participate in these courses. Future plans call for a MS program in Precision Engineering to be offered via the television network.

TECHNICAL REPORTS

Volume 1 - 1983	December 1983	136 pages
Volume 2 - 1984	January 1985	168 pages
Volume 3 - 1985	January 1986	294 pages
Volume 4 - 1986	January 1987	255 pages
Volume 5 - 1987	December 1987	336 pages
Volume 6 - 1988	December 1988	362 pages
Volume 7 - 1989	March 1990	357 pages
Volume 8 - 1990	March 1991	385 pages
Volume 9 - 1991	March 1992	382 pages
Volume 10 - 1992	March 1993	289 pages
Volume 11 - 1993	March 1994	316 pages
Volume 12 - 1994	March 1995	268 pages
Volume 13 - 1995	January 1996	251 pages
Volume 14 - 1996	January 1997	232 pages
Volume 15 - 1997	January 1998	298 pages

PUBLICATIONS

PAPERS PUBLISHED

1. Austin, B., B. Love, T.A. Dow, J. Eischen and R.O. Scattergood, "Bending Deflections Due to Scribe-induced Residual Stresses", *Proceedings of the 2000 American Society for Precision Engineering 15th Annual Meeting,* pp. 559-562.

2. Bauer, M.G., T.A. Dow, "Design of a Linear High Precision Ultrasonic Piezoelectric Motor", *Proceedings of the 2000 American Society for Precision Engineering 15th Annual Meeting,* pp. 180-183.

3. Buckner, Gregory D., "Intelligent Sliding Mode Control of Turning Operations", 9th International Conference on Intelligent Systems (ICIS-2000), Louisville, KY, June 2000.

4. Buckner, Gregory D., Karl T. Schuetze, and J. Beno, "Active Vehicle Suspension Control Using Intelligent Feedback Linearization", American Controls Conference, Chicago, IL, June 2000.

5. Cerniway, M.A. and T.A. Dow, "Three-dimensional Machining of Optical Quality Surfaces", *Proceedings of the 2000 American Society for Precision Engineering 15th Annual Meeting,* pp. 42-45.

6. Gill, D.D., T.A. Dow, A. Sohn, "Precision Replication of Optics", *Proceedings of the 2000 American Society for Precision Engineering 15th Annual Meeting,* pp. 136-139.

7. Heinrich, M.D., T.A. Dow, "Design of a Piezo Actuator for Cryogenic Environments", *Proceedings of the 2000 American Society for Precision Engineering 15th Annual Meeting,* pp. 203-206.

8. Hong, D.H., P.I. Ro, "The Law of Large Numbers for Fuzzy Numbers with Unbounded Supports", *International Journal of Fuzzy Sets and Systems*, Vol. 116, No. 2, pp. 269-274, 2000.

9. Kim, C.and P.I. Ro, "Reduced Order Modeling and Parameter Estimation for Quarter Car Suspension System", *Journal of Automobile Engineering, IMechE*, Vol. 214, Part D, pp. 851-864, 2000.

10. Loh, B.G., P.I. Ro, “Change of Propagation Direction of Flexural Ultrasonic Traveling Waves by Modulating Excitation Frequency” , *Journal of Sound and Vibration,* 238(1), pp. 171-178, 2000.

11. Loh, B.G., P.I. Ro, “On Object Transport System Using Flexural Ultrasonic Progressive Waves Generated by Two-Mode Excitation”, *IEEE Trans. On Ultrasonics, Ferroelectrics, and Frequency Control,* Vol. 47, No. 4, pp. 994-999, July 2000.

12. Ro, P.I., B G. Loh, and J. Santiago, “ Feasibility of Contact and Non-contact Approaches o Material Handling using Traveling Waves and Transition Characteristics”, *IEEE Trans. On Industrial Electronics,* Vol. 47, No. 6, pp. 1134-1135. 2000.

13. Shih, A.J. "An Experimental Investigation of Rotary Truing and Dressing of Vitreous Bond Wheels for Ceramic Grinding", *International Journal of Machine Tool and Manufacture*, Vol. 40, pp. 1755-1774, 2000.

14. Shih, A.J., M.B. Grant, T.M. Yonushonis, T.O. Morris and S.B. McSpadden, "High speed and High Material Removal Rate Grinding of Ceramics Using the Vitreous Bond CBN wheel", *Machining Science and Technology,* Vol. 4, No. 1, pp. 43-58, 2000.

15. Shim, W. and P.I. Ro, “Robust Friction Compensation for Submicron Positioning and Tracking for a Ball-screw Driven Slide System”, *Precision Engineering*, *Jour. of the International societies for Precision Engineers and Nanotechnology,* Vol. 24, No.2, pp. 160-173, April 2000.

16. Sohn, A., T.A. Dow and E.A. Marino, "A New Design for a Three-dimensional Measurement :robe", *Proceedings of the 2000 American Society for Precision Engineering 15th Annual Meeting,* pp.537-541.

REPORTS PUBLISHED

1. Sohn, A., T.A. Dow, "A New Design for a Three-dimensional Measurement Probe", 2000 Precision Engineering Center Interim Report, pp. 1-6, August 2000.

2. Austin, B.W., R.O. Scattergood, "Bend Effect Due to Scribing”, 2000 Precision Engineering Center Interim Report, pp. 7-12, August 2000.

3. Love, B.M. J.W. Eischen, "Distortion Due to Mechanical and Laser Scribing”, 2000

Precision Engineering Center Interim Report, pp. 13-18, August 2000.

4. Bauer, M.G., T.A. Dow, "Design of a Linear High Precision Ultrasonic Piezoelectric Motor", 2000 Precision Engineering Center Interim Report, pp. 19-24, August 2000.

5. Heinrich, M.D., T.A. Dow, ”Design of a Piezo Actuator for Cryogenic Environments,” 2000 Precision Engineering Center Interim Report, pp. 25-30, August 2000.

6. Loh, B.G., P.I. Ro, “Acoustic Streaming Induced by Ultrasonic Flexural Vibrations and Associated Enhancement of Convective Heat Transfer” 2000 Precision Engineering Center Inerim Report, pp. 31-38, August 2000.

7. Miller, E.L., T.A. Dow, "Deflection Prediction and Error Correction of High Speed Miniature Milling Tools", 2000 Precision Engineering Center Interim Report, pp. 39-44, August 2000.

8. Gill, D.D., T.A. Dow, "Precision Replication of Optics”, 2000 Precision Engineering Center Interim Report, pp. 45-50, August 2000.

9. Cerniway, M.A., T.A. Dow, "3-Dimensional Machining of Optical Quality Surfaces", 2000 Precision Engineering Center Interim Report, pp. 51-56, August 2000.

10. Qu, J., B. Rhoney, A.J. Shih, "Cylindrical Wire EDM of Cermets", 2000 Precision Engineering Center Interim Report, pp. 57-61, August 2000.

PAPERS SUBMITTED OR ACCEPTED FOR PUBLICATION AND PRESENTATIONS

1. Buckner, Gregory D., "Intelligent Sliding Mode Control of Cutting Force During Single-Point Turning Operations", accepted, *ASME Journal of Manufacturing Science and Engineering*.

2. Buckner, Gregory D., Karl T. Schuetze and J. Beno, "Intelligent Feedback Linearization for Active Vehicle Suspension Control", in review, *ASME Journal of Dynamic Systems,* Measurement, and Control.

3. Caprio, Matthew T. and Buckner, Gregory D., "Controlling the Torque-Speed

Characteristics of a Polyphase Induction Motor Using a Switched Rotor Ballast Network", in review, American Controls Conference, Washington, DC, June 2001.

4. Gutierrez, H., P.I. Ro, “A Modified Sliding Mode Control for Non-affine Systems with Algebraic Input Invertibility”, submitted to *the IEEE Trans. on Control Systems Technology,* 11/2000.

5. Kim , C., P.I. Ro, “An Accurate Full Car Ride Model Using Model Reduction Technique”, submitted to the *ASME Journal of Mechanical Design,* 8/00

6. Kim, C., P. I. Ro, “An Accurate Simple Model for Vehicle Handling using Model Reductin Technique”, submitted to the *Transactions of the SME, Journal of Passenger Cars,* 8/00

7. Loh, B.G. S. Hyun, P.I. Ro, C. Kleinstreuer, “Acoustic Streaming Induced by Ultrasonci Flexural Vibrations and Associated Enhancement of Convective Heat Transfer,” submitted to the *Journal of Acoustical Society of America,* 1/01

8. Ro, P.I.and B.G. Loh, “Feasibility of Using Ultrasonic Flexural Waves as a Cooling Mechanism”, *IEEE Trans. On Industrial Electronics*, accepted for publication, 8/00, in press

9. Shih, A.J. and J.L. Akemon , "Wear of the Blade Diamond Tools in Truing Vitreous Bond Grinding Wheels. Part I ˆ Wear Measurement and Results," accepted by *Wear.*

10. Shih, A.J. W.I. Clark, and J.L. Akemon, "Wear of the Blade Diamond Tools in Truing Vitreous Bond Grinding Wheels. Part II Truing and Grinding Forces and Wear Mechanism", accepted by *Wear.*

11. Shih, A.J., "A New Regulating Wheel Truing Method for Through-Feed Centerless Grinding", accepted by *ASME Journal of Manufacturing Science and Engineering*.

12. Shim, W., P.I. Ro, “Nonlinear Microdynamic Friction Compensation by Sliding Mode Control with Variable Switching Gain”, submitted to the *Journal of Mechatronics*, 8/00

THESES AND DISSERTATIONS

1. Austin, Bradford, *Scribing of Brittle Materials,* MS. Dissertation, North Carolina State University, July, 2000.

2. Long, Michael, *High Stiffness, Miniature Magnetoelastic Force Sensor* , Ph.D. Dissertation, North Carolina State University, May, 2000.

3. Miller, Edward, *Deflection Prediction and Error Correction of High Speed Miniature Milling Tools,* MS Dissertation, North Carolina State University, December, 2000.

4. Shim, Wonbo, *Robust Control and Characterization of Nonlinear Microdynamics in a Ball-Screw Driven Slide System,* Ph.D. Dissertation, North Carolina State University, January 2000.

PATENTS

1. Shih, A.J. and T.M. Yonushonis, "High infeed rate method for grinding ceramic workpiece with silicon carbide grinding wheels" US Patent Number 6,030,277, Feb. 29, 2000.

2. Shih, A.J., M.B. Grant and T.M. Yonushonis, "Constant force truing and dressing apparatus and method" US Patent Number 6,113,474, Sep. 5, 2000.